HAL open science

Study of the fatigue strength in the gigacycle regime of metallic alloys used in aeronautics and off-shore industries

Perez Mora Ruben

To cite this version:

Perez Mora Ruben. Study of the fatigue strength in the gigacycle regime of metallic alloys used in aeronautics and off-shore industries. Mechanics of materials [physics.class-ph]. Arts et Métiers ParisTech, 2010. English. NNT : 2010ENAM0027 . pastel-00671657

HAL Id: pastel-00671657

https://pastel.hal.science/pastel-00671657v1

Submitted on 18 Feb 2012

HAL is a multi-disciplinary open access archive for the deposit and dissemination of scientific research documents, whether they are published or not. The documents may come from teaching and research institutions in France or abroad, or from public or private research centers.

L'archive ouverte pluridisciplinaire **HAL**, est destinée au dépôt et à la diffusion de documents scientifiques de niveau recherche, publiés ou non, émanant des établissements d'enseignement et de recherche français ou étrangers, des laboratoires publics ou privés.

2010-ENAM-0027

École doctorale n° 432 : Sciences et Métiers de l'ingénieur

Doctorat ParisTech
T H È S E

en cotutelle internationale avec le

CIATEQ, A.C. (Centro de Tecnología Avanzada)

pour obtenir le grade de docteur délivré par

l'École Nationale Supérieure d'Arts et Métiers

Spécialité " Mécanique "

présentée et soutenue publiquement par

Rubén PEREZ MORA
le 8 septembre 2010

Study of the fatigue strength in the gigacycle regime of metallic alloys used in aeronautics and off-shore industries

Directeurs de thèse : **Thierry PALIN-LUC et Gonzalo Mariano DOMINGUEZ ALMARAZ**

Co-encadrement : **Claude BATHIAS**

Jury

M. Pedro GARNICA GONZALEZ, Dr., Posgrado en Metalurgia, Instituto Tecnológico de Morelia	Président, Rapporteur
M. Gérard MESMACQUE, Professeur, Laboratoire de Mécanique de Lille, Univ. de Lille	Rapporteur
M. Claude BATHIAS, Professeur, LEME, Université Paris X	Examinateur
M. Thierry PALIN-LUC, Professeur, LAMEFIP, Arts et Métiers ParisTech Bordeaux	Examinateur
M. Gonzalo Mariano DOMINGUEZ ALMARAZ, Dr., Facultad de Ingeniería Mecánica, UMSNH	Examinateur
M. José MARTINEZ TRINIDAD, Dr., ESIME, Instituto Politécnico Nacional de México	Examinateur
M. Oscar César De SANTIAGO DURAN, Dr., CIATEQ A.C	Examinateur

T H È S E

Arts et Métiers ParisTech - Centre de Bordeaux
LAMEFIP

Acknowledgements

This work would not have had a good end without the strong support of several people and institutions that I want to acknowledge in these few words.

I would first like to acknowledge my wife Elsa and my daughter Regina, who have been my greatest motivation for being with me these past three years. I appreciate your love and your patience throughout this time.

To my parents, my brothers and sisters, I want to say thanks for your support and your strength because I was not able to be with you in several important moments or I was far away during a lot of time.

I want to thank Mr. Thierry Palin-Luc for his invaluable supervision of this thesis, I appreciate your teaching and your drive to succeed, you always encouraged me to have an attitude of leadership and autonomy and I really appreciate that.

In the same way, I thank Mr. Gonzalo Dominguez for his supervision of this thesis, I am grateful for having included me in this project since its inception. It was really a great experience having worked on it.

I appreciate also the helpful support of the co-supervisors of this work, Mr. Claude Bathias in France and Mr. Carlos Poblano in Mexico. I want to thank specially to Mr. Paul C. Paris, who contributed in some parts of my work always with enthusiasm even when he was not my supervisor.

I want to acknowledge Arts et Métiers ParisTech through its director Mr. Jean Paul Hautier, to the Doctoral School of Arts et Métiers ParisTech through its director Mr. Gerard Coffignal and to the LAMEFIP laboratory through its director Mr. Ivan Iordanoff; I acknowledge for allowing me to develop this thesis work in their facilities using the multiple experiences of their people.

I acknowledge CIATEQ, A.C., Centro de Tecnología Avanzada, for its financial support during my doctoral stays in Mexico. I thank its director Mr. Victor Lizardi Nieto, the coordinator of the PICYT postgrade program, Mr. Guillermo Frades Castedo and to the manager of the Turbomachinery Department of CIATEQ, Mr. Fernando Aboites Dávila, for accepting me in his workgroup as PhD student and more recently as engineer. Special thanks to my immediate chief, Mr. Oscar De Santiago, for his encouragement for finishing the PhD.

I thank also to the French Program of Cooperation for Postgraduates (PCP France-Mexico) and the Mexican Council of Science and Technology (Conacyt) for their financial support of the exchange program.

I appreciate the confidence of the French company Turbomeca and the Spanish Vicinay Cadenas with the LAMEFIP laboratory, to be considered for the study of their special materials which allowed to have matter of study for this thesis. Specially thanks to Mr. José Luis Arana from the Basque Country University, for his friendship and his strong support.

I want to recognize the help of the technicians in the French side, Christophe Lemaire, Jonathan Merzeau, Jean-Marie Medard and Mathieu Lasserre, who helped me a lot when several technical problems, not always easy, arrived.

To the staff of LAMEFIP in general, I want to say thanks for their friendly reception and for their help in diverse aspects, such as the French language, because you were patient with me during my learning.

Thanks to my colleagues at CIATEQ in Mexico who helped me in many technical and administrative aspects; to Maritza Robles Gómez, Helen Zuñiga Osorio, Guadalupe López Quintana, Conin Arcega Escobedo, José Saul Sosa, José Bernabé Hernández, Vicente Rangel Fajardo, José Guadalupe Rico, Mariano Pérez Mora, Manuel Luna Tovar, Rómulo Hernández Ferrer and Carlos Aguilar Barrón.

I want to thank the staff of CIATEQ in general, particularly the people of the Turbomachinery Department, for your friendship, your encouragement and the nice working environment that has made my stay enjoyable.

Table of notations

a	Crack length.
A	Parameter of the Wöhler or Basquin curve.
α	Exponent of the slope in the threshold of the da/dN curve following the Paris-Hertzberg crack growth law.
b	Burgers' vector
B	Parameter of the Wöhler or Basquin curve.
c	Wave velocity
C	Constant of the Paris law equation
C_A	Parameter of calibration of the strain gauge
d	Distance between two pits
da/dN	Crack growth rate
ρ	Density
E	Elastic modulus
E_d	Dynamic elastic modulus
e, ε	Engineering or true strain
$\dot{\varepsilon}$	Strain rate
f	Frequency
F	Force
Φ	Diameter of crack initiation specimen
Hz	Hertz
Kt	Stress concentration factor
k	Stiffness
K	Stress intensity
ΔK, ΔK_{th}, ΔK_{eff}	Stress intensity range, threshold and effective
ω	Frequency
M	Modal mass
m	Exponent of the Paris law equation
N_f	Number of cycles to failure
ν	Poisson's ratio
P	Static load
Pa, MPa	Pascal, megapascal
p_S	Probability of failure
R	Stress ratio

R	Radius of pit
R_m	Static strength
R_a	Average roughness
S, S_{max}, S_{min}, S_m	Stress, maximum, minimum and mean
s	Standard deviation or seconds
σ_a, S_a	Alternating stress
σ_{max}, σ_{min}, σ_m	Maximum, minimum and mean stress
U_0, A_0	Displacement amplitude of the ultrasonic amplifier
T	Temperature
V, V_{RMS}	Tension voltage, root mean square
$Y(a/w)$	Dimensionless correction function of Wu's Equation
w	Width of crack growth specimen
w	Weight
$\sqrt{area}$	Square root of the area of a defect

Table of Contents

Introduction 5

CHAPTER I: Literature review.....7

1. General concepts of fatigue.....8
   1.1. Fatigue crack initiation 10
   1.2. Fatigue crack growth 11
   1.3. Regimes of fatigue.....13
   1.4. Influence of mean stress on fatigue 14
2. Gigacycle fatigue.....16
   2.1. Gigacycle fatigue interpretations.....18
   2.2. Gigacycle fatigue testing machines 20
   2.3. Ultrasonic fatigue principles.....23
   2.4. Gigacycle fatigue of steel and aluminium alloys.....29
3. Effect of corrosion on fatigue.....31
   3.1. Corrosion fatigue crack initiation.....31
   3.2. Corrosion crack initiation interpretations.....37
   3.3. Corrosion fatigue crack propagation.....38
   3.4. Corrosion fatigue crack propagation interpretations 40
4. Effects of defects on fatigue.....44

References of Chapter I.....51

CHAPTER II: Experimental conditions, materials and tests results 55

1. Gigacycle fatigue testing device.....56
   1.1. Crack initiation tests features 57
      1.1.1 Specimen generalities.....57
      1.1.2. Tension-compression tests (R=−1).....58
      1.1.3. Tension-tension tests (R>0) 58
      1.1.4. Tests with imposed temperature 59
      1.1.5. Tests in sea water flow.....61
      1.1.6. How to carry out crack initiation tests.....61

1.2. Crack growth tests features 62
1.2.1. Specimen generalities 62
1.2.2. Crack growth observation 63
1.2.3. How to carry out crack growth tests 64
1.3. Machine components calculations 67
1.3.1. Horns 67
1.3.2. Elongation bars 69
1.4. Calibration 71
2. Fatigue tests on AS7G06 cast aluminium alloy 75
2.1. AS7G06 characteristics 75
2.2. Specimen geometry 78
2.3. Temperature measurement of AS7G06 during tests 80
2.4. AS7G06 fatigue results 82
2.4.1. Crack initiation tests at room temperature 83
2.4.1.1. Tension-compression: R=-1 at room temperature 83
2.4.1.2. Tension-tension: R=0.01 at room temperature 85
2.4.1.3. Tension-tension: R=0.5 at room temperature 86
2.4.2. Crack initiation tests at 150 °C 87
2.4.2.1. Tension-compression: R=-1 at 150 °C 87
2.4.2.2. Tension-tension: R=0.01 at 150 °C 89
2.4.3. Synthesis of the results on AS7G06 90
3. Fatigue tests on R5 steel 93
3.1. R5 steel characteristics 94
3.2. Specimen geometry 97
3.3. Temperature measurement of R5 steel during testing 98
3.4. R5 steel fatigue results 101
3.4.1. Crack initiation tests without any corrosion 101
3.4.1.1. Tension-compression: R=–1 101
3.4.1.2. Tension-tension: R=0.3 103
3.4.2. Effect of corrosion on fatigue crack initiation 104
3.4.2.1. Crack initiation with pre-corrosion: R=-1 104
3.4.2.2. Crack initiation with artificial sea water in situ: R=-1 105
3.4.2.3. Surface roughness effect on fatigue strength under sea water flow 107
3.4.2.4. Corrosion with and without cyclic loading. 108
3.4.3. Synthesis of crack initiation results 115
3.4.4. Crack growth tests results 117
References of chapter II 118

CHAPTER III: Fractography analysis and discussion 119

1. Analysis of AS7G06 cast aluminium alloy results 120
   1.1. Fractography of specimens tested at room temperature 120
      1.1.1. Tension-Compression (R=-1) at room temperature 120
      1.1.2. Tension-Tension (R=0.01) at room temperature 121
      1.1.3. Tension-Tension (R=0.5) at room temperature 124
   1.2. Fractography of specimens tested at 150 °C 126
      1.2.1. Tension-Compression: R=-1 at 150 °C 126
      1.2.2. Tension-Tension (R=0.01) at 150 °C 129
   1.3. Discussion 131
2. Analysis of R5 steel results 134
   2.1. Fractography of specimens tested without any corrosion 134
      2.1.1. Tension-Compression (R=–1) 134
      2.1.2. Tension-Tension (R=0.3) 136
   2.2. Fractography of specimens with corrosion 138
      2.2.1. Tension-Compression (R=-1) with pre-corrosion 139
      2.2.2. Tension-Compression (R=-1) under sea water flow 142
   2.3. Discussion 147

References of Chapter III 151

CHAPTER IV: Assessment of the fatigue crack initiation and propagation duration 153

1 Paris-Hertzberg crack growth law 154
2 Application of the Paris-Hertzberg law to corrosion pits 158
   2.1 Assumptions 159
   2.2 Short crack initiation 160
3 Determination of the propagation stages duration 165
   3.1 From a_{int} to a_0 (microstructural short crack growth regime) 166
   3.2 From a_0 to a_i (physical short crack growth regime) 167
   3.3 From a_i to a_{final} (long crack growth) 168
   3.4 Calculation of total propagation duration 170
4 Calculation for R5 steel with pre-corrosion 172
5 Calculation for R5 steel with sea water corrosion 174
6 Discussion 176

References of chapter IV 178

Conclusion 179

Résumé..... 183

List of Annexes:

Annex 1: High speed rotating bending fatigue machine

Annex 2: Geometry of Horns and extensions and finite element analysis

Annex 3: Geometry plans of endurance specimens

Annex 4: Geometry plan of crack growth specimens

Annex 5: Methods of ultrasonic displacement Calibration

Annex 6: Data sheet of results of AS7G06-T6 tests

Annex 7: Data Sheet results of R5 steel tests

Annex 8: Crack growth duration calculations for R5 steel with corrosion

Introduction

This PhD thesis was co-directed by Prof. Thierry Palin-Luc from LAMEFIP (Laboratoire Matériaux Endommagement et Ingénierie des Procédés) at Arts et Métiers ParisTech Center of Bordeaux in France and Dr. Gonzalo Domínguez Almaraz from the University of Michoacan (UMSNH) in Mexico, with the participation of Prof. Claude Bathias, emeritus professor at LEME (Laboratoire Energétique Mécanique Electromagnétisme), Paris X University, France. The student was attending in parallel to the Doctoral School of Arts et Métiers ParisTech, France, and in Mexico at the Center of Advanced Technology (CIATEQ) of Querétaro through the Inter-Institutional Postgraduate Program of Science and Technology (PICYT). This cooperation is supported by both CONACYT in Mexico and the PCP-France-Mexico program in France. Both CONACYT and PCP are acknowledged for their financial support.

A lot of researches have been done in the world to study the fatigue strength of metals and structures under low cycle fatigue (less than ~10^5 cycles) and in the conventional megacycle range (10^6 – 10^7 cycles). But from less than 20 years, researches have been started to investigate the fatigue life of metals under a very high number of cycles (10^9 cycles and beyond), this is called gigacycle fatigue. The fatigue knowledge in gigacycle domain is recent, but of prior importance for design purpose because a lot of industrial components are designed for such a very high number of cycles; wheel of high speed train, fan or aeronautic turbine, etc.

This PhD thesis concerns the study of the gigacycle fatigue strength of two materials, the first one used in the gearboxes of turbines for the aeronautic sector (turbines for helicopters) and the second one used in offshore chain lines (for petroleum offshore platforms).

A cast aluminium alloy AS7G06-T6 coming from Turbomeca is studied. This alloy is used in the frame of the gearboxes of helicopters turbines. It is submitted to very high number of cycles due to the working duration of the engine (3,000 hours) and the rotation speed of the turbine in operating conditions: around 30,000 rpm. Specimens coming from real components were tested at both room temperature and 150 °C in air, and at three different stress ratios, R=–1, R=0.01 and R=0.5 to investigate both the temperature and the mean stress effect on the gigacycle fatigue strength. The fatigue strength at high number of cycles (10^9) and the crack initiation cause have been investigated.

A non-standard hot rolled low alloy steel, designed R5 according to the international denomination of the International Classification Societies of offshore systems, manufactured by Vicinay-Cadenas, has been studied too. This high strength steel is used for manufacturing mooring chains for offshore petroleum platforms in the European North Sea. This steel is requested to have high strength, as well as good corrosion resistance. Indeed, chains are designed for 30 years, and they are loaded at low frequency (~0.5 Hz) due to the waves in sea water environment during long time (25 to 30 years) all the day and all the year long. This represents more than 10^8 cycles!. Specimens made of R5 steel chains were tested in fatigue at

R= –1 and R=0.3 with three different conditions: (i) virgin specimens tested in air and (ii) and under artificial sea water flow in-situ, and (iii) pre-corroded specimens tested in air. Fatigue strength in the very high cycle regime and the causes of the crack initiation were investigated too.

Fatigue tests in the gigacycle domain were carried out at LAMEFIP in Bordeaux to study the behavior of the alloys of interest. The experiments were carried out using an experimental device for ultrasonic fatigue tests at high frequency (20 kHz), developed by Prof. Claude Bathias. The analysis of the fracture surfaces of the tested specimens, carried out by optical and scanning electron microscopy (SEM) of the different materials allowed us to know the causes of crack initiation (defects most of times).

In particular, it is looked for to understand the effect of the defects of materials on the resistance to the gigacycle fatigue. The fatigue failure in AS7G06-T6 cast aluminium alloy is due to shrinkages and porosities because of the manufacturing process (casting). In case of R5 steel, corrosion pits are the cause of fatigue failure in the specimens tested with pre-corrosion or under sea water flow, or in some cases failure is caused due to internal defects such as inclusions.

This document shows first a literature review of the fatigue general concepts and the basics of gigacycle fatigue. An important point about the effect of the defects on megacycle and gigacycle fatigue strength is presented. Corrosion fatigue is raised due to the characteristics of the use conditions on R5 steel in sea water environment in the North Sea.

An explanation of the testing conditions and the methodology followed to carry out the fatigue tests are shown in the second chapter. Mechanical and microstructural properties of the materials tested are presented. A compendium of all experimental results is also presented at this second chapter.

In the third chapter the fractography analysis and the discussion of the tests results of tests are presented explaining the crack initiation characteristics observed by SEM on the fracture faces of the broken specimens. Since most of the crack initiation causes are defects (shrinkages, pits, inclusions), an important question is debated in the next chapter: does crack propagation dominate the fatigue life or not in the gigacycle regime?

An assessment of the fatigue crack initiation and propagation duration is presented in the fourth chapter. Using the Paris-Hertzberg crack growth law and developing analytical equations considering the fracture mechanics around defects the period of crack propagation is estimated and applied to some practical cases. It is shown that the fatigue crack initiation phase is dominating under low stress amplitudes leading to fatigue life in the gigacycle regime

Finally the conclusions and prospects are presented.

CHAPTER I. Literature review

Table of contents

1. General concepts of fatigue 8
   1.1. Fatigue crack initiation 10
   1.2. Fatigue crack growth 11
   1.3. Regimes of fatigue 13
   1.4. Influence of mean stress on fatigue 14
2. Gigacycle fatigue 16
   2.1. Gigacycle fatigue interpretations 18
   2.2. Gigacycle fatigue testing machines 20
   2.3. Ultrasonic fatigue principles 23
   2.4. Gigacycle fatigue of steel and aluminium alloys 29
3. Effect of corrosion on fatigue 31
   3.1. Corrosion fatigue crack initiation 31
   3.2. Corrosion crack initiation interpretations 37
   3.3. Corrosion fatigue crack propagation 38
   3.4. Corrosion fatigue crack propagation interpretations 40
4. Effects of defects on fatigue 44
References of Chapter I. 51

This PhD thesis is focused on the gigacycle fatigue behavior of metallic alloys for industrial applications, such as aeronautics and offshore petroleum platforms.

This chapter is divided in four main parts. First, general concepts of fatigue of metals are presented in regard to crack initiation and crack propagation. The different fatigue regimes and the mean stress effect on fatigue are presented too.

The second part of the chapter extends the investigation on the gigacycle fatigue regime, also known as high cycle fatigue (HCF) and very high cycle fatigue regime (VHCF). In this part the basics of ultrasonic fatigue testing devices are presented.

It is also important to present an investigation about a main point in this work, which is the effect of defects in different regimes of fatigue looking for specially the effect of defects such as pores (manufacturing defects) and pits (corrosion defects) in the high and very high cycle regime. This kind of defects are present in the two alloys studied in this work. AS7G06-T6 containing defects such as porosities and R5 steel containing defects such as corrosion pits.

1. General concepts of fatigue

Very often mechanical components are subjected to cyclic loadings lower than the material yield stress. This cyclic loading can be resulting of rotation, bending, tension or vibration. Even when stresses applied are lower than material static strength, the component can fail after several applications of such stress. This is the basic concept of the fatigue of materials [1].

In general, the term failure is known as the complete rupture of a material or a component, which can also refer to a condition when the component has exceeded its maximum load or load limit and it is not able to function in a correct way.

The fatigue is a progressive fail of a component under repeated, recurrent or fluctuating loadings versus time. A material subjected to this type of loadings can fracture at levels of stresses lower than those required to cause failure under static conditions: stress below the macroscopic yield stress.

Askeland [1] mentions that fatigue failures in materials can be usually characterized in three stages: first, a minuscule crack initiates on the surface or internally during cyclic load application, which is called crack initiation. Then, the small crack grows gradually while cyclic loading continues, which is called crack growth. Finally, when the transversal section remaining is too small in order to support the applied load the component fractures [1].

Machine components, vehicles and structures are frequently subjected to these kinds of cyclic loads, and the resulting cyclic stresses can lead to microscopic physical damage in the involved materials. According to Dowling [2], even at stresses well below a given material's ultimate strength, this kind of damage can accumulate with continued cyclic loading, until it develops into a crack or other macroscopic damage that leads to failure of the component [2].

At the present there are three major approaches for analyzing and designing components against fatigue failures. The traditional stress-based approach is based on the nominal (average) stresses in the affected region of the component. The nominal stress that can be resisted under cyclic loading is determined by considering mean stresses and by adjusting for the effects of stress concentrators, such as notches, grooves, holes, fillets, and keyways. Another approach is the strain-based approach, which involves a deeper analysis (microscopically) of the localized yielding that may occur at stress concentrators during cyclic loading. The third approach is the fracture mechanics approach, which is specifically related to crack growth analysis [2].

To determine the fatigue strength of materials, there are several kinds of fatigue tests, in different ways, for instance: single or rotating bending fatigue tests, tension or compression tests, torsion or even multiaxial fatigue tests (combined loadings). Fatigue tests show the time or number of cycles that a component will resist under cyclic loading, or the maximum bearable stress without failure before a given number of cycles.

A typical relationship between the stress and the number of cycles to failure for an endurance specimen is the *S-N* curve (Figure 1.1). An *S-N* curve (Stress vs. Number of cycles) can be presented in terms of stress amplitude or maximum stress vs. the number of cycles. Such kind of curve is sometimes also called the Wöhler curve, in attribution to the work of August Wöhler in Germany in the 1850s.

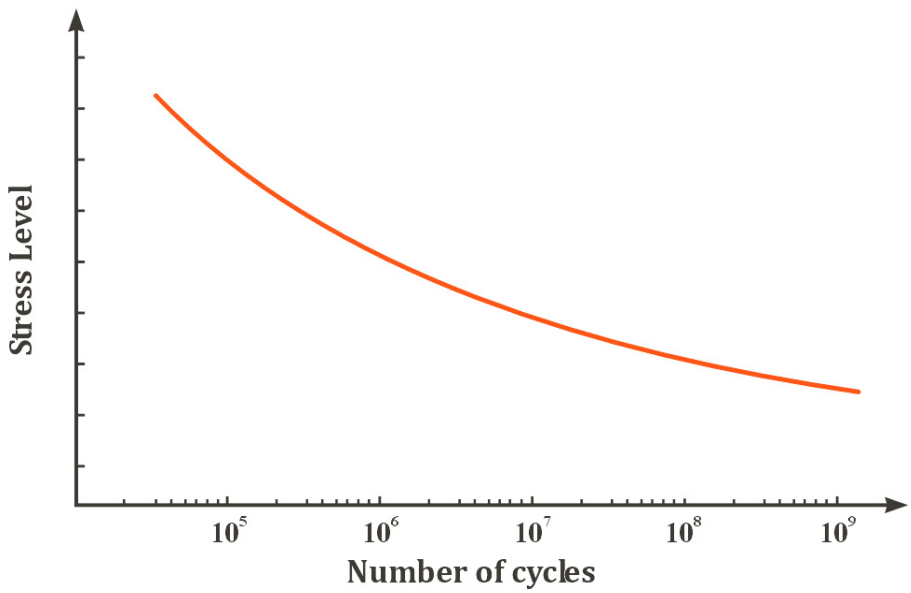

Figure 1.1. Shape of a typical *S-N* curve.

Often, the components are subjected to oscillating loading conditions that generate stress not equal in tension than in compression. Some practical applications involve cycling between maximum and minimum stress levels. This is called stress amplitude (σ_a), which is defined as the half of the difference between the maximum and minimum stress, and the mean stress (σ_m) is defined as the average between the maximum and minimum stress for a symmetrical cyclic loading. The R ratio is also a key factor in fatigue testing, because the fatigue results depend on the maximum and minimum stress conditions. R ratio is defined as the coefficient of the minimum stress and maximum stress, $R=\sigma_{min}/\sigma_{max}$.

1.1. Fatigue crack initiation

The first part of the general process of fatigue is the crack initiation. According to Arana and Gonzalez [3], this is a period of nucleation and initiation of cracks in zones where stress concentration cause cyclic plastic deformations. This is an accumulation of plastic damage on certain microstructural defects, surface defects or volumetric defects, that creates the apparition of cracks [3].

Felbeck and Atkins [4] mention that fatigue would probably not occur in a perfectly homogeneous material that is absolutely smooth on its external surfaces and uniformly loaded. Under elastic stresses the material would uniformly deform elastically, and when the stress is removed the elastic deformation would be completely reversed and thus be returned to the initial configuration, no matter how many times this stress cycle is repeated, there would be no permanent change in the structure. But, it is the non-uniform characteristics of real materials that lead to fatigue failures under cyclic stress. Metals can contain non-metallic impurities or inclusions, natural dislocations, porosities or shrinkages, all with relation with the fabrication process, and metal components can also have surface imperfections due to the manufacturing process or due to environment effects (Figure 1.2). When a component made of these metals is loaded in the nominal elastic range, portions of many dislocations will move and can contribute to very small irreversible changes in the configuration of the component [4].

This process of fatigue initiation is complex and involves frequently slip band processes. These mechanisms consider only one of several possible ways that dislocations can lead to fatigue cracking. A foreign impurity particle, a surface imperfection or a plastically deforming grain surrounded by elastic grains can act to cause local stress concentrations that will lead in a similar way to the creation and growth of small cracks [4].

The nucleation of fatigue cracks at grain boundaries also occurs under the influence of embrittling environments which preferentially attack grain boundaries and the particles, if any, on them [5]. At elevated temperatures where grain boundary cavitation and sliding are promoted, crack nucleation at grain boundaries can also occurs. Intergranular fracture is also commonly observed in brittle solids due to the residual stresses induced by thermal contraction mismatch between adjacent grains or to the presence of brittle phases on grain boundary [5].

According to Forrest [6] the origin of fatigue cracks is usually found at some surface discontinuities. This is because any change in section, such as a hole, a change in shaft diameter, a groove, a keyway or even a tool mark, can generate stress concentration [6].

As previous authors, many researchers in fatigue field consider important to know the mechanisms of fatigue crack initiation viewing even at different scales. Many coincide in the importance of the effect of macroscopic defects but the microscopic aspects are also studied.

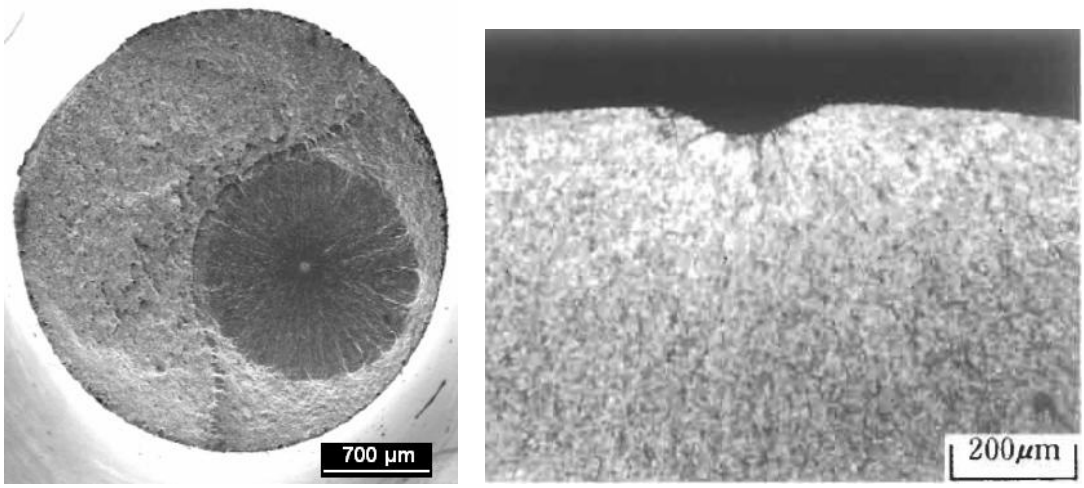

Figure 1.2. Crack initiation at inclusion in 4240 steel (left) [7] and crack initiation at corrosion pit in SUP10M steel (right) [8].

1.2. Fatigue crack growth

Several times, a component could not be in risk of failure even with a crack is present, that is the reason why the fatigue crack growth tests are important. In these tests a relationship is found between the crack growth rate and the range of the stress intensity factor of the crack (ΔK), which characterizes the crack geometry and the applied stress amplitude. Below a ΔK threshold the crack will not propagate. For ΔK slightly upon the threshold the cracks will grow slowly and for higher ΔK the cracks will grow according to the Paris Law (Eq. 1.1):

$$\frac{\mathrm{d}a}{\mathrm{d}N} = C(\Delta K)^n$$

Eq. 1.1

where C and n are constants depending of the material.

In 1961 Paris [3] suggested that for a cyclic stress variation, a variation on the stress intensity factor should be expressed by Eq. 1.2:

$$\Delta K = K_{\max} - K_{\min}$$

Eq. 1.2

where K_{max} and K_{min} are the maximum and minimum stress intensity factors during a cycle of fatigue. If the cyclic loading enters in the compression zone, it is conventionally considered that K_{min}=0, because the crack growth take place in the tension part of the cycle [3].

In the practice is not always limited only the fluctuating stresses on components and structures so that fatigue cracks will not occur. Sometimes it is necessary to carry out periodic inspections on service parts to assure that fatigue crack will not propagate to cause complete failure [6]. Then, the knowledge of the crack growth data of the materials is very useful.

Once fatigue crack is originated, its growth is governed by certain mechanisms that can be presented in different stages.

In the scheme of Figure 1.3 the three stages of fatigue propagation have been represented with reference to the crack growth mechanisms at each stage. The Paris Law application in the left extreme of the Phase I would give a lower estimation of the real rate. In the Phase III, the crack growth is faster than indicated by the Paris equation. Many data published involve the results for the Phase II and Phase I describing an extension of the Paris equation (Eq. 1.1) [3].

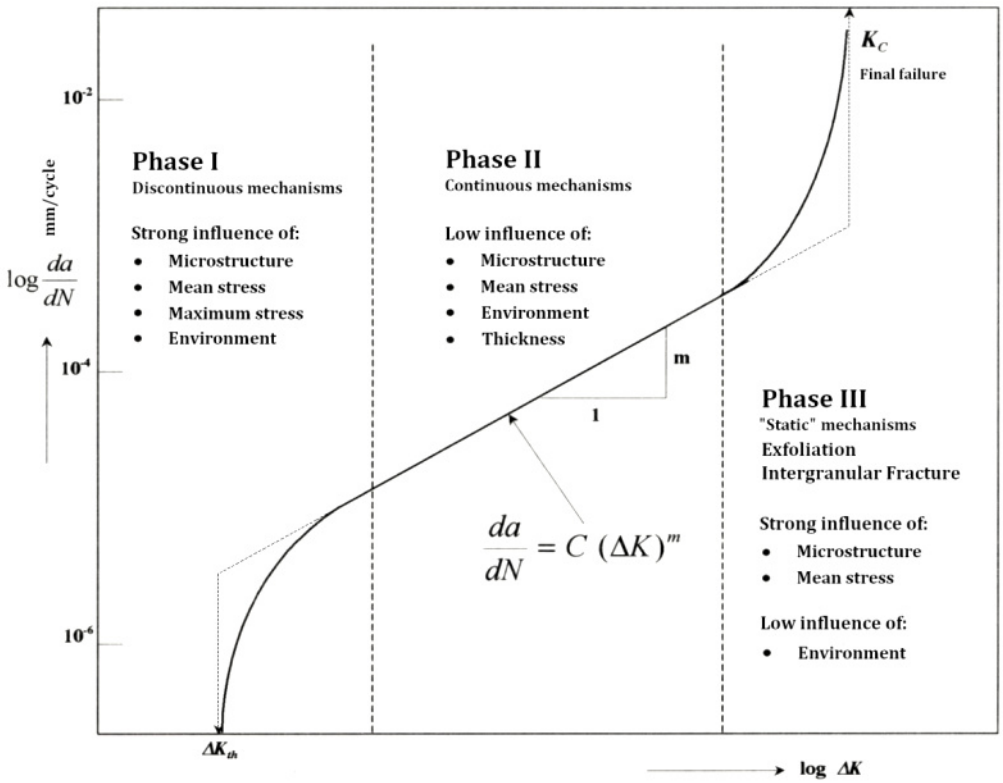

Figure 1.3. Characteristic crack growth curve for a ductile material [3].

The presence of a crack can significantly reduce the strength of an engineering component. However, it is unusual for a crack of dangerous size to exist initially and go unnoticed, although this can occur, as when there is a large defect in the material used. Crack growth is caused by cyclic loading, a behavior called “fatigue crack growth”. But, if a hostile chemical environment, such as corrosive agent is present, even a steady load can cause a phenomenon called “environment crack growth”. Both types of crack growth can occur if cyclic loads are applied in the presence of an aggressive environment, especially if the cyclic is slow or if there are periods of steady load interrupting the cycling [2]. The effect of corrosion in fatigue crack growth and crack initiation will be raised in a next section of this literature review.

Some attempts to determine the fatigue crack growth life as portion of the total fatigue life have been carried out considering flaw aspects of the materials such as “fish eyes” [9] small cracks [10] or corrosion pitting [11]. The actual agreement is that crack growth in fatigue on metallic materials is only a small part of the total fatigue life, but this is even discussed if it occurs in all the different regimes of fatigue.

1.3. Regimes of fatigue

The fatigue damage corresponds to the initiation of a fatigue crack originated by cyclic loading on the material. The number of cycles to failures can change according with stress level and may range over several orders of magnitude. For this reason, the numbers of cycles are usually plotted on a logarithmic scale [2] as presented in Figure 1.1.

On this curve three domains of fatigue are conventionally defined (Figure 1.4).

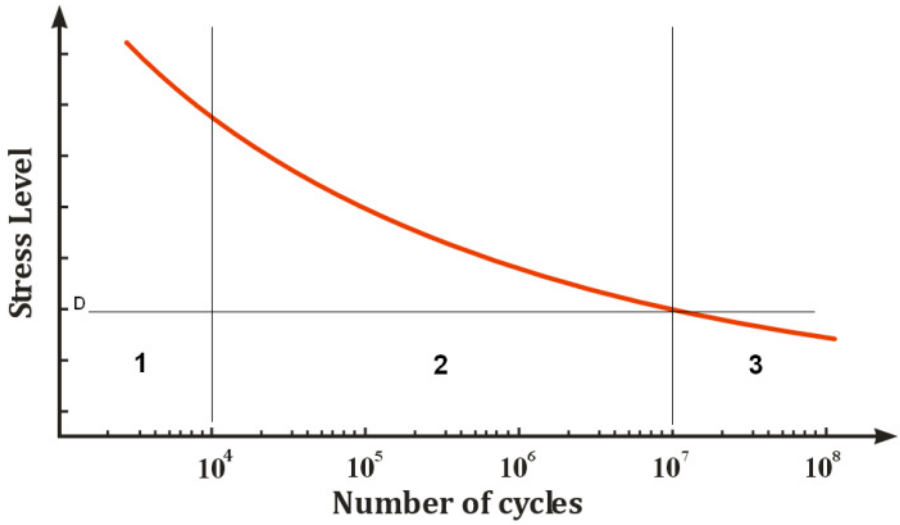

Figure 1.4. The different domains of fatigue life [12].

The first domain in Figure 1.4 corresponds to the so called "low cycle fatigue" (LCF). This domain of fatigue is characterized by the fracture at very low number of cycles, from 1 to 10^4 cycles. At short fatigue lives, the high stress involved may be accompanied by plastic strain [2]. Normally in this domain high stress levels are applied on the materials, observing important macroscopic plastic deformations [12].

The domain 2 in Figure 1.4 corresponds to the so called "fatigue limits" or "endurance limits". In some materials, notably plain-carbon and low-alloy steels, there seems to be a distinctive stress level below which fatigue failure does not occur under certain conditions. At this location, the *S-N* curve appears to become a flat and to asymptotically approach [2]. In this domain plastic strains are much lower than the domain 1 due to lower stress levels. A general behavior integrally elastic at the macroscopic scale is observed around 10^5 cycles [12]. Actually, the term "fatigue strength" is used to specify a stress value from an *S-N* curve at a particular life.

The domain 3 in Figure 1.4 corresponds to the "high cycle fatigue" regime (HCF), characterized by fatigue lives from 10^6 to 10^8 cycles. It is observed a characteristic approximately asymptotic of the *S-N* data in this domain but not totally asymptotic, which would correspond to a "fatigue limit". This theoretical limit corresponds to a stress level that describes a threshold of non fatigue failure after an infinite number of cycles [12]; but in recent years this is discussed if it exists or not [7, 13].

In the domain 3 is also comprehended the "gigacycle fatigue" or "very high cycle fatigue" regime (VHCF) which is characterized by fatigue lives that exceed 10^8 cycles. This last is the topic of interest of this work and gigacycle fatigue will be described more detailed in a next section.

1.4. Influence of mean stress on fatigue

The greatest portion of the fatigue data available has been determined from alternating stress tests, it means that mean stress of the cycling is equal to zero (σ_m=0) [2, 6]. That is because many times is easier to obtain data at R=–1; for instance, with rotating bending machines that not allow the application of a mean stress different to zero [6].

However, *S-N* curves that include data for various mean stresses are widely available for some materials. A procedure used for developing data on mean stress effect is to select different values of mean stress, running the tests at various stress amplitudes for each of these. The results can be plotted in an *S-N* diagram alone with the curve for each mean stress, as shown in Figure 1.5. It is noticeable that an effect of mean stress falls or raises the *S-N* curve. For a given fatigue life, the allowed stress amplitude can be lower or higher if the mean stress is in tensile or compressive respectively.

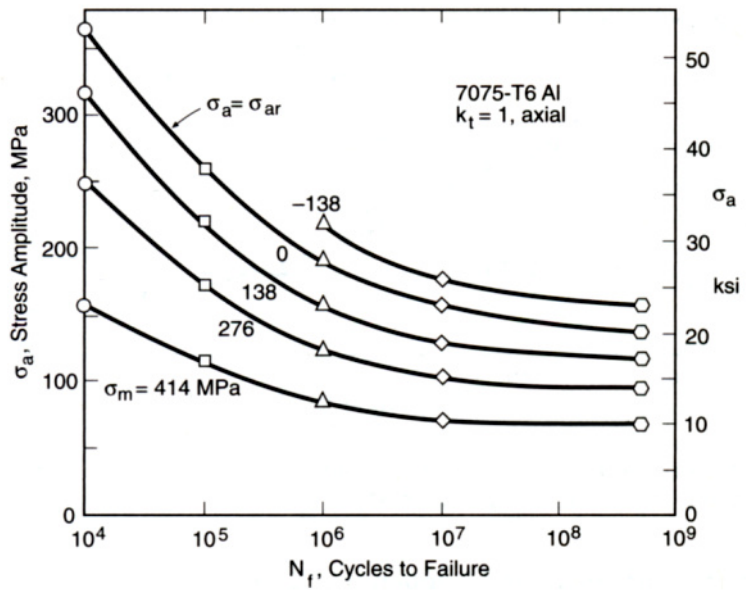

Figure 1.5. *S-N* curves at various mean stresses for an aluminium alloy [2].

In real service, many components and structures are subjected to stresses which fluctuate between different values of tension or compression. According to Forrest [6] the most important condition to be considered is an influence of static tensile stresses superimposed on alternating tension-compression stresses. A number of empirical relations have been proposed for estimating the fluctuation of the fatigue strength if the alternating fatigue strength and the tensile strength of the material are known.

Alternative means presenting the same kind of information in Figure 1.5, corresponding to a constant-life diagram. That is done taking points from the *S-N* curves at various values of fatigue life and then plotting combinations of stress amplitude and mean stress that produce each of these lives. Interpolation between the lines on either type of plot can be used to obtain fatigue lives for various applied stresses.

Another procedure often used for developing data on mean stress effect is to choose several values of stress ratio R, running the tests at various stress levels for each of these. A family of *S-N* curves can be obtained, each one corresponding to a different R value.

The Haigh diagram is another way of presenting the fatigue data with regard to the mean stress effect. On this diagram the stress amplitude is plotted as function of the mean stress, as shown in Figure 1.6; the line A-B is for a constant number of cycles.

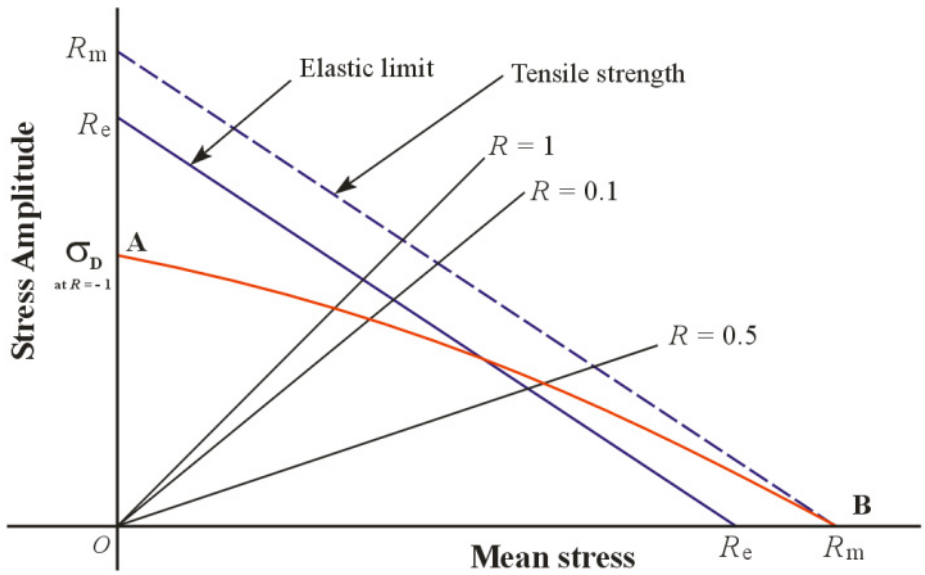

Figure 1.6. Theoretical Haigh diagram [14].

The point A corresponds to the fully reverse loading, it is located at zero mean stress. The point B is associated with zero stress amplitude, which corresponds to the stress of fracture in a tensile static test. The fatigue strength determined from the tests for certain life duration can be located on the straight lines corresponding to the R ratio at which they were obtained. Points of different R ratio can be placed on a line, parabola or any curve that could be adjusted to the data. The fatigue strength of another stress ratio R not tested can be approximated following this last curve.

Some experimental works have been carried out to determine the influence of mean stress on the fatigue strength. Nadot et al [15] studied the effect of mean stress on the fatigue strength (5×10^6 cycles) for C35 steel with artificial defects under tension and torsion. Under tension, with a positive mean stress lower fatigue strength was obtained, while with negative mean stress the fatigue strength was higher.

Morel et al [16] studied the effect of high mean stress on the cast aluminium alloy AlSi7Cu0.5Mg0.3 at different ratios from R=–1 to R=0.95. Fatigue strengths were presented in the Haigh diagram. At higher stress ratio the fatigue strength was lower.

2. Gigacycle fatigue

As mentioned before, gigacycle fatigue is a term used to describe the regime of fatigue at which some materials fail after 10^8 cycles and beyond.

In several industries, such as aeronautics, aerospace, high speed train, marine and ground transportation, there are several structural elements that are subjected to recurrent loads of high frequency and low amplitude, many times more than 10^8 cycles during their work duration. An example can be the life of the motor of an automobile whose components operate in the range of 10^8 cycles. For the big motors of ships or high-speed trains the life can reach 10^9 cycles, while in the turbines of airplanes, the fatigue life is around 10^{10} cycles (Figure 1.7) [7, 17].

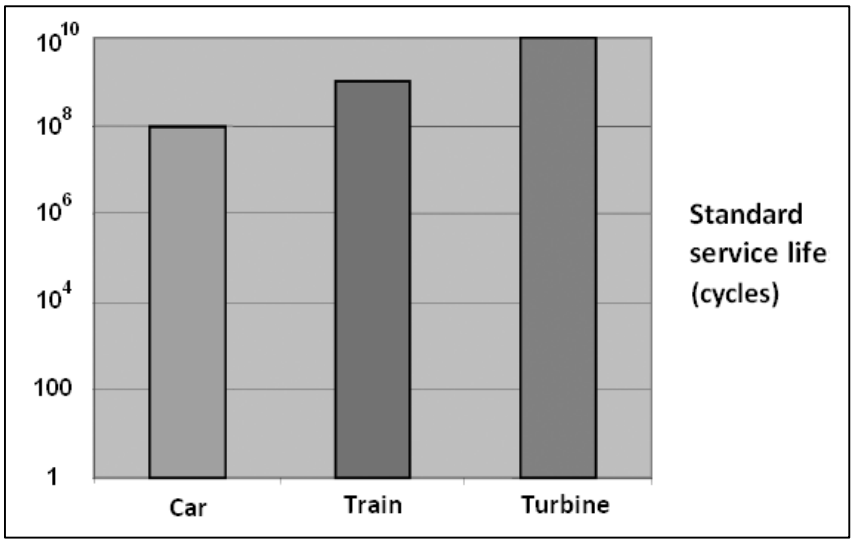

Figure 1.7. Service lives of different machines and components [7].

In the past, the "fatigue limit" was defined as the stress value which it does not exist risk that a failure occurs at some number of cycles. In the ASTM standard is defined at 10^6 cycles (Figure 1.8) for structural steels. On the contrary, the "fatigue life" is a term that indicates the time or number of cycles that a material will resist at certain stress level and the "fatigue strength" is the stress level at which a material fails at a given number of cycles [7].

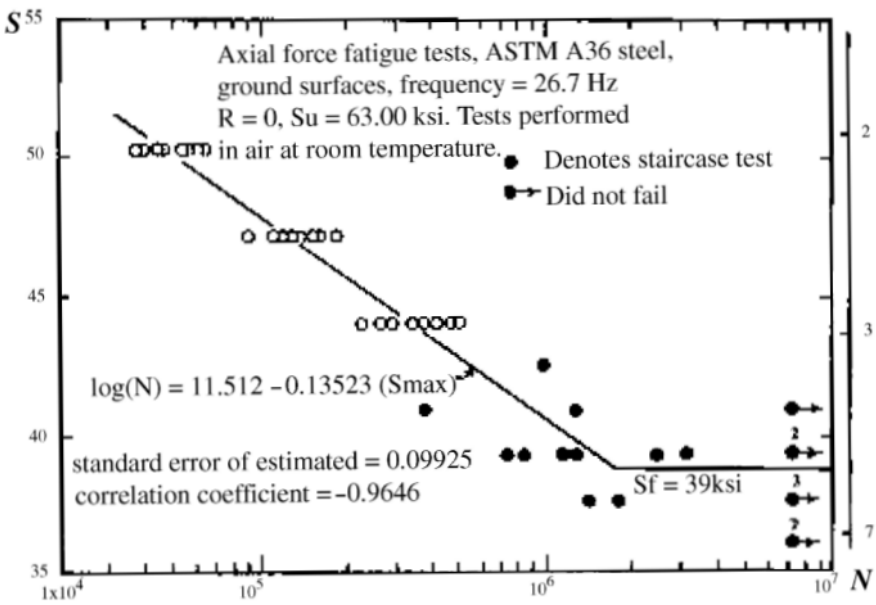

Figure 1.8. SN curve defined by ASTM A36 for carbon structural steel [7].

In 1984 Japanese researchers found that metallic materials as low alloy steels can fail in fatigue after 10^7 cycles [18, 19]. Since 1984, more and more researchers began to study the phenomenon of fatigue at high number of cycles. Several research works revealed that a fatigue limit does not exist, even if it had been affirmed for such materials as steels [13, 20]. Although the *S-N* curves of some materials show an asymptote in the gigacycle range, under certain conditions like high temperature or corrosion, this asymptote disappears. For this reason, it becomes very interesting to investigate the phenomenon of fatigue in the gigacycle regime to study such behavior (Figure 1.9).

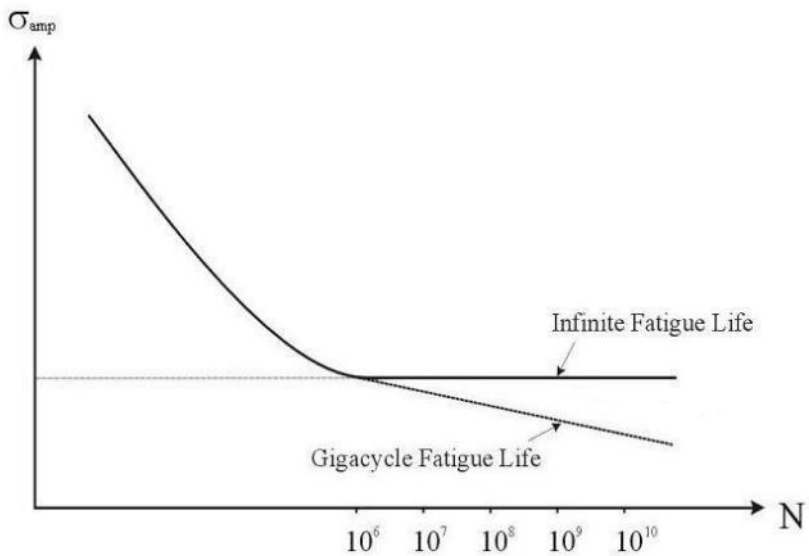

Figure 1.9. General concept of gigacycle fatigue life against fatigue limit [13].

2.1. Gigacycle fatigue interpretations

A criterion of infinite fatigue life was initially used by Wöhler who basically related the stress life to the asymptotic behavior of some steels in the *S-N* curve, normally after 10^6 cycles. Some materials show a "fatigue limit" but most other materials do not exhibit this behavior, instead displaying a continuously decreasing of the stress life response, even at number of cycles longer than 10^7 cycles. Such behavior is more correctly described by fatigue strength at a given number of cycles [7].

Bathias et al [13] have presented a large number of *S-N* curves for steel and irons loaded in tension-compression or in tension-tension where fatigue crack initiation appeared up to 10^9 cycles or beyond. The differentiation of fatigue strength from a kind of materials with another was noticed. For a first class of alloys the difference between the fatigue strength at 10^6 cycles and 10^9 cycles was only a few MPa. Low carbon steel, stainless steel 304, 12Cr steel and spheroidal graphite cast iron exhibited such behavior. On the contrary, 4240 steel, bearing steels, rail steel, spring steels, and martensitic stainless steel exhibited a higher slope of the *S-N* curve in the gigacycle regime, with differences between the fatigue strength at 10^6 cycles and 10^9 cycles of 50 to 200 MPa. A roughly explanation is that there is a progressive transition of mechanisms around 10^7–10^8 cycles that induces a step in the *S-N* curve. Three different types crack initiation for each regime are proposed. For the low cycle fatigue (10^4 cycles) the crack initiations are more often multiple on the surface. For gigacycle fatigue (>10^8 cycles) the initiation is located at an internal zone. According to [13] a transition of mechanisms may exist between 10^7–10^8 cycles.

Some concepts of very high cycle fatigue on ductile materials without inclusions and with non-metallic inclusions, like high strength steels, have been proposed by Mughrabi [21]. Multi-stage fatigue diagrams in conventional high cycle fatigue regime strength (HCF) and possible lower fatigue strength in the very high cycle regime (VHCF) are discussed for both kinds of materials in terms of the fatigue crack mechanisms. These diagrams in the form of Coffin-Manson plot (plastic strain amplitude $\Delta\varepsilon_{pl}/2$ versus N_f) were proposed to describe the fatigue lives of both type of materials from the low cycle fatigue regime to the very high cycle fatigue regime (Figure 1.10). In these diagram are shown four ranges: (I) the low cycle fatigue (LCF) range or Coffin Manson range [21]; (II) the PSB (persistent slip bands) threshold related to the high cycle fatigue (HCF) plastic strain "fatigue limit" where an asymptotic shape of the *S-N* curve appears; (III) the transition range from HCF to VHCF which present a slope in the *S-N* curve; and (IV) the irreversibility threshold corresponding to the VHCF which presumably exhibit an asymptotic behavior again. The author discussed the fact of fatigue failure can occur at very high numbers of cycles at stress levels below the conventional HCF "fatigue limit", because even when the stress is too low for persistent slip bands (PSBs) to develop, the accumulation of slightly irreversible random slip can lead to a sufficiently strong surface roughening to initiate surface fatigue cracks.

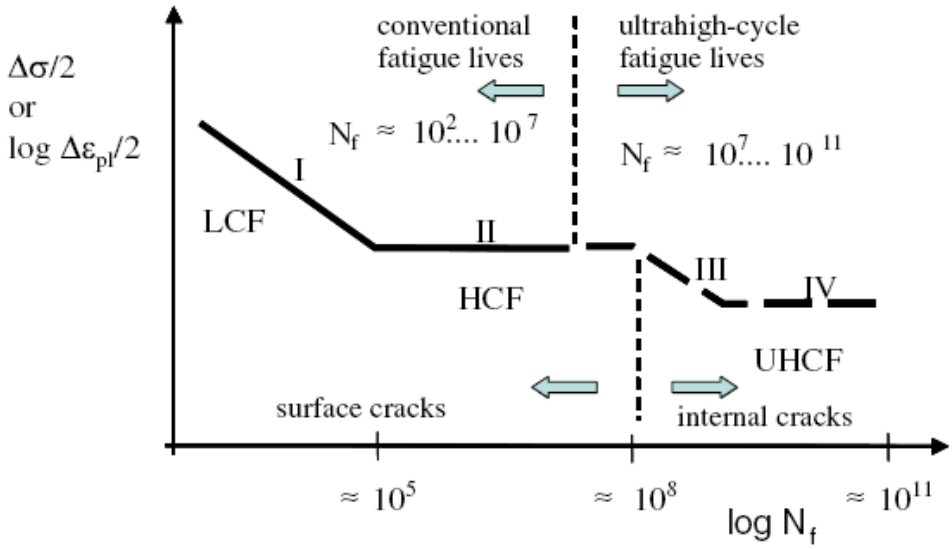

Figure 1.10. Schematic diagram for the fatigue lives of high strength steel with non-metallic inclusions [21].

Other authors as Murakami et al [22] consider some morphological aspects of the fractured materials in fatigue to try explain the gigacycle fatigue mechanisms. A Cr-Mo steel and a SAE52100 equivalent steel were tested in tension-compression, R=–1, between 27–100 Hz above 10^8 cycles. All specimens had particular fracture morphology alongside a non-metallic inclusion which was called Optically Dark Area (ODA) (Figure 1.11) and they observed the size of this area. Specimens that failed in the regime of 10^5 cycles had almost no such area, while the specimens failed near to 10^8 cycles or more had a dark area more than double size of the original inclusion at the crack initiation size. The mechanism of formation of such areas is presumed caused by cyclic stress coupled with the internal hydrogen trapped by non-metallic inclusions. It is presumed that when the size of the dark area exceeds a critical size in absence of hydrogen, the fatigue crack become a propagating crack [22].

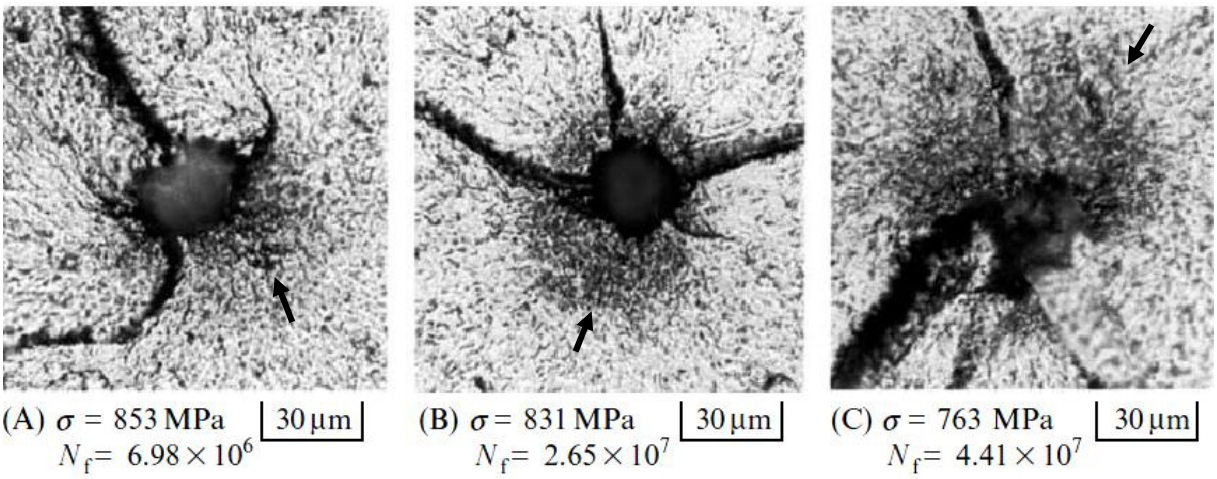

Figure 1.11. Fatigue crack initiation sites and Optically Dark Areas of SUJ2 steel (SAE52100) [22].

According to Miller and O'Donnell [23] very long life fatigue failures involve very low crack growth rates. In engineering materials, there are sufficient defects to obviate an initiation phase. Then probably the most dangerous conditions for an engineering component designed to survive more of 10^6 cycles are the introduction of very low cyclic stress vibrations at high mean stress level, fluctuating or intermittent stress cycles or very high frequencies and low cyclic stresses that can generate a failure from an internal flaw or surface defect.

2.2. Gigacycle fatigue testing machines

The usual procedure for determining fatigue strength is by testing a number of similar specimens, subjecting each one to a particular alternating load until it fails. It has been shown that this relation gives a typical diagram known as *S-N* curve (Figure 1.1 and Figure 1.4).

Fatigue testing machines can be classified by the type of straining action that is applied to the specimen. That is direct or axial stress, bending, torsion, and combined or complex stress (multiaxial stresses). Another classification could be related with the number of cycles that can be reached with the machine, according with its testing frequency.

To determine the *S-N* curve for a metal up to a fatigue life of 10^8 cycles requires a minimum of 8 tests, the longest of which will last about two weeks if the frequency of the machine is around 90 Hz. The total time of testing if only one fatigue machine is available, will be around 8 or 10 weeks. That is an example that can be carried out using a rotating bending fatigue machine. Some of them can run up to 199 Hz, reducing the half the testing time. An example of a rotating bending fatigue machine of variable speed is presented in Annex 1. This work was carried out in CIATEQ, A.C. in Mexico under supervision of Dr. Oscar de Santiago and Dr. Gonzalo Domínguez [24].

However, to simulate the fatigue damages with conventional hydraulic or pneumatic testing machines that just reach a frequency between 10 and 200 Hz, it limits in certain way the study of fatigue in a complete range. The capacities of these machines are very far from the frequency of work of some materials of structural components, such as the turbines. Also, these components are subjected to a great number of cycles (more than 10^8) during their work life. Test up to such long life with a conventional machine at 100 Hz like a vibrophore could take more than 10 days [25, 26] for one specimen only, but they are even carried out.

The design and prototype manufacturing of high frequency ultrasonic testing machines has made possible the study of the fatigue of materials under loads at a cyclic frequency of 20 kHz, decreasing the time of the test thoroughly [26].

An experimental method of ultrasonic fatigue has been developed based on the application of the ultrasonic theory and technology by Prof. Bathias [26]. LAMEFIP laboratory at Arts et Métiers in Bordeaux, France, has one of these ultrasonic fatigue testing machines.

This kind of machine is a displacement controlled machine. There are three most important components in these fatigue testing machines: a high frequency generator, a piezoelectric transducer or converter, and a displacement control system. (Figure 1.12). The explanation of each component is given next:

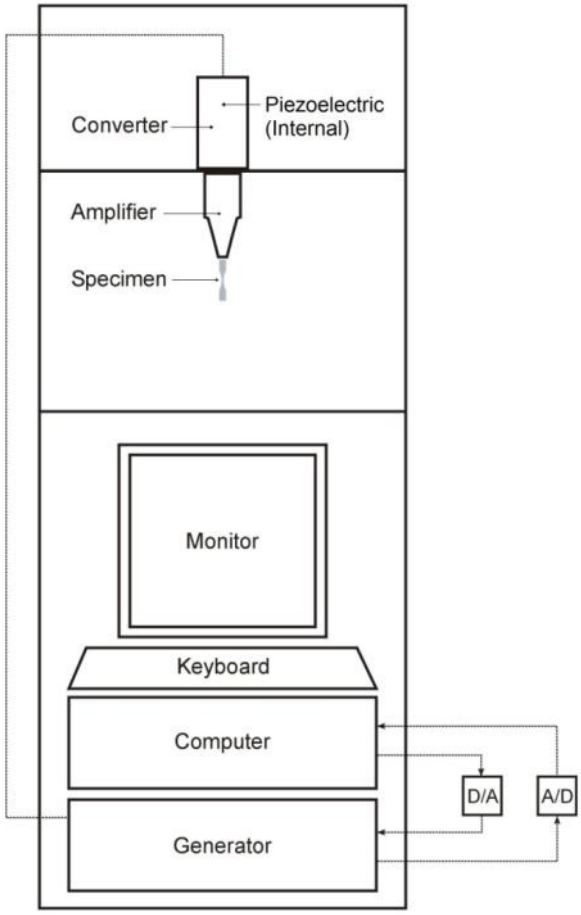

Figure 1.12. Schematic diagram of an ultrasonic fatigue testing machine for R=-1 and room temperature [7].

Ultrasonic Generator. A power generator transforms a 50 or 60 Hz voltage signal into ultrasonic electrical sinusoidal signal at 20 kHz. In Paris X University and at LAMEFIP (Arts et Métiers), a BRANSON generator is used with a maximum power output of 2 kW generating an ultrasonic signal at 20 ± 0.5 kHz.

Piezoelectric Converter. This is excited by the ultrasonic generator. It transforms the electric signal into longitudinal ultrasonic waves and mechanical vibration at the same frequency.

Ultrasonic amplifier. Due that the vibration amplitude of the piezoelectric converter is small (between 0 and ~5 μm), an ultrasonic amplifier increases the vibration amplitude. The result of this amplification depends on the geometry of the amplifier, and the received electric signal of the converter.

Displacement control system. Ultrasonic fatigue tests with this machine are displacement controlled tests. The displacement control system contains a computer that takes charge of controlling the displacement amplitude, as well as the acquisition of data. The acquisition of

data is carried out through an A/D and a D/A converter. The A/D card transforms the data similar to digital.

The function of the system shown in Figure 1.12 is to make the specimen vibrate in ultrasonic resonance. The generator excites the converter causing a vibration that is amplified in the so called component "sonotrode" or "horn" (mechanical amplifier) [7]. The displacement amplitude reaches its maximum U_0 at the end of the specimen, which can be measured by a dynamic sensor, while the maximum stress is reached in the middle section of the specimen (with a load ratio R= –1) Figure 1.13. During ultrasonic fatigue tests, the strain can be measured directly using strain gauges glued on the specimen surface.

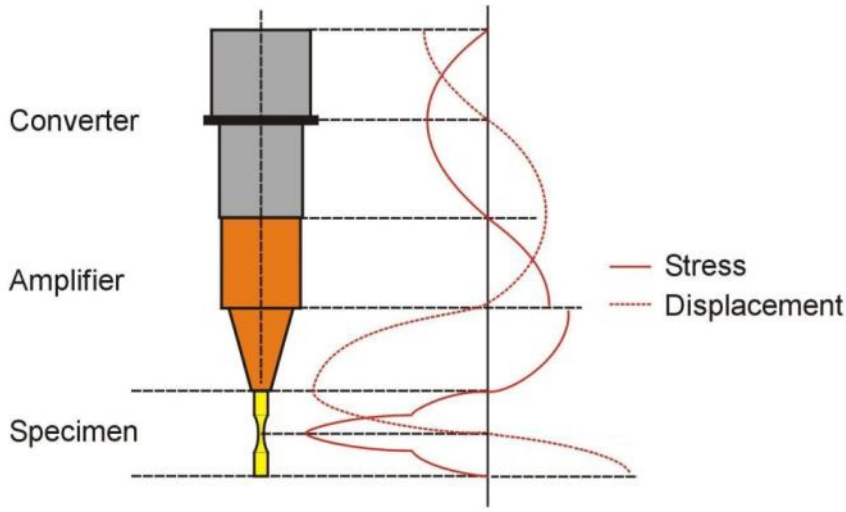

Figure 1.13. Vibratory stress and displacement field (R= –1) [7].

The mechanical system formed with a converter, an amplifier and a specimen is linear and all stress and displacement fields are linear [7]. That is because the components are vibrating in resonance in the elastic domain of the materials. Then, the determination of stress-displacement relation is necessary. Such relation will be lineal up to the elastic limit of the materials.

Previously the tests, the calibration of the fatigue machine must be carried out. The verification that the vibration system is working with the correct displacements with each horn is necessary to verify that the stress level applied is the correct one. For this an optical, capacitive or resistive sensor could be used, finding displacements adapted in the amplifiers of the vibration system.

The nominal resonance frequency of the vibration system must be 20 kHz (for the system shown in Figure 1.13). A criterion for stopping the test is if this frequency decreases more than 0.5 kHz due to crack initiation (specimen stiffness decreasing). Thus, if the control system detects less than 19.5 kHz the test system is stopped.

2.3. Ultrasonic fatigue principles

In 1950, the Manson's testing machine marked an important point of advance in the ultrasonic fatigue testing systems. In those times were introduced the piezo-electric and magnetostrictive types of transducers that allowed to transform 20 kHz electrical voltage signals into displacement at 20 kHz (mechanical vibration).

The conventional fatigue tests usually work at the frequency of the external load system of the testing machine, which is different to the specimen natural frequency. In an ultrasonic fatigue testing machine the external frequency supplied by the testing machine must be one of the natural frequencies of the specimen [25].

Normally, in gigacycle fatigue testing, high frequency excitation is used (10–190 kHz). It is assumed that the materials studied are isotropic and homogeneous and the material has an elastic behavior during the cyclic loading. Stresses above the elastic limit of the material are not applied in ultrasonic fatigue testing [27].

In the elastic wave theory the displacements (u, v, w) have to verify three differential equations for a general homogeneous three-dimensional isotropic elastic body (Figure 1.14) in a Cartesian co-ordinate system, these are:

$$\rho \frac{\partial^2 u}{\partial t^2} = \frac{E}{(1+\nu)}\left(\frac{1}{1-2\nu}\frac{\partial e}{\partial x} + \nabla^2 u\right)$$

Eq. 1.3

$$\rho \frac{\partial^2 v}{\partial t^2} = \frac{E}{(1+\nu)}\left(\frac{1}{1-2\nu}\frac{\partial e}{\partial y} + \nabla^2 v\right)$$

Eq. 1.4

$$\rho \frac{\partial^2 w}{\partial t^2} = \frac{E}{(1+\nu)}\left(\frac{1}{1-2\nu}\frac{\partial e}{\partial z} + \nabla^2 w\right)$$

Eq. 1.5

where u, υ and w are displacements along x, y and z respectively, E and ν the Young's modulus and the Poisson's ratio, ρ the mass density, ∇^2 the Laplacian, and e is the volume dilatation.

$$e = \frac{\partial u}{\partial x} + \frac{\partial v}{\partial y} + \frac{\partial w}{\partial z} = \varepsilon_{xx} + \varepsilon_{yy} + \varepsilon_{zz}$$

Eq. 1.6

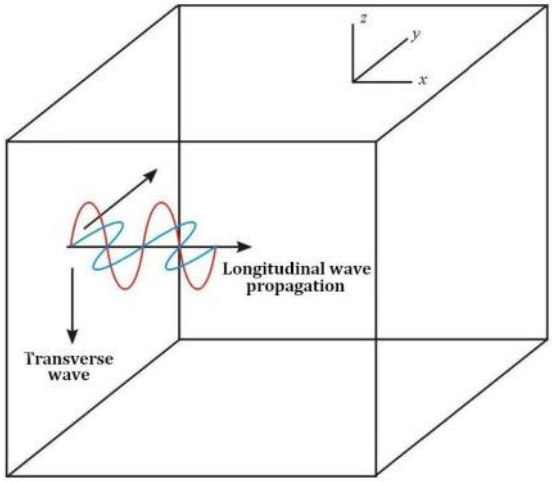

Figure 1.14. Model of wave propagation in an isotropic elastic body.

There are two types of wave for an infinite isotropic elastic body according to the elastic wave theory; longitudinal and transverse:

Longitudinal wave

A longitudinal wave has a curl of displacement field zero and the velocity of wave propagation is:

$$c = \sqrt{\frac{E(1-\nu)}{(1+\nu)(1-2\nu)\rho}}$$

Eq. 1.7

Transversal wave

For a transverse wave, the velocity of wave propagation is:

$$c = \sqrt{\frac{E}{2\,(1+\nu)\rho}}$$

Eq. 1.8

For instance: In a one-dimensional straight cylindrical specimen an axial vibration is at one end of the bar with certain amplitude and at a frequency that is one of the natural frequencies of the bar, being in resonance. At the central section of the specimen there is a node of zero displacement and maximum strain while at the extremes of the specimen there are the nodes of zero stress-strain (Figure 1.15).

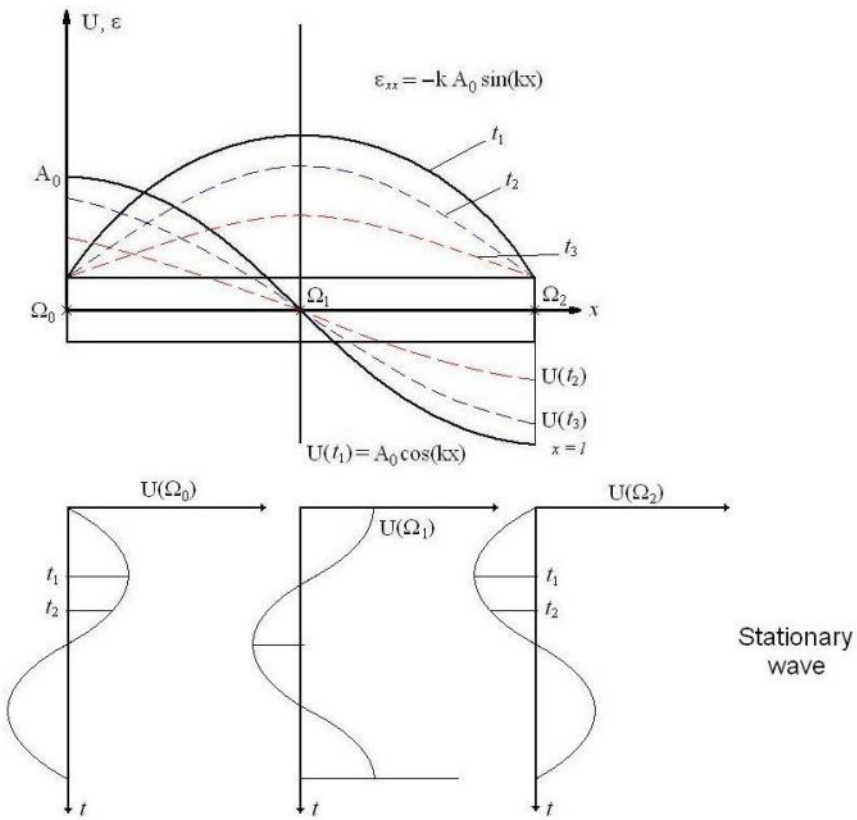

Figure 1.15. Displacement and strain variation in a cylindrical bar [7].

The Longitudinal wave velocity could be determined directly from Eq. 1.7 with ν= 0 for consideration of a one-dimensional example [7].

$$c = \sqrt{\frac{E}{\rho}}$$

Eq. 1.9

And the differential equations (Eq. 1.3 to Eq. 1.5) are reduced to a single equation and only for x axis.

$$\frac{\partial^2 u}{\partial t^2} = \frac{E}{\rho}\frac{\partial^2 u}{\partial x^2}$$

- Eq. 1.10

The solution for the last equation is given by:

$$u = \sum_{n=1}^{\infty} u_n(x,t)$$

Eq. 1.11

Where

$$u_n(x,t) = \left(A_{n-1}\cos\frac{n\pi ct}{l} + B_{n-1}\sin\frac{n\pi ct}{l}\right)\cos\frac{n\pi x}{l}$$

Eq. 1.12

The boundary conditions of ultrasonic fatigue testing require the displacement to be maximum at both ends whereas the strain disappears at the same place. That is

$$\left(\frac{\partial u}{\partial x}\right)_{x=0,l} = 0$$

Eq. 1.13

Then Eq. 1.12 for the first mode of vibration will be

$$u_n(x,t) = A_0\cos(kx)\sin(\omega t)$$

Eq. 1.14

Where

$$k = \frac{\pi}{l}, \qquad \omega = \frac{\pi c}{l}$$

Eq. 1.15

The amplitude of vibration at each point along the bar will be

$$U_a(x) = A_0\cos(kx)$$

Eq. 1.16

where A_0 is the displacement amplitude at the end of the bar. The strain ε at each point is

$$\varepsilon(x,t) = -k\,A_0\sin(kx)\sin(\omega t)$$

Eq. 1.17

with its maximum

$$\varepsilon(x)_{\max} = -k\,A_0\sin(kx)$$

Eq. 1.18

The strain rate is

$$\dot{\varepsilon}(x,t) = -k\,\omega A_0\sin(kx)\cos(\omega t)$$

Eq. 1.19

with its maximum

$$\dot{\varepsilon}(x)_{\max} = -k\,\omega A_0\sin(kx)$$

Eq. 1.20

From Eq. 1.9 and Eq. 1.15

$$l = \frac{1}{2f}\sqrt{\frac{E_d}{\rho}}$$

Eq. 1.21

For the first mode of vibration, $f = \omega/2\pi$ is the frequency and E_d is the dynamic elastic modulus. The length of resonance of the one-dimensional specimen is given by Eq. 1.21 for this first vibration mode. This equation shows an important fact: the resonance length is inversely proportional to the frequency, which explains why some very high frequencies are not practicable, for example 92 kHz and 199 kHz [7].

For a fatigue specimen of variable section, amplitudes of strain and stress vary with the section. Usually, the resonance amplitude is function of the specimen geometry and is determined numerically.

The longitudinal wave equation for a specimen with a variable section can be written as

$$\rho S(x)\frac{\partial^2 u}{\partial t^2} = \frac{\partial f}{\partial x}$$

Eq. 1.22

where $S(x)$ is the area of cross section at position x, and

$$f = E_d S(x)\frac{\partial u}{\partial x}$$

Eq. 1.23

is the force acting on the section, therefore

$$\frac{\partial^2 u(x,t)}{\partial t^2} = c^2\left\{p(x)\frac{\partial u(x,t)}{\partial x} + \frac{\partial^2 u(x,t)}{\partial x^2}\right\} = 0$$

Eq. 1.24

where $c = \sqrt{\frac{E_d}{\rho}}$ and $p(x) = \frac{S'(x)}{S(x)}$

Usually, the specimens for ultrasonic fatigue tests are designed with a reduced section in the center (Figure 1.16a), similar to fatigue crack initiation specimens at conventional frequency. The length L1 is so-called the resonance length, the determination of which involves a numerical approach, such as a finite element method (FEM). At the same way, the specimens for fatigue crack growth (Figure 1.16b) test are designed to be in resonance but a triangular notch is conceived to concentrate the stress at the getting crack growth.

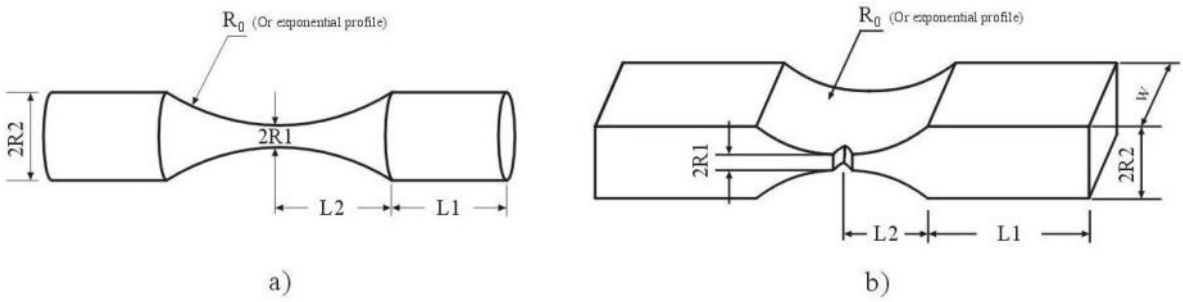

Figure 1.16. Ultrasonic specimen geometry: a) Endurance specimen, b) Crack growth specimen [7].

With the boundary conditions that an ultrasonic fatigue specimen must satisfy, the solution of Eq. 1.24 takes the form $u(x,t) = U(x)\sin(\omega t)$, and Eq. 1.16 at each point along the specimen can be written:

$$U''(x) + p(x)U'(x) + k^2U(x) = 0$$

Eq. 1.25

where k = ω / c .

In order to obtain the solution of Eq. 1.25 it is necessary to define the curve in the central part of the specimen given in the Figure 1.16. For the axis-symmetric specimen in Figure 1.16a, the solution of Eq. 1.25 is

$$U(x) = A_0\varphi(L_1, L_2)\frac{\sin(\beta x)}{\cosh(\alpha x)}, \qquad |x| \leq L_2$$

Eq. 1.26

$$U(x) = A_0 \cos[k(L - x)], \qquad L_2 \leq |x| \leq L$$

Eq. 1.27

Where

$$\varphi(L_1, L_2) = \frac{\cos(kL_1)\cosh(\alpha L_2)}{\sinh(\beta L_2)}$$

Eq. 1.28

The strain and stress are obtained from this solution for the reduced section part and for the cylindrical part.

<u>Stress and strain for a specimen of reduced section</u>

For the reduced section part ($|x| \leq L_2$):

$$\varepsilon(x) = A_0\varphi(L_1, L_2)\frac{[\beta\cosh(\beta x)]\cosh(\alpha x) - \alpha\sinh(\beta x)\sinh(\alpha x)}{\cosh^2(\alpha x)}$$

Eq. 1.29

$$\sigma(x) = E_d A_0\varphi(L_1, L_2)\frac{[\beta\cosh(\beta x)]\cosh(\alpha x) - \alpha\sinh(\beta x)\sinh(\alpha x)}{\cosh^2(\alpha x)}$$

Eq. 1.30

<u>Stress and strain for a specimen of constant section</u>

For the cylindrical part ($L_2 < |x| \leq L$):

$$\varepsilon(x) = k\,A_0\sin\big(k(L - x)\big)$$

Eq. 1.31

$$\sigma(x) = E_d k\, A_0 \sin\big(k(L - x)\big)$$

Eq. 1.32

The difference between the revolution surfaces with the hyperbolic cosine profile and a circular profile is very small for the axisymmetric ultrasonic fatigue specimen. Nevertheless, for fatigue crack growth specimen, it is possible to use a numerical solution for the calculation of the resonance length using FEM [28].

It is necessary to remark that some precautions in fatigue testing materials must be taken into account in order to have adequate fatigue tests and results. Very precise machining of specimens respecting tolerances is necessary in order to have the good length of resonance. Calibration of vibration at high frequency must be verified in order to have accurate amplitude of displacement.

Another important aspect to take into account is the possibility of heating the specimens during the high frequency loading. Some materials, like steel, can be heated some degrees due to high frequency vibration. In this case, cooling means must be used, such as compressed air on the specimen surface.

2.4. Gigacycle fatigue of steel and aluminium alloys

Gigacycle fatigue tests on several metallic alloys have been carried out in the laboratory of Prof. C. Bathias in France for 20 years [7] that include ferrous materials, such as Cr-V or Cr-Si steels, 17-4PH steel; titanium alloys Ti6246, T6A4V; Nickel alloys Udimet 500 and Inconel 706; and aluminium alloys such as AC4CH, AC8C, Al2024, Al6061T6 and other AlSi alloys.

S-N curves for high strength steels and spring steels have been obtained through ultrasonic fatigue tests at 20 kHz observing that specimens continued to fail over 10^7 cycles and even 10^8 cycles. Steel 17-4PH is a martensitic stainless steel that was also tested at 20 kHz [7]. It was observed that fatigue failure can occur between 10^8 and 10^{10} cycles.

Results of cyclic tests of various steels alloys in the range of high-cycle and gigacycle regime were presented by Terentev [29], tests were carried out at R=−1 and 20 kHz for a high strength Cr-Si steel. It has been shown that in all the cases the fatigue curves have two sections separated by a horizontal region (discontinuity of fatigue curves). As a rule, the first section ends between 1×10^6 and 5×10^6 cycles, and the second branch begins after 10^8 cycles (Figure 1.17).

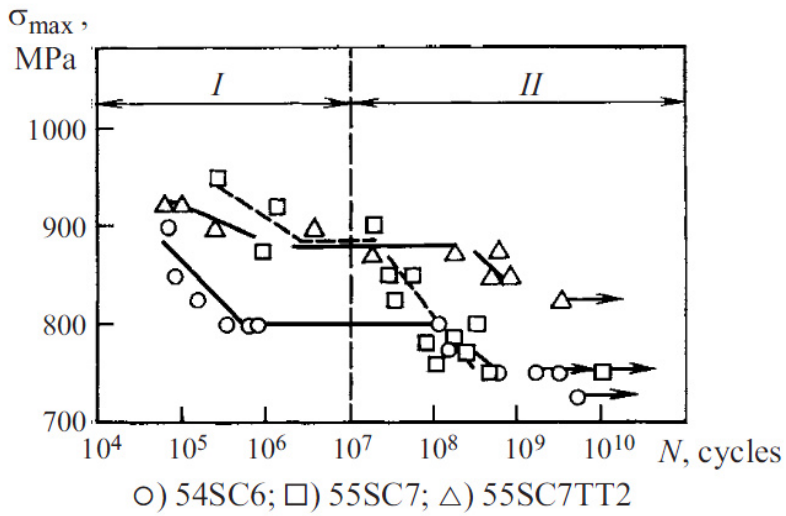

Figure 1.17. Fatigue curves for Cr-Si spring steel and ranges of crack initiation [29].

Related with aluminium alloys, for 2219 and 6061 alloys Bathias et al [7] found the existence of about 100 MPa of difference between the fatigue strengths at 10^6 and 10^8 cycles on tests carried out at R=–1 and 20 kHz.

Stanzl-Tschegg and Mayer [30] carried out ultrasonic fatigue tests at constant and random amplitude at 20 kHz and room temperature on the 2024-T351 aluminium alloy, which is a 1.5% Mg and 1.0% Si (in weight) aluminium alloy. Other experiments were done under distilled water. Fatigue strengths continued to decrease after 10^7 and 10^8 cycles. The effect of distilled water cause the decrease of the fatigue strength (Figure 1.18)

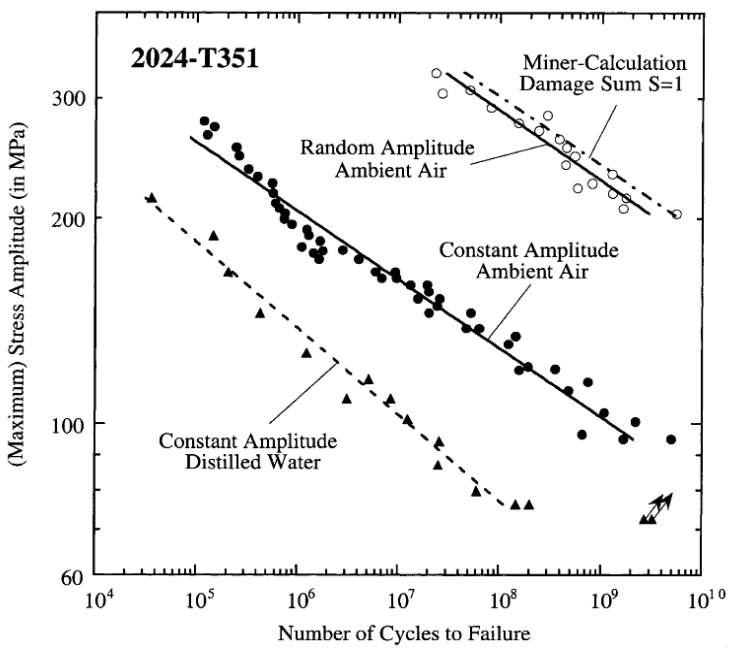

Figure 1.18. Fatigue data for 2024-T351 aluminium alloy [30].

3. Effect of corrosion on fatigue

The term “corrosion fatigue” has been defined as the phenomenon of fracture of metallic materials subjected to cyclic loadings (fatigue) in an aggressive environment (corrosion) [3]. This phenomenon occurs in several engineering alloys in presence of different environments, and it is the cause of failure of several engineering structures, such as these used in chemical plants, ships or off-shore platforms. Corrosion fatigue is also present in boiler and super-heater tubes, turbine and pump components and pipes carrying corrosive liquids [6].

Hostile chemical environments can accelerate the initiation and growth of fatigue cracks. One mechanism is the development of corrosion pits, which then act as stress concentrators. In other cases, environment causes cracks to grow faster by chemical reactions and dissolution of material. Even humidity and gases in the air can act as an aggressive environment.

The fatigue crack initiation and propagation processes will be raised in the next sections.

3.1. Corrosion fatigue crack initiation

The corrosion-fatigue appears by the combined action of both corrosive environment and cyclic loadings. The main characteristic of corrosion fatigue is the decreasing of the metal fatigue strength. Harbor structures and petroleum platforms are often subjected to cyclic loads, in particular at low frequency vibrations [4].

In many instances corrosive action on the surface of a metal may cause a general roughening of the surface and the formation of pits or cavities at certain points and that can result in a considerable decrease in fatigue strength if the metal is subjected to fluctuating loads. Much greater reduction in fatigue strength result from the combined effect of both corrosion and fluctuating loads acting together than from either factor acting separately. In this case usually, corrosion can lead to surface pitting that will reduce substantially the fatigue strength of the material [6].

It is expected some of the characteristics of both fatigue and stress-corrosion cracking to be associated with corrosion fatigue fracture. Corrosion pits are often seen on the fracture surface. In fact, the fracture surface may be coated with corrosion products that are difficult to remove; these no conductive products appear white in a SEM image because they will cause an electron charge [4].

In contrast to stress-corrosion cracking, corrosion fatigue does not require a range of specific environments, any effective corrosive agent may contribute to corrosion fatigue fracture, and higher concentrations are usually more effective. This suggest the possibility of a mechanism of corrosion fatigue, in which crack growth by corrosive attack in the region of the crack tip is accelerated by high local plastic strain in this region that results from the fatigue cycling [4].

In order to study experimentally the corrosion fatigue strength of metals, cyclic loadings or periodic strains are applied on specimens using fatigue machines similar to these in order to carry out conventional fatigue test, but in this case, the test are carried out in corrosive environment [31].

The fatigue tests with smooth specimens have the aim to measure the life time until the failure t_f that is expressed in number of cycles: $N_f = f\ t_f$. Here, N_f is the number of cycles until the failure of specimen and f is the loading frequency. Corrosion decreases the life time to failure. Corrosion takes particular importance in low cycle fatigue, in this kind of fatigue, the stress applied causes a plastic strain and the life time, even without corrosion, is not longer than 10^4 or 10^5 cycles. The same type of *S-N* curve than in fatigue without corrosion can be obtained. Figure 1.19 shows a general shape of the *S-N* curve for corrosion fatigue of metals [31].

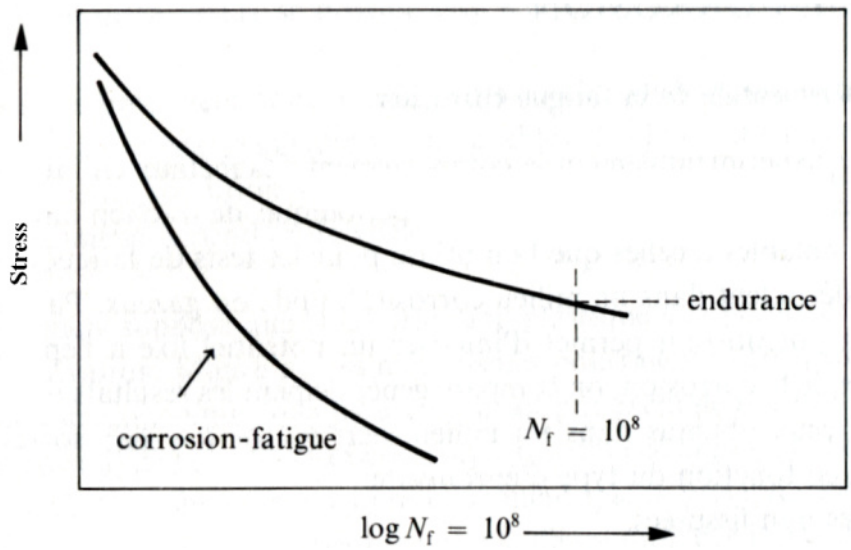

Figure 1.19. *S-N* curve showing a general characteristic of corrosion-fatigue [31].

Figure 1.20 shows an example of the general characteristic of corrosion fatigue. It shows the number of cycles of failure as function of the applied stress for specimens of ferrite-austenitic stainless steel, in air, or immersed in solutions of NaCl 3% or H_2SO_4 0.05 M respectively. The author does not mention the frequency of tests. It is observed that specimens deteriorate faster in sulfuric acid than in salt solution or in air [31].

In general, corrosion fatigue is much more important than the intrinsic corrosion rate of the metal. In Figure 1.20 the uniform corrosion of the metal is faster in sulfuric acid than in salt solution. The fatigue strength in sulfuric acid is the lower. It is observed that the decreasing of fatigue strength is higher in the high cycle regime than in low cycle regime.

The mechanisms that control the crack initiation in corrosion fatigue are not good known. It is supposed that corrosion plays a preponderant role in different ways: by pits, intergranular, acid located or linked to the presence of inclusions. The influence of the aggressiveness of the environment on the life time during the fatigue corrosion tests confirm that (Figure 1.20), this type of tests provide basically the fatigue life under hostile environments [31].

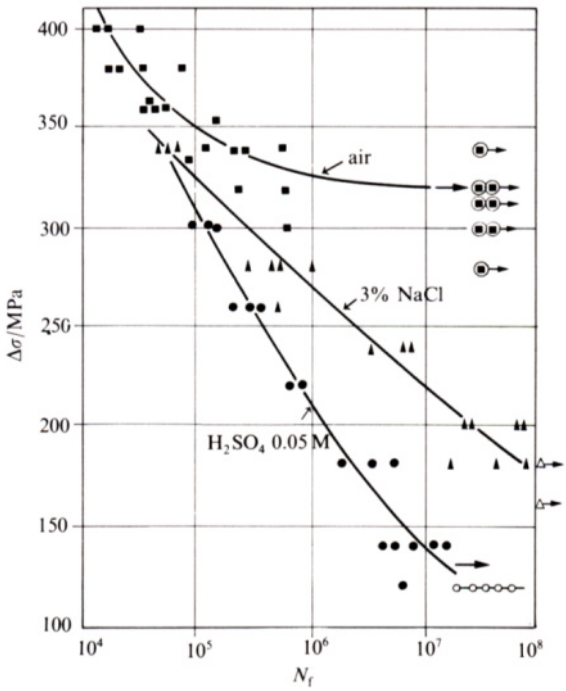

Figure 1.20. Influence of environment on fatigue life of an austenitic stainless steel Fe17Cr12Ni [31].

Truchon and Rabbe [32] presented the fatigue corrosion results of a stainless steel X3CrNiMoCu 21-7 in 3% NaCl solution with different electrochemical potentials and also in air. The tests were carried out in rotating bending fatigue at 50 Hz. In Figure 1.21 [32] it is observed that fatigue strength decreases at higher potential imposed and all the saline environments cause a detriment of the fatigue strength.

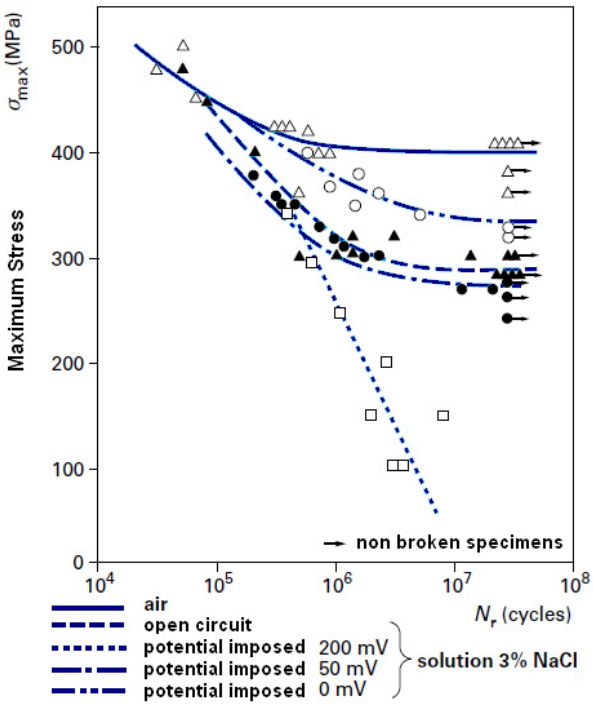

Figure 1.21. Influence of electrochemical conditions on the corrosion fatigue strength of X3CrNiMoCu 21-7 stainless steel [32].

Magnin and Lardon [33] analyzed the fatigue damage in low cycle fatigue of a 316L stainless steel in air and in 3.5% NaCl aqueous solution, observing the evolution of the specimen surface roughness. Smooth specimens (5 mm diameter) were tested at symmetrical tension-compression at prescribed plastic strain amplitude ($\Delta\varepsilon p/2 = 4\times10^{-3}$) and at constant total strain rate ($\dot{\varepsilon} = 10^{-2}$ s^{-1}) in a servohydraulic machine. Tests were conducted at room temperature in dry air and in an aerated and replenished 3.5% NaCl solution at pH 6 under potentiostatic control. The decreasing in fatigue life in the corrosive environment was observed and they related this to located dissolution effects which favor a more rapid coalescence of the mechanically nucleated microcracks at the surface. They showed that a transition occurs from microcracks nucleation to macrocracks propagation by series of micropropagation and microcoalescence processes at the metal surface. It is presumed that such process takes a long part of the life time. The effect of a corrosive environment on the fatigue behavior of 316L stainless steel results in the reduction of the fatigue life by a factor of 2 in the corrosive solution compared with that in air. Transgranular microcracks of length roughly equal to the grain size (Figure 1.22) nucleate in slip bands at around 10^3 cycles in air as in corrosion [33].

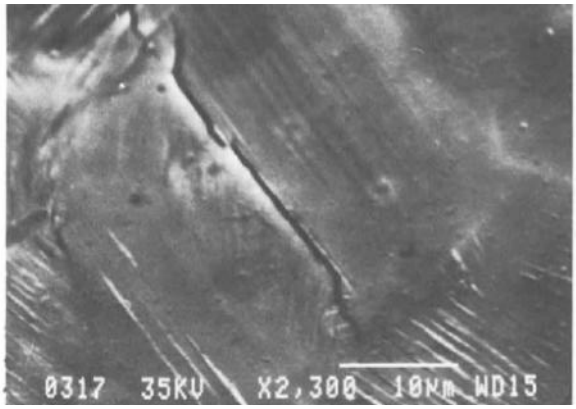

Figure 1.22. Nucleation of microcrack in slip band for 316L stainless steel in 3.5% NaCl solution at N≈1000 cycles, $\Delta\varepsilon p/2 = 4\times10^{-3}$, $\dot{\varepsilon} = 10^{-2}$ s^{-1} [33].

Magnin and Coudreuse [34] have shown that cyclic strain can enhance local electrochemical reactions which are closely dependent on the plastic deformation mode and the strain localization during cyclic loading. Symmetrical tension-compression tests were carried out under plastic strain control at given strain rates (10^{-4}, 10^{-3} and 10^{-2} s^{-1}) using a servohydraulic machine. Fe-26Cr-1Mo stainless steel specimens with a diameter of 5 mm were tested in aerated 3.5% NaCl solution at room temperature. Particular attention was paid in the influence of the strain rate on both plastic deformation and the dissolution characteristics which govern the crack initiation process, according with these authors. At high strain rates (10^{-2} s^{-1}) strain was localized at the grain boundaries and then dissolution was localized at the grain boundaries, crack initiation was intergranular and life time was around 1000 cycles. At intermediate strain rates (10^{-3} s^{-1}) dissolution was entirely located at the grain boundaries, crack initiation was intergranular and life time was shorter (~1600 cycles) that at high strain rates. At low strain rates (10^{-4} s^{-1}) the amount of dissolution was lower, crack initiation was induced by mechanical loading and it was transgranular and fatigue life was similar than in air around 9×10^4 cycles (Figure 1.23) [34].

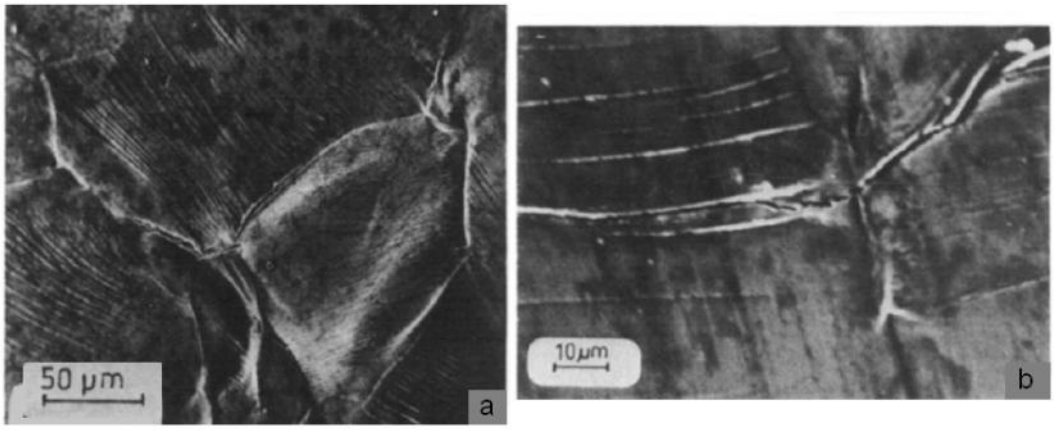

Figure 1.23. Influence of strain rate on the crack initiation mode, (a) 10^{-3} s^{-1}, intergranular crack, (b) 10^{-4} s^{-1}, transgranular crack [34].

Fatigue tests in low cycle regime were carried out by Zhu et al [35] on structural AISI 4130 steel exposed to neutral perchlorate of sodium solution 0.1 M (NaClO4). They chosen an environment almost neutral (pH=6.3) in order to maintain the oxide films produced by potentiostatic control in the anodic region. Fatigue tests were carried out under plastic strain control with plastic strain amplitudes 7×10^{-4} and 2.2×10^{-4}. The frequency of cycling was 0.5 Hz. As expected, the fatigue life was reduced in corrosive environment in comparison with tested in air. In air fatigue crack initiated at inclusions (Figure 1.24) while in perchlorate solution fatigue crack initiated at the grain boundaries. A particular experiment of pre-corrosion was done, they tested some specimens during some thousand of cycles in corrosive environment and after they tested the same specimen in air until failure. The result of this experiment was that fatigue crack initiated at inclusions after pre-corrosion, like specimens tested in air, this confirmed that continuous presence of corrosive agent was necessary to have the cracking mechanism of corrosion fatigue [35].

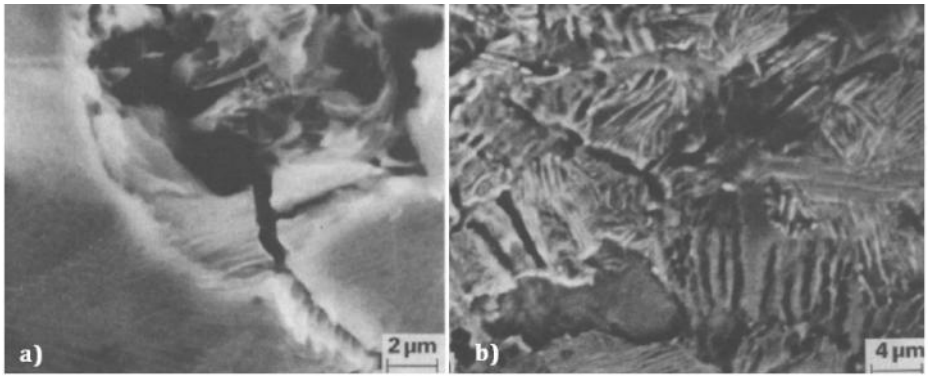

Figure 1.24. Crack nucleated at an inclusion in air (a) and intergranular and transgranular crack in 0.1 M NaClO4 (b) in AISI 4130 steel [35].

For aluminium alloy, an example of the influence of environment is presented in Figure 1.25. Al-7.5Zn-2.5Mg alloy was tested in bending fatigue at R=–1 in a 3% NaCl solution up to 10^7 cycles. The fatigue strength was around 60 MPa lower in salt solution than in air at 10^6 cycles, while at $>10^7$ cycles the difference was around 100 MPa.

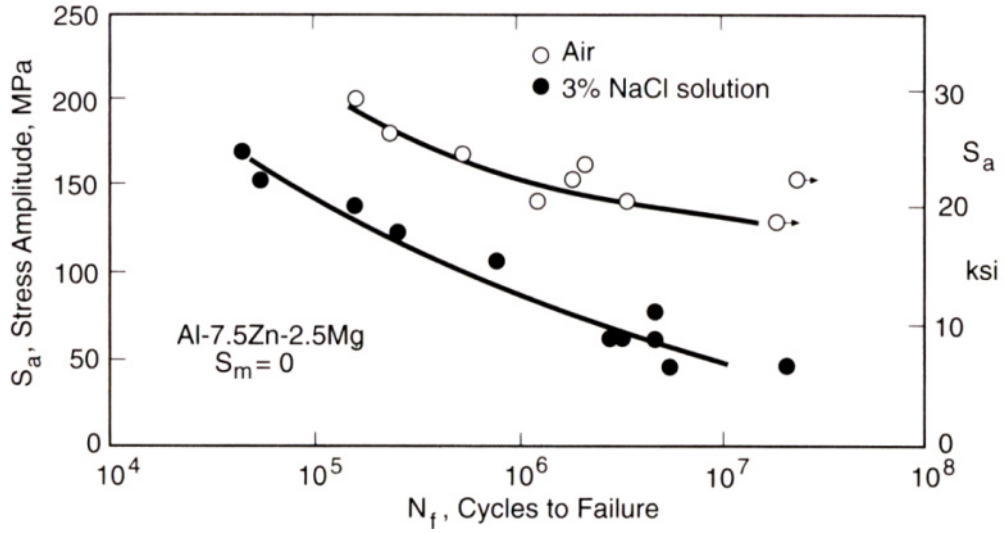

Figure 1.25. Influence of salt solution on the bending fatigue of Al-7.5Zn-2.5Mg at R=–1[2].

Corrosion fatigue has not been widely studied in the high cycle or very high cycle regime. A few of investigations exist about corrosion fatigue in this regime. Wang [36] studied the effect of pitting corrosion on the very high cycle fatigue regime on a 7075T6 aluminium alloy using a piezoelectric machine at R=–1 and 20 kHz. Specimens were immersed in saline (3.5% NaCl) solution during 1, 4, and 7 days. After this procedure of pre-corrosion the pits obtained were around 30, 50 and 60 µm of diameter respectively for 1, 4 and 7 days. The results showed that the presence of pre-existing corrosion pits reduced significantly the fatigue life of the aluminium alloy.

Yeske and Roth [37] studied the effect of corrosion on the fatigue strengths of 403 stainless steel (with 12% Cr) exposed to 22% NaCl solution. They observed that fatigue strengths are the same at two different loading frequencies: 40 Hz and 20 kHz (Figure 1.30).

On the other hand, Ebara and Yamada [38] carried out tests at high frequency (16 kHz) at R=–1 on a 13Cr stainless steel (SUS 304 Japanese) in different environments, such as distilled water, and aerated 3 to 3×10^{-4} percent of NaCl aqueous solution, all at room temperature. They observed that fatigue strength decreases under ultrasonic frequency of 16 kHz and the lower NaCl content in the environment the longer is the fatigue life.

3.2. Corrosion crack initiation interpretations

It is known that corrosion fatigue appears in several alloys; the presence of different environments is an important cause of failure of components and structures for engineering. The knowledge of the mechanisms and the kinetic characteristic of corrosion fatigue are essential for the prediction of service life, fracture and fatigue strength of many metallic alloys.

The fatigue crack initiation in corrosion environment has been classified in three regimes according to Pelloux and Genkin [39]. Active dissolution, electrochemical passivity and local rupture of passivity regime. The initiation under electrochemical passivity conditions has been explained by sequences of rupture/formation of an oxyde layer. This oxyde layer is locally fractured by the tension loading application or by the emergence of slip bands. Each oxyde layer fracture results in a local dissolution of the metal and the posterior formation of a micro notch. When such notch reaches enough dimensions, corrosion fatigue cracks initiate [39].

Under active dissolution conditions, the persistent slip bands act with the corrosive environment and provide an intensification of the slipping irreversibility. Slipping band distribution is modified by the presence of the environment. Electrochemical reactions are stimulated by the presence of mobile dislocations generated by the interaction between slipping phenomenon and the material surface. The persistent slip bands become anodic in comparison with the non deformed material and they are preferentially dissolved [39].

A layer rupture model is also discussed by Kramer and Kumar [40]. It is proposed in this model that the layer is fractured at the crack tip by plastic deformation. This produces localized anodic dissolution because crack walls remain passive [40].

Several fatigue cracks are initiated at a free surface, slip bands or at an interface (grain boundary, inclusion). And, with the exception of gold, all metal surfaces are covered by oxides. However, many surfaces are covered by films for corrosion protection. For this reason Grosskreutz [41] consider important to take into account the effect of surface films on the mechanisms of fatigue crack initiation. A surface layer that loses its integrity by fracture will stop to give environmental protection and will not play the expected influence on subsurface plasticity at the point of rupture. In fact, under an applied stress, the broken point will become a region of concentrated plastic deformation in the substrate. The addition of another environmental attack at this point usually will become in a crack initiation [41].

The appearance of corrosion fatigue failures have been explained in a simple way by Forrest [6]. First, the surface is often discolored by the corrosion process, although this is not an essential characteristic. Another feature is the appearance of multiple cracks. There are normally many more cracks present in corrosion fatigue than in fatigue alone [6].

3.3. Corrosion fatigue crack propagation

An important characteristic that is found in corrosion fatigue is that the crack growth rates are faster and it is found that it depends of several chemical and electrochemical variables that are not present in other inert environments.

A first approximation of the problem of corrosion fatigue is the hypothesis that independent mechanisms acts on the cracks. That is to say, a linear superposition of the corrosion and fatigue contributions in the propagation rate for a material in corrosion environment [42].

$$\frac{\mathrm{d}a}{\mathrm{d}N} = \left(\frac{\mathrm{d}a}{\mathrm{d}N}\right)_f + \int \left(\frac{\mathrm{d}a}{\mathrm{d}N}\right)_{SCC} dt$$

Eq. 1.33

Where $\left(\frac{\mathrm{d}a}{\mathrm{d}N}\right)_f$ is the fatigue propagation rate without corrosive environment and $\left(\frac{\mathrm{d}a}{\mathrm{d}N}\right)_{SCC}$ is the propagation rate of the crack with a corrosive environment.

In many corrosion fatigue situations contradictions are observed with the results of the linear superposition hypothesis, which makes difficult practical applications [42]. Some facts are that it does not exist a unique specific environment for corrosion fatigue for each material; all the non inert environments cause a certain extent acceleration of fatigue crack growth.

As fatigue alone, fatigue crack growth tests can be carried out for obtaining d*a*/d*N* curves as function of Δ*K*. Commonly is known that corrosive environment increase the crack growth rate for a given Δ*K* [31]. An example of such curves is illustrated in Figure 1.26 where are shown the d*a*/d*N* curves for an austenite-ferrite stainless steel in inert and saline environment.

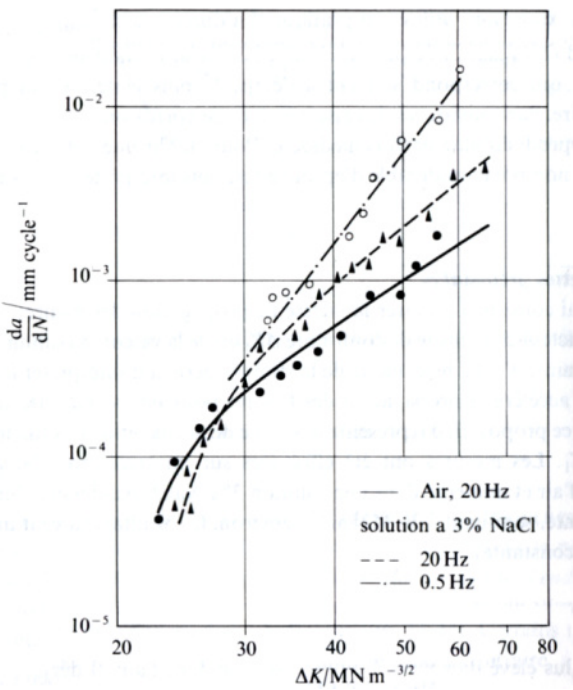

Figure 1.26. Effect of saline environment on the crack growth rate of an austenite-ferrite stainless steel [31].

Another example is the steel jacket type platform on a pile foundation, which is the most common kind of offshore structure existing worldwide. The "substructure" or "jacket" is fabricated with steel tubes and is pinned to the sea floor with steel piles, which are driven through piles guides on the outer members of the jacket. In the North Sea these steel structures are used and fatigue can limit their service life. Thorpe et al [43] reported the effect of through-thickness defects on a structural steel BS4360:50D in air and in real sea water. Tests on compact tension specimens were carried out at constant amplitude sinusoidal cyclic loads. They showed that sea water favor crack growth by an amount which increases with increasing stress ratio and decreasing applied test frequency in the range of 10 Hz to 10^{-3} Hz (Figure 1.27). They proposed two corrosion processes in order to explain the fatigue crack growth mechanisms, the first is that exists an anodic dissolution of the freshly exposed material at the tip of the crack, corrosion rate here could be higher than bulk corrosion rate because of highly local strained condition of material, and the production, by plastic deformation, of highly active slip steps in this region. The second is that hydrogen evolution can lead the embrittlement of the crack tip; this reaction would be favored by the anaerobic local conditions. They emphasize that this mechanism is the only one which could explain the favored crack growth rates observed with hydrogen [43].

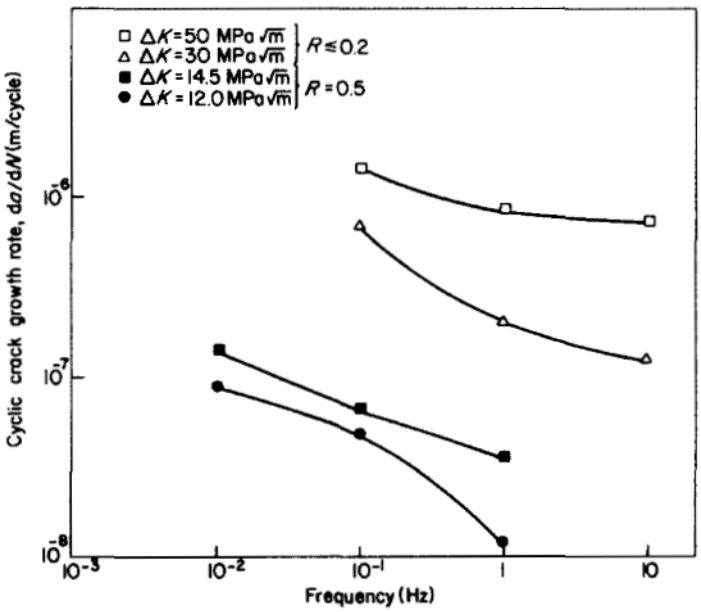

Figure 1.27. Frequency dependence of corrosion fatigue crack propagation in sea water for BS4360:50D steel [43].

Bolton and Redington [44] studied the fatigue crack propagation of 316 stainless steels for surgical implants in saline aqueous environment simulating physiological solution. Fatigue crack growth was determined experimentally on a servohydraulic machine using compact tension specimens inside a corrosion cell, in which saline solution was pumped. Frequencies of test were between 0.2 and 15 Hz. They found faster crack growth rates in the saline aqueous solution than in air, but at higher stress intensities the crack growth in saline solution became slower than in air. The proposed crack growth mechanism which rates are altered due to corrosion fatigue is that a corrosive environment influences crack tip plasticity during loading [44].

Offshore structural steels are subjected to cyclic loadings under corrosive environment. The fatigue behavior of these structures is an interesting topic. Fatigue crack growth was measured by Horstmann et al [45] on structural steels TStE355 (S355NL European designation) for offshore. They studied the influence of both testing frequency and specimen thickness carrying out tests in air, in synthetic sea water and in sea water with cathodic polarization. Tests were carried out on servohydraulic machines in load control at frequencies varying from 0.008 to 40 Hz with sinusoidal waveform. Load ratios 0.1, 0.27 and 0.7 were examined. In air, a minimal effect of thickness on the fatigue crack growth rates was observed. In salt water the fatigue crack growth rate increased. Under conditions of cathodic polarization at low testing frequencies (0.05–0.5 Hz) thickness effect became apparent [45]. Figure 1.28shows the crack propagation curves determined in tests with sea water.

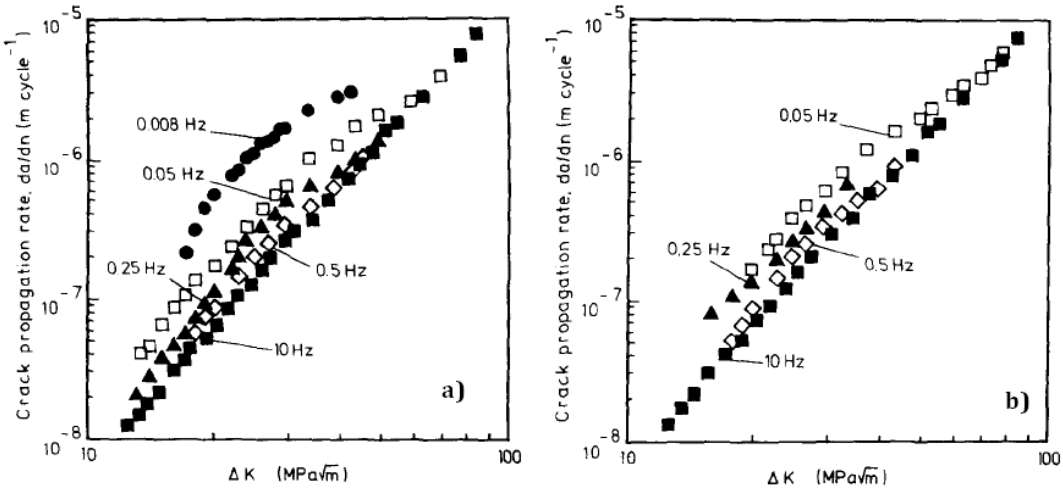

Figure 1.28. Fatigue crack growth rates for offshore structural steel TStE355 in sea water freely corrosion (a) and in sea water with cathodic polarization (b) at different frequencies [45].

3.4. Corrosion fatigue crack propagation interpretations

Some hypotheses have been proposed about the mechanisms that govern the fatigue corrosion crack growth processes. According to Arana and Gonzalez [3] corrosion fatigue implies the presence of a cracking induced by hydrogen that can include the cyclic process of rupture of the oxide layer or anodic dissolution in the edge of the crack.

It is very difficult to establish a difference and to analyze separately the effect of each one of these phenomenon. It is mentioned that these processes compete to each other so that only one of them contributes more in the crack growth and consequently in the failure [3].

In corrosion fatigue, hydrogen is generated by reaction between the compounds present in the environment, gaseous or liquids, and more ahead with the cracked material in front of the crack. This hydrogen is adsorbed by the metal surface and transported, by diffusion or slipping dislocations, to the region with high stresses in front of the crack (plastic zone),

where it causes localized damage and increases the crack growth caused by only the fatigue process. Figure 1.29 illustrates a scheme of the steps of the crack growth process in corrosion fatigue according to [3].

According to [3] the more influent mechanical variable in the process of corrosion fatigue for its differentiation with fatigue alone is the frequency of loading application. Taking as reference the fatigue behavior of a metallic material in inert environment which is independent of the cycle loading frequency, the addition of a corrosive environment with a behavior as the described in Figure 1.29 where the slowest process controls the global behavior produces a crack growth faster than in fatigue alone. The processes illustrated in Figure 1.29 are sequential; therefore the crack growth rate is controlled by the slowest process of all the sequence [3].

According to Arana and Gonzalez [3] when the loading frequency is high, the effect of corrosive environment is just noticeable; if the frequency decreases the effect of the corrosive environment is more noticeable.

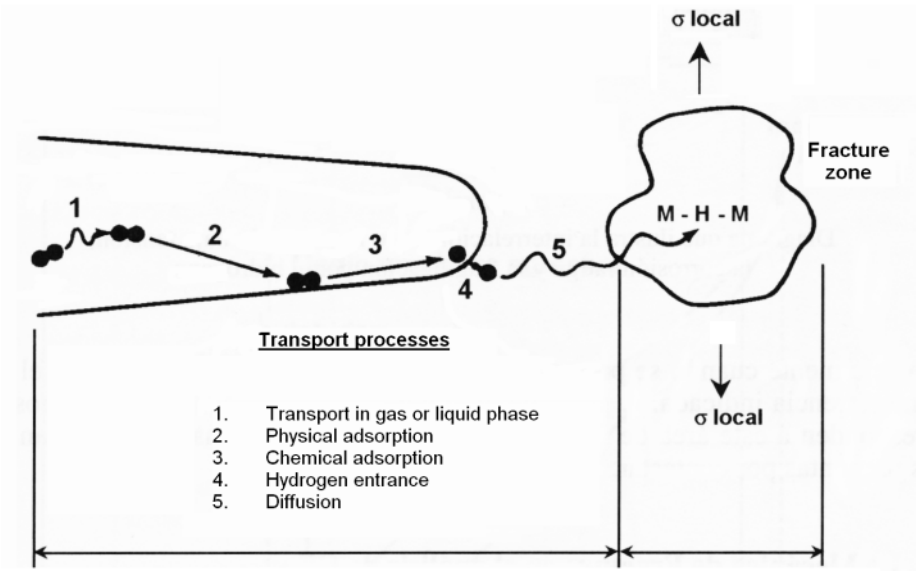

Figure 1.29. Sequence of steps that are present in the crack growth during corrosion fatigue in metallic alloys [3].

On the contrary, Yeske and Roth [37] have shown that the corrosion fatigue strengths of 403 stainless steel (with 12% Cr) exposed to 22% NaCl solution are the same at two different loading frequencies: 40 Hz and 20 kHz. Although large effects were induced by environmental changes, the S-N curves (Figure 1.30) and the crack initiation morphologies were similar for the tests at both frequencies. The reported that cracks initiated at the base of pits formed on the specimens at both frequencies, even though some of the tests at 20 kHz lasted only 100 seconds.

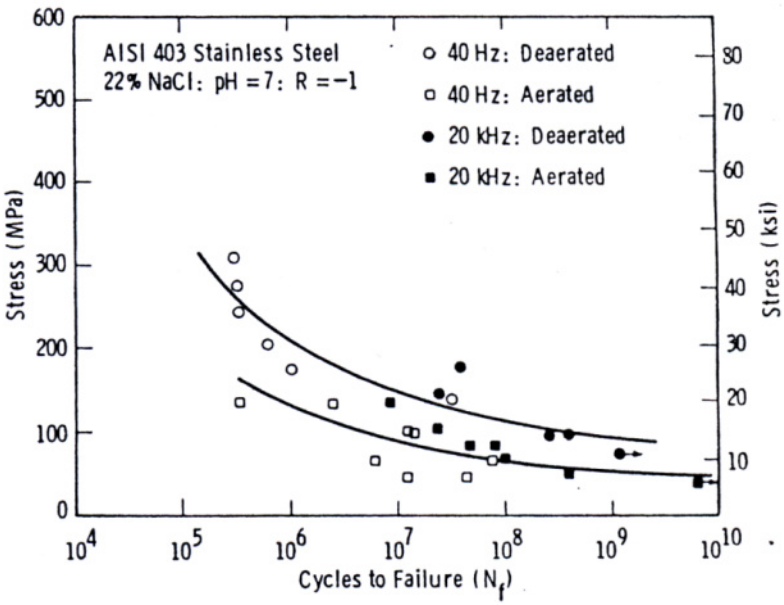

Figure 1.30. Comparison of fatigue results for 403 stainless steel at 40 Hz and 20 kHz in 22% NaCl Solution [37].

A possibly explanation for this similarity with very different frequencies is proposed by Yeske and Roth [37]. Transport of metal ions out of the pit electrolyte must occur at a high rate in ultrasonic fatigue but it appears that transport may be accelerated by convection induced by the high frequency loading.

A model of dissolution have been presented by Pelloux and Genkin [39] and it suggests that the increasing of the crack growth rate in corrosion fatigue is completely caused by the dissolved metal amount in the front of a crack. This model suppose that metal is in the passivity domain, it means that its surface is covered by a protector film. The imposed deformation at the front of crack fractures this protector film; the exposed surface is corroded again while the film is reformed. At each fatigue cycle the crack will grow.

Another interpretation is in relation with the crack length. A distinction between short cracks and long cracks is done. The crack length is normally the same order of size of a characteristic distance of microstructure. The assumption of an isotropic body is taken. For instance, the cracks can interact with the grain boundaries. This phenomenon is observed when the plastic zone is of the same order of size than the grain size [39]. A crack is considered physically "short" when the plastic closure does not exist normally for crack lengths shorter than 1 mm. In corrosion fatigue, the environment at the crack front is determined by the diffusion, convection, and migration of chemical compounds and the electrochemical reactions in the metal/solution interfaces. That is a complex process.

In the case of "large" cracks, crack growths in corrosive environment become similar to those obtained in air for ΔK values near to Kc (Stress intensity factor for the final fracture of the specimen) [39].

In a general way it is said that the frequency has an effect on the crack growth rate depending on the ΔK. In the domain of moderated ΔK the behaviors can be different depending of the material. An example for stainless steel under two different environments (air and saline solution) can be observed in Figure 1.31. Crack growth rate seems faster at low frequency under corrosive environment, although the slope is the same and the differences of crack growth rates are not very high between 1 and 10 Hz.

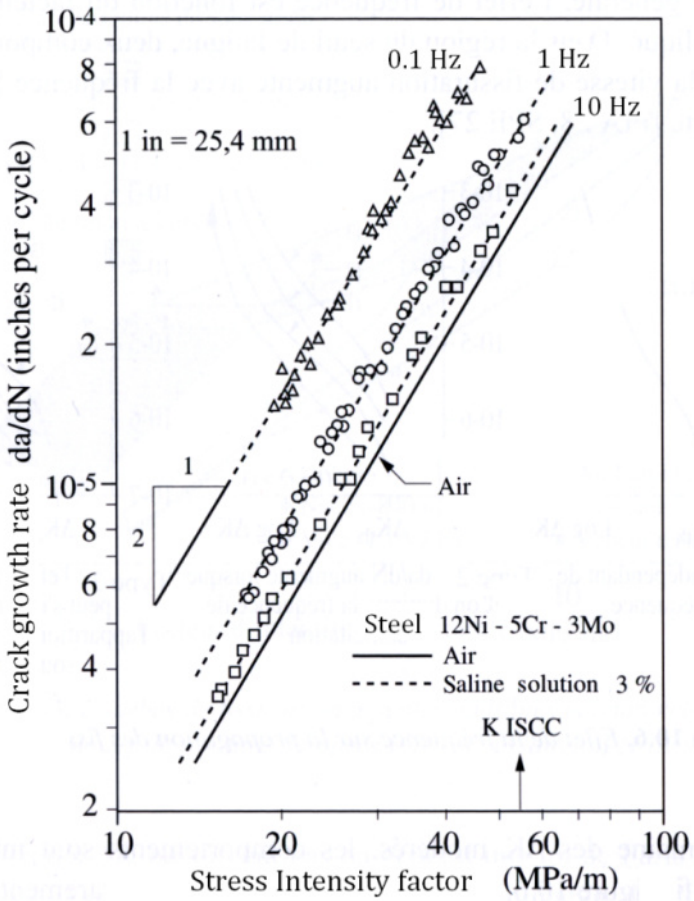

Figure 1.31. Corrosion fatigue crack growth rates for 12Ni-5Cr-3Mo steel at different frequencies [39].

4. Effects of defects on fatigue

Numerous reasons exist for which structural components fail under repeated loadings. Some causes of these failures in materials can be due to unique effect or combined conditions of the material, such as design geometrical defects or notches, manufacturing defects, inadequate or insufficient maintenance, overloads in operational conditions, environmental factors like heat or corrosion, secondary efforts not considered in the normal service conditions.

Defects like inclusions or porosities are present in most commercial materials as a result of deoxidization additions, impurities or entrained exogenous material. These defects are common sites for fatigue crack nucleation; they are known to be really harmful in high strength steels, for instance. In middle cycle fatigue crack initiation usually occurs on the specimen surface. The crack propagation is important in structures containing cracks in low cycle fatigue, but the crack initiation controls fatigue life in high cycle fatigue [46].

According to Pang and Reed [47] fatigue crack initiation and crack growth are important in the life time of the majority of components subjected to several types of loading. Microstructure and environment play an important role in fatigue crack initiation and subsequent crack growth, especially when crack lengths are comparable to the scale of microstructural features. Fatigue cracks have been observed to initiate from slip bands, grain boundaries, twin boundaries, inclusions and other defects [47].

Fractography analysis is usually useful to examine the crack initiation feature in fractured specimens, C. Bathias and coworkers have shown that most of the time in the high cycle regime (10^7 cycles and beyond) for high strength steels, the initiation sites are found at inclusions located in the interior of the specimens. Figure 1.32 shows typical stages of crack initiation in gigacycle regime [46].

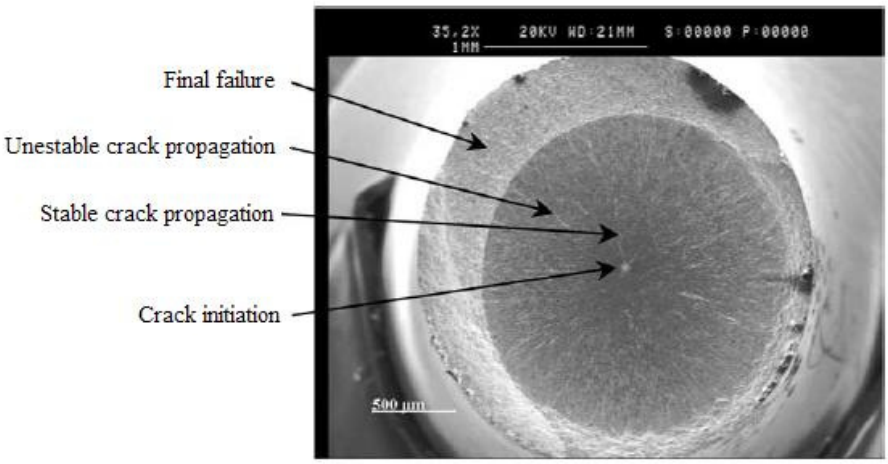

Figure 1.32. Stages of crack propagation on the gigacycle fatigue fracture surface [46].

To understand and predict the fatigue life in terms of crack initiation and small crack propagation is very important. Generally, it has been accepted that at high stress levels, fatigue life is governed by crack growth, while at low stress levels life time is mainly consumed by the process of crack initiation [7]. Some authors [9, 11] demonstrated that the portion of the life attributed to crack nucleation is over 90% in the high cycle regime for steel, aluminium, titanium and nickel alloys [7]. In several cases the crack nucleates at the defects, like inclusions or porosities, it is said that a relation should exist between the fatigue strength and the crack growth threshold [27].

In the gigacycle regime the initiation sites are usually located inside the specimens for nickel and titanium alloys, and high strength steels. In aluminium and magnesium alloys, fatigue crack initiation appears at the surface of specimens, especially in castings where voids at the surface are the main locations for crack formation [7].

Observations from literature show that crack initiation in gigacycle fatigue seems usually to occur inside the specimen and not at the surface if there are defects inside the metal [7, 46, 47].

Theory says that three types of crack initiation occur in cylindrical specimens with a polished surface depending on whether it is low cycle (10^4 cycles), megacycle (10^6 cycles) or gigacycle fatigue (10^9 cycles). Figure 1.33 shows schematically that for the smallest number of cycles to fracture, the initiation sites are multiple and on the surface, according to usual observations. At 10^6 cycles there is only one surface initiation site. For very high number of cycles to fracture, the initiation is located in an internal zone. Generally, the crack initiates from a defect, but sometimes the crack initiation is related to microstructure anomalies, for example, long platelets or perlite colonies [7].

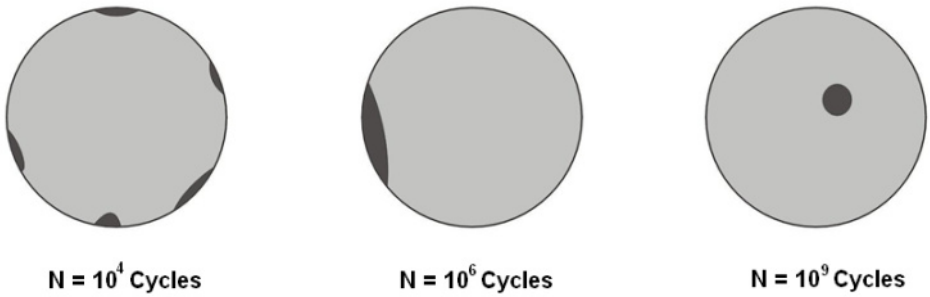

Figure 1.33. Schematic representation of mechanism of fatigue initiation according the number of cycles to rupture [7].

Bathias and Paris [7] explain that at 10^9 cycles, three main factors operate as initiation requirements for cyclic strain and maximum strain:

Anisotropy of metals: The plastic strain is very small, then, the plasticity appears only if the grain orientation and the grain size are in agreement with dislocation sliding at the surface or in the volume of metals.

Stress concentration: It is thought that stress concentration due to metallurgical microstructure disordered becomes an important factor when the applied load is low. Defects and grain size effect are among efficient concentrators.

Statistical conditions: Statistically, the probability to find an enough stress concentration is more probable in the bulk than in the surface of the metals.

At the moment, the probability of an offensive stress concentrator in the bulk of the metal is the best explanation for the localization of crack initiation in gigacycle fatigue [7].

It is well know that fatigue crack initiates mainly at surface defects in the short fatigue life range, but may shift to subsurface in the long life range. Recent results on conventional materials, such as steel, have extended the knowledge about ultra-high cycle fatigue [27]. The mechanisms of crack initiation at subsurface defects, such as subsurface inclusions and pores has been investigated in some iron materials and light metal alloys [46].

Zuo et al [48] have studied the fatigue behavior of Ti-6Al-4V in the ultra-high cycle fatigue regime. According to them, in the fatigue damage stage, cyclic stress attacks both surface and internal defects, and they considered that the site which is selected for main crack initiation is always competitive and depends on the size of the potential sites and the stress level, it means that there is a transition of crack initiation from surface to interior at certain stress level. They observed internal fatigue cracks at low stress levels and superficial fatigue cracks at high stress levels [48].

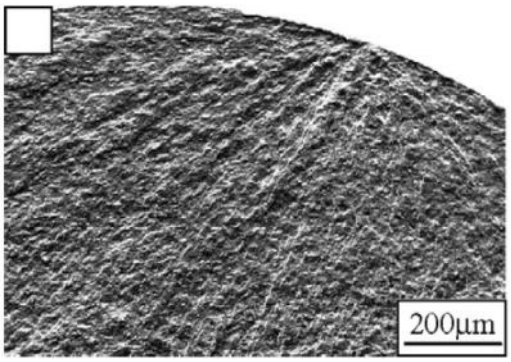

Figure 1.34. Surface crack initiation at defect on Ti-6Al-4V (R=–1 , σ_a=540 MPa, N_f=5×10^6 cycles) [48].

The use of cast aluminum components under cyclic loading has generated the interest in the fatigue properties of these alloys. These fatigue properties are strongly influenced by the presence of casting defects and microstructural characteristics of the casting. Porosity, voids or cavities that form within a casting during its solidification are the more common defects found in Al-Si casting alloys and results in poor mechanical properties such as limited strength and ductility, variable fracture toughness, irregular crack initiation and crack propagation characteristics. Several studies have shown that porosity is the key factor which controls the fatigue properties of Al-Si cast aluminum alloys. The effect of porosity on high cycle fatigue life (10^7 cycles) has been summarized as follows: pores reduce the time for crack initiation by creating a high stress concentration in the material adjacent to the pores; because of this, most of the fatigue life is spent in crack growth [49]. Figure 1.35 shows an example of the crack initiation in porosities on Al-Si cast aluminium alloy at R= –1 failed over 10^7 cycles [7].

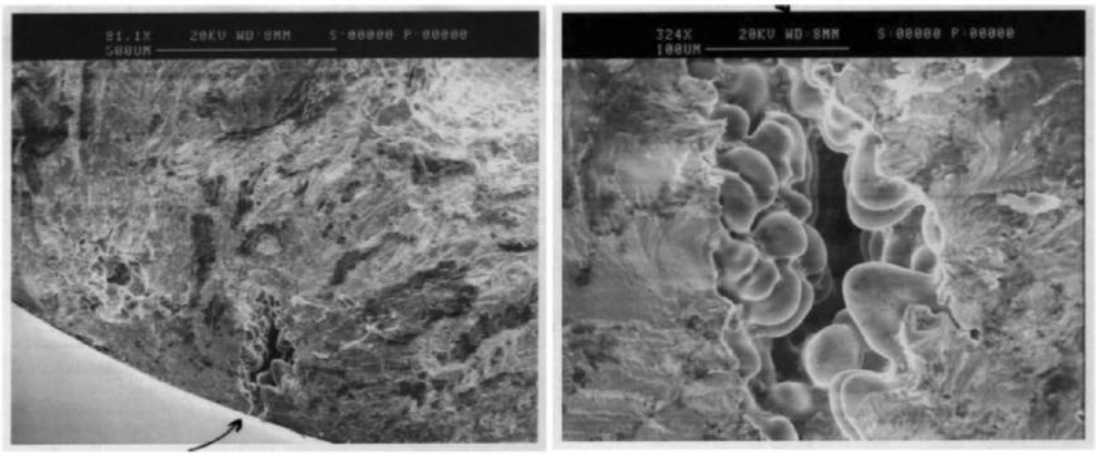

Figure 1.35. Crack initiation site on an Al-Si cast aluminium alloy in high cycle regime [7]

Fatigue criteria on defective materials

Some researchers have presented studies of the fatigue behavior of non defective materials, such as zero inclusion steels [21] or zero inclusion titanium alloys [7]. Researches who are mainly interested in the mechanisms of a microscopic scale have coincided in the study of the dislocation behavior including many experiments and theories on persistent slip bands and various dislocation structures [21, 8]

Ti-6246 titanium alloy is an alloy with any inclusions or porosities presented by Bathias [7] in a study to look where fatigue crack initiates if internal or geometrical defects are not present. Fatigue failure occurred even up to 10^9 cycles and fractographic observations by SEM revealed that initiation was located near at the specimen surface observing quasi cleavage facets in primary alpha phase, demonstrating that fatigue in the high cycle regime is not always correlated to defects such inclusions or pores [7].

But the defects are presents in the most of metallic materials, whether they come from melting fabrication or manufacturing modifications. In high cycle fatigue these defects are stress concentrators and they are preferential sites for the crack initiation in fatigue [50]. The stress at the edge of such defects has a higher value than the remote or nominal stress [8]. Some interpretations of the fatigue on defective materials are presented then:

Murakami

Murakami has proposed the $\sqrt{area}$ of a defect as parameter for determining the stress concentration around the defect [8] such as a crack. In a first approximation the stress concentration factor around a crack is given by $K_I = 0.5\ \sigma_0\sqrt{\pi\sqrt{area}}$. Considering such area as shown in Figure 1.36-a [8] for a defect localized in the plane *x-y*.

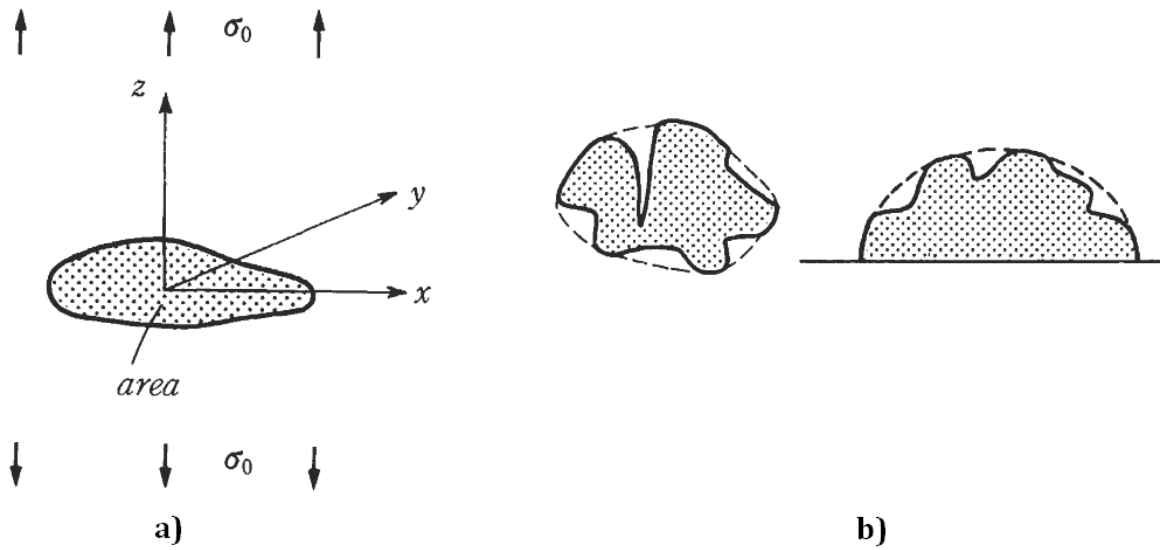

Figure 1.36. Murakami approximation for an arbitrary internal defect to an area [8].

At the same way, the "effective area" parameter is proposed considering a smooth contour that involves the original irregular area of the defect (Figure 1.36-b). Then the previous equation for stress intensity factor become to: $K_I = 0.65\ \sigma_0\sqrt{\pi\sqrt{area}}$ [8].

This parameter has been used by Billaudeau [50] for the characterization of artificial defects created on specimens of C36 low alloy steel tested in tension and torsion. Hemispherical and semielliptical defects with different size and orientation were created using micromachining, laser and electro-erosion. An example is shown in Figure 1.37.

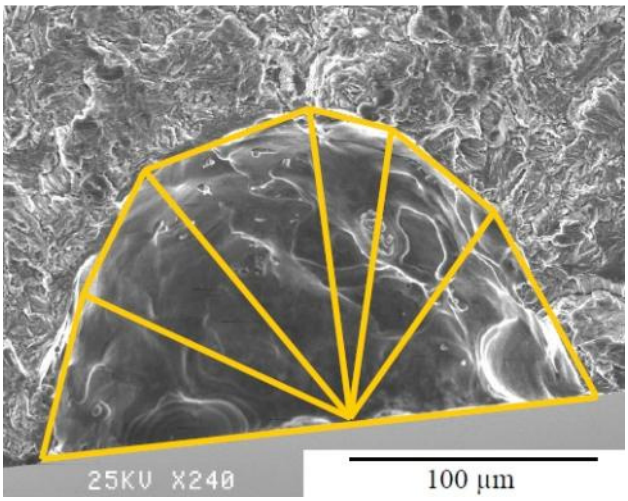

Figure 1.37. Example of an artificial spherical defect on a C36 steel specimen [50].

Defect sizes in the order of 50 µm to 900 µm were created. Curves presenting the fatigue strength as function of the defect size were presented. Figure 1.38 shows a chart of the fatigue strength as function of hemispherical defect size [50]. It is observed a decreasing of the fatigue strength while larger the defect is.

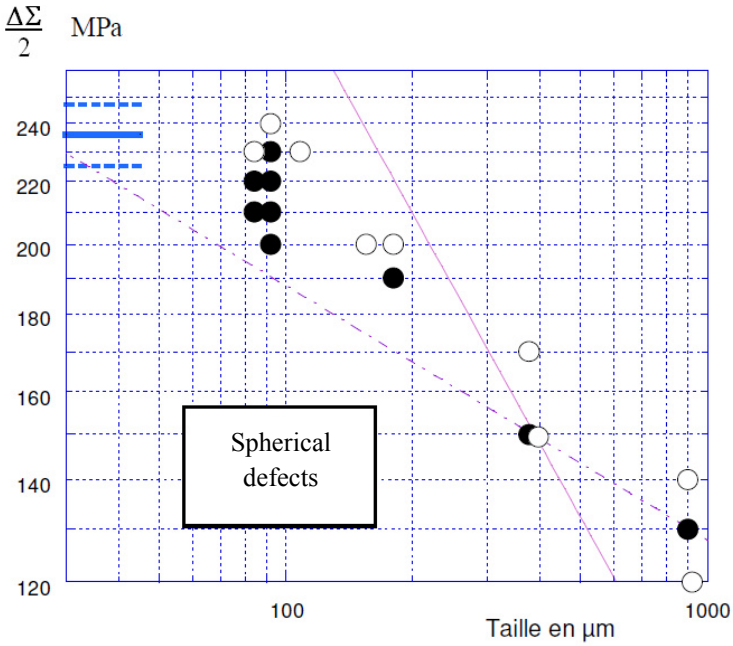

Figure 1.38. Fatigue strength results (10^7 cycles) as function of defect size for C36 steel R=-1 [50].

Kitagawa

On the other hand Kitagawa and Takahashi have been the first presenting experimentally the influence of the cracks size on the stress threshold of fracture. They showed that for smaller crack higher stress threshold of fracture [51]. Kitagawa and Takahashi showed the existence of a critical size of defect below which ΔK_{th} decrease if the crack length decrease. Below this critical size the threshold can be represented by a stress amplitude $\Delta\sigma_{th}$ similar to the fatigue strength $\Delta\sigma_D$ for a non defective material [52]. From there, a Kitagawa diagram can be represented by plotting log($\Delta\sigma$) as function of log(a) where a is the size of the defect. This diagram contains two lines, the first one corresponding to $\Delta\sigma = \Delta\sigma_D$, thereafter a critical defect size a slope is described. An example of this diagram is shown in Figure 1.39 constructed from the fatigue data (10^6 cycles) of human dentin [53].

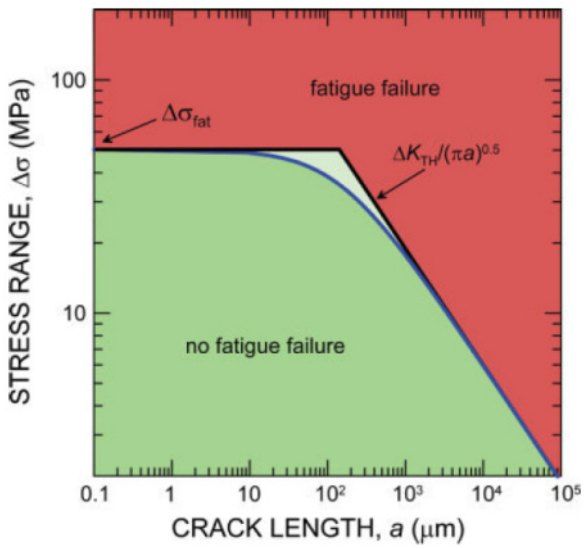

Figure 1.39. Kitagawa diagram for human dentin [53].

Murakami-Endo

Murakami and Endo [54] determined experimentally the influence of defects in the fatigue strength (at 10^6 cycles) of different materials varying the size of defects. The results are presented in Figure 1.40. It is observed that the results have a similar tendency of the Kitagawa diagrams (Figure 1.39).

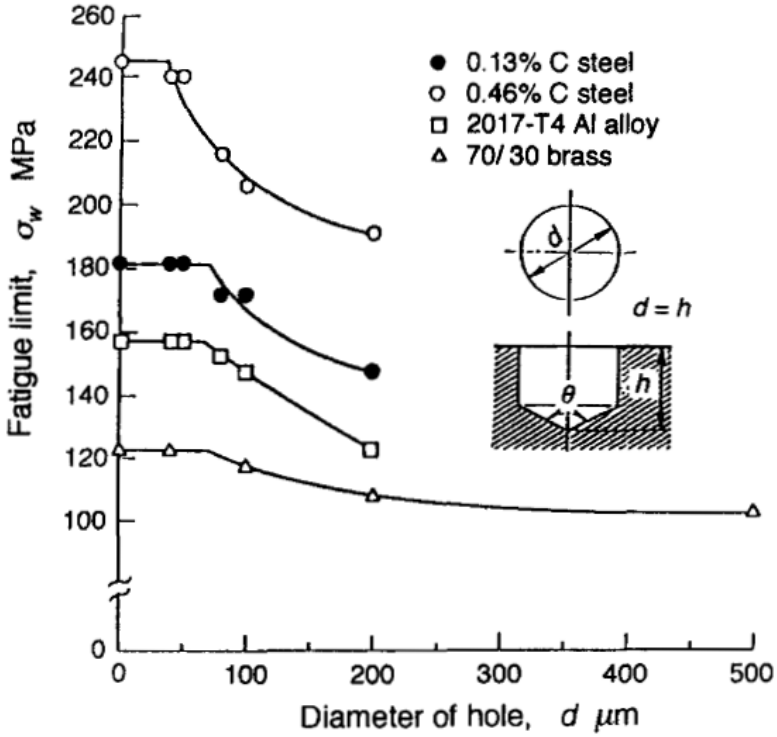

Figure 1.40. Effect of small holes on the fatigue strength of various materials [54].

The importance of the characteristics of defects is then important for the fatigue strength of the materials in the different domains of fatigue. Since original or artificial defects are present in metallic materials, it is interesting to investigate the influence of these in the fatigue behavior.

Nadot

Nadot [55] have studied the mechanisms of fatigue damage at high number of cycles in the GS cast iron. This material has a heterogeneous structure constituted by grains of ferrite, nodules of graphite and voids. To establish a link between these defects (type, size and position) and the fatigue properties of the material, the author determined the fatigue strength at different loads. He observed a decreasing in the fatigue strength as the size of the defect increased. The author also found in his studies that the voids are always responsible of the fatigue fracture. The fatigue strength is related to both the size and position of defects. Indeed, for the same stress, a surface defect and a twenty times larger internal defect lead to the same lifetime.

References of Chapter I

1. Askeland, D.R., 1989, *Ciencia e Ingeniería de los Materiales*, 3ª Edición, International Thompson Editores, México D.F. pp. 150-155, pp. 400-421.
2. Dowling, N.E., 2007, *Mechanical Behavior of Materials: Engineering methods for deformation, fracture and fatigue*, Third Edition, Pearson Education Inc, NJ USA, Chapter 9.
3. Arana, J. L., and González, J., 2002, *Mecánica de Fractura*, Editorial de la Universidad del País Vasco, Bilbao Spain.
4. Felbeck , D.K., and Atkins, A.G., 1984, *Strength and Fracture of Engineering Solids, Prentice Hall*, Inc, New Jersey, Chapter 18.
5. Suresh, S., 1991, *Fatigue of materials*, Cambridge University Press, Chapter 3.
6. Forrest, P.G., 1970, *Fatigue of Metals*, Pergamon Press Ltd, London, UK.
7. Bathias, C., and Paris, P.C., 2005, *Gigacycle Fatigue in Mechanical Practice*, Marcel Dekker Publisher Co., New York USA.
8. Murakami, Y., 2002, *Metal Fatigue: Effect of small defects and non metallic inclusions*, Elsevier Science Ltd, Oxford UK.
9. Marines García, I., and Paris, P.C., and Tada, H., and Bathias, C., 2007, *Fatigue crack growth from small to long cracks in very-high-cycle fatigue with surface and internal "fish-eye" failures for ferrite-perlitic low carbon steel SAE 8620*, Materials Science and Engineering A 468-470, pp. 120-128.
10. Newman, J.C., and Philips, E.P., and Swain, M.H., 1999, *Fatigue-life prediction methodology using small crack theory*, International Journal of Fatigue, 21, pp. 109-119.
11. Palin-Luc, T., and Perez Mora, R., and Bathias, C., and Dominguez, G., and Paris, P.C., and Arana, J.L., 2010, *Fatigue crack initiation and growth on a steel in the very high cycle regime with sea water corrosion*, Engineering Fracture Mechanics 77, pp. 1953-1962.
12. Bidouard, H., 2009, *Etude de l'effet de surcharges sur la tenue en fatigue a grand durée de vie d'un acier ferrito-bainitique sous chargement d'amplitude variable*, PhD Thesis, Arts et Métiers ParisTech, Bordeaux France, pp. 7-9.
13. Bathias, C., and Drouillac, L., and Le Francois, P., 2001, *How and why the fatigue S-N curve does not approach a horizontal asymptote*, International Journal of Fatigue 23, pp. 143-151.
14. Lieurade, H.P., 1982, *La pratique des essais de fatigue*, Societé française de métallurgie, PYC Édition, Paris, France, pp. 27-35, 62-99.
15. Gadouini, H., and Nadot, Y., and Rebours, C., 2008, *Influence of mean stress on the multiaxial fatigue behavior of defective materials*, International Journal of Fatigue 30, pp. 1623-33.
16. Koutiri, I., and Morel, F., and Bellett, D., and Augustins, L., 2009, *Effect of high hydrostatic stress on the fatigue behavior of metallic materials*, Proceedings of the 12th international conference on Fracture, Ottawa, Canada.
17. Marines García, I., Bin, X., Bathias, C., 2003, *An understanding of very high cycle fatigue of metals*, International Journal of Fatigue 25, pp. 1101-1107.
18. Asami, K., and Sugiyama, Y., 1985, *Fatigue strength of various surface hardened steels*, Japanese Heat Treatment Technology Association , Volume 25(3): pp. 147-150.

19. Kanazawa, K., and, Nishijima, S., 1997, *Fatigue of low alloy steel at ultra-high cycle regime under elevated temperature conditions*, Japanese Society of Materials Science 46(12), pp. 1396-1401.
20. Bathias, C., 1999, *There is not infinite fatigue life in metallic materials*, Fatigue & Fracture of Engineering Materials and Structures 22, pp.559-565.
21. Mughrabi, H., 2006, *Specific features and mechanisms of fatigue in the ultrahigh cycle regime*, International Journal of Fatigue 28, pp. 1501-1508.
22. Murakami, Y., and Yokoyama, N.N., and Nagata, J., 2002, *Mechanisms of fatigue failure in ultralong life regime*, Fatigue and Fracture of Engineering Materials and Structures 25, pp. 735-746.
23. Miller, K.J., and O'Donnell, W.J., 1999, *The fatigue limit and its elimination*, Fatigue and Fracture of Engineering Materials and Structures, 22, pp. 545-557.
24. Arcega, C., 2010, Validación *y puesta en marcha de un banco de fatiga en flexión rotativa*, Engineering Thesis, Instituto Tecnológico de Querétaro/CIATEQ, A.C.
25. Bathias, C., and De Monicault, and J.M., Baudry, G., 2002, A*utomated Piezoelectric Fatigue Machine for Several Enviroments*, American Society for Testing and Materials, Standard Technical Publication 1411, pp. 3-15.
26. Bathias, C., 2006, *Piezoelectric fatigue testing machines and devices*, International Journal of Fatigue 28, pp. 1438-445.
27. Marines Garcia, I., 2004, *Exploration de la fatigue des metaux au dela du milliard de cycles*, PhD Thesis, Conservatoire National des Arts et Metiers, France, pp. 19-23.
28. Wu, T., and Bathias, C., 1994, *Application of fracture mechanics concepts in ultrasonic fatigue*, Engineering Fracture Mechanics 47(5), pp. 683-690.
29. Terentev, V.F., 2004, *On the problem of the fatigue limit on metallic materials*, Metal Science and Heat Treatment 46, pp. 244-249.
30. Stanzl-Tschegg, S.E, and Mayer, H., 2001, *Fatigue and fatigue crack growth of aluminium alloys at very high number of cycles*, International Journal of Fatigue 23, pp. 231-237.
31. Dieter, L., 1993, *Traité des Matériaux Vol. 12 Corrosion et chimie de surfaces des métaux*, Première Edition.
32. Truchon, M., and Rabbe, P., 1982, *Comportement en fatigue-corrosion de différents matériaux métalliques en milieu chloruré*, Mémoires Scientifiques Revue de Métallurgie, Mars 1983, p. 117-130.
33. Magnin T. and Lardon M., 1985, *The influence of a 3.5% NaCl solution on the fatigue damage evolution in a planar slip f.c.c. stainless steel*, Materials Science and Engineering 76, pp. L7-L10.
34. Magnin T. and Coudreuse L., 1985, *The effect of strain rate on the corrosion fatigue behavior of b.c.c. Fe-26Cr-1Mo stainless steel*, Materials Science and Engineering 72, pp. 125-134.
35. Zhu, Z.Y., Farrington G.C. and Laird C., 1987, *Fatigue crack initiation and propagation in AISI 4130 steel exposed to neutral perchlorate solution*, Materials Science and Engineering 91, pp. 125-135.
36. Wang, Q. Y., and Kawagoishi, N., and Chen, Q., 2003, *Effect of pitting corrosion on very high cycle fatigue behavior*, Scripta Materialia 49, pp. 711-716.

37. Yeske, R.A., and Roth, L.D., 1982, *Environmental effects on fatigue of stainless steel at very high frequencies*, In: Wells (Westinghouse) JM, Buck, Roth, Tien, Editors. Ultrasonic fatigue. New York: The Metallurgical Society of AIME, pp. 365–85.
38. Ebara, R., and Yamada, Y., 1982, *Corrosion Fatigue Behavior of 13Cr stainless steel and Ti-6Al-4V at ultrasonic frequency*, In: Wells (Westinghouse) JM, Buck, Roth, Tien, Editors. Ultrasonic fatigue. New York: The Metallurgical Society of AIME, pp. 349-364.
39. Pelloux, R., and Genkin, J.M., 2008, *Fatigue-Corrosion,* in Fatigue des Matériaux et des structures 2 Chapitre 10, Lavoisier Ed., Paris, France.
40. Kramer, I.R., and Kumar, A., 1986, *The Influence of environment and the surface layer on crack propagation and cyclic behavior*, in Corrosion Fatigue: Chemistry, Mechanics and Microstructure, NACE, Texas, USA.
41. Grosskreutz, J.C., 1986, *The effect of surface films on fatigue crack initiation*, in Corrosion Fatigue: Chemistry, Mechanics and Microstructure, NACE, Texas, USA.
42. Meizoso, A.M, and Martínez Esnaloa, J.M., 2003, *Mecánica de la Fractura*, Escuela Superior de Ingenieros, Universidad de Navarra. San Sebastián, Spain, Chapter 5.
43. Thorpe T.W., Scott P.M., Rance A. and Silvester D., 1983, *Corrosion fatigue of BS4360:50D structural steel in sea water*, International Journal of Fatigue 5, pp. 123-133.
44. Bolton J.D. and Redington M.L., 1983, *The effects of saline aqueous corrosion on fatigue crack growth rates in 316 grade stainless steels*, International Journal of Fatigue 5, pp. 155-163.
45. Horstmann M., Gregory J.K. and Schwalbe K.H., 1995, *Geometry effects on corrosion-fatigue in offshore structural steels*, International Journal of Fatigue 17, pp. 293-299.
46. Wang, Q.Y., and Bathias, C., and Kawagoishi, N., and Chen, Q., 2002, *Effect of inclusion on subsurface crack initiation and gigacycle fatigue strength*. International Journal of Fatigue 24, pp. 1269-1274.
47. Pang, H.T., and Reed, P.A.S., 2007, *Microstructure effects on high temperature fatigue crack initiation and short crack growth in turbine nickel-base superalloy Udimet720Li*, Materials Science and Engineering A 448, pp. 67–69.
48. Zuo, J.H., and Wang, Z.G., Han E.H., 2008, *Effect of microstructure on ultra-high cycle fatigue behavior of Ti-6Al-4V*, Materials Science and Engineering A 473, pp. 147-152.
49. Ammar, H.R., and Samuel, A.M., and Samuel, F.H., 2008, *Effect of casting imperfections on the fatigue life of 319-F and A356-T6 Al-Si casting alloys*. Materials Science and Engineering A 473, pp. 65-75.
50. Billaudeau, T., 2002, *Fatigue multiaxiale des matériaux à défauts: mécanismes et critère d'endurance*, PhD Thesis, Poitiers University, France.
51. Nadot, Y., 1997, *Influence des défauts de fonderie sur la résistance a la fatigue d'une fonte GS*, PhD Thesis, Poitiers University, France.
52. Pessard, E., 2009, *Comportement Anisotrope en fatigue des composants mécaniques forgés*, PhD Thesis, Angers University, France.
53. Kruzic, J.J., Ritchie, R.O., 2006, *Kitagawa-Takahashi diagrams define the limiting conditions for cycle fatigue failure in human dentin*, Journal of biomedical materials research 79A-3, pp. 747-751.
54. Murakami, Y., Endo, M., 1994, *Effect of defects, inclusions and inhomogeneities on fatigue strength*, International Journal of Fatigue 16, pp. 163-182.

55. Nadot, Y., 1997, *Influence des défauts de fonderie sur la résistance à la fatigue d'une fonte GS*, PhD Thesis, ENSMA Poitiers, France.

Chapter II. Experimental conditions, materials and tests results

Table of contents

1. Gigacycle fatigue testing device....56
   1.1. Crack initiation tests features....57
      1.1.1 Specimen generalities....57
      1.1.2. Tension-compression tests (R=−1)....58
      1.1.3. Tension-tension tests (R>0)....58
      1.1.4. Tests with imposed temperature....59
      1.1.5. Tests in sea water flow....61
      1.1.6. How to carry out crack initiation tests....61
   1.2. Crack growth tests features....62
      1.2.1. Specimen generalities....62
      1.2.2. Crack growth observation....63
      1.2.3. How to carry out crack growth tests....64
   1.3. Machine components calculations....67
      1.3.1. Horns....67
      1.3.2. Elongation bars....69
   1.4. Calibration....71
2. Fatigue tests on AS7G06 cast aluminium alloy....75
   2.1. AS7G06 characteristics....75
   2.2. Specimen geometry....78
   2.3. Temperature measurement of AS7G06 during tests....80
   2.4. AS7G06 fatigue results....82
      2.4.1. Crack initiation tests at room temperature....83
         2.4.1.1. Tension-compression: R=-1 at room temperature....83
         2.4.1.2. Tension-tension: R=0.01 at room temperature....85
         2.4.1.3. Tension-tension: R=0.5 at room temperature....86
      2.4.2. Crack initiation tests at 150 °C....87
         2.4.2.1. Tension-compression: R=-1 at 150 °C....87
         2.4.2.2. Tension-tension: R=0.01 at 150 °C....89
      2.4.3. Synthesis of the results on AS7G06....90
3. Fatigue tests on R5 steel....93
   3.1. R5 steel characteristics....94
   3.2. Specimen geometry....97
   3.3. Temperature measurement of R5 steel during testing....98
   3.4. R5 steel fatigue results....101
      3.4.1. Crack initiation tests without any corrosion....101
         3.4.1.1. Tension-compression: R=−1....101
         3.4.1.2. Tension-tension: R=0.3....103
      3.4.2. Effect of corrosion on fatigue crack initiation....104
         3.4.2.1. Crack initiation with pre-corrosion: R=-1....104
         3.4.2.2. Crack initiation with artificial sea water in situ: R=-1....105
         3.4.2.3. Surface roughness effect on fatigue strength under sea water flow....107
         3.4.2.4. Corrosion with and without cyclic loading....108
      3.4.3. Synthesis of crack initiation results....115
      3.4.4. Crack growth tests results....117
References of chapter II....118

The aim of this chapter is the presentation of the fatigue test results carried out on the materials studied. *S-N* curves in the gigacycle regime (10^6 – 10^9 cycles or more) for both AS7G06-T6 cast aluminium alloy and R5 steel for different testing conditions are presented. Before the presentation of results, experimental testing conditions are detailed. A brief explanation of machine calibration and fatigue testing equipment is developed too. Additionally, the main characteristics of investigated materials are introduced, such as chemical composition, microstructural features and mechanical properties.

1. Gigacycle fatigue testing device

Correlating metals fatigue and fracture to their properties requires extensive analysis and testing. The control has become a high priority of designers and materials researches. ASTM test method E466 [3] and E606 [4] are some fatigue testing standards, but they are focused to low cycle fatigue testing. Hydraulic or pneumatic machines are normally used in these fatigue testing methods. Such methods work at different frequencies, not more than some hundred Hertz.

The use of ultrasonic systems for gigacycle fatigue testing as new field of study does not have a specific standard, researchers have created their own methodologies taking some items of standards and adjusting them to their testing systems.

At the beginning of this work the fatigue tests were carried out in the laboratory of Prof. Claude Bathias at Paris X University with an ultrasonic fatigue testing machine at 20 kHz. Then this machine was moved to LAMEFIP where the tests continued (Figure 2.1-left). Next, a new model of ultrasonic fatigue testing machine was installed in LAMEFIP laboratory at Arts et Métiers ParisTech (Bordeaux) in order to continue the fatigue crack initiation tests and fatigue crack growth tests at 20 kHz (Figure 2.1-right).

Figure 2.1. Ultrasonic fatigue testing machine at 20 kHz from Prof. Bathias laboratory (left) installed at LAMEFIP and new model at LAMEFIP (right).

The principle of working of this machine was detailed in Chapter I, Section 2. Mainly, a piezoelectric convertor changes the electrical energy in mechanical vibration that allows applying a sinusoidal displacement in one specimen end.

The ultrasonic fatigue testing machine of LAMEFIP laboratory is a displacement controlled machine, like all the ultrasonic fatigue testing devices. According to elastic theory explained in Chapter I, for each material the specimen geometry is designed. These specimens have a stress/displacement factor; it means that it is necessary to have a control of displacement in the ultrasonic fatigue machine in order to apply a specific stress.

The control in the ultrasonic generator voltage of the fatigue machine is in fact the control of the stress applied in the specimen tested, because the voltage controls the amplitude of the displacement imposed at the top of the specimen.

1.1. Crack initiation tests features

In this section the crack initiation fatigue tests characteristics are presented. Ultrasonic fatigue testing machine has been adapted for different testing conditions which are detailed.

1.1.1. Specimen generalities

The determination of fatigue strength of the materials is carried out by testing hourglass shaped specimens which are designed in order to work in resonance with the fatigue machine, as explained in Section 2.3 of Chapter I. Figure 2.2 shows a general overview of the specimens tested in this work. The calculation of the dimensions can be also done by finite element analysis and will be explained in a next section for each studied material in this work. Annex 3 present the geometries of these specimens.

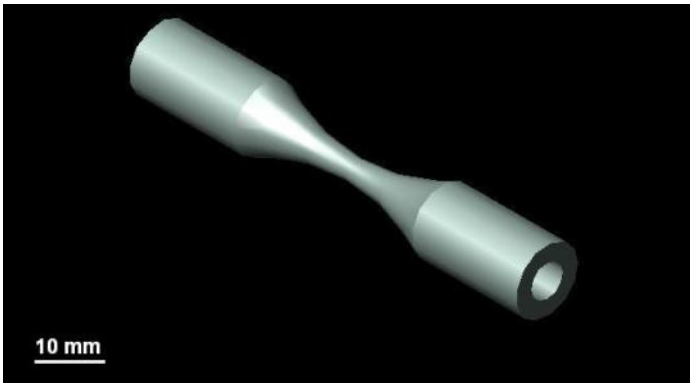

Figure 2.2. Hourglass shaped specimen for ultrasonic fatigue testing (20 kHz).

1.1.2. Tension-compression tests (R=–1)

Figure 2.3 shows a picture of the machine configuration for testing specimens at R= –1. In this case the specimen is attached to the horn only in the upper part. In some cases, compressed air as cooling is put to avoid heating of specimen at narrow section.

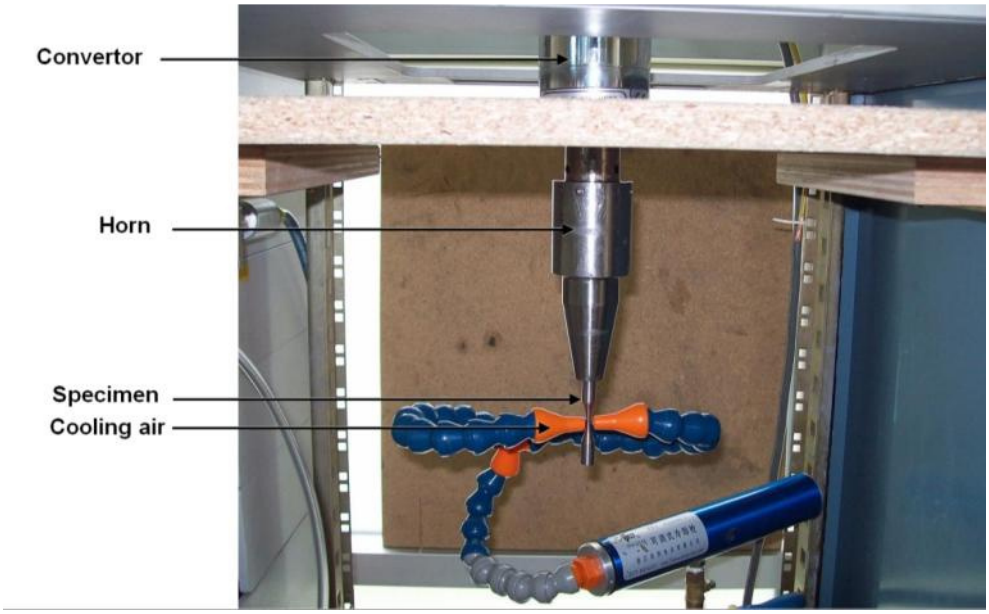

Figure 2.3. Image of the fatigue machine configuration for testing at R=-1.

It is important to remark that in some materials, heating can occur on the specimen due to high frequency excitation. Because of that, temperature measurements have been carried out by using an infrared camera. That have been done for each material studied in this work and it is explained in next Sections 2.3 and 3.3. In some cases, such as R5 steel, air cooling with compressed air is necessary in order to avoid a high temperature increasing. That is not the case for AS7G06-T6 cast aluminium alloy.

1.1.3. Tension-tension tests (R>0)

Figure 2.4 shows a picture of the machine configuration for testing specimens at R>0. In this case the specimen is attached to two horns, at the top and the bottom, but only the top horn is applying vibration. In some cases, compressed air as cooling is flowing on the specimen.

The static mean stress is applied by using an electromechanical tensile testing machine or attaching masses to the vibration system (Figure 2.5).

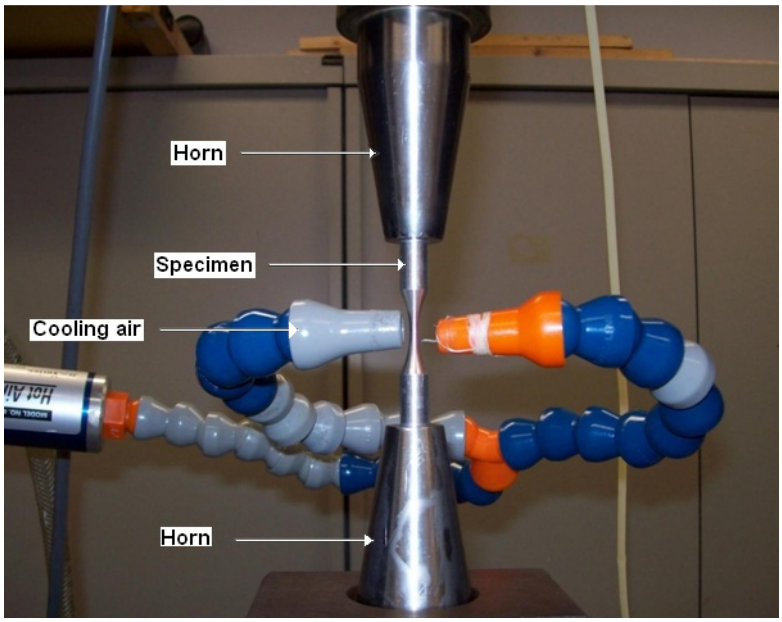

Figure 2.4. Image of the fatigue machine configuration for testing at R>0

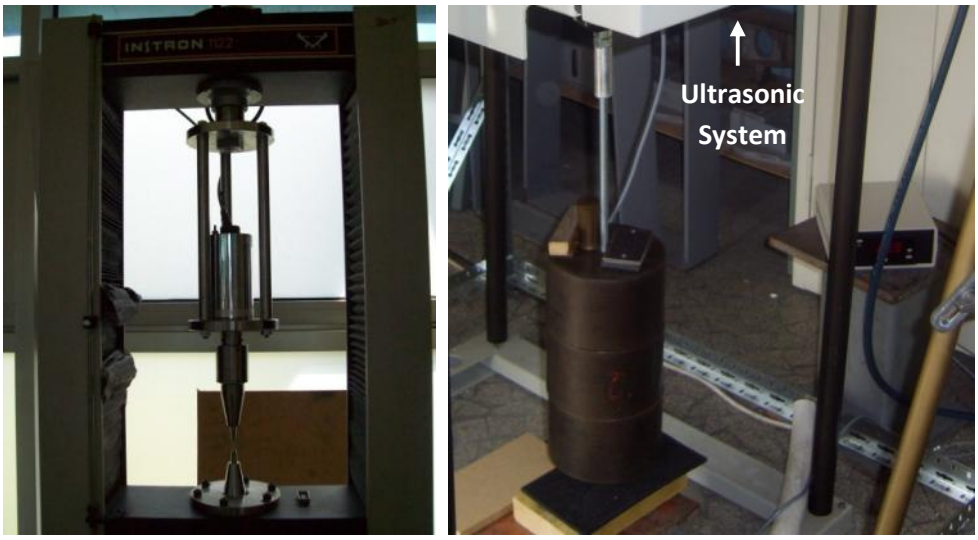

Figure 2.5. Application of static mean stress by tensile machine and applying masses.

1.1.4. Tests with imposed temperature

A climatic chamber Zwick EC76B (Figure 2.6) has been used to carry out fatigue tests at imposed temperature in air environment. This climatic chamber allows imposing and controlling the temperature between -70 to 250 °C. Extensions have been machined in order to allow putting the specimen inside of the chamber, one extension is put between a horn and a specimen for R=–1 fatigue testing. Two extensions must be used for tests at R>0. Figure 2.7 shows a schematic diagram of this adaptation. The extensions were designed in order to maintain the resonance of the vibration system. Finite element calculations of the complete set were carried out to verify that they work at 20 kHz. The dimensions of the extensions are detailed in Annex 2.

Figure 2.6. Image of the Zwick EC76B climatic chamber (right) and an internal view of a specimen in R=–1 test configuration.

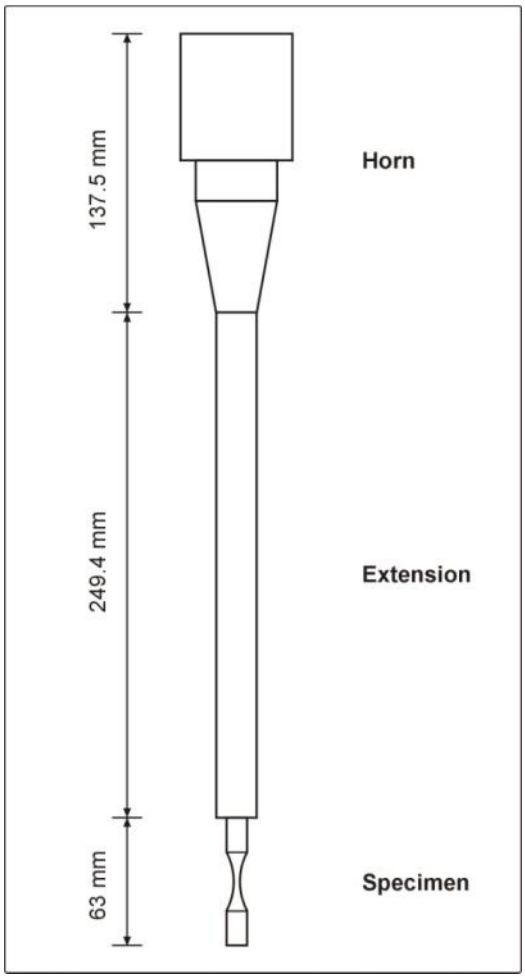

Figure 2.7. Scheme of the set Horn-Extension-Specimen for R= –1.

The temperature in the specimen surface has been controlled using a sensor type PT100 (Resistive thermocouple). Several measures have been done during the tests finding a variation of ±1°C from desired temperature.

1.1.5. Tests in sea water flow

A corrosion cell was constructed in order to carry out fatigue crack initiation tests with simultaneous artificial sea water corrosion (Figure 2.8). It consists of a tank sealed with flexible silicon and a peristaltic pump that flow the sea water on the specimen surface at different flow rates. Varying the diameter of the flexible tube of the peristaltic pump, flow rate can change from 7 to 360 mL/min.

In our case, 100 mL/min were used in order to carry out fatigue test in sea water corrosion on steel specimens.

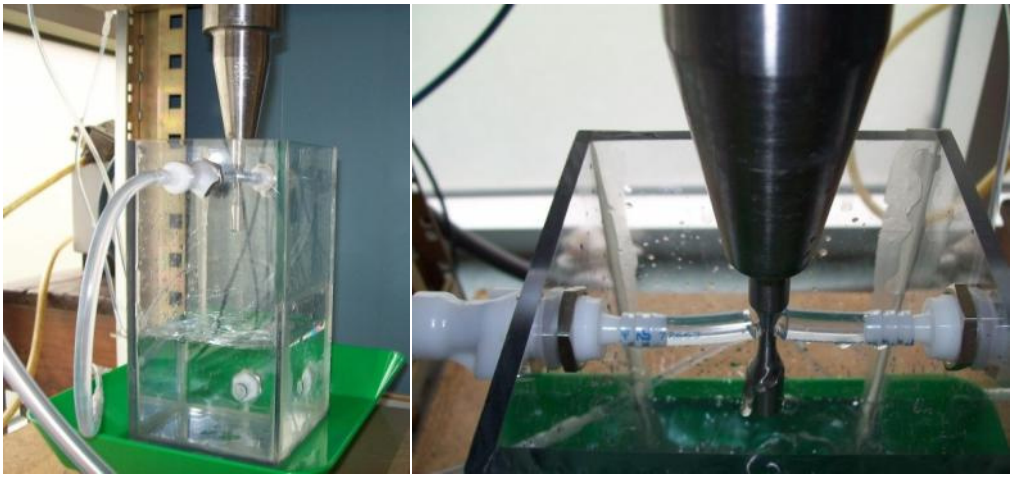

Figure 2.8. Corrosion cell and pump in order to circulate A3 sea water on the specimen.

The liquid circulated for this kind of experiment is the synthetic sea water A3. This is an aqueous solution whose components have a weight composition as follow:

NaCl: 24.53%	MgCl: 5.2%
Na2SO4: 4.09%	Ca2Cl: 1.16%
CaCl: 0.695%	$NaHCO_3$: 0.201%

In fact, this synthetic sea water is more concentrated in salt than real sea water. That is done to accelerate the corrosion process to compensate with the high frequency of the tests. A3 synthetic sea water is a standar water for aeronautics and offshore industry.

1.1.6. How to carry out crack initiation tests

The methodology to carry out fatigue crack initiation tests in a gigacycle ultrasonic fatigue testing machine is particular. There is not a specific standard that guides this kind of tests.

In this work, the tests were carried out using the staircase method. In the staircase method a first specimen is tested to a stress level up to a considered number of cycles, in this case 10^9, or until the specimen fails. If this fault prematurely (less than 10^9 cycles in this case), the following specimen is tested to a level of stress which is a decrease downwards of the first

stress level. But if the first specimen does not fail, then the second specimen is tested to a level of stress that is an increase upon the first stress level. The third sample is tested to a level of stress higher or lower than the stress of the second specimen, depending if the second specimen survived or failed [16].

The vibration system for tension-compression tests consists of a converter, amplifier and the specimen, under the excitation of a system of ultrasonic resonance. The amplifier and the specimen must have a length of resonance corresponding to 20 kHz. Due to the vibration in resonance, if the final end of the specimen is free, it is sufficient to obtain a relation for symmetrical stress of R=−1. For tension-tension tests a static load is applied using a tensile testing machine or masses.

Compressed air for cooling the specimens has been used to avoid that the samples increase their temperature and modify the fatigue process of steel. The displacement is produced by the converter and amplified by the horn. This last one amplifies the vibration and generates the stress on the specimen. The horn used for the tests has certain geometry, each geometry produces characteristic amplitudes.

The samples have been designed theoretically using the elastic theory of wave propagation by finite element method, calculating for a frequency of 20 kHz. The dimensions of the specimens, as well as the stress-displacement ratio is calculated using this method, and depends on the density and the dynamic modulus of elasticity of the metallic alloys.

1.2. Crack growth tests features

Fatigue crack growth tests can be carried out with an ultrasonic fatigue machine using notched specimens in order to obtain the characteristic crack growth rate of a material [9, 10]. The advantage is that with ultrasonic testing machine very low crack growth rates, such as the threshold region can be obtained in short time due to the high frequency of the machine.

1.2.1. Specimen generalities

A notched specimen is necessary to carry out fatigue crack growth tests. Specimens are designed in order to work in resonance at 20 kHz. Figure 1.15-b (Chapter I) shows a general scheme of fatigue crack growth tests. The fatigue crack growth specimens used in this work have the dimensions shown in Figure 2.9. A detailed plan of the crack growth specimen geometry is presented in Annex 4.

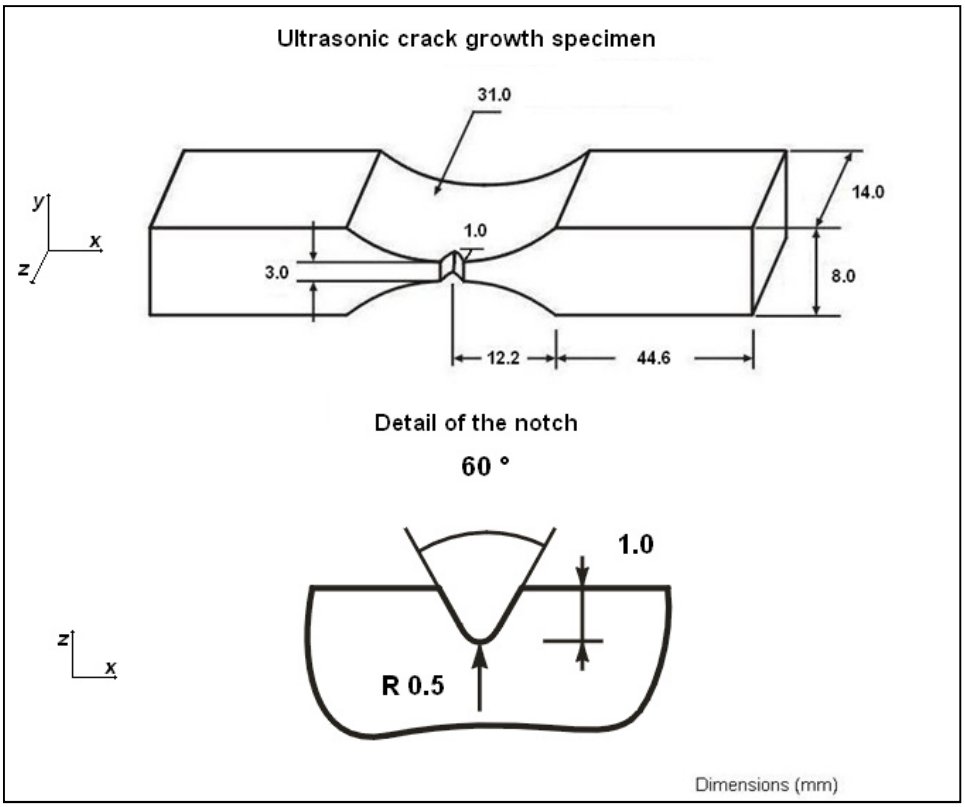

Figure 2.9. Geometry of ultrasonic fatigue crack growth specimen of R5 steel.

1.2.2. Crack growth observation

The fatigue testing machine was adapted in order to carry out crack growth tests. The same configuration than fatigue crack initiation tests described in Section 1.1.2 have been used. It means that crack growth tests were done at R= –1.

To carry out crack growth tests it is necessary to have a good measurement of the crack propagation. For this reason, an optical microscope has been used in order to verify the crack length after applying cyclic loading. A Zeiss optical binocular microscope able to magnify up to 200 times with an integrated digital camera have been used. A source of light have been used to illuminate de narrow section of the specimen; this source is a fresh light to avoid heating on the specimen surface. Furthermore, compressed air is flowing onto the specimen surface and in the notch to avoid any heating. Figure 2.10 shows a picture of this set up.

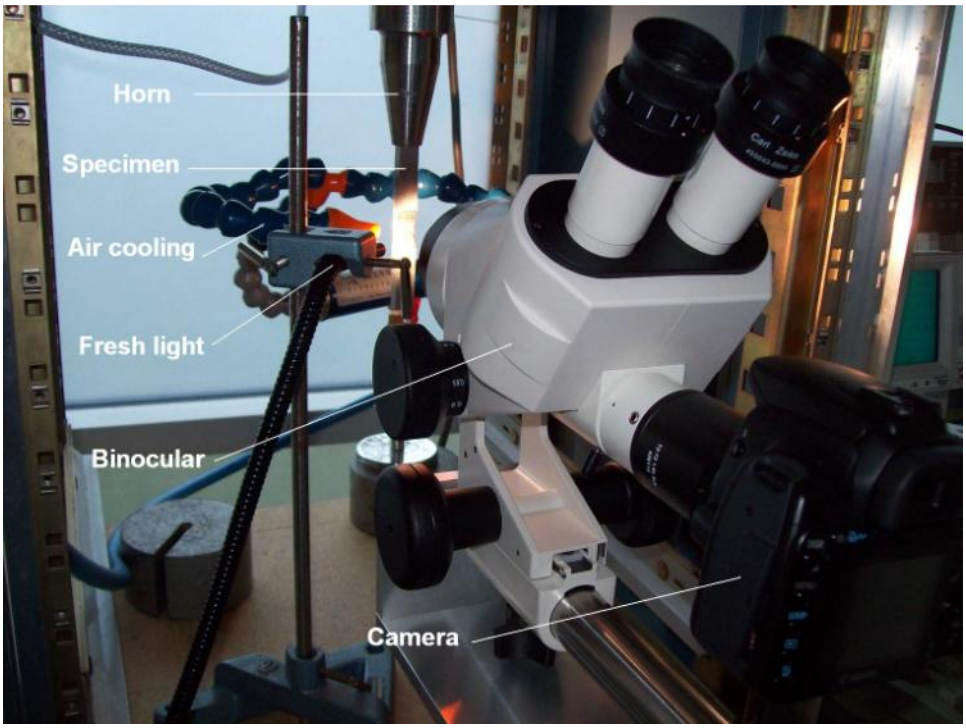

Figure 2.10. Configuration of fatigue machine for crack growth tests.

1.2.3. How to carry out crack growth tests

The methodology to carry out fatigue crack growth tests is given by the standard ASTM E647 [5] and it says that fatigue crack growth rate expressed as function of crack-tip stress-intensity factor range, da/dN versus ΔK, characterizes a material resistance to stable crack extension under cyclic loading. This allows to have da/dN versus ΔK data that can be utilized in the design and evaluation of engineering structures.

Fatigue crack growth tests carried out at LAMEFIP laboratory follow a similar methodology as this standard but particular adjustments were done to operate at 20 kHz in agreement with the work of Wu et al [9, 10]. The procedure followed is described next:

Getting a natural crack

Crack growth tests have been carried out at R= –1 at room temperature with air and sea water environment. The fatigue ultrasonic testing machine at 20 kHz has been used. Polishing each specimen in the central section where the crack initiates is necessary before the tests in order to obtain a good image when observing with the binocular and the camera. The polishing is done by using different emery papers during 10 minutes each one, the numbers of these emery papers are 320, 500, 1200, 2500 and 4000 [8]. For the tests under sea water flow it is necessary to cover the polished surface with a transparent varnish to avoid that corrosion hides the crack.

The equation proposed by Wu [9, 10] has been used in order to compute the displacement in the horn in order to obtain the desired ΔK.

$$\Delta K = \frac{E}{1-\nu^2}\sqrt{\frac{\pi}{a}}U_0 Y(a/w) \tag{2.1}$$

where E is the Young's Modulus, ν is the Poisson's ratio, U_0 is the amplitude of displacement at the end of the specimen and $Y(a/w)$ is polynomial factor that depends of the material and the geometry of the specimen [9, 10].

Polynomial $Y(a/w)$ depends only of $\sqrt{\frac{E}{\rho}}$ value of the material. For metals working at room temperature this value varies between 4.8 and 5.1 km/s. For R5 steel $\sqrt{\frac{E}{\rho}}$ is 5.18 km/s. Wu [9, 10] established a unique curve for this polynomial factor:

$$Y(a/w) = 0.635(a/w) + 1.731(a/w)^2 - 3.979(a/w)^3 + 1.963(a/w)^4 \tag{2.2}$$

With Equations (2.1) and (2.2) it is possible to start to produce a natural crack on the specimen of 0.5 mm.

Starting with ΔK_0 = 1 MPa√m during 1×10^7 cycles. If there is not crack it is necessary increase ΔK_0 to ΔK_1 = 1.25 MPa√m and so on, by increments of 0.25 MPa√m or less.

Table 2.1 shows an example of calculation of U_0 using Equations (2.1) and (2.2) and according with the specimen geometry and the material properties, in this example R5 steel.

Suffix	ΔK (MPa√m)	U_0 (m)	a (m)	w (m)	a/w	$Y(a/w)$
0	1	1.45769E-06	0.001	0.014	0.071429	0.0527898
1	1.25	1.82211E-06	0.001	0.014	0.071429	0.0527898
2	1.5	2.18653E-06	0.001	0.014	0.071429	0.0527898
3	1.75	2.55095E-06	0.001	0.014	0.071429	0.0527898
4	2	2.91537E-06	0.001	0.014	0.071429	0.0527898
5	2.2	3.20691E-06	0.001	0.014	0.071429	0.0527898
6	2.4	3.49845E-06	0.001	0.014	0.071429	0.0527898
7	2.6	3.7900E-06	0.001	0.014	0.071429	0.0527898
8	2.8	4.0815E-06	0.001	0.014	0.071429	0.0527898
9	3	4.3731E-06	0.001	0.014	0.071429	0.0527898
10	3.2	4.6646E-06	0.001	0.014	0.071429	0.0527898

Table 2.1. Example of calculation of U_0 at different levels of ΔK when crack does not start

When the crack length reaches 0.5 mm the procedure to obtain the natural crack is completed. Then it will be an initial crack of length 1.5 mm (Figure 2.11).

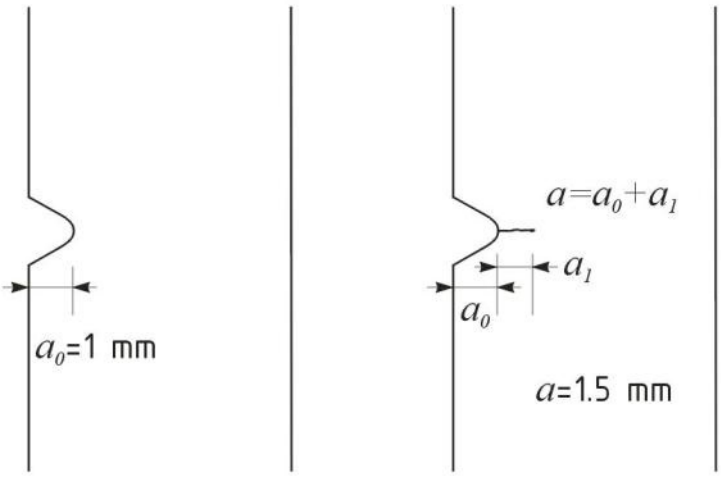

Figure 2.11. Addition of the length of the notch and the produced crack will be the initial crack length in the next step.

Getting the da/dN vs. ΔK curve

In the previous step a natural crack of length 0.5 mm have been obtained in addition with the length of the notch in the specimen, the length a is 1.5 mm, it is called "pre-crack".

The test starts with a value ΔK_i at which the crack growth started, tests are done during a corresponding time to 10^6 cycles (blocks). The crack will growth, therefore ΔK will decrease and then, a calculation of amplitude U_0 must be carried out again to obtain ΔK_i.

In example: A pre-crack of a=1.54 mm obtained with ΔK = 5.5 MPa√m since a_0=1.08 mm. Recalculating U_0 in order to obtain ΔK = 5.5 MPa√m U_0 will be 6.122 μm:

a=1.54 mm, ΔK = 5.5 MPa√m, E=211 GPa, ν = 0.3, w = 14 mm. Using Equations (2.1) and (2.2)

$$U_0 = 6.122\ \mu\text{m}$$

Then, the test starts at ΔK = 5.5 MPa√m with U_0 = 6.122 μm.

Next step is to grow the crack length until ΔK decreases around 5% but not more than 7%. For that it is necessary to know which crack length corresponds to this ΔK. In example: Using Equations (2.1) and (2.2) for a ΔK decreasing up to 5.225 MPa√m (5% of 5.5 MPa√m)

$$a_1 = 0.00171\ \text{m} = 1.71\ \text{mm}$$

It means that crack length should grow 0.17 mm in this step (da), when that occurs it is necessary to note the number of cycles that took such growth (dN). A table of da and dN can be made: the expected crack length can vary in the real experiment. Then it is necessary to measure correctly the crack length comparing the pictures and calibrating the image with a good scale.

1.3. Machine components calculations

The components of the ultrasonic fatigue testing machine must work in resonance. The piezoelectric ultrasonic converter works at 20 kHz, then, the components are designed to work at the same frequency. To verify that, numerical calculations by finite element analysis have been carried out for the amplifiers (horns) and other components such as elongation bar.

1.3.1. Horns

Three types of horns are available for the ultrasonic fatigue testing machine at LAMEFIP laboratory, all of them are manufactured in TA6V titanium alloy. These horns and their finite element analysis are presented in Annex 2.

Conical horn TC (Figure 2.12) of medium amplification produces larger displacement amplitude than the piezoelectric converter up to around 5 times at the maximum amplitude of the converter.

In the following is presented the modal analysis that has been carried out by the using finite element analysis ANSYS software in order to find the modes of vibration of this conical horn. Table 2.2 shows the modal frequencies of this conical horn obtained by finite element calculation. It is observed that one of these frequencies is 20137 Hz which is practically the same of the piezoelectric converter.

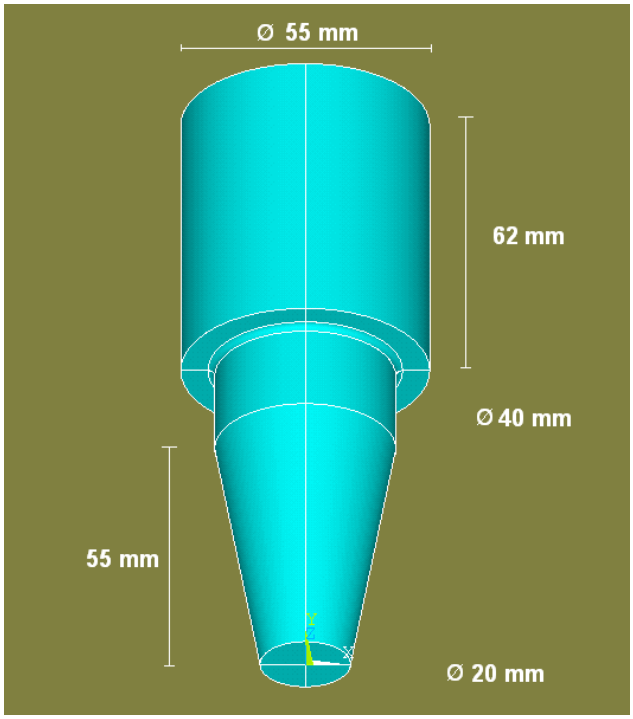

Figure 2.12. TC horn (conical shape medium amplification) in TA6V material (ρ=4430 kg/m^3).

***** INDEX OF DATA SETS ON RESULTS FILE *****

SET	TIME/FREQ	LOAD STEP	SUBSTEP
1	0.0000	1	1
2	0.0000	1	2
3	0.0000	1	3
4	0.15517E-02	1	4
5	0.21749E-02	1	5
6	0.26804E-02	1	6
7	8772.8	1	7
8	8773.0	1	8
9	15178.	1	9
10	19066.	1	10
11	19066.	1	11
12	20137.	1	12
13	25037.	1	13
14	29573.	1	14
15	29574.	1	15
16	33316.	1	16
17	36624.	1	17
18	36873.	1	18
19	36875.	1	19
20	38219.	1	20
21	38220.	1	21
22	40616.	1	22
23	40619.	1	23
24	42633.	1	24
25	42638.	1	25
26	47861.	1	26
27	47864.	1	27
28	47953.	1	28
29	48798.	1	29
30	48802.	1	30

Table 2.2. Modal frequencies of TC conical horn (TA6V material) from ANSYS calculation.

A harmonic analysis at 20137 Hz has been carried out in order to verify the amplification factor of the TC conical horn. A harmonic displacement of 5 µm was applied on the top of the horn, which is around the maximum amplitude displacement of the converter. In Figure 2.13 it is observed that with a displacement applied of 5 µm at the top of the horn, the maximum displacement at the bottom of the TC horn is around 26 µm.

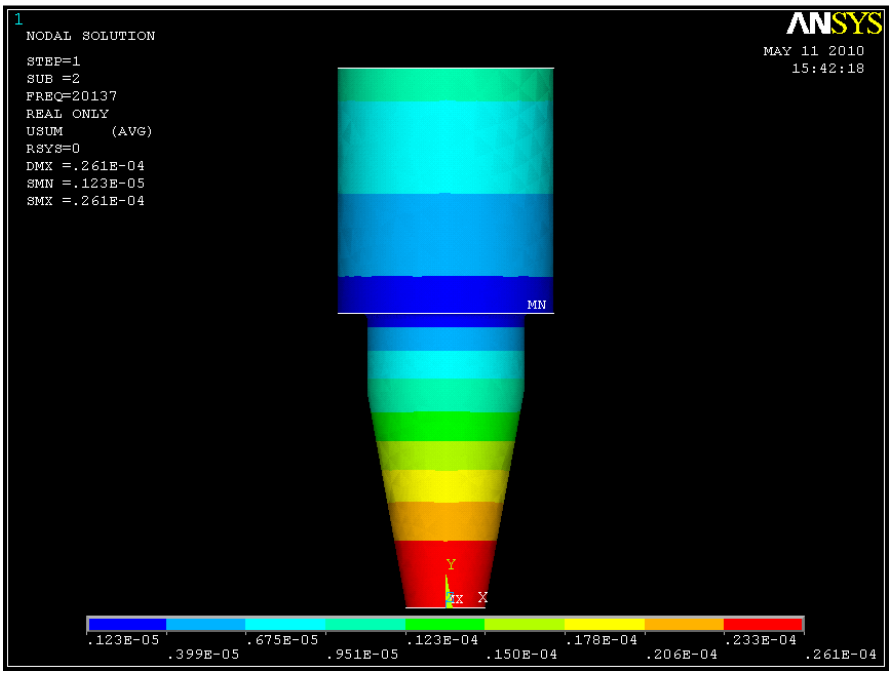

Figure 2.13. Harmonic analysis of TC conical horn (TA6V material) with 5 µm top vibration.

Cylindrical horn of very low amplification which basically produces the same vibration displacement of the piezoelectric converter and only works as extension due that converter has a big thread and is not possible transmit its vibration directly to specimens, then it works as assembling between converter and specimens.

Conical high amplification horn TGD produces much larger displacement amplitude than the piezoelectric converter, around 20 times at the maximum displacement amplitude of the converter.

1.3.2. Elongation bars

In some fatigue tests it is necessary to put the specimens at different heights or inside a chamber, such a climatic chamber. Then, extensions or attachments (Figure 2.14) must be used coupled to the amplifiers (as the example in Section 1.1.4). In this case, these components must be designed to work at the same frequency of the system to work in resonance. Two extensions were fabricated in order to carry out tests in a temperature chamber (Figure 2.6 and Figure 2.7). These extensions were designed with two times the resonance length. The plan of this extension is presented in Annex 2.

A modal analysis has been carried out by using the finite element software ANSYS software in order to find the modes of vibration of these extensions. Table 2.3 shows the modal frequencies of this extension obtained by finite element calculation. One of the modal frequencies is 20020 Hz. Then it can works in resonance with the piezoelectric converter.

Figure 2.15 shows the solution of a harmonic analysis carried out on the extension at 20020 Hz with ANSYS, applying 5 µm of harmonic displacement at the top. It is observed that the same displacement is reflected in the bottom of the extension. There is also a node of maximum displacement at the middle of the extension, because it has two times the resonance length.

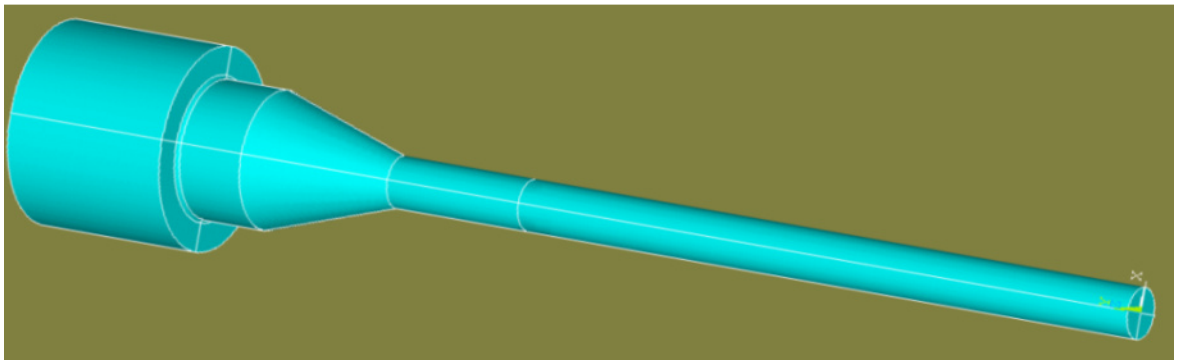

Figure 2.14. Extension for climatic chambers adaptation (XC36 material).

***** INDEX OF DATA SETS ON RESULTS FILE *****

SET	TIME/FREQ	LOAD STEP	SUBSTEP
1	0.0000	1	1
2	0.0000	1	2
3	0.0000	1	3
4	0.0000	1	4
5	0.25060E-02	1	5
6	0.34123E-02	1	6
7	1362.3	1	7
8	1362.3	1	8
9	3656.8	1	9
10	3656.8	1	10
11	6218.0	1	11
12	6916.8	1	12
13	6916.8	1	13
14	10020.	1	14
15	10954.	1	15
16	10954.	1	16
17	12438.	1	17
18	15601.	1	18
19	15602.	1	19
20	18664.	1	20
21	20020.	1	21
22	20717.	1	22
23	20717.	1	23
24	24899.	1	24
25	26187.	1	25
26	26188.	1	26
27	29979.	1	27
28	31140.	1	28
29	31936.	1	29
30	31936.	1	30

Table 2.3. Modal frequencies of extension attachment (XC36 material).

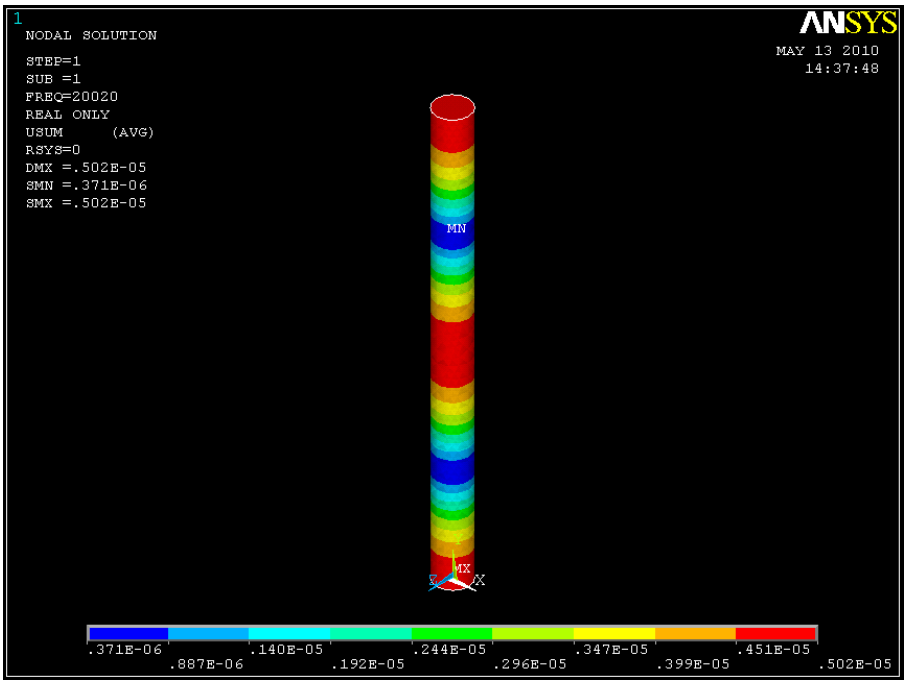

Figure 2.15. Harmonic analysis of the extensions (XC36 material) with 5 µm top vibration.

1.4. Calibration

It is fundamental to check carefully the calibration of equipments in order to have the certainty that the results are correct.

In our case, the ultrasonic fatigue machine was calibrated in displacement amplitude of each horn, using different methods: a laser interferometer sensor and strain gauges glued on the specimen. The last solution was the best option after checking results. The different horn shapes were presented in Section 1.3.1 and the geometry plans are presented in Annex 2.

For application of static load in the case of tension-tension tests it is necessary to use an electromechanical tensile testing machine. It was carried out the calibration of applied load in such device using a ring dynamometer.

Calibration of static load

An electromechanical tensile testing machine Instron model 1122 is used to apply static load during tension-tension fatigue tests. The correct static load involves a calibration with a ring dynamometer checking the electrical response with the load cell of the tensile machine. To measure the load a ring dynamometer Testwell has been used. To measure the electrical response as function of the load in the Instron machine a Philips voltmeter was used.

Calibration of vibration displacement amplitude with laser interferometer

It was done a calibration of one of the TC horns of ultrasonic fatigue machine using a laser interferometer sensor that measures high frequency displacements. This has been done at the Laboratory of Mechanics Physicas (LMP) of Bordeaux 1 University.

Laser interferometer equipment gives a tension signal and it is calibrated at different velocities of answer (125, 1000 m/s/V).

A calibration curve of the amplitude displacement versus tension in the fatigue testing machine have been plotted (Figure 2.16). The procedure of calibration is detailed in Annex 5.

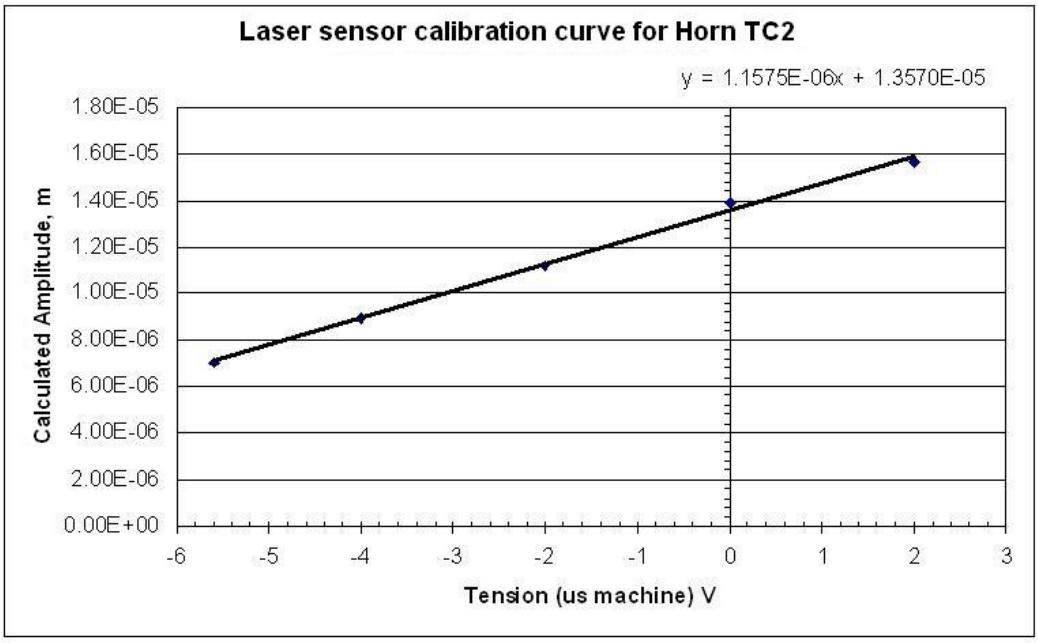

Figure 2.16. Calibration curve and linear function of amplitude from laser sensor according with voltage in the fatigue machine.

Using the previous curve and the linear function it is possible to calculate the amplitude for all the range of tension in ultrasonic fatigue machine.

Calibration of vibration displacement amplitude using strain gauges

Calibration of vibration displacement amplitude has been done by using glued strain gauges in specimens (non pre-corroded R5 steel, pre-corroded R5 steel and AS7G06-T6 cast aluminium alloy) for the three different horns.

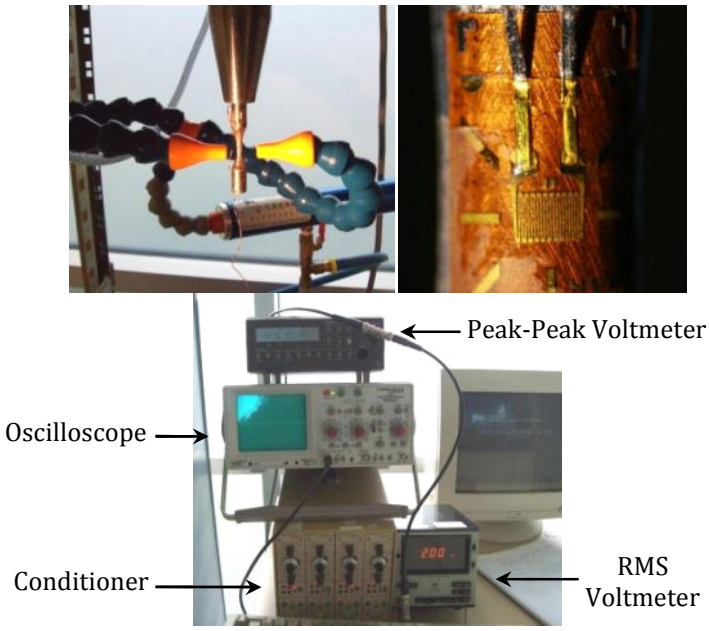

Figure 2.17. Strain gauge on specimen, and conditioning and measuring devices for calibration.

The strain gauges with a small grid (1.0×0.75 mm) were carefully glued at the central section of specimens (Figure 2.17 right) and the conditioning was done by using 2210 Vishay micro measurement conditioner (Figure 2.17 left) with a full bandwidth of 100 kHz. A digital voltmeter Philips PM2525 has been used in order to measure the peak-peak tension signal obtained from the strain gauge and amplified by the conditioner. An auto-ranging digital voltmeter B&K 2427 has been used for measuring the RMS tension signal from the strain gauge. The shape of the signal was observed by using an analogical oscilloscope. The detailed procedure of calibration with strain gauges is presented in Annex 5.

In order to calculate the amplitude displacement Equation (2.3) is used

$$\varepsilon_a(\mathrm{RMS}) = \frac{\mathrm{V_{RMS}}\sqrt{2}}{V_C} C_A \tag{2.3}$$

Where:

V_{RMS} = Root mean square tension measured
C_A = Calibration Constant = 1176.5 μm/m
V_C = Calibration tension value

Figure 2.18 shows an example of curve for strain amplitude versus tension in ultrasonic fatigue machine for R5 steel using a conical horn TC. Figure 2.19 shows the strain curve for AS7G06-T6 cast aluminium alloy using the same TC horn. A linear fit of the data has been adjusted to estimate other values of tension for both cases. The rest of examples for other horns are presented in Annex 5.

Knowing the correct strain it is possible to compute the stress for R5 steel. Using (S/D) ratio related to the specimen geometry and according with the material of what is made.

$$\sigma_a = \varepsilon_a E \tag{2.4}$$

Then:

$$U_0 = \frac{\sigma_a}{(S/D)_{\mathrm{ratio}}} \tag{2.5}$$

Where:

σ_a = Stress amplitude, ε_a = Strain amplitude measured, E = Young's modulus

U_0 = Displacement amplitude, $(S/D)_{\mathrm{ratio}}$ = Stress/Displacement ratio of a specimen geometry made of a certain material excited at 20 kHz.

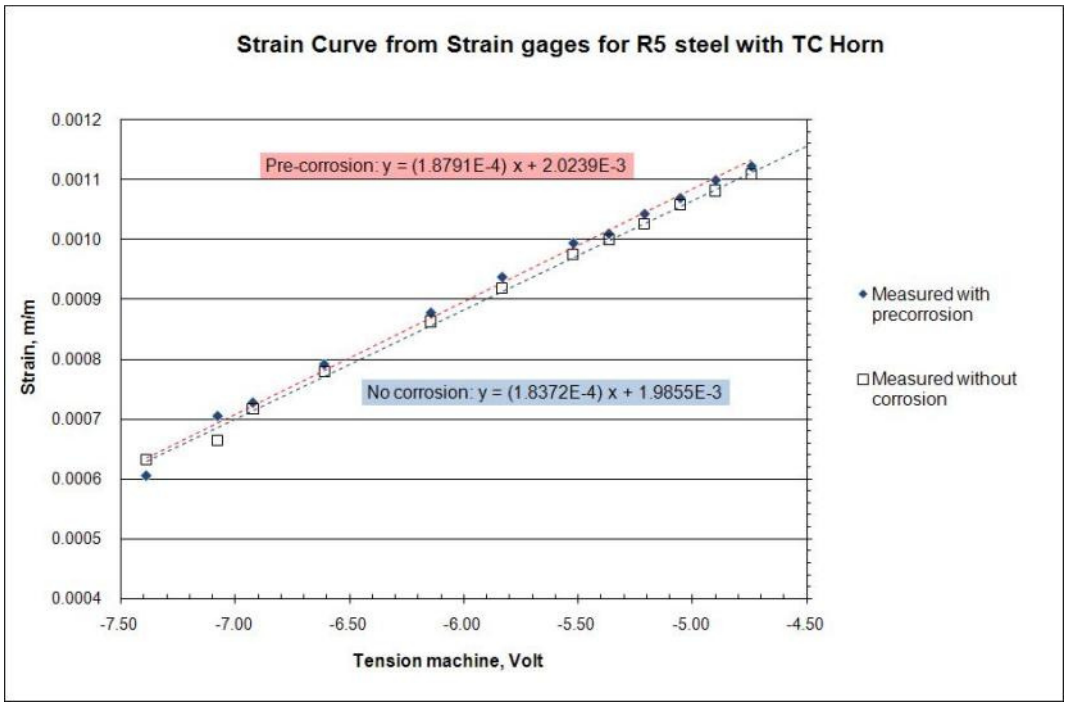

Figure 2.18. Strain chart from strain gauges measures for R5 steel versus the voltage signal applied by the fatigue machine to the piezoelectric converter.

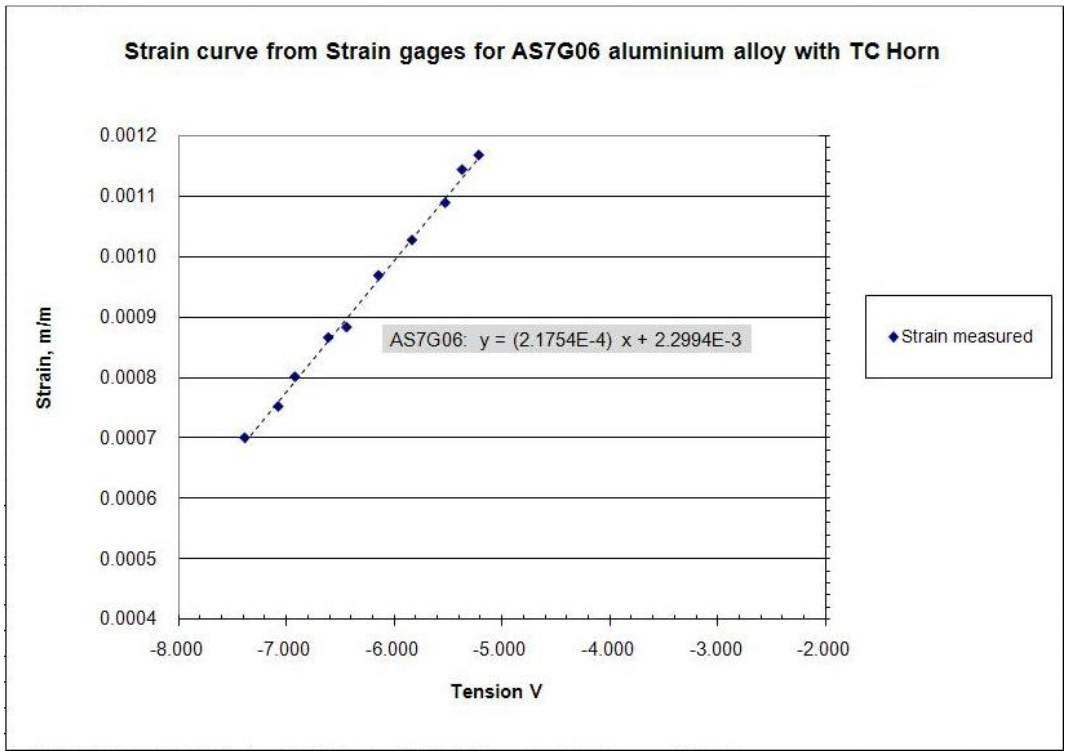

Figure 2.19. Strain curve from strain gauges measures for AS7G06-T6 cast aluminium alloy versus the voltage signal applied by the fatigue machine to the piezoelectric converter.

2. Fatigue tests on AS7G06-T6 cast aluminium alloy

Gigacycle fatigue tests were carried out on AS7G06-T6 cast aluminium alloy specimens by using an ultrasonic fatigue testing machine. *S-N* curves of this alloy were obtained.

Three different stress ratios R were used to carry out fatigue crack initiation tests: R≈0, R=–1 and R=0.5. Additionally, tests were carried out at both room temperature (~20 °C) and 150 °C using a climatic chamber. Table 2.4 shows the scheme of fatigue crack initiation tests carried out on AS7G06-T6 cast aluminium alloy.

Room temperature	150 °C
R= –1	R= –1
R= 0.01	R= 0.01
R= 0.5	-

Table 2.4. List of fatigue crack initiation tests carried out on AS7G06-T6 cast aluminium alloy.

The objective of these tests is to determine the fatigue strength in the gigacycle regime of this AS7G06-T6 cast aluminium alloy under fully reversed tension-compression conditions as well in tension-tension conditions, including high mean stress (R=0.5). The mean stress effect as well the effect of casting defects on the fatigue strength are observed.

At 150 °C, tests were carried out at R= –1 and R=0.01. The temperature effect on the fatigue strength is compared with the tests results obtained at room temperature at the same R ratio.

In the following sections the results of AS7G06-T6 cast aluminum alloy for different testing conditions are presented. Previously the main AS7G06-T6 characteristics are presented as well as the specimen geometry. Another important fact is the possible heating of the specimen during ultrasonic fatigue tests and the influence that it may has on the fatigue results. Because of that, a thermal analysis have been carried out and is presented before the results.

2.1. AS7G06-T6 characteristics

AS7G06-T6 is a cast aluminum alloy used for intricate castings with medium or thick walls for a wide range of technical applications. This alloy is used by Turbomeca for fabrication of gearboxes of helicopters turbines. Specimens of AS7G06-T6 cast aluminum alloy were subtracted from real pieces produced by Turbomeca and they were received for testing.

Table 2.5 shows the typical chemical composition of AS7G06-T6 cast aluminium alloy. This alloy is mainly composed by aluminum, magnesium and silicon. Due to the high Mg-content, high strength can be achieved by heat treatment, such as T6. It has very good corrosion resistance and welding properties.

Si	Fe	Cu	Mn	Mg	Zn	Ti	Other
6.5-7.5	0.15	0.03	0.1	0.6	0.07	0.15	0.1

Table 2.5. Chemical composition of AS7G06-T6 cast aluminum alloy (% weight, Al balance).

The AS7G06-T6 cast aluminium alloy presents a microstructure (Figure 2.20) that includes eutectic silicon precipitates (dark gray) around a matrix of aluminium α dendrites (white). Defects of casting as voids or porosities are revealed in microstructure. The elongated clear gray particles are Fe-rich intermetallic particles. Figure 2.21 shows a microstructure picture taken with scanning electron microscope. Silicon precipitates and the elongated particles are observed. Figure 2.22 shows the X-Ray microanalysis spectrum found in the matrix which is mainly composed by aluminium, silicon and magnesium. Figure 2.23 shows the X-Ray microanalysis spectrum obtained on the eutectic particles verifying that they are Al-Si and Mg-Si compounds. Figure 2.24 shows the X-Ray spectrum found in the elongated particles noting an important concentration of iron, which mainly can be in form of Fe-Al.

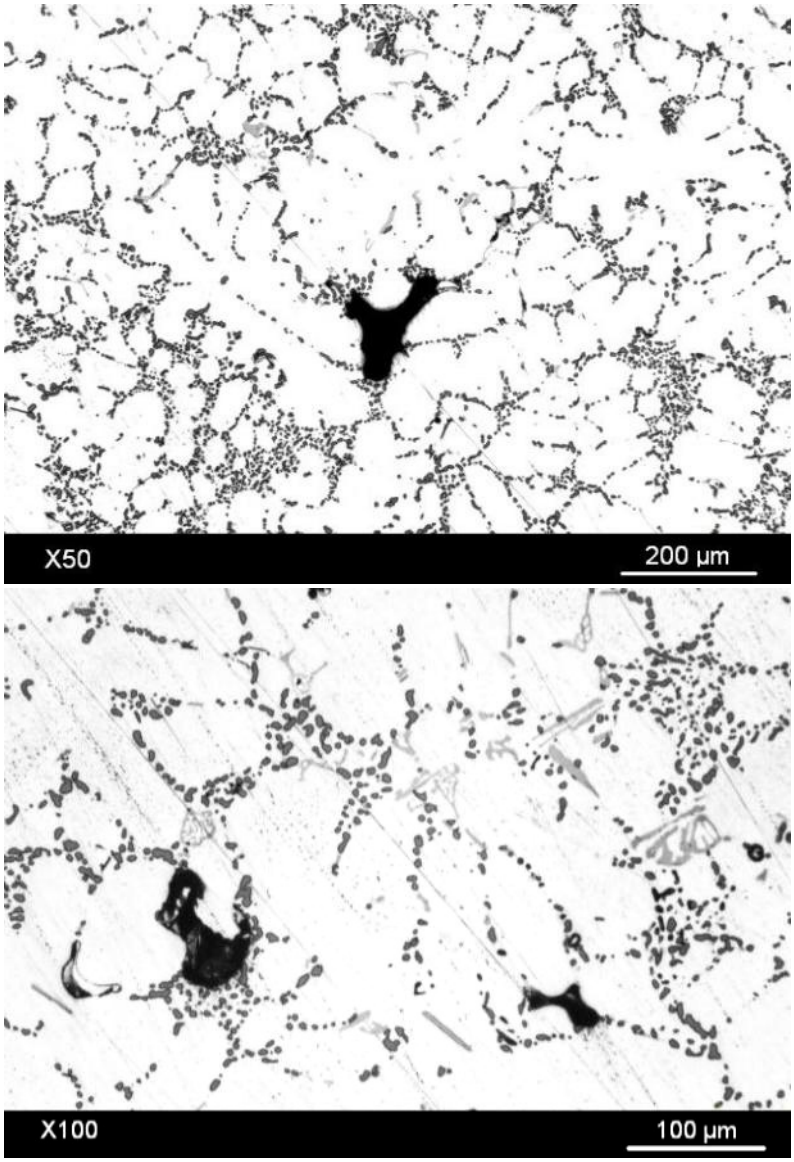

Figure 2.20. AS7G06-T6 microstructure from optical microscopy

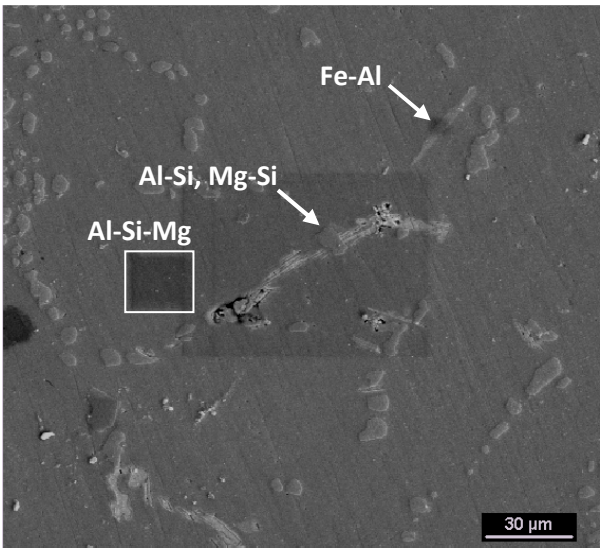

Figure 2.21. AS7G06-T6 microstructure from scanning electron microscopy

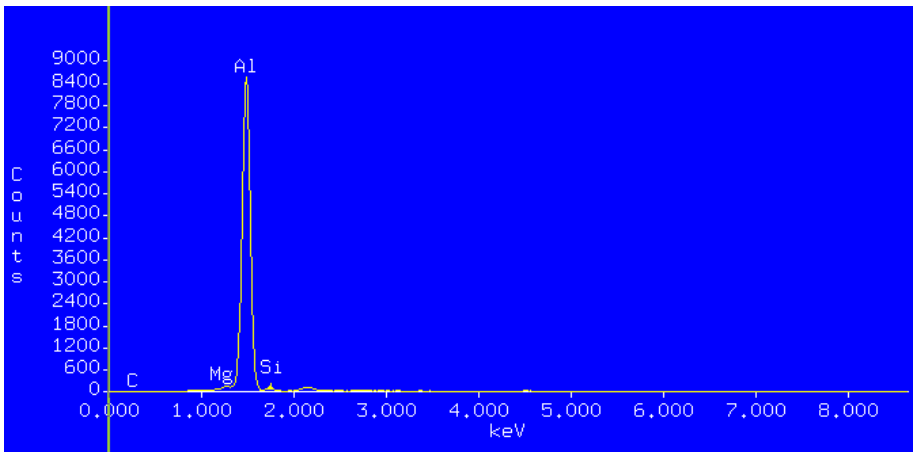

Figure 2.22. X-Ray microanalysis spectrum of AS7G06-T6 material matrix.

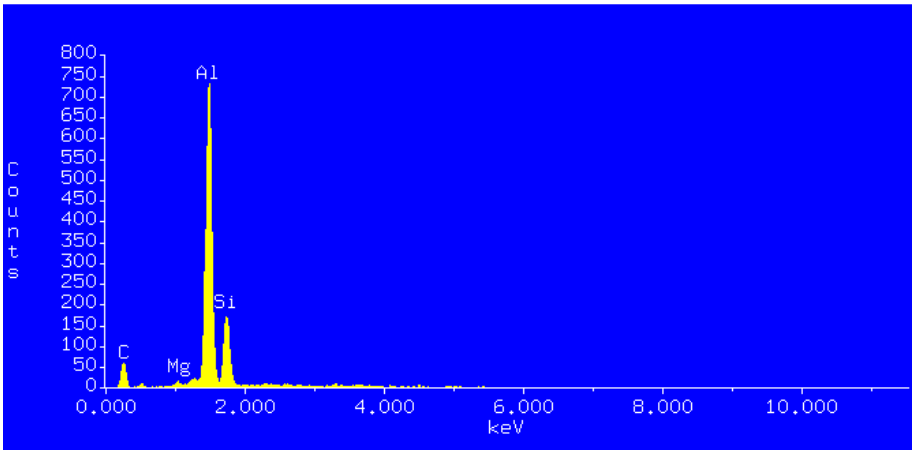

Figure 2.23. X-Ray microanalysis spectrum of eutectic precipitates on AS7G06-T6.

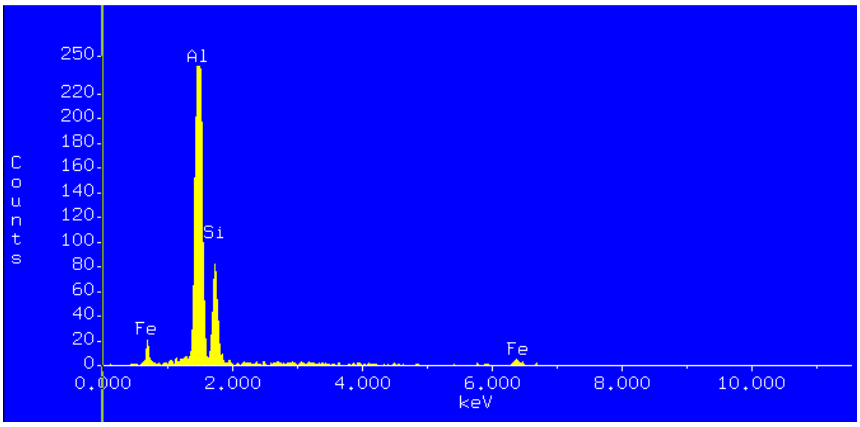

Figure 2.24. X-Ray microanalysis spectrum of intermetallic elongated particles on AS7G06-T6.

Table 2.6 shows the typical physical and mechanical properties of AS7G06-T6. The standard heat treatment for this alloy is a solution treatment by artificial ageing (T6). This ageing consists in submitting the materials during 6-12 hrs at 155-165 °C in air environment.

Density	2680 kg/m^3
Young's Modulus	68 GPa
Yield Strength	210-280 MPa
Tensile Strength	288 MPa
Hardness	112 HV

Table 2.6. Mechanical and physical properties of AS7G06-T6 cast aluminium alloy.

2.2. Specimen geometry

Figure 2.25 shows a sketch of the AS7G06-T6 specimens used for testing in gigacycle fatigue (A detailed plan is presented in Annex 3).

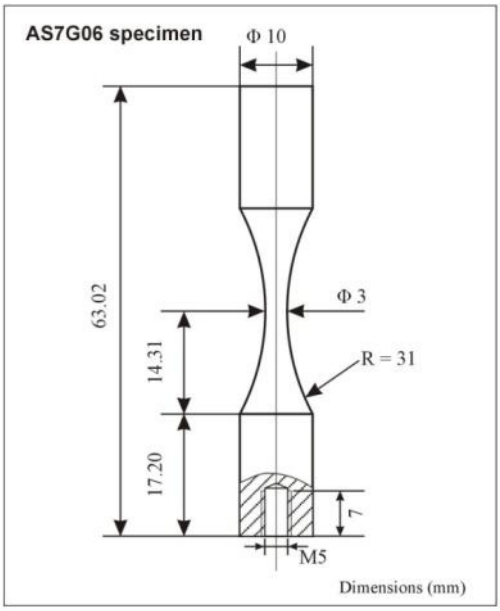

Figure 2.25. Sketch of the geometry of AS7G06-T6 specimens.

The dimensions of the AS7G06-T6 specimens were calculated to vibrate with a resonance at 20 kHz using the theory presented in Section 2.3 of Chapter I and verified by using finite element analysis.

Table 2.7 shows the mode frequencies calculated using the finite element ANSYS software. One of the modes of vibration is 20195 Hz, which is practically the required frequency to work in resonance with all vibration system.

Figure 2.26 shows the result of the harmonic analysis of the stresses on specimen at 20195 Hz, when a harmonic displacement of 5 µm is applied at the top in the *y* direction. It is observed that the maximum calculated stress is 44 MPa, which correspond to a stress/displacement ratio of around 8.8 MPa/µm. Then, one can say that specimens have correct dimensions and they can work in resonance with the rest of the components.

***** INDEX OF DATA SETS ON RESULTS FILE *****

SET	TIME/FREQ	LOAD STEP	SUBSTEP
1	0.0000	1	1
2	0.0000	1	2
3	0.0000	1	3
4	0.0000	1	4
5	0.68578E-02	1	5
6	0.80138E-02	1	6
7	2638.9	1	7
8	2639.0	1	8
9	4842.4	1	9
10	13564.	1	10
11	13564.	1	11
12	20195.	1	12
13	47668.	1	13
14	47669.	1	14
15	67680.	1	15
16	67681.	1	16
17	84264.	1	17
18	85796.	1	18
19	85967.	1	19
20	85969.	1	20
21	0.10962E+06	1	21
22	0.10962E+06	1	22
23	0.10992E+06	1	23
24	0.12322E+06	1	24
25	0.12572E+06	1	25
26	0.13445E+06	1	26
27	0.13445E+06	1	27
28	0.14987E+06	1	28

Table 2.7. Modal frequencies of AS7G06-T6 specimen

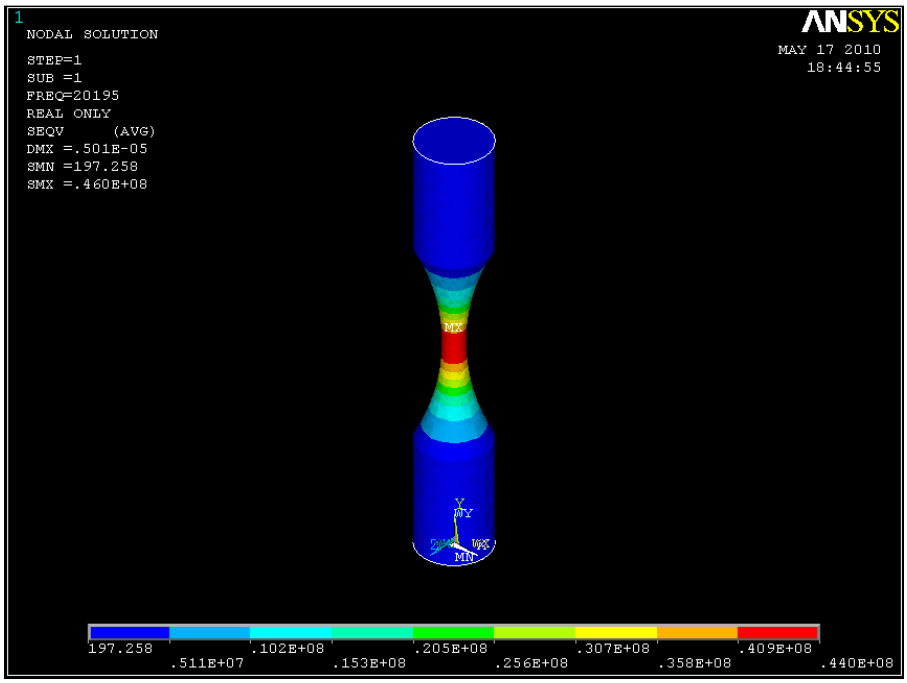

Figure 2.26. Harmonic analysis of AS7G06-T6 specimen with 5 µm of vibration at the top.

2.3. Temperature measurement of AS7G06-T6 during tests

Due to the high frequency vibration self heating can be observed for during ultrasonic fatigue tests. According to Bathias and Paris [11], heating in the specimens during ultrasonic fatigue tests is caused by absorption of ultrasonic energy. Bathias mentions [12] the temperature of some metallic alloys during fatigue testing at 20 kHz in the gigacycle regime (10^8-10^9 cycles) before crack initiation; for aluminium alloys it is 35 °C at R= –1.

In our case, the temperature of AS7G06-T6 cast aluminium alloy during high frequency loading at 20 kHz was measured in some tests (R= –1) of this work by using an infrared camera to be sure that temperature do not affect the fatigue tests results. Infrared camera is a device from CEDIP Infrared Systems available at LAMEFIP laboratory: the model is JADE III (Medium wave radiation, wavelength: 3–5 µm)

Two different stress levels were tested with and without air cooling. These stress levels are presented in Table 2.8.

Stress levels for experiments at R= –1	
σ_a = 70 MPa	Without air cooling
	With air cooling
σ_a = 80 MPa	Without air cooling
	With air cooling

Table 2.8. Testing conditions for temperature measuring in AS7G06-T6.

Figure 2.27shows the average temperature measured with the infrared camera in the narrowest section of an AS7G06-T6 specimen at σ_a=70 MPa, R=–1 and 20 kHz without air cooling. The average temperature measuring was specifically where stress is more concentrated (square marked zone). The same thing is shown in Figure 2.29 but for σ_a=80 MPa (R= –1), the average temperature on the square marked zone is presented.

In both cases, the temperature does not increase more than 19 °C even without air cooling with a temperature at the beginning of the test of 17.6 °C. This does not affect the material behavior because any microstructural change occurs at this temperature. It is observed in the curve of temperature versus time that temperature becomes stable after around 8 min. That is around 9.6×10^6 cycles.

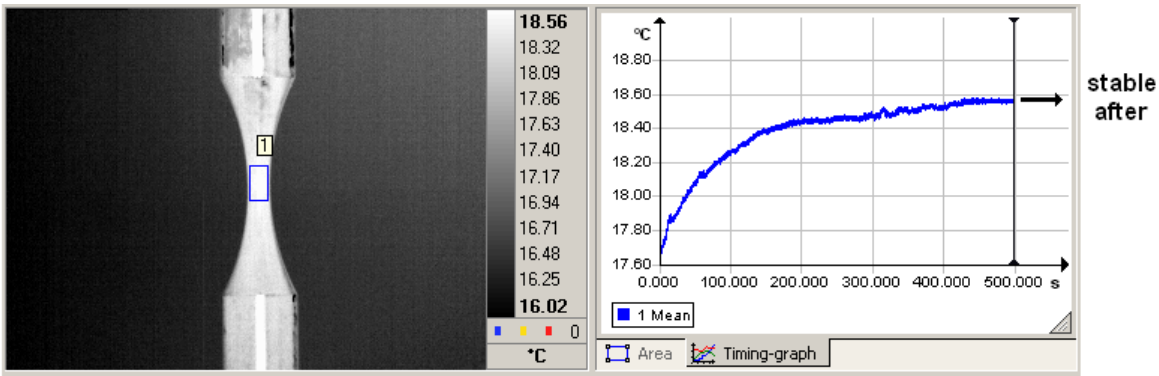

Figure 2.27. Temperature measure during testing of AS7G06-T6 at 70 MPa, R=–1, 20 kHz without cooling air.

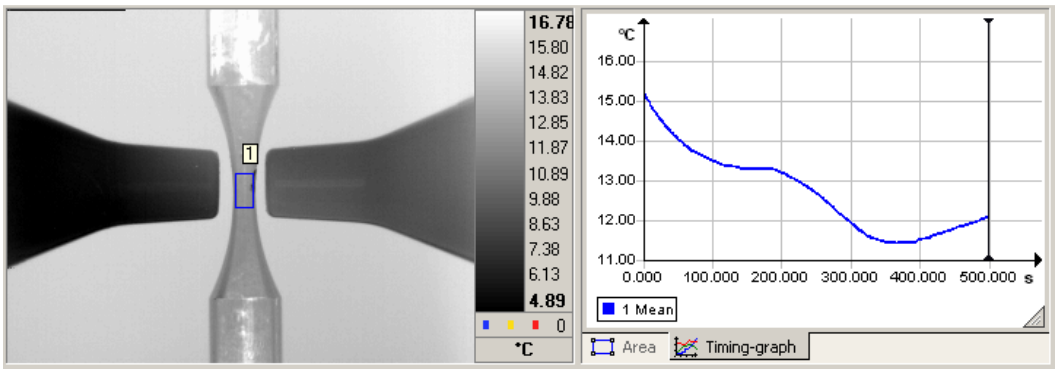

Figure 2.28. Temperature measure during testing of AS7G06-T6 at 70 MPa, R=–1, 20 kHz with air cooling.

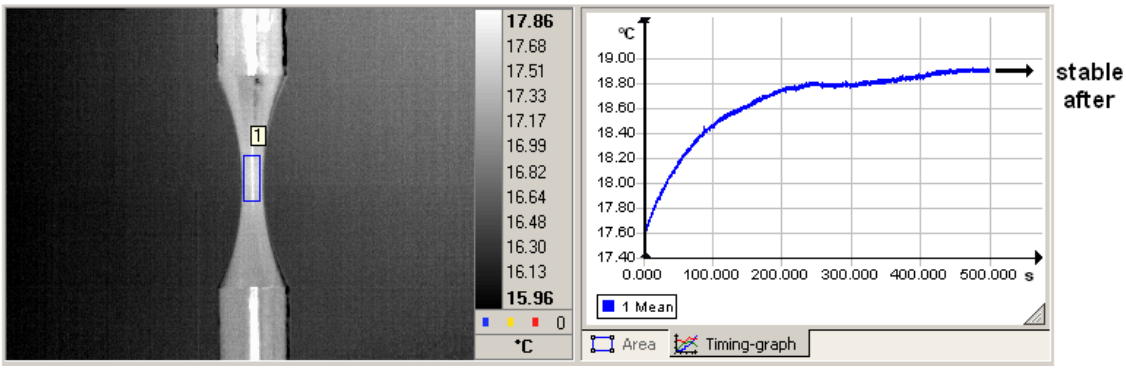

Figure 2.29. Temperature measure during testing of AS7G06-T6 at 80 MPa, R=–1, 20 kHz without cooling air.

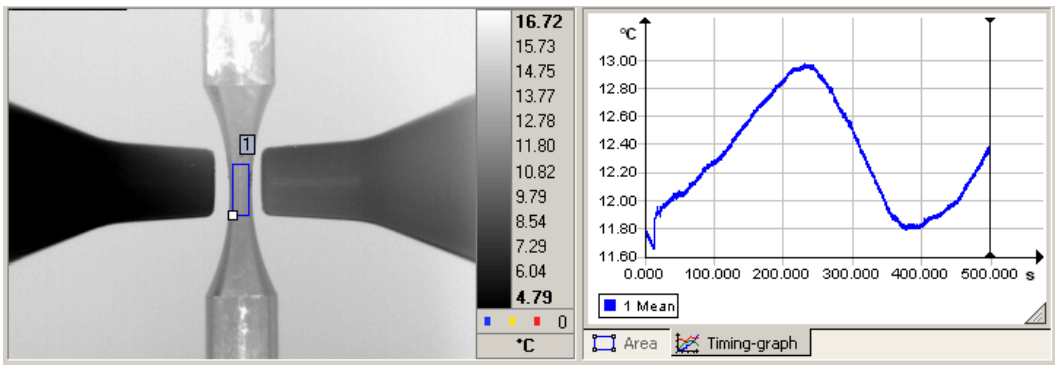

Figure 2.30. Temperature measure during testing of AS7G06-T6 at 80 MPa, R=–1, 20 kHz with cooling air.

Figure 2.28 and Figure 2.30 show the average temperature measured in the central section of the specimen at R= –1 at σ_a=70 MPa and σ_a=80 MPa respectively. In this case, the maximum temperature measured is oscillating between 11°C and 15 °C. That is because the flow rate of air cooling is not constant because the air compressor works by batches to increase the pressure in the air pressure vessel. When the pressure is 10 bars the compressor stops, it starts when the pressure is 5 bars. In all the cases, it is not a problem because the temperature is very low to influence the microstructure and then fatigue results.

After the measure of temperature, it was decided to carry out the tests of AS7G06-T6 cast aluminium alloy planned at room temperature without using air cooling.

2.4. AS7G06-T6 fatigue results

The *S-N* curves presented in this section have been obtained by using ESOPE software [17]. This software is based on statistical analysis of fatigue data and the work of Bastenaire [18]. Equation (2.6) proposes a specific a *S-N* curve model adjusting data to a curve [14] with an asymptote ("fatigue limit" *E*). But since in gigacycle regime there is no fatigue limit this model has not been used.

$$N = \frac{A}{S-E} \exp\left[-\left(\frac{S-E}{B}\right)^{C}\right] \tag{2.6}$$

where

S = Stress applied
E= Fatigue limit of the material
A: Parameter setting the curve along the cycles axis
B: Scale parameter
C: Shape parameter

This formulation allows to report the entire *S-N* curve up to the fatigue strength in the low cycle regime, but is not commonly used in gigacycle regime. The statistical fitting method comprehended in ESOPE software allows to take into account the tested specimen broken as well as the not broken.

One advantage of this method is that it gives a complete description of the dispersion related to the fatigue strength. In fact, the S-N curves obtained show the relation between the stress and the median fatigue life of the material corresponding to 50% of probability to break.

With ESOPE software the parameters for the *S-N* curves described by different models and the corresponding standard deviations can be identified (if they are statistically representative). In this work, Wöhler model (Equation (2.7)) and Basquin model (Equation (2.8)) are used to represent the obtained results because there is no fatigue limit in such models.

Wöhler Model:

$$\text{Log}\, N = A \cdot S_a + B \tag{2.7}$$

Basquin Model:

$$\text{Log}\, N = A \cdot \text{Log}\, S_a + B \tag{2.8}$$

A and B are constant depending on the material and the R ratio.

For the estimation of *P-S-N* curves with p_s=16% and p_s=84% (survival probability) one standard deviation is added or subtracted one time to the stress (S_a) in the previous models, corresponding to the median curve (p_s=50%)

2.4.1. Crack initiation tests at room temperature

Crack initiation tests were carried out at room temperature (~20 °C), at the three different R ratios mentioned before. In the three next sections both Wöhler and Basquin models of *S-N* curves will be presented for R=–1 and R=0.01. For the case of R=0.5 only *S-N* curve obtained graphically will be presented because the small number of specimens did not allow us to treat the data with ESOPE software (statistically not representative with a confidence level of 0.95).

2.4.1.1. Tension-compression: R=-1 at room temperature

The results for R=–1 in air and room temperature are represented in Figure 2.31 and Figure 2.32. They show the *P-S-N* curves for the Wöhler model and for the Basquin model respectively. In these curves the median is presented with the bold line (Survival probability p_s=0.5). The dashed lines represent the curves for survival probabilities p_s=0.16 and p_s=0.84. These models of curves have been identified between 10^6 and 10^9 cycles.

The results data sheet and the staircase data for AS7G06-T6 cast aluminum alloy in air, R=–1 and room temperature are presented in Annex 6. The fatigue strength at 10^9 cycles obtained by staircase method is 72 MPa in stress amplitude. The standard deviation is 3.5 MPa.

One notes a constant decreasing of fatigue strength when lifespan increases. Fatigue strength amplitude decreases from 110 MPa at 10^6 cycles to 72 MPa at 10^9 cycles. It is important to take into account in calculations such significant decreasing for designing purposes.

Looking the *S-N* curves we can note that the behavior in fatigue seems to change after 10^9 cycles to a pseudo[1]-asymptotic tendency, such as the explanation proposed by Mughrabi presented in Section 2.1 of Chapter I (Figure 1.9). It was not possible to carry out more tests up to 10^{10} cycles or more due to the long time that takes to tests a specimen up to this number of cycles, even at 20 kHz.

[1] Because this is only a tendency without any physical evidence

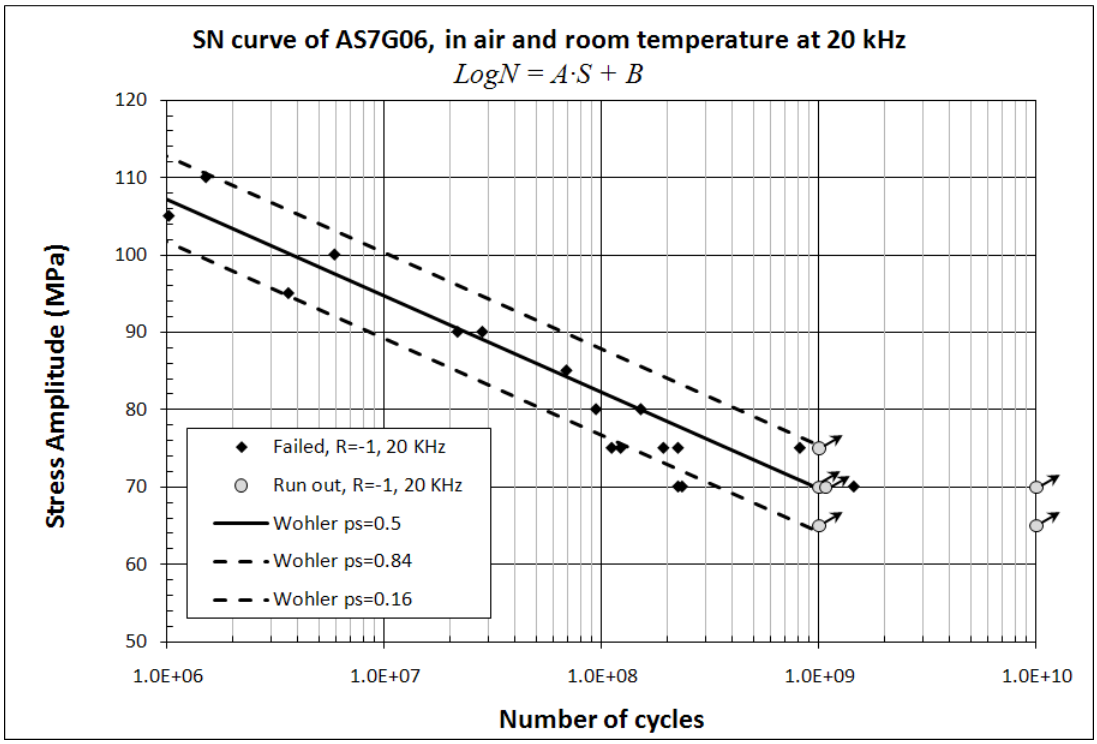

Figure 2.31. Wöhler *P-S-N* curve for AS7G06-T6 in air, R=–1 and room temperature.

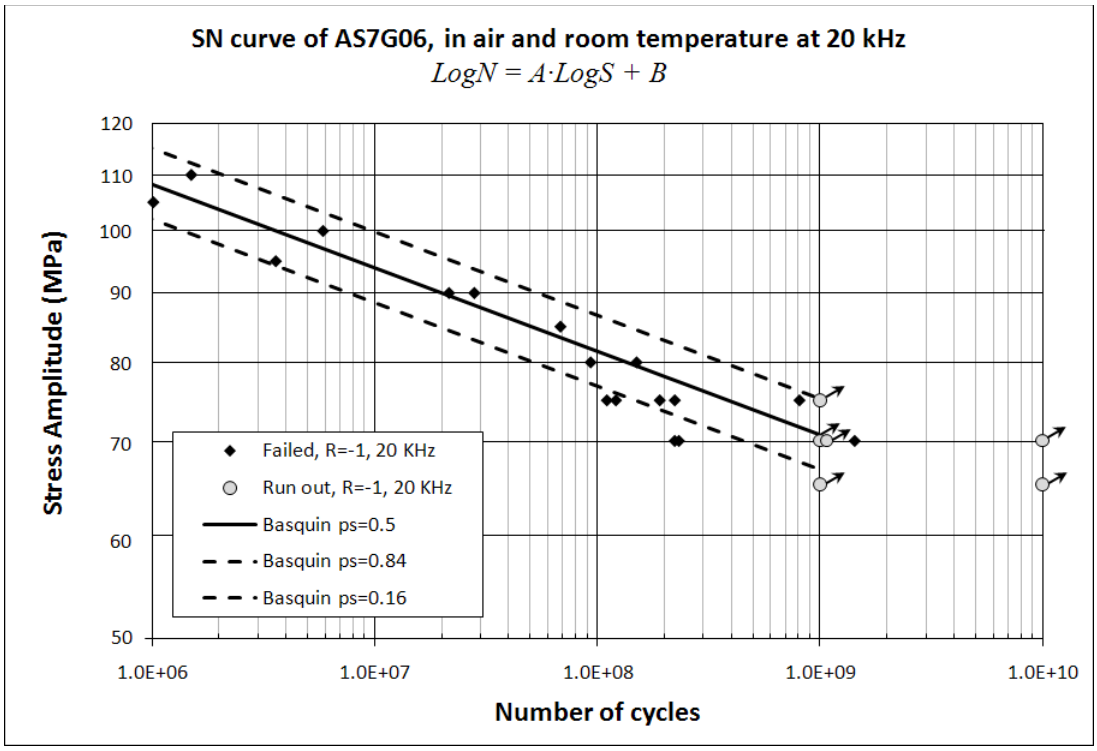

Figure 2.32. Basquin *P-S-N* curve of AS7G06-T6 in air, R= –1 and room temperature.

2.4.1.2. Tension-tension: R=0.01 at room temperature

Figure 2.33 and Figure 2.34 show the *PSN* for AS7G06-T6 cast aluminum alloy tests at R=0.01 in air and room temperature. They represent the curves for the Wöhler model and for the Basquin model respectively. In these curves the median is presented with the bold line (survival probability p_s=0.5). The dashed lines represent the curves for survival probabilities p_s=0.16 and p_s=0.84. These models of curves have been identified between 10^5 and 10^9 cycles.

The data sheet of results for AS7G06-T6 cast aluminum alloy in air, R=0.01 and room temperature are detailed in Annex 6. In this case the staircase method was followed but it did not give satisfactory results, because only two specimens did not fail. The stress levels tested have been distributed the best in order to estimate the *SN* curve.

Looking at the Figure 2.33 and Figure 2.34 the average fatigue strength at 10^9 cycles is around 35 MPa (amplitude) according to the Basquin model and 39 MPa (amplitude) according to the Wöhler model. The fatigue strength at 10^6 cycles is around 72 MPa for both models. This is a decreasing of 33 MPa between the fatigue strength at 10^6 and 10^9 cycles: it is significant.

Although the number of tests reaching more than 10^9 cycles is small, it seems that a pseudo[2]-asymptotic behavior of the fatigue strength is described by the curve as explained by Mughrabi. That could be verified carrying out other tests in further investigations.

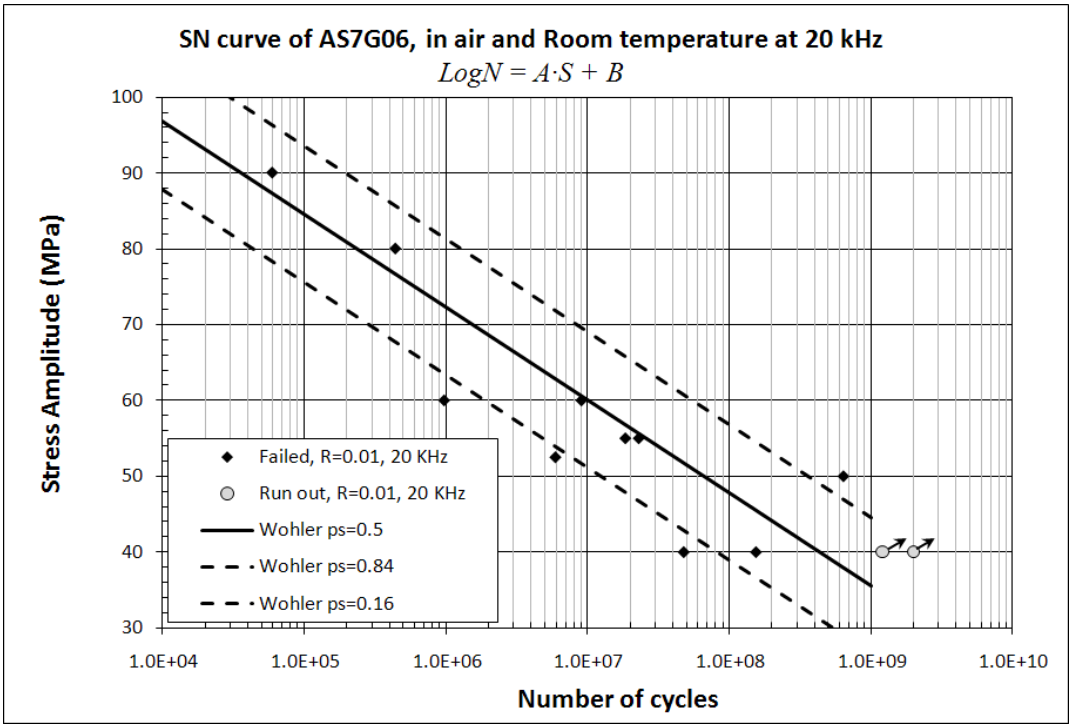

Figure 2.33. Wöhler *P-S-N* curve for AS7G06-T6 in air, R=0.01 and room temperature.

[2] This is a tendency without physical evidence

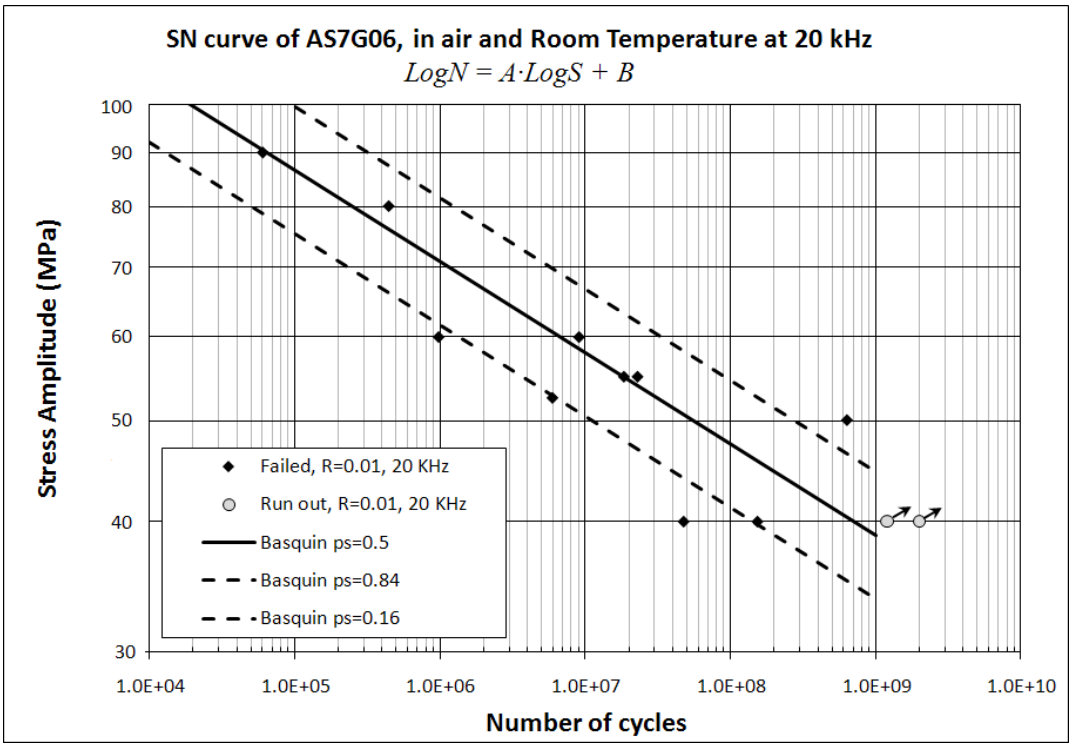

Figure 2.34. Basquin *P-S-N* curve of AS7G06-T6 in air, R=0.01 and room temperature.

2.4.1.3. Tension-tension: R=0.5 at room temperature

The tests results at R=0.5 in air and room temperature are shown in Figure 2.35. The detailed table of results is in Annex 6. In this case only 10 specimens were tested, then it was practically impossible to have the parameters of Wöhler and Basquin *S-N* curve models from ESOPE software; the fatigue strength at 10^9 cycles is however estimated.

The detailed staircase results and data for AS7G06-T6 at R=0.5 in air and room temperature are presented in Annex 6. The obtained fatigue strength by the staircase method is 54 MPa in stress amplitude. The standard deviation could not be obtained due to the small quantity of specimens but it is probably smallest than the interval between two steps of the staircase which is 5 MPa.

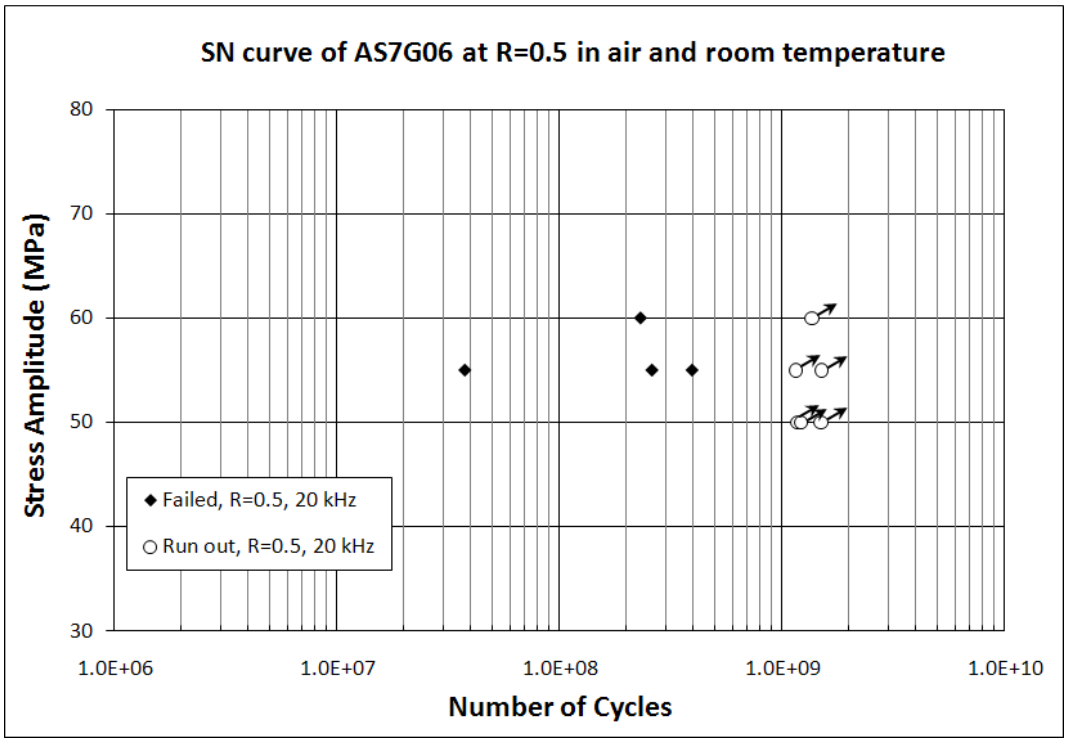

Figure 2.35. SN curve for AS7G06-T6 at R=0.5 in air and room temperature.

2.4.2. Crack initiation tests at 150 °C

Following the same methodology, tests at 150 °C were carried out on AS7G06-T6 specimens. the *S-N* curves presented in next subsections are adjusted to the Wöhler and Basquin models presented before.

2.4.2.1. Tension-compression: R=-1 at 150 °C

The tests results for AS7G06-T6 cast aluminum alloy in tension-compression R=-1, in air and 150 °C are presented in Figure 2.36 and Figure 2.37. The data and staircase are presented in Annex 6.

Figure 2.36 and Figure 2.37 show the *PSN* curves for the Wöhler and Basquin models respectively. These models were identified from 10^6 to 10^9 cycles by using ESOPE software.

According with staircase method the fatigue strength at 10^9 cycles is 61 MPa in stress amplitude. The standard deviation is 4.5 MPa. Fatigue strength at 10^9 cycles compared with the fatigue strength at 10^6 cycles is around 30 MPa lower, which confirms that no asymptotic behavior between 10^6 and 10^9 cycles occurs.

Fatigue strength at 10^9 cycles, 150 °C and R=–1 is only 11 MPa lower in stress amplitude compared to same tests at room temperature.

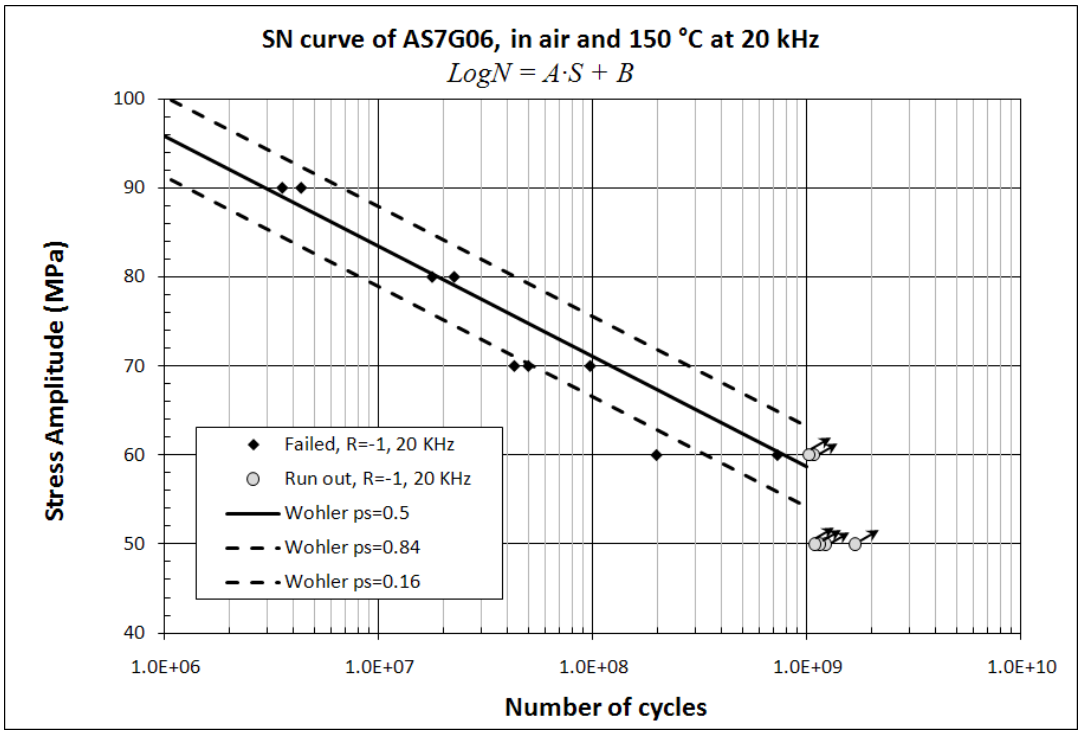

Figure 2.36. Wöhler *P-S-N* curve for AS7G06-T6 at R=-1, in air and 150 °C.

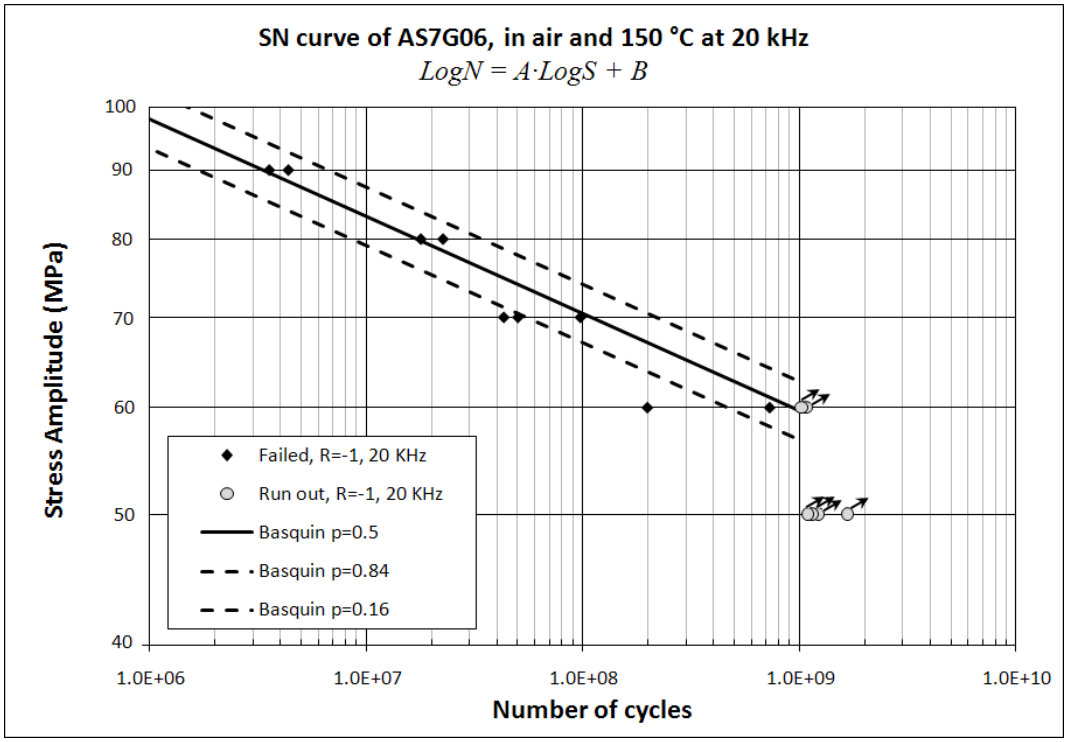

Figure 2.37. Basquin *P-S-N* curve for AS7G06-T6 at R=-1, in air and 150 °C.

2.4.2.2. Tension-tension: R=0.01 at 150 °C

Figure 2.38 and Figure 2.39 show the results obtained in the test in tension-tension at R=0.01, in air and 150 °C. The results data tables and staircase data are presented in Annex 6.

Figure 2.38 and Figure 2.39 show the *PSN* curves obtained for both Wöhler and Basquin models for AS7G06-T6 at R=0.01 in air and 150 °C, respectively. These models were determined in the range of 10^6 and 10^9 cycles.

According to the results of the staircase method for AS7G06-T6 at R=0.01, in air and 150 °C, the fatigue strength at 10^9 cycles is 48 MPa in stress amplitude. The standard deviation is 4.1 MPa.

The fatigue strength at 10^9 cycles determined in this conditions is around 47 MPa lower compared with the fatigue strength at 10^6 cycles. It means there is no asymptotic behavior between 10^6 and 10^9 cycles although it is not possible to determine the behavior tendency beyond 10^9 cycles.

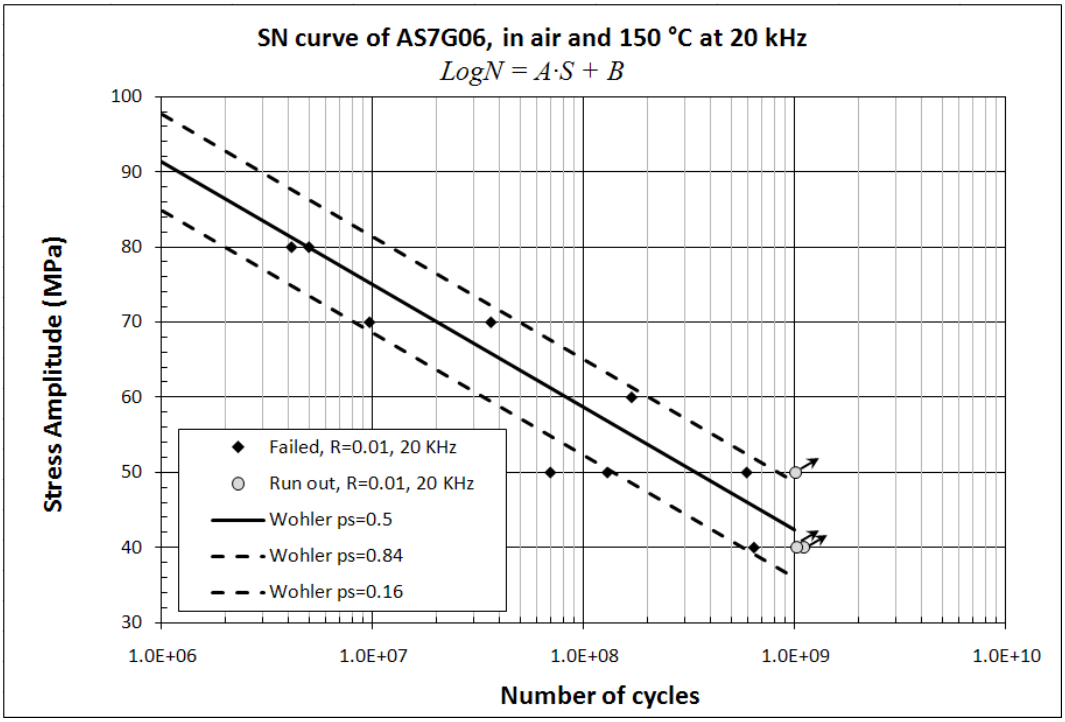

Figure 2.38. Wöhler *P-S-N* curve for AS7G06-T6 at R=0.01, in air and 150 °C.

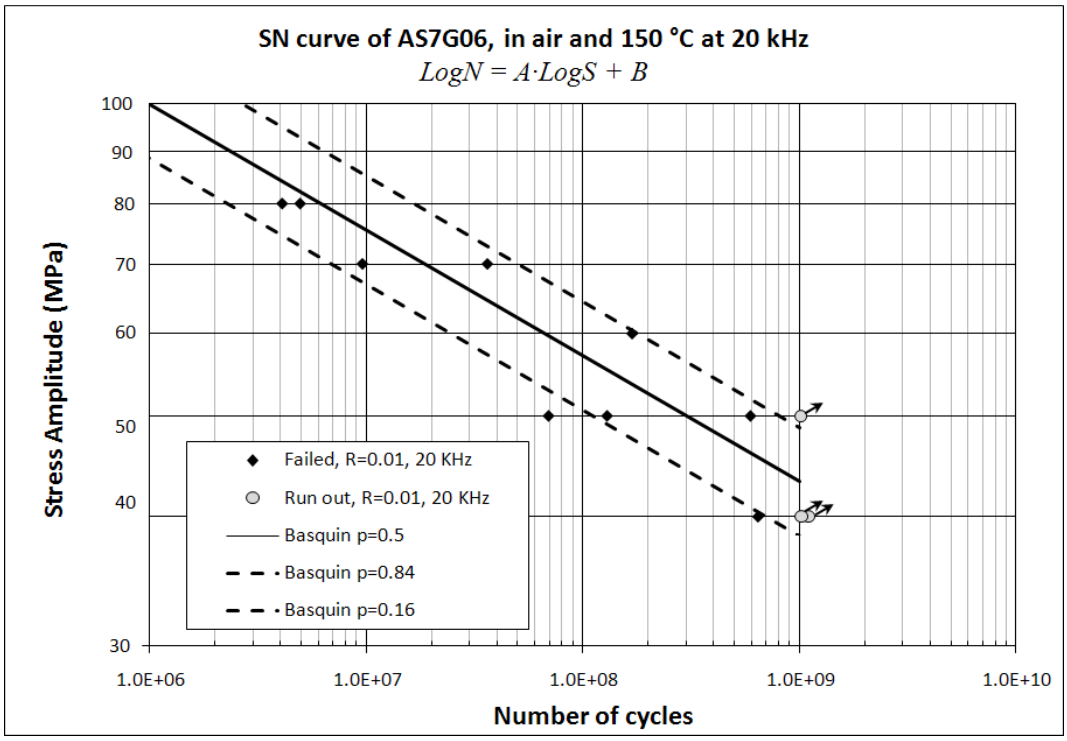

Figure 2.39. Basquin *P-S-N* for AS7G06-T6 at R=0.01, in air and 150 °C.

2.4.3. Synthesis of the results on AS7G06-T6

A resume of the fatigue test results is presented in Table 2.9. This table shows the fatigue strengths at 10^6 and 10^9 cycles at different R ratio and temperatures of smooth specimens.

Temperature °C	R	Fatigue strength at 10^6 cycles, MPa			Fatigue strength at 10^9 cycles, MPa			Staircase Std Deviation, MPa	ESOPE Std Deviation, MPa
		amp	mean	max	amp	mean	max		
20	-1	110	0	110	72	0	72	3.5	5.55
20	0.01	72	73.5	145	~39	~39	~78	Inestimable	8.98
20	0.5	Non tested			54	162	216	Inestimable	Inestimable
150	-1	72	0	72	61	0	61	4.5	4.48
150	0.01	95	95	192	48	48	96	4.1	6.4

Table 2.9. Fatigue results of AS7G06-T6 cast aluminium alloy in air at 20 kHz.

Looking at the fatigue results presented in Table 2.9 it is possible to establish the comparison between the fatigue strength at 10^6 and 10^9 cycles at each testing conditions, except for R=0.5 at 20 °C, because data at 10^6 cycles are not available. It is noted that for all the cases the fatigue strength decreased considerably at 10^9 cycles compared with 10^6 cycles. This denotes that there is not asymptotic fatigue behavior at least in the range of 10^6 and 10^9 cycles.

On the other hand, these results allow observing the effect of two important factors in the AS7G06-T6 fatigue strength: the temperature and mean stress.

The temperature effect between 20°C and 150 °C is small for tests at R= –1. The fatigue strength at 150 °C is 11 MPa lower than fatigue strength at 20 °C. On the contrary, for the tests at R=0.01the fatigue strength at 150 °C is higher than fatigue strength at 20 °C, although 9 MPa in stress amplitude only. It is possible that the fatigue behavior is practically similar at 20 °C than 150 °C, but that will be analyzed in next chapter with the fractography analysis.

The fatigue strengths for AS7G06-T6 obtained experimentally are presented in the Haigh diagram as shown in Figure 2.40. This diagram shows that the results at room temperature do not follow the Goodman threshold. It is observed that fatigue strength is lower if the mean stress is more than zero (tension-tension), but with high stress ratio, R, the fatigue strength is higher than with lower R. This is contradictory with the written in literature where it is said that fatigue strength is lower if the mean stress is more tensile.

On the other hand, the effect of the temperature in the fatigue strength for R=–1 is shown in the Haigh diagram (Figure 2.40). It is observed a decreasing of around 10 MPa from the Goodman threshold.

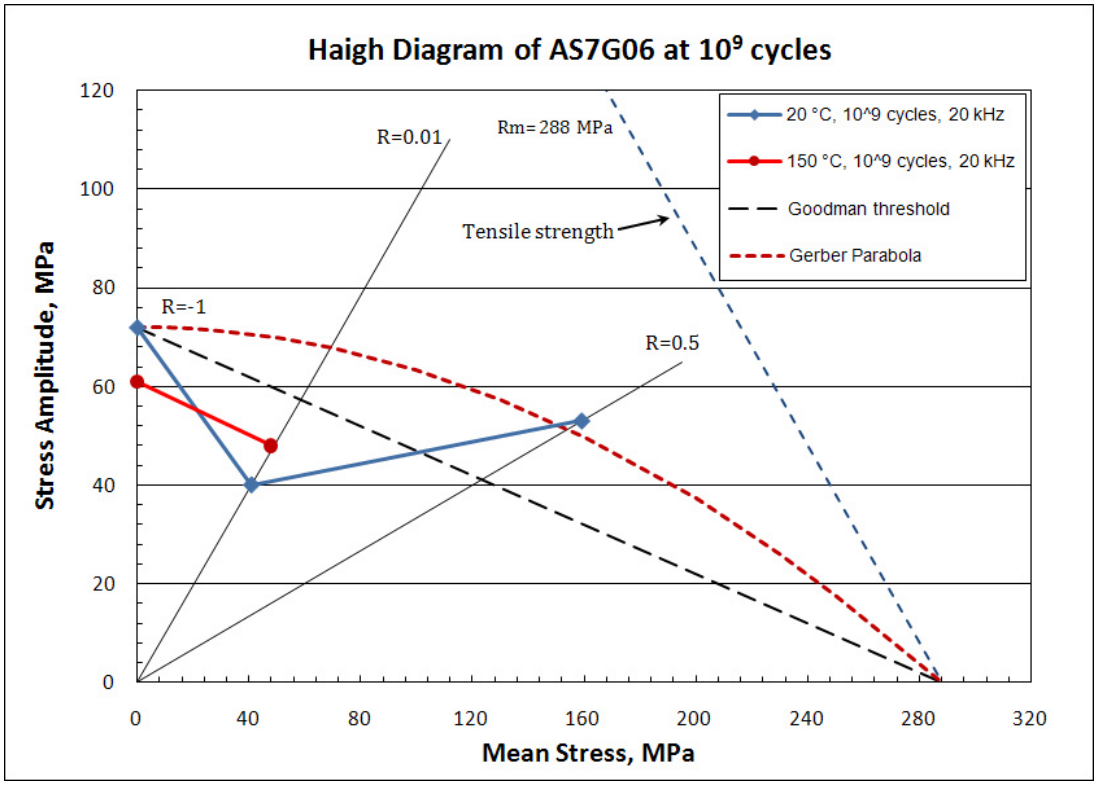

Figure 2.40. Haigh diagram of AS7G06-T6 at 10^9 cycles and 20 kHz.

The fatigue results of AS7G06-T6 at R=–1 at room temperature can be compared with other works in the same alloy, but there are not many references of the fatigue strength in the gigacycle regime. Bathias and Paris presented in [11] a large compilation of fatigue curves on aluminium alloys. In the gigacycle regime, at R=–1 and room temperature, these alloys have a fatigue strength between 70 to 130 MPa. Specifically, for AS7G06-T6 alloy, the fatigue strength has been reported to 75 MPa in stress amplitude. In this work we have obtained 72 MPa in stress amplitude: this is in agreement with literature.

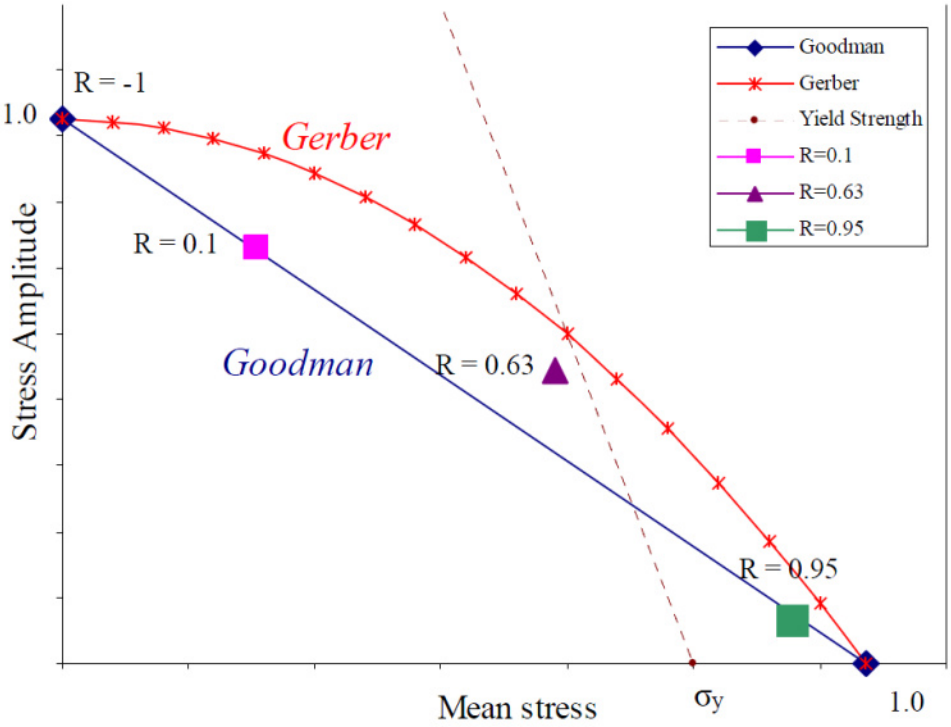

Figure 2.41. Haigh diagram of AlSi7Cu0.5Mg0.3 (uniaxial fatigue) [15].

The effect of the mean stress have been reported by Morel et al [15] for a AlSi7Cu0.5Mg alloy, which is an alloy with aluminium, silicon and magnesium but with a high copper content than AS7G06-T6. High stress levels were tested on specimens of this alloy at 80 Hz. The fatigue strengths values were not presented but the effect of the mean stress was indicated. The fatigue strength was lower while mean stress is more tensile. A fact not mentioned by Morel et al [15] is observed in a Haigh diagram presented (Figure 2.41); the fatigue strengths at low R ratio lie on the Goodman threshold, but at higher R ratio, such as 0.63, the fatigue strength lies on the Gerber's parabola. That is observed in our results at R=0.5 too. No explanation is proposed by Morel et al. and we do not know how to explain that too.

3. Fatigue tests on R5 steel

Gigacycle fatigue tests were carried out on R5 steel specimens using the ultrasonic fatigue testing machine presented in Section 1.1 of this chapter. The S-N curves obtained at different testing conditions are presented in next sections.

Table 2.10 shows in a scheme the planning of tests carried out in this work, parameters and conditions of these tests are explained in this scheme. All the tests on R5 steel were carried out at room temperature (~20 °C).

Crack initiation tests	
Without any corrosion	R = –1
	R = 0.3
With corrosion	R= –1, with pre-corrosion
	R= –1, with sea water corrosion in situ, Roughness: Ra=0.6 µm
	R = –1, with sea water corrosion in situ, Roughness: Ra=0.1 µm
Crack growth tests	
In air	R = –1
In sea water corrosion	R = –1

Table 2.10. List of fatigue tests on R5 steel.

Without any corrosion in air, two different stress ratios R were used to carry out crack initiation tests: R= –1 and R=0.3 in order to observe the effect of the mean stress on the fatigue strength of R5 steel.

With corrosion, two different specimen conditions were used for crack initiation tests: specimens with pre-corrosion and virgin specimen with artificial sea water corrosion in real time. For tests with corrosion in sea water flow, virgin specimens were used with two different roughness (Ra=0.6 µm and Ra=0.1 µm). That is with the aim of determining the effect of the surface finishing in fatigue corrosion behavior.

The objective of the study is to determine the fatigue strength in the gigacycle regime of R5 steels without corrosion and after corrosion. In that is related the corrosion effect on the steels used in off-shore mooring systems that have been developed in recent years. According to our investigations, there is no study in literature on gigacycle fatigue of this type of steel.

Crack growth tests were carried out at R= –1 in air and with sea water corrosion, using the methodology described in Section 1.2.

In next sections one present the experimental results for R5 steel at different testing conditions. Previously the main physical-mechanical properties and chemical composition of R5 steel are shown.

3.1. R5 steel characteristics

R5 steel is a non-standard hot rolled low alloy steel, designed R5 according to the international denomination of the International Classification Societies of Offshore Systems, fabricated by Vicinay-Cadenas society by means of Electric Arc Furnace steelmaking process and subsequent refining by Ladle Furnace plus vacuum degassing. Hot rolled bars of steel are used for manufacturing mooring chains for offshore petroleum platforms in the European North Sea. The links of chains are formed by hot bending and joined by flash welding. After, a double quenching in water at 920 °C then 880 °C and tempering at 650 °C with water cooling. After this heat treatment its mechanical properties under quasi-static monotonic tension are presented on Table 2.13.

Figure 2.42 shows a scheme of a chain link showing from where specimens were obtained. The specimen tested in this work were obtained from the longest straight section of the link where there is not welding, in longitudinal sense.

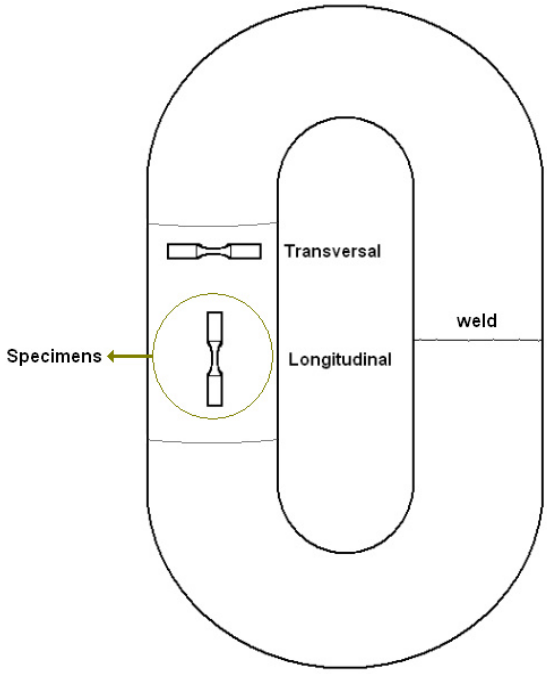

Figure 2.42. Scheme of specimen subtraction from a chain link.

This steel has a typical fine grain microstructure composed of tempered martensite and banite as shown in Figure 2.43-b. Its low alloyed elements are mainly Chromium, Nickel, Manganese and Molybdenum. Its general chemical composition is presented in Table 2.11. A microanalysis spectrum of a specimen is presented in Figure 2.44 showing the presence of these elements.

The R5 steel is vacuum degassed with low hydrogen content (1 ppm maximum in the molten metal after the vacuum treatment) and very low non-metallic inclusions content is achieved (Figure 2.43-a). These are typical non-metallic inclusions according to both the ASTM E45 and AMS 2301 standards as presented in Table 2.12 [1, 6].

C	Mn	Si	P	S	Cr	Ni	Mo	V	O
0.22	1.22	0.3	0.009	0.003	1.07	1.07	0.5	0.09	12 ppm

Table 2.11. Chemical composition of R5 steel (% weight, Fe balance).

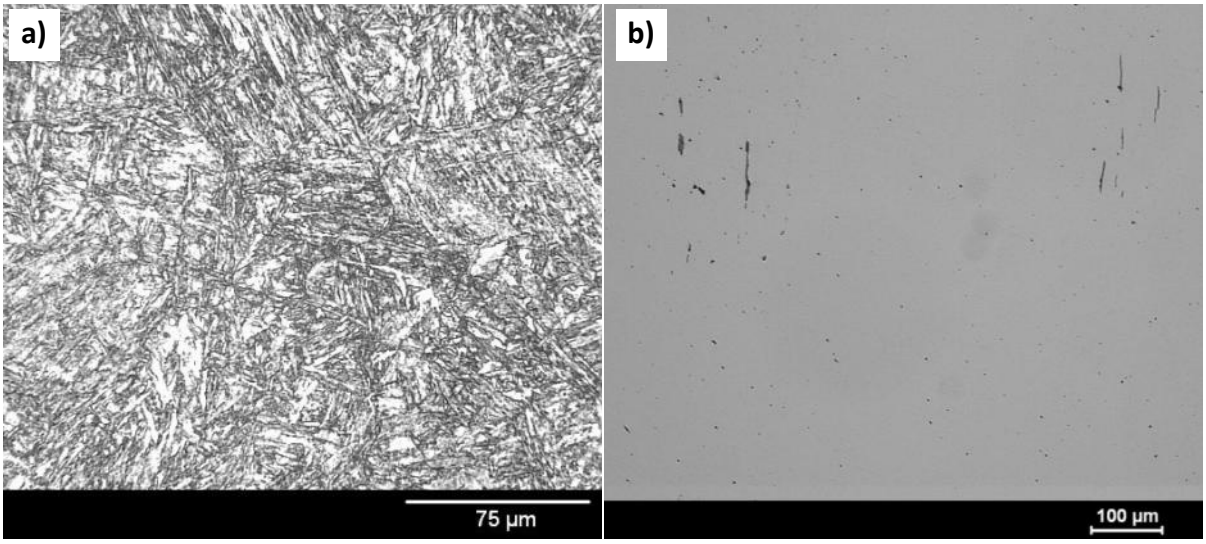

Figure 2.43. a) R5 steel microstructure (after heat treating) and nital etching, b) non-metallic inclusions (in dark).

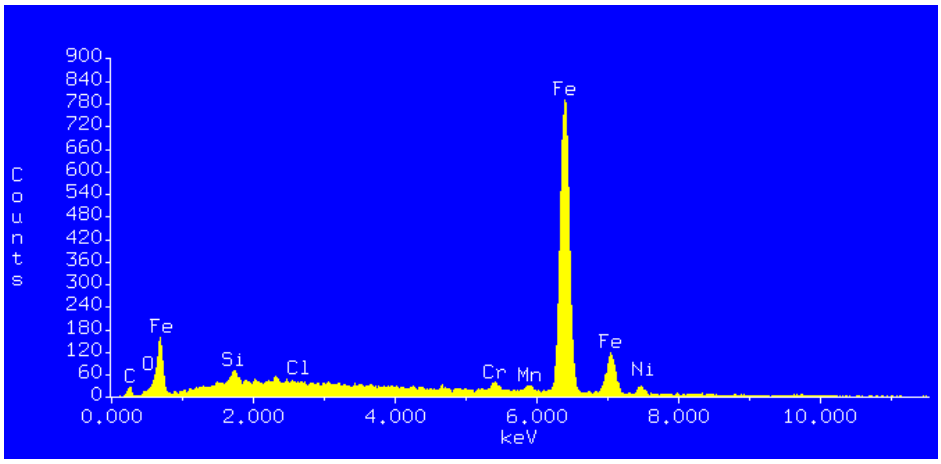

Figure 2.44. Micronalysis spectrum on the whole surface of an R5 steel specimen.

Type A: Sulphides		Type B: Alumina		Type C: Silicates		Type D: Globular oxides	
Thin	Heavy	Thin	Heavy	Thin	Heavy	Thin	Heavy
0.5	0	1.0	0	0	0	0	0.5

Table 2.12. Non-metallic inclusions of R5 steel according to ASTM E45 and AMS 2301 standards [1, 6].

Density	7850 Kg/m3
Hardness	317 HV
Yield Strength	970 MPa
UTS	1018 MPa
Young's Modulus	211.187 GPa
Fatigue Strength (at 10^6 cycles, R=0.1, in air and room temperature)	500 – 600 MPa (Maximum stress)

Table 2.13. Physical and Mechanical properties of R5 steel.

Fatigue specimens of R5 with pre-corrosion and specimens without any corrosion were received from the company Vicinay Cadenas. Specimens for endurance test and crack growth test were received too.

Some fatigue specimens of R5 steels have been submitted to corrosion in a saline environment in order to simulate ocean conditions.

The saline corrosion has been caused in a cabinet of 1 m^3, according to the ASTM standard G85 [2]. This operation was carried out by Vicinay Cadenas, before testing with the gigacycle fatigue testing machine.

The apparatus required for salt spray (fog) testing consists of a fog chamber, a salt solution reservoir, a supply of suitably conditioned compressed air, one or more atomizing nozzles, specimen supports, provision for heating the chamber, and necessary means of control.

The chamber temperature is 35 ºC and its humidity 95%. The salt solution contains 5 % NaCl,, its pH is 6.6 and it is applied in the chamber with a rate flow of 1,52 ml/h.

The specimens were located at 25º in relation with the vertical position avoiding the direct application of the solution. The total time of the process in salt fog is approximately 600 hours.

After the pre-corrosion process the specimens were removed from the corrosion chamber, first chemically cleaned and then cleaned with emery paper to remove the oxide layer. Many pits were created by the salt fog, as shown in Figure 2.45, their diameter are around 30 to 80 µm.

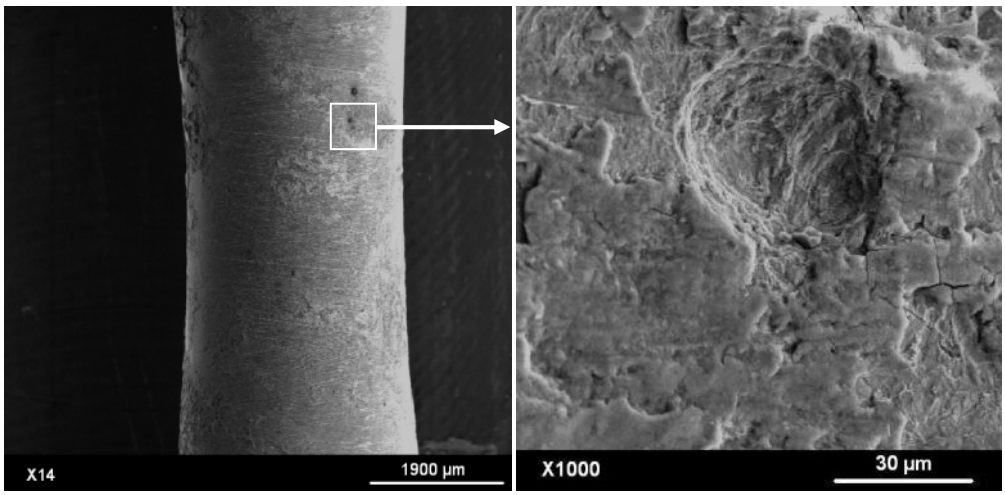

Figure 2.45. Microstructure of R5 steel after pre-corrosion showing some pits.

3.2. Specimen geometry

Figure 2.46 shows a sketch of the R5 steel specimens for fatigue crack initiation testing (A detailed plan is presented in Annex 3).

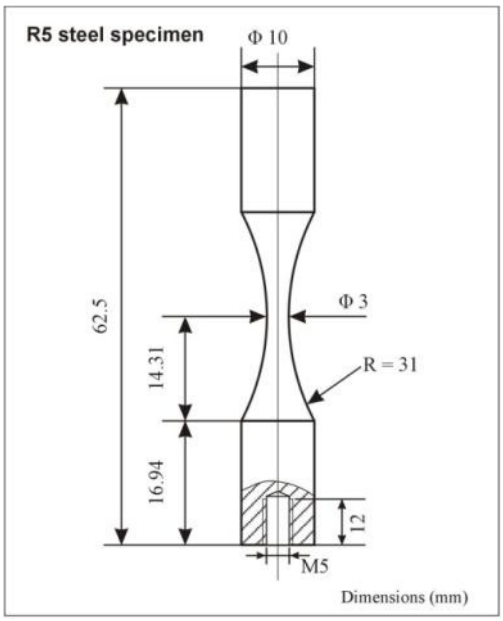

Figure 2.46. Plan of dimensions for a R5 steel specimen.

The dimensions of R5 steel specimens were calculated to work in resonance vibration at 20 kHz using the theory of elastic wave presented in Section 2.3 of Chapter I and they were verified by using finite element analysis software ANSYS (with isotropic and homogeneous elastic material behavior hypothesis).

Table 2.14 shows the mode frequencies found using ANSYS. One of the modes of vibration is 20089 Hz, which is practically the frequency of work of the converter and amplifiers.

***** INDEX OF DATA SETS ON RESULTS FILE *****

SET	TIME/FREQ	LOAD STEP	SUBSTEP
1	0.0000	1	1
2	0.0000	1	2
3	0.0000	1	3
4	0.45908E-02	1	4
5	0.65958E-02	1	5
6	0.91812E-02	1	6
7	2523.4	1	7
8	2523.4	1	8
9	4836.1	1	9
10	13269.	1	10
11	13269.	1	11
12	20089.	1	12
13	47232.	1	13
14	47233.	1	14
15	65391.	1	15
16	65391.	1	16
17	81911.	1	17
18	83139.	1	18
19	83142.	1	19
20	83171.	1	20
21	0.10751E+06	1	21
22	0.10752E+06	1	22
23	0.10878E+06	1	23
24	0.12305E+06	1	24
25	0.12579E+06	1	25
26	0.13202E+06	1	26
27	0.13203E+06	1	27
28	0.15010E+06	1	28
29	0.15302E+06	1	29
30	0.15303E+06	1	30

Table 2.14. Modal frequencies of AS7G06-T6 specimen

Figure 2.47 shows the stresses calculated by the harmonic analysis on specimen at 20089 Hz. A harmonic displacement of 5 µm is applied at the top of the specimen in the *y* direction. It is observed that the maximum stress calculated is 138 MPa, which correspond to a stress/displacement ratio of around 27.6 MPa/µm.

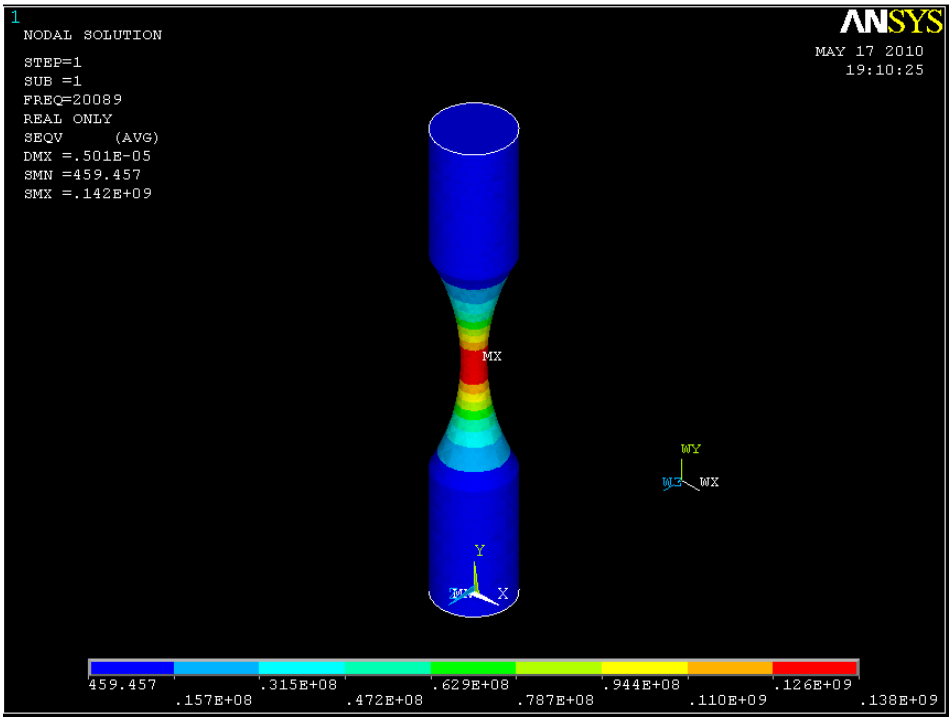

Figure 2.47. Harmonic analysis of AS7G06-T6 specimen with 5 µm of vibration at the top.

3.3. Temperature measurement of R5 steel during testing

According to Bathias [12] the temperature due to self heating during fatigue testing at 20 kHz and R= –1 in the gigacycle regime (10^8-10^9 cycles) before crack initiation is around 80 °C for low carbon steels or 4240 steel. For the same testing conditions the temperature on a 316 stainless steel is around 300 °C.

For R5 steel there is no register about the temperature during ultrasonic tests, but the experience in ultrasonic fatigue tests says that steels normally increase their temperature during high frequency loading [13]. The temperature of R5 steel specimens during high frequency loading at 20 kHz was measured in some tests (R= –1) of this work by using an infrared camera CEDIP Infrared Systems.

Two different stress levels were tested with and without air cooling. These stress levels are presented in Table 2.15.

Stress levels for experiments at R= –1	
σ_a = 375 MPa	Without air cooling
	With air cooling
σ_a = 400 MPa	Without air cooling
	With air cooling

Table 2.15. Testing conditions for temperature measuring in R5 steel.

Figure 2.48 shows the average temperature measured with the infrared camera in the narrowest section of an R5 steel specimen at σ_a=375 MPa, R= –1 and 20 kHz without using air cooling. The charts show the average temperature measured in the square marked zone, where stress is maximum. At the same way, Figure 2.50 show the average temperature on the square marked zone for σ_a=400 MPa, R= –1 and 20 kHz.

It is observed in Figure 2.48 an increment in the temperature of the specimen in the reduced section up to 98 °C when σ_a=375 MPa and air cooling is not used. The temperature is higher when σ_a=400 MPa, around 105 °C. Stabilization in the temperature occurs around 8 min after started the tests without air cooling.

Figure 2.49 and Figure 2.51 show the average temperature measured in the central section of the R5 specimens with air cooling, at R= –1 at and σ_a=400 MPa respectively. The oscillation observed in the measures is due to the difference of air cooling flow rate because the air compressor do not work continuously. The temperatures oscillate between 50 °C and 55 °C for σ_a=375 MPa and it oscillates between 55 °C and 62 °C for σ_a=400 MPa. These are practically the maximum applied stresses in fatigue crack initiation tests on R5 steel specimens in this work. These heating do not produce any crystallographic or microstructural changes that affect the fatigue behavior.

After observing the heating of specimens during fatigue testing at high frequency (20 kHz) it has been decided to use air cooling in all fatigue tests on R5 steel, except for the tests under sea water flow in situ. In such last case heat exchange with sea water flow is at least as good as air convection, cooling is thus adequate.

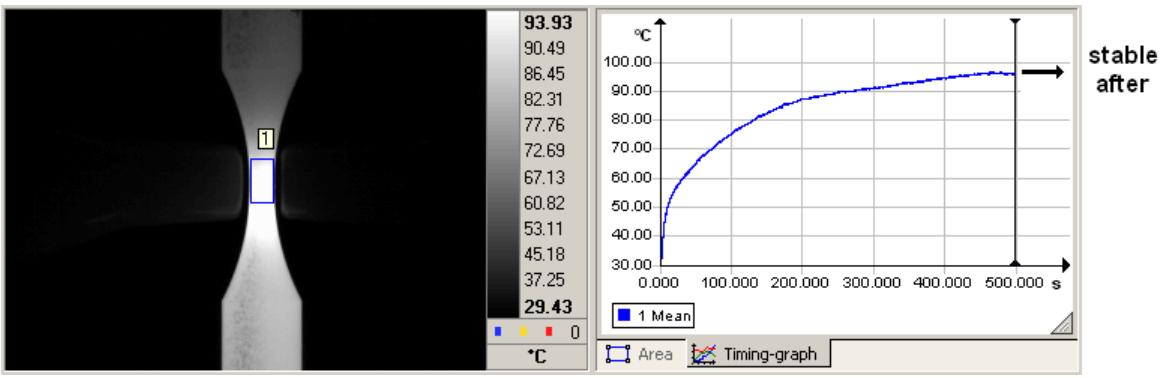

Figure 2.48. Temperature measure on R5 steel at 375 MPa, R=–1, 20 kHz without air cooling.

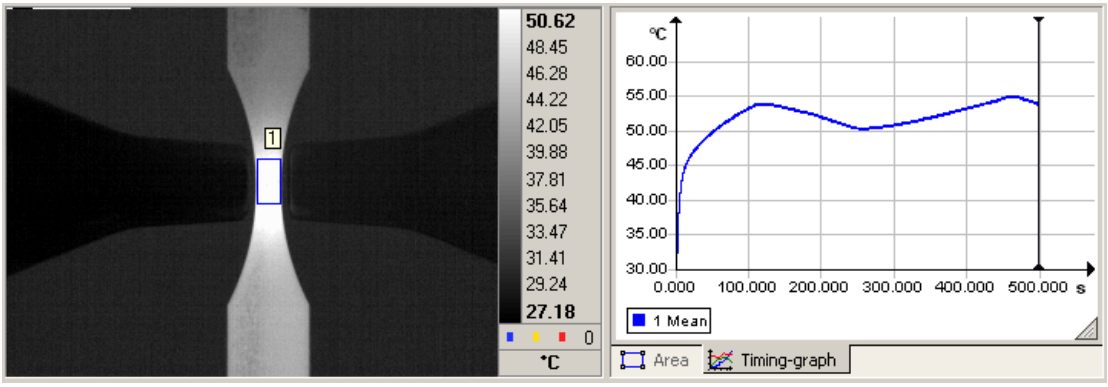

Figure 2.49. Temperature measure on R5 steel at 375 MPa, R=–1, 20 kHz with air cooling.

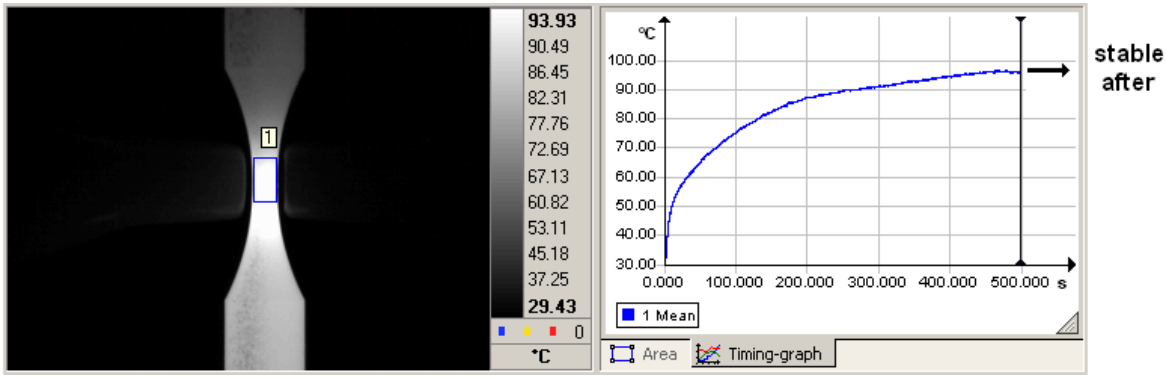

Figure 2.50. Temperature measure on R5 steel at 400 MPa, R=–1, 20 kHz without air cooling.

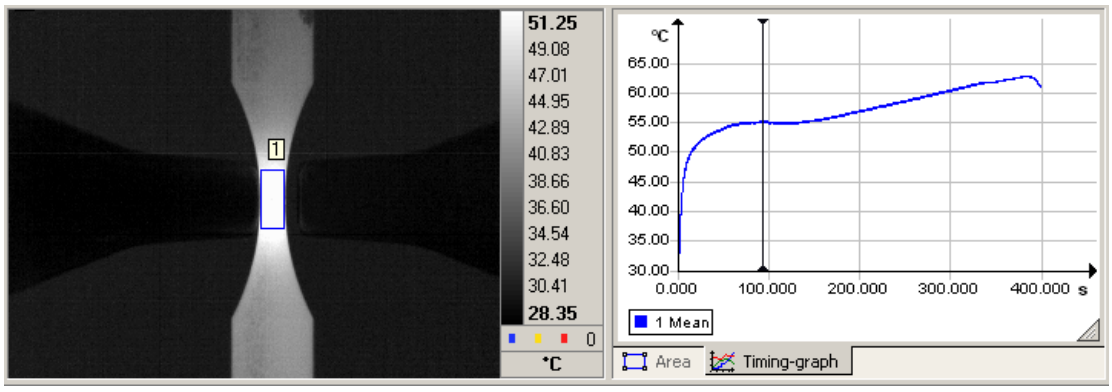

Figure 2.51. Temperature measure on R5 steel at 400 MPa, R=–1, 20 kHz with air cooling.

3.4. R5 steel fatigue results

Two types of fatigue tests were carried out on R5 steel: Crack initiation tests and crack growth tests. The methodology was described in Sections 1.1.6 and 1.2.3.

In next sections, the results of these fatigue tests are presented and analyzed; *S-N* curves for fatigue crack initiation tests and d*a*/d*N* curves for fatigue crack growth tests.

3.4.1. Crack initiation tests without any corrosion

The crack initiation tests results presented in this section were obtained by using the staircase method. The fatigue strength in the gigacycle regime is determined and compared for the different testing conditions. The fatigue curves showing the results present also the models of *S-N* curves determined by using ESOPE software [17], presenting the same models explained in Section 2.4: Wöhler and Basquin.

3.4.1.1. Tension-compression: R=−1

The fatigue results of R5 steel without any corrosion tested in air and room temperature, at R=−1 and 20 kHz are presented in Figure 2.52 and Figure 2.53. The data and staircase are presented in Annex 7. Figure 2.52 and Figure 2.53 show in the same way the *PSN* curves for the Wöhler and Basquin models respectively. The bold line represents the average curve which corresponds to p_s=0.5 (50% of survival probability). The dashed lines represent the survival probabilities p_s=0.16 and p_s=0.84.

The fatigue strength at 10^9 cycles determined by staircase method is 381 MPa with a calculated standard deviation of 7.4 MPa. Fatigue strength at 10^9 cycles can be compared with the fatigue strength at 10^6 cycles observing a difference around 50 MPa. This is in agreement with the mentioned in Section 2.1 of Chapter I for 4240 steel, bearing steels, rail steel, spring steels, and martensitic stainless steel exhibit a high slope of the *S-N* curve in the gigacycle regime, with differences between the fatigue strength at 10^6 cycles and 10^9 cycles comprised between 50 and 200 MPa. Then, it is noted for R5 steel does not exhibit an asymptotic behavior after 10^6 cycles.

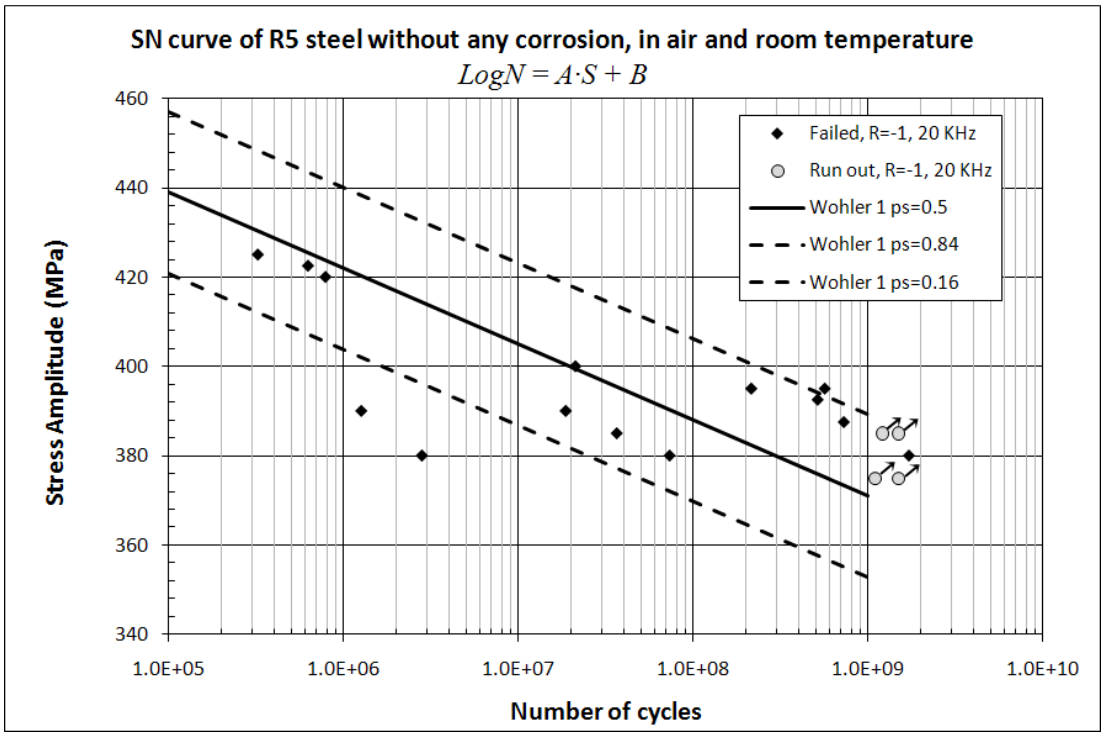

Figure 2.52. Wöhler *PSN* curve for R5 steel without any corrosion at R=-1 in air and room temperature.

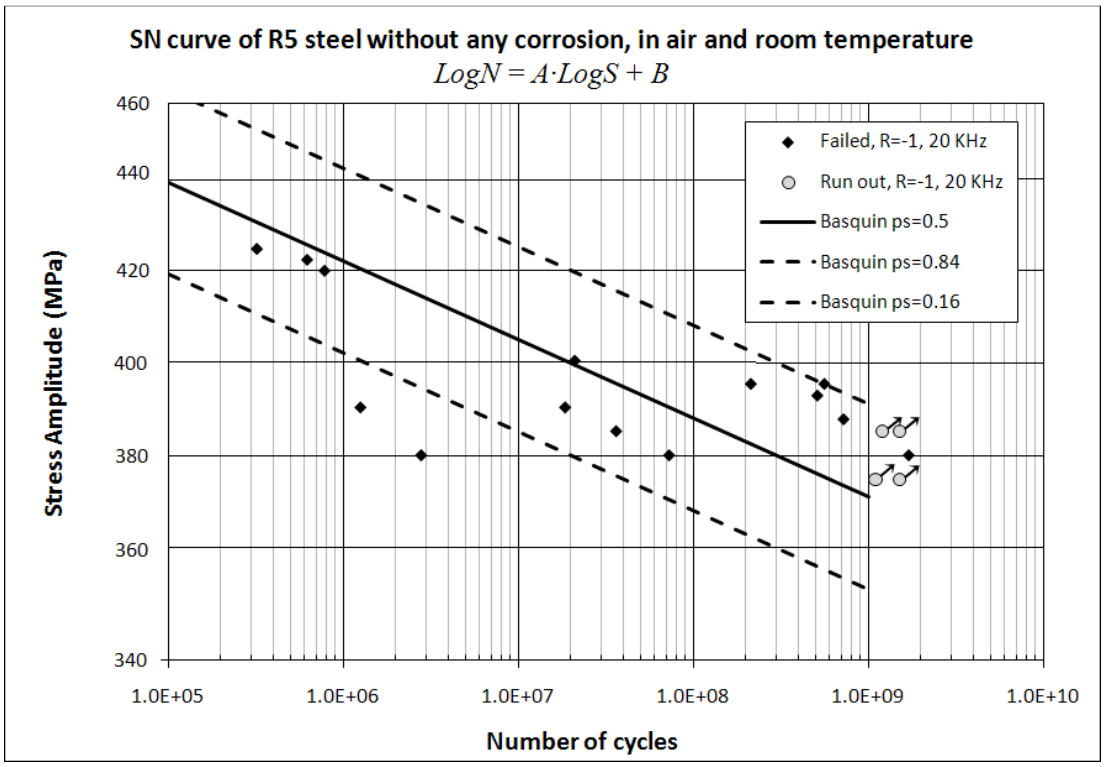

Figure 2.53. Basquin *PSN* curve for R5 steel without any corrosion at R=-1 in air and room temperature.

3.4.1.2. Tension-tension: R=0.3

Figure 2.54 show the *S-N* curve for R5 steel without any corrosion at R=0.3 in air and room temperature. The detailed table of results and staircase data are presented in Annex 7.

The staircase results show that fatigue strength at 10^9 cycles is 270 MPa. The standard deviation is 4.5 MPa.

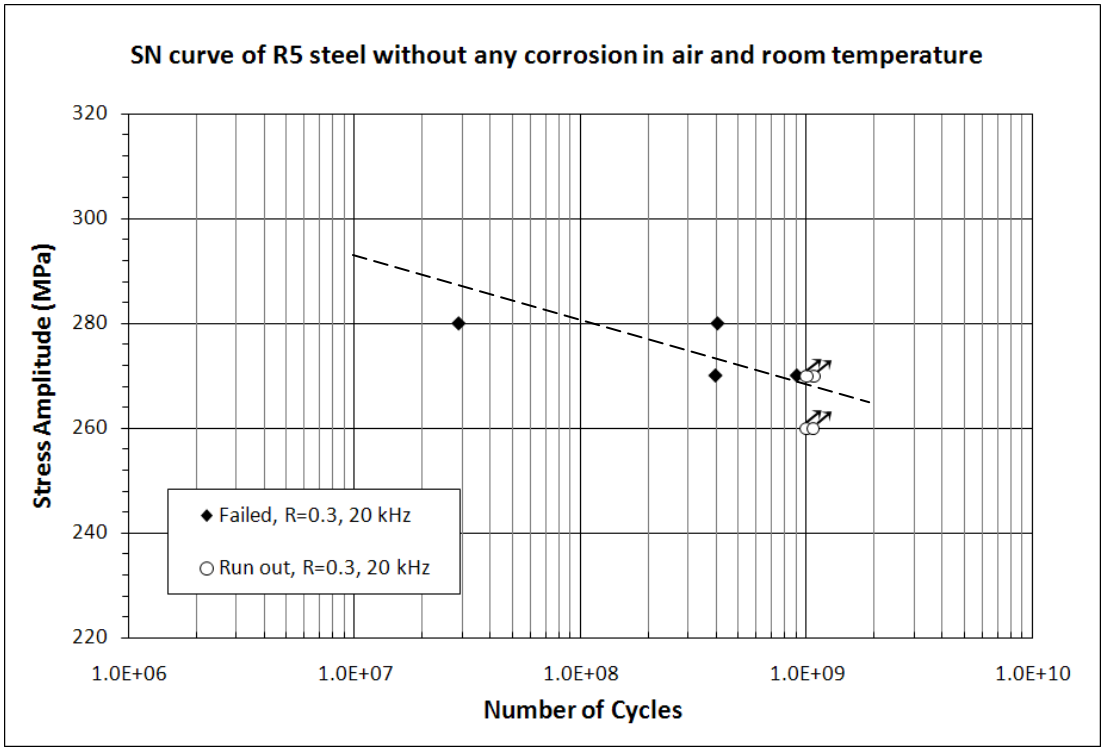

Figure 2.54. *S-N* curve for R5 steel without any corrosion at R=0.3 in air and room temperature.

Due to the small number of specimens available for this test, it was not possible to indentify the parameters of equations of the models as Wöhler or Basquin. The dashed line in Figure 2.54 is a hypothetical idea of the possible fatigue behavior of R5 steel at R=0.3 at room temperature.

It is very possible that the fatigue curve does not have an asymptotic behavior with these testing conditions, between 10^6 and 10^9 cycles and the difference would be around 35 MPa in stress amplitude.

3.4.2. Effect of corrosion on fatigue crack initiation

Two types of corrosion were induced in the specimens for fatigue crack initiation tests: Pre-corrosion and corrosion with sea water in situ. The process of pre-corrosion is explained in Section 3.1. Corrosion in real time with artificial A3 sea water has been carried out by using the machine configuration explained in Section 1.1.5. This is representative of the "splash zone" on the mooring chains: where the chain is between air and sea water. When the determination of Wöhler and Basquin models is possible, they are represented in the *S-N* curves.

3.4.2.1. Crack initiation with pre-corrosion: R=-1

Fatigue crack initiation tests were carried out under fully reversed tension on R5 steel pre-corroded specimens. The pre-corrosion process is explained in the Section 1.1. The data results and staircase data are presented in Annex 7.

Figure 2.55 shows the *S-N* curve for R5 steel with pre-corrosion, in air and room temperature.

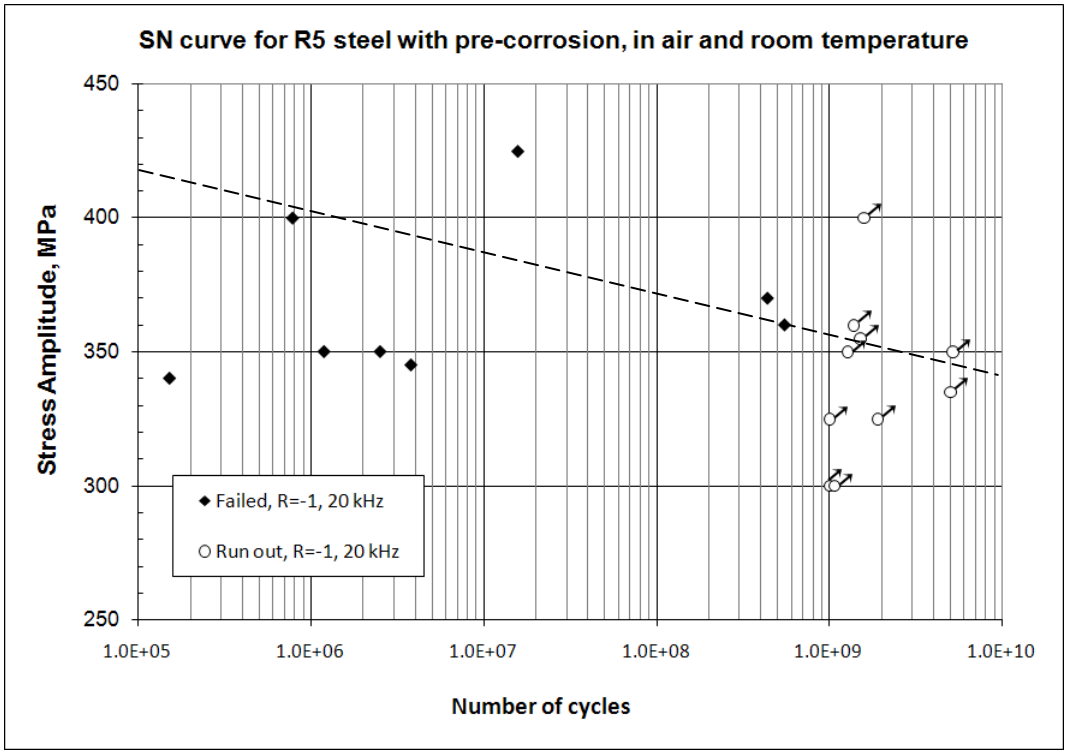

Figure 2.55. SN curve for R5 steel with pre-corrosion at R=-1, in air and room temperature.

According to the staircase results, the fatigue strength at 10^9 cycles is 360 MPa. If this is compared with the fatigue strength of R5 steel without any corrosion the difference is about 21 MPa. The standard deviation is non estimable due to scattering of results. In this case it was not possible to indentify a model as Wöhler or Basquin due to the strong scattering of the results.

Tracing a hypothetical line according to the distribution of the results it is possible to figure up an idea of the fatigue behavior of R5 steel with pre-corrosion at R=–1.

Following this hypothetical line, one can think that fatigue strength at 10^6 cycles is around 400 MPa. Such fatigue strength is 25 MPa lower than fatigue strength at 10^6 cycles of R5 steel without any corrosion. Therefore, it is possible to think in a shift down of the pre-corrosion *S-N* curve of about 20 to 30 MPa in relation to the *S-N* curve without any corrosion.

3.4.2.2. Crack initiation with artificial sea water in situ: R=-1

Figure 2.56 shows the results for R5 steel at R= –1 in sea water flow in situ, at room temperature. The table of data and results are reported in Annex 7. Figure 2.57 and Figure 2.58 show the indentified *PSN* curves according with the Wöhler and Basquin models respectively.

It is observed a drastic reduction on the fatigue strength due to strong corrosion effect of the sea water flow. The effect of the sea water in the very high cycle fatigue regime is very important. However, the fatigue strength at 10^7 cycles is around 340 MPa, around 50 MPa lower compared with pre-corroded specimens at the same number of cycles. Thereafter, the fatigue strength decreases significantly as the life is approaching the gigacycle regime. The fatigue strength at 3×10^8 cycles is only 100 MPa while a 10^9 cycles is around 40 MPa. This decrement is very important compared with specimens without corrosion or even with pre-corroded specimens.

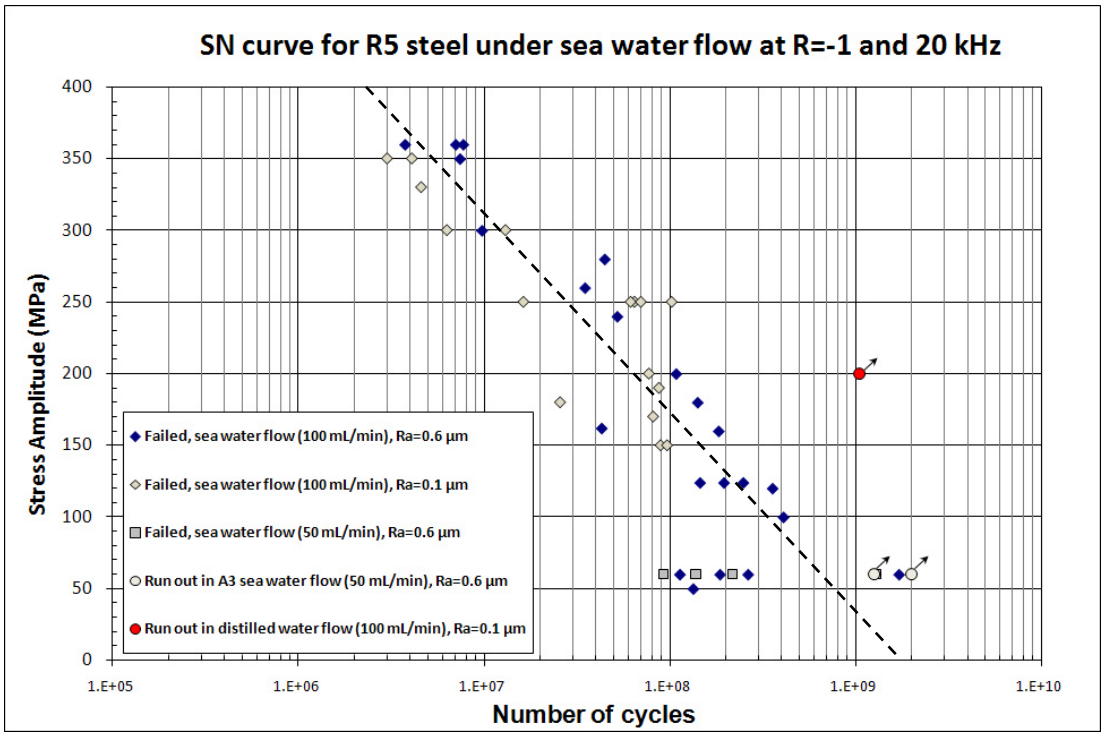

Figure 2.56. SN curve for R5 steel at R=-1, in sea water flow and room temperature, results with two flow rates and two surface conditions.

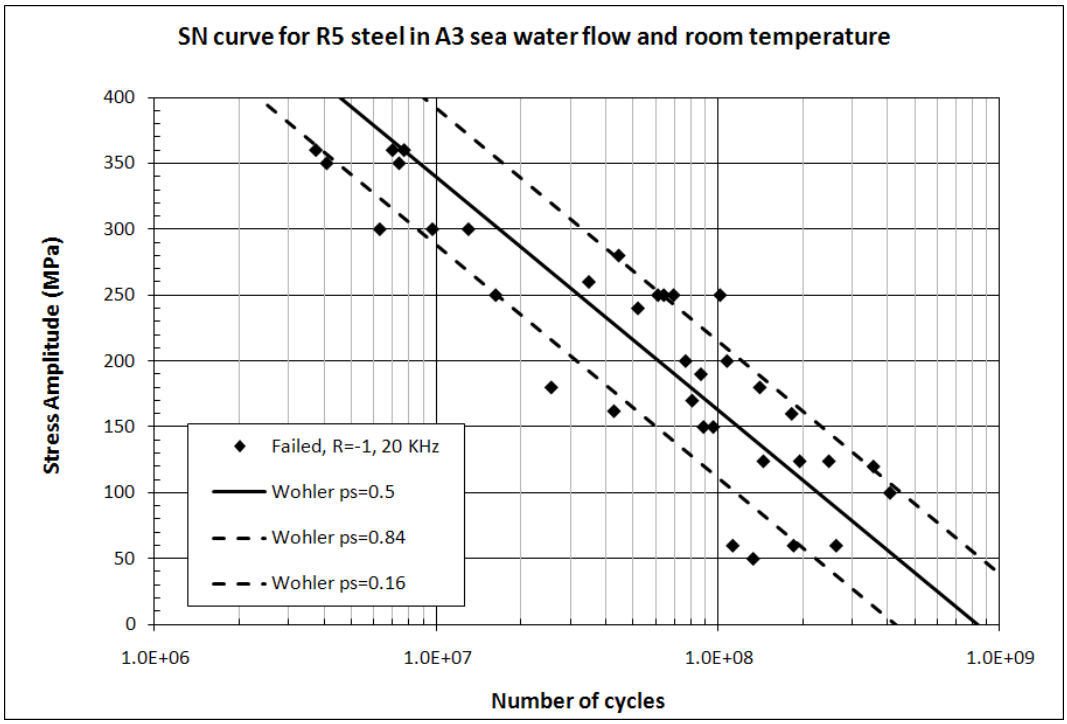

Figure 2.57. Wöhler PSN curve for R5 steel at R=-1, in sea water flow and room temperature.

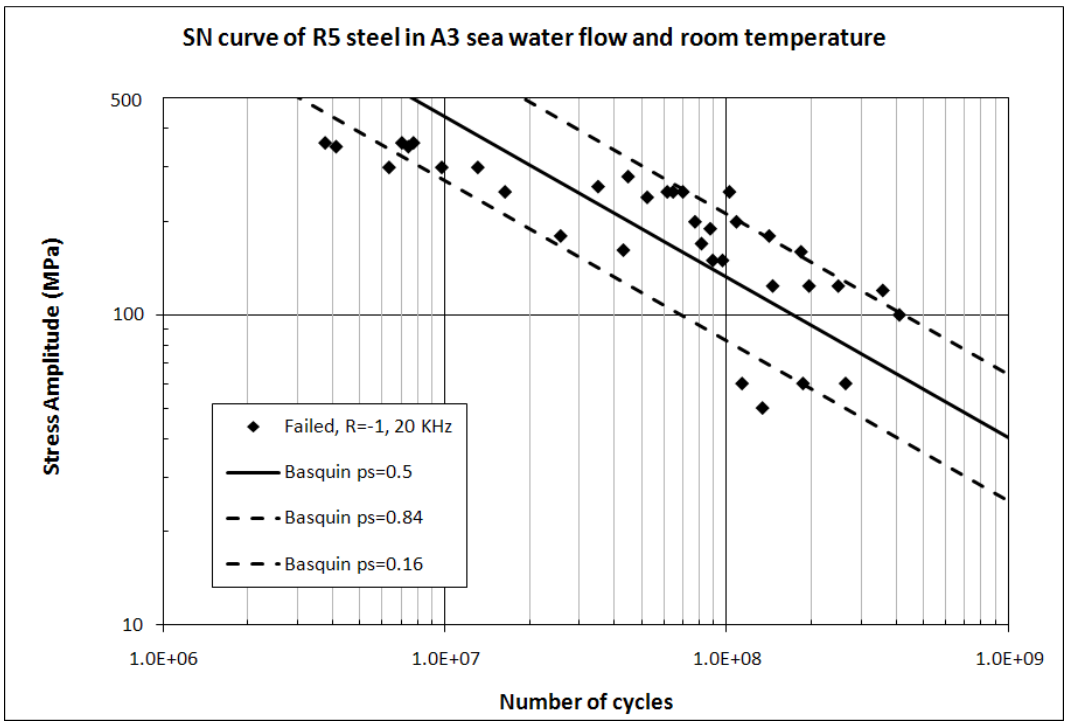

Figure 2.58. Basquin PSN curve for R5 steel at R=-1, in sea water flow and room temperature.

On the other hand, the effect of sea water flow rate was investigated by changing the flow rate during five experiments with a lower flow rate, that induces a less aggressive environment around the specimen. With changing the flow rate of the sea water to 50 mL/min, two not broken specimens after 10^9 cycles were obtained at very low stress levels (round empty points in Figure 2.56). Nevertheless, they seem to lie in the same distribution of fatigue results than tests with sea water flow rate 100 mL/min.

Finally, one specimen with surface roughness Ra=0.1 µm was tested under distilled water flow (non-corrosive) at a stress amplitude σ_a=200 MPa with the intention that it fails around 10^8 cycles. The results of these tests were very significant, because no fracture was observed after 10^9 cycles (Figure 2.56). ***This confirms a coupling between fatigue and corrosion***.

3.4.2.3. Surface roughness effect on fatigue strength under sea water flow

Initially, specimens with the same geometry described in Figure 2.46 with a surface roughness Ra=0.6 µm were tested using artificial A3 sea water flow of 100 mL/min.

Many questions have been arisen about the surface effect on the fatigue strength of metallic materials. It is said that materials with better surface roughness have higher fatigue strength than materials with bad surface roughness. But, in corrosion fatigue of steels and in the high cycle regime there is no much information about surface roughness effect.

Itoga et al [19] have shown that surface roughness has an effect on the fatigue strength without corrosion in high strength steel (Ni-Cr-Mo) in the low cycle regime (10^5 cycles). On the contrary, after 10^7 cycles there is no discernible difference in fatigue strength indicating any roughness effect.

In order to observe the effect of the specimen surface, specimens with the same geometry with a better surface roughness Ra=0.1 µm were tested at the same sea water flow rate. It was observed that surface finishing of the specimen does not affect the fatigue behavior under simultaneous cyclic loading with sea water corrosion (as shown in Figure 2.56)

3.4.2.4. Corrosion with and without cyclic loading.

A coupling between sea water corrosion and mechanical loading as cause of the strong detriment on the fatigue strength in the high cycle regime is presumed due to the fatigue results presented before. It is supposed that corrosion process has a behavior very different if cyclic loading is applied, and it was proved that fatigue strength is higher if the corrosive environment is absent.

To better understand this, two experiments were carried out. First, specimens without any corrosion were submitted to sea water corrosion in the same corrosion cell which has been used for crack initiation tests under sea water flow with the difference that vibration was not applied.

After, one cylindrical specimen calculated in order to vibrate at 20 kHz was tested under sea water flow in order to check how corrosion is developed on the specimen surface depending on the zone. Here, we must remember that in a cylindrical bar, the strain and stress are variable as function of length, because at resonance no wave propagates along the specimen but a stationary regime is present.

Corrosion with sea water flow without cyclic loading.

Three tests on R5 steel under same sea water flow rate (100 mL/min) than crack initiation tests in sea water flow were carried out but without cyclic loading. Temperature was the same room temperature. Specimens without any corrosion and roughness Ra=0.1 µm were placed in the sea water corrosion cell at three different times corresponding to 10^7, 10^8 and 10^9 cycles as shown in Table 2.16. The objective is to observe the amount of corrosion pitting that occurs at the different times.

Test	Life	Corresponding time at 20 kHz
1.	10^7 cycles	8.33 min = 8 min 20 s
2.	10^8 cycles	83.33 min = 1 h 23 min 20 s
3.	10^9 cycles	833.33 min = 13 h 53 min 20 s

Table 2.16. Corresponding time to number of cycles at 20 kHz.

The results are the next:

Test 1: After 8 minutes 20 seconds there were not changes practically in the specimen surface, after an immediate cleaning of the specimens the SEM observation of the surface showed some salt spots but any pits (Figure 2.59).

Test 2: After 1 hour 23 minutes and 20 seconds the changes in the specimen surface were minimum. The observations show that some traces of corrosion appear on the specimen surface but they are only patches and not really pits (Figure 2.60).

Test 3: After 13 hours 53 minutes and 20 seconds the changes in the specimen surface were noticeable. Traces of corrosion are observed, corrosion pits are in both sides of the specimen (Figure 2.61).

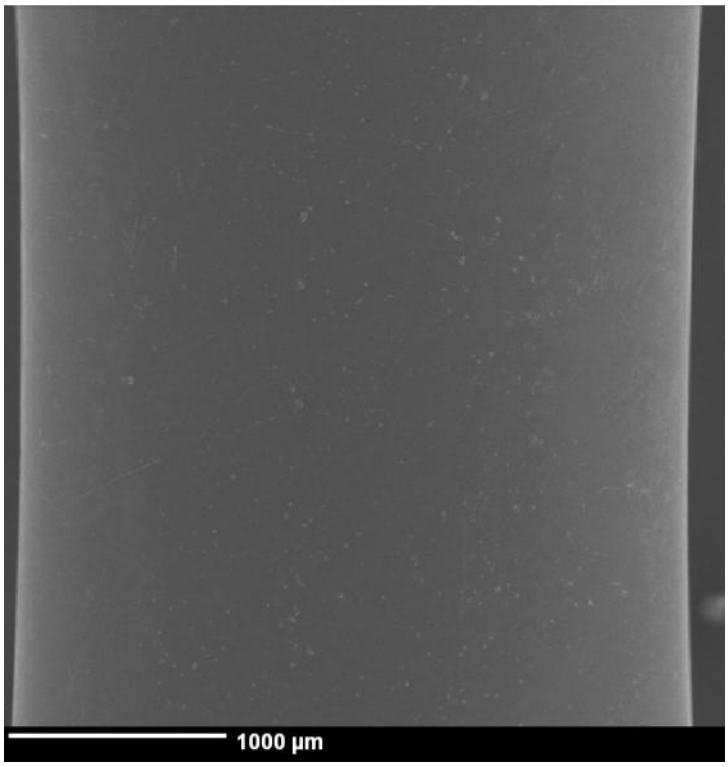

Figure 2.59. Specimen surface after 8 min 20 s under A3 sea water flow (100 mL/min).

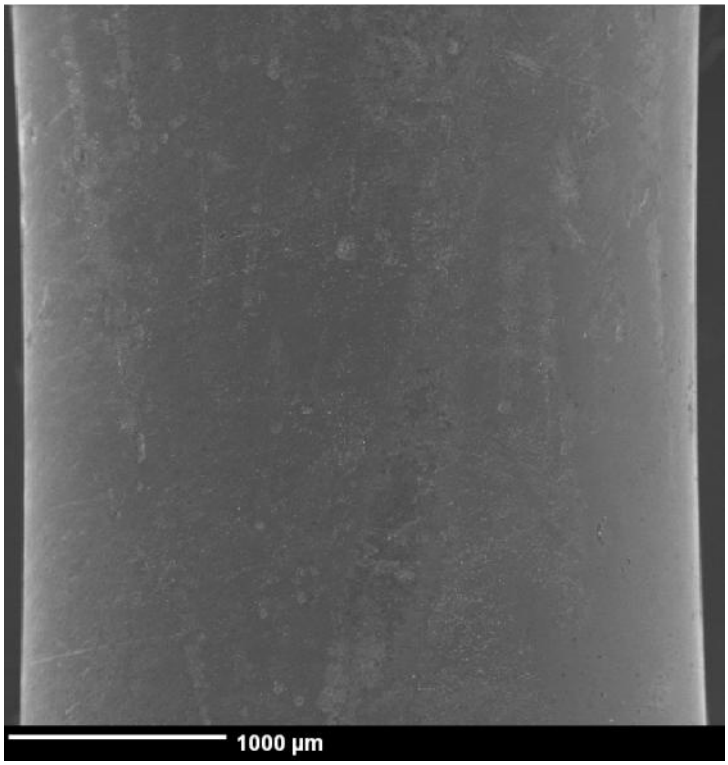

Figure 2.60. Specimen surface after 1 h 23 min 20 s under A3 sea water flow (100 mL/min).

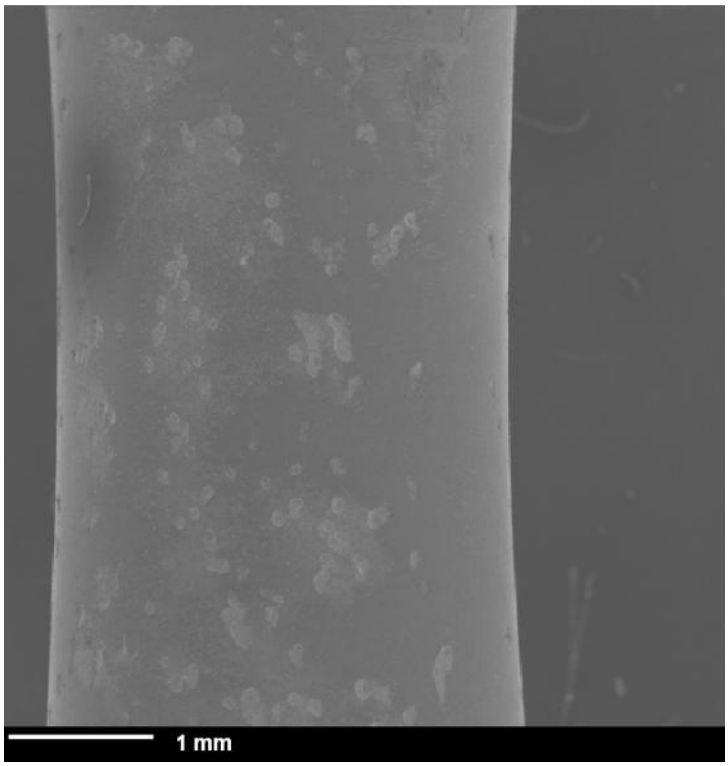

Figure 2.61. Specimen surface after 13 h 53 min 20 s under A3 sea water flow (100 mL/min).

It is difficult to determine an exact distribution of the pits when they exist. But, the size of the pits created by sea water flow vary from 30 (Figure 2.62 left) µm to 60 µm around (Figure 2.62 right) if specimen is under sea water flow during 13 h 53 min 20 s.

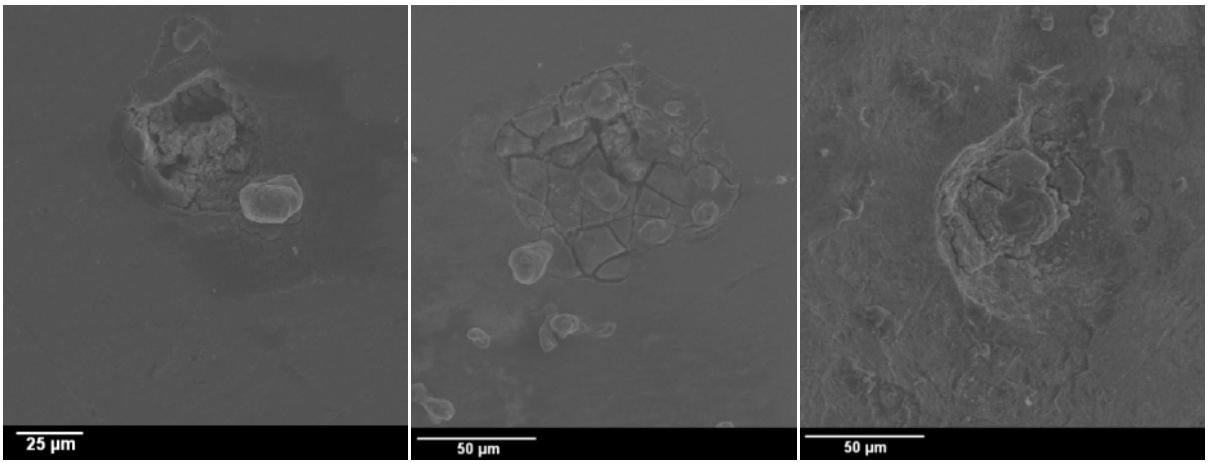

Figure 2.62. Different dimensions of the pits after after 13 h 53 min 20 s under A3 sea water flow without cyclic loading.

If these pits are compared with the pits created with cyclic loading and sea water flow simultaneously they are almost in the same order of size with the pits created at 5×10^7 cycles (Figure 2.63) which have lasted around 42 min. Longest fatigue tests carried out at low stress levels had pits around 80 to 200 µm on the specimen surface in around 3 h.

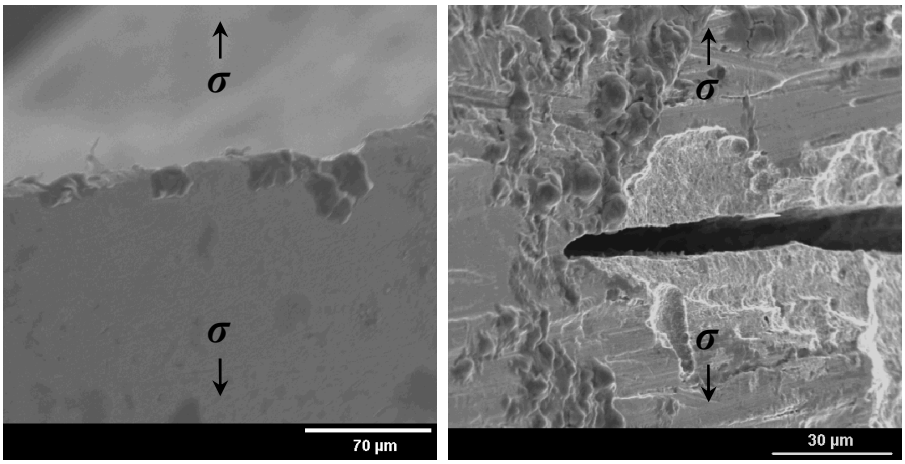

Figure 2.63. Corrosion pits created during cyclic loading and simultaneous sea water flow (specimens with fatigue lives ~5×10^7 cycles).

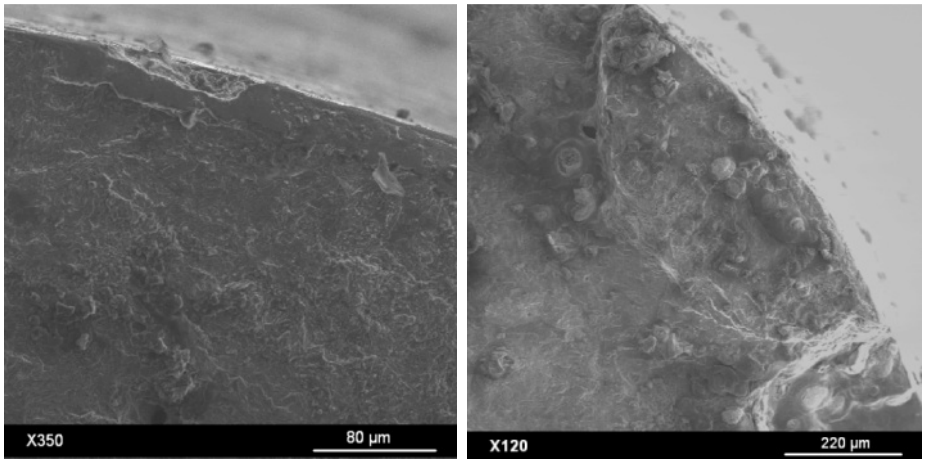

Figure 2.64. Corrosion pits created during cyclic loading and simultaneous sea water flow, view perpendicular to applied stress (specimens with fatigue lives ~2×10^8 cycles)

Therefore, it is clear that the process of corrosion pitting has a coupling with the cyclic loading. No pitting corrosion appeared after 1 h 53 min on a R5 specimen under sea water flow without cyclic loading, but with cyclic loading, pitting appeared in only 42 min. This is a complex mixed mechanism that remains unknown in detail and can be explained in further works.

Corrosion with sea water flow during cyclic loading in a cylindrical bar.

A cylindrical specimen designed to work in resonance in ultrasonic fatigue machine (20 kHz) was submitted to cyclic loading under sea water flow simultaneously (100 mL/min) in order to check how corrosion is developed on the specimen surface depending on the stress amplitude. The specimen geometry is presented in Figure 2.65.

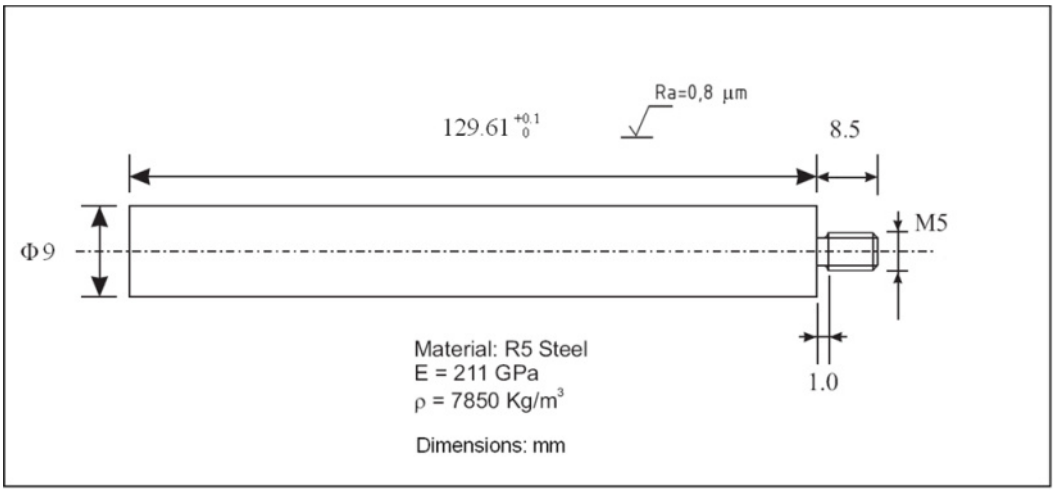

Figure 2.65. Dimensions of a R5 steel cylindrical test bar for gigacycle fatigue.

Recalling to Figure 1.14 (Section 2.3 of Chapter I) a one-dimensional straight cylindrical specimen excited axially at one end certain displacement amplitude at the resonance frequency has on the central section a node of zero displacement and maximum strain and stress. The strain varies depending of the position along the specimen length. At the extremes of the specimen strain/stress is zero.

The specimen was placed into the corrosion cell trying that sea water wet all the length of the specimen as shown in Figure 2.66.

The specimen was tested at R=-1, σ_a=120 MPa, room temperature, in A3 sea water flow (100 mL/min) at 20 kHz. These testing conditions were chosen with the intention of specimen fails around 10^8 cycles, according to the results presented in Figure 2.56.

The specimen failed at N_f=7.37×10^7 cycles. This number of cycles is in agreement with previous results on smooth specimens (Figure 2.56). A crack was found in the specimen at around 58 mm from the free side (end) of the cylindrical specimen (Figure 2.68).

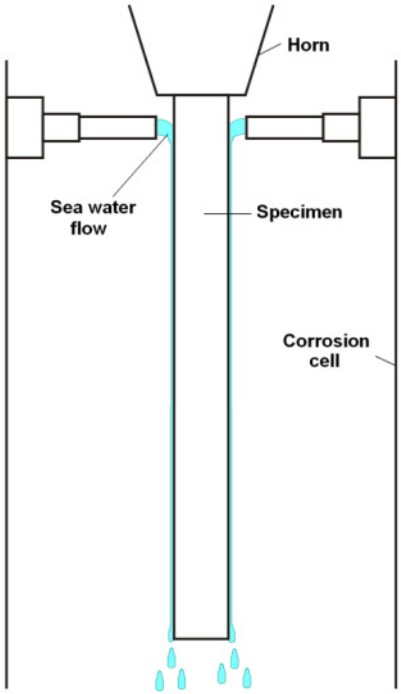

Figure 2.66. Scheme of positioning of the specimen for testing under sea water flow.

The specimen was divided in 13 sections of around 10 mm each one, in order to observe it at the optical microscope. Figure 2.67 shows a scheme of this division. It is needed to have an idea of the strain and stress at each zone number. This can be calculated with the Equations (1.31) and (1.32) presented in Section 2.3 of Chapter I. The calculated stresses along the specimen are presented in Figure 2.67.

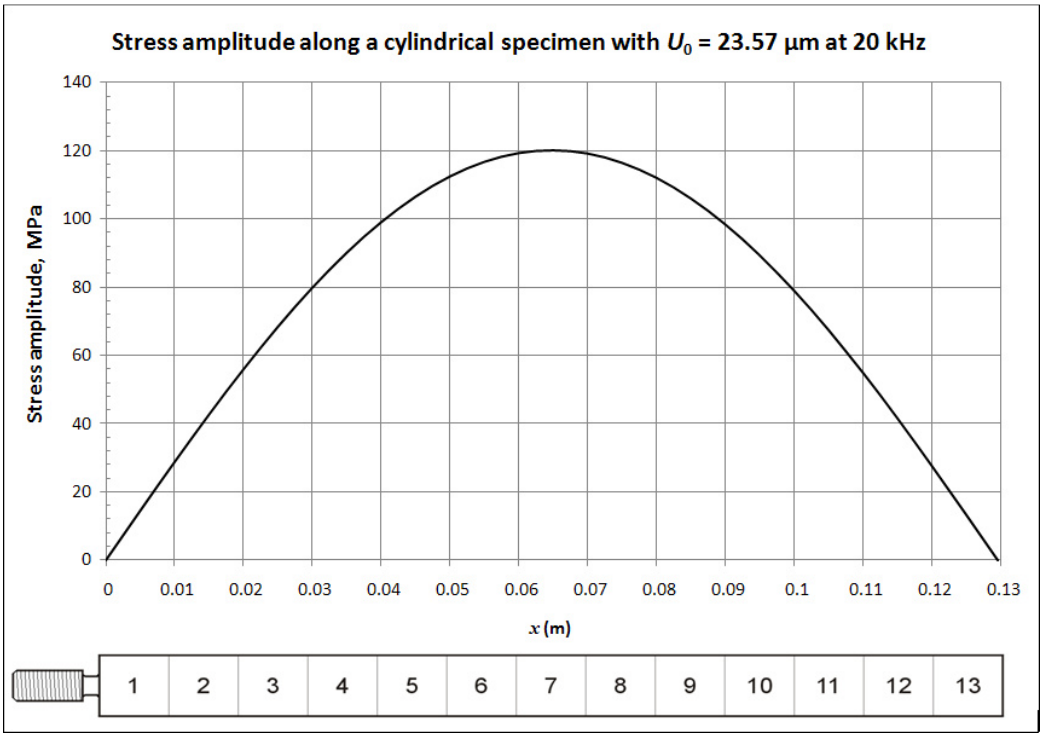

Figure 2.67. Stress at the divisions of a cylindrical specimen applying 23.57 µm at 20 kHz.

Table 2.17 shows analysis of observation by optical microscopy.

Zone	σ_a,MPa	Pit density, units/282.7 mm^2	Pit size, mm	Observations
1	0 – 28	-	-	This area was not touched by sea water due to the distance needed to attach the specimen to the horn.
2	28 – 56	-	-	Pits were not observed. This area was not touched totally for the same reason than zone 1.
3	56 – 80	320	0.005 – 0.01	Pits are very dispersed
4	80 – 99	300	0.01 – 0.02	Bigger pits than previous zone
5	99 – 112	280	0.01 – 0.015	-
6	112 – 119	260	0.015 – 0.022	Less concentration than zone 5 but bigger pits
7	119 – 119	240	0.01 – 0.025	-
8	119 – 112	230	0.01 – 0.05	Here appeared the crack
9	112 – 99	180	0.005 – 0.04	-
10	99 – 80	160	0.01 – 0.02	-
11	80 – 56	150	0.005 – 0.01	-
12	56 – 28	100	0.01 – 0.03	Some traces of layer oxides
13	28 – 0	90	0.005 – 0.02	In the rest of the areas sea water flows down and the layer is thin. In this section specially a thicker layer of sea water stayed. But even like that, concentration of pits is not high, although pits are big.

Table 2.17. Observations at each zone of cylindrical specimen tested at σ_a=120 Mpa, 20 kHz.

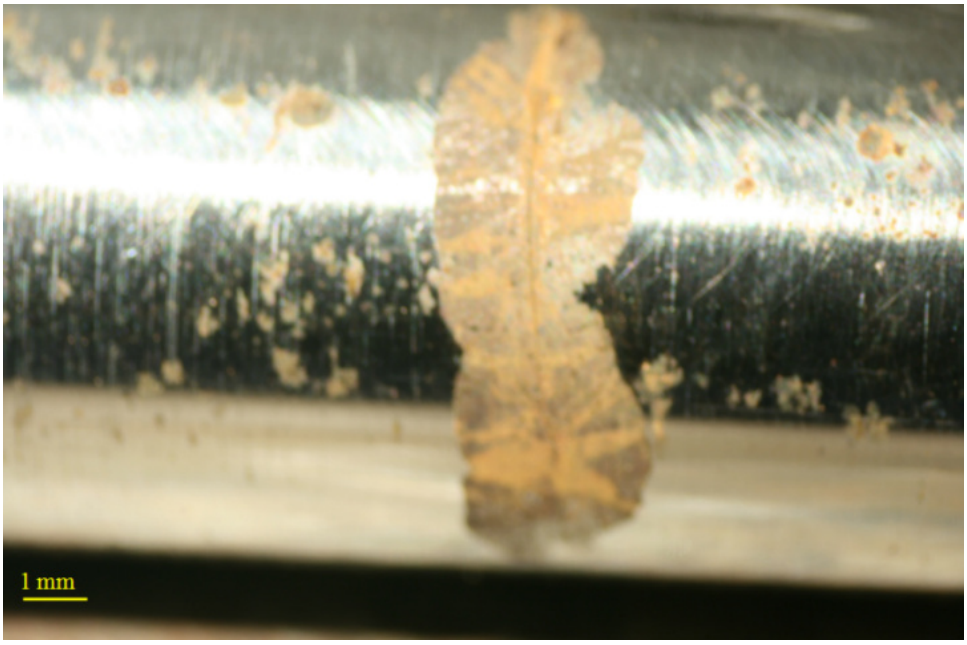

Figure 2.68. Image of the section 8 where crack was found.

The previous analysis allowed appreciating the interaction between cyclic loading and corrosion process. First, it was observed that corrosion pitting created by sea water flow was not the same when cyclic loading was not applied than when it was. After, corrosion pitting was stronger in the section of the specimen where stress and strain amplitude is maximal. This reveals that a coupling of cyclic loading and corrosion pitting process exists really.

3.4.3. Synthesis of crack initiation results

A resume of fatigue tests results is presented in Table 2.18. In this table are presented the fatigue strength at 10^6 and 10^9 cycles at 20 kHz, in air and in sea water flow at room temperature.

Condition	R	Fatigue strength at 10^6 cycles, MPa			Fatigue strength at 10^9 cycles, MPa			Staircase Std Deviation, MPa	ESOPE Std Deviation, MPa
		amp	mean	max	amp	mean	max		
Without any corrosion	–1	430	0	430	381	0		7.4	18.2
	0.3	~31	~57	~88	270	501	771	4.5	Inestimable
Pre-corrosion	–1	400	0	400	360	0	360	Inestimable	Inestimable
Sea water	–1	~40	0	~40	40	0	40	No calculated	52.1

Table 2.18. Fatigue results of R5 steel at room temperature in air at 20 kHz.

The previous results can be presented graphically in the Haigh diagram in order to observe the effect of mean stress in the tests without any corrosion and the effect of corrosion when exists.

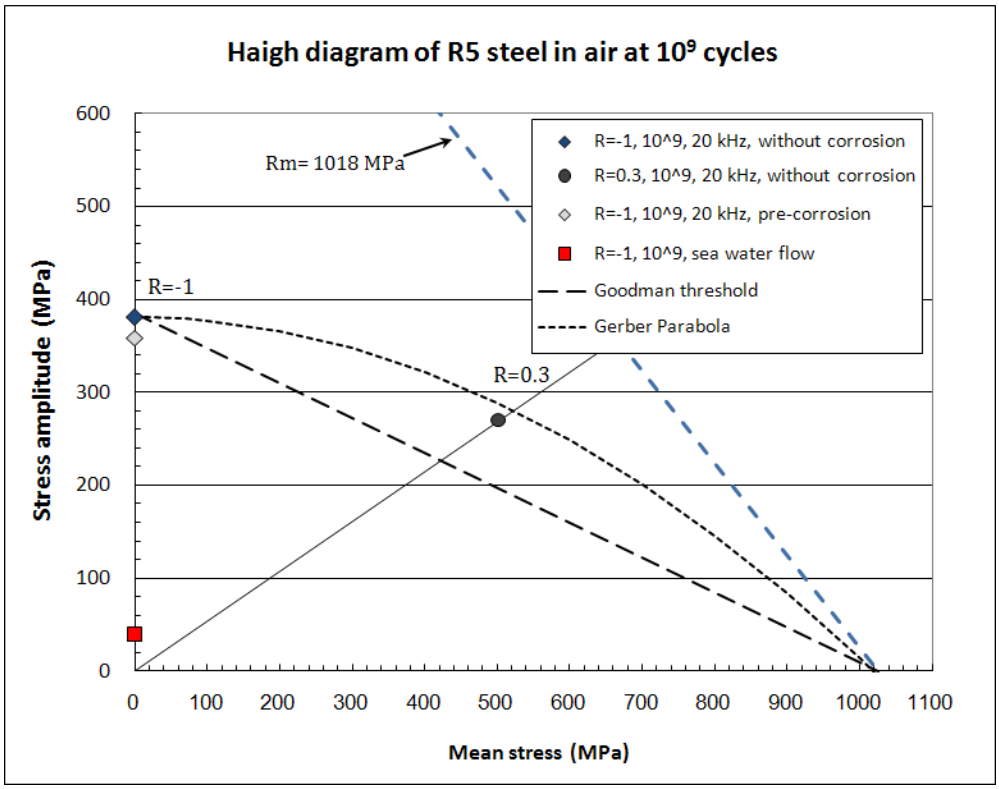

Figure 2.69. Haigh diagram of R5 steel fatigue results in air and room temperature.

Recalling the previous results, it is noted that fatigue strength at 10^9 cycles, R= –1, in air and room temperature, is around 381 MPa without any corrosion and 360 MPa with pre-corrosion. The effect of corrosion is drastic when artificial sea water is put on the specimen surface. The fatigue strength at 10^9 cycles is around 40 MPa only under corrosion with sea water flow. Furthermore, fatigue test on pre-corroded specimens is not representative because not coupling is possible with the corrosion process.

On the other hand, the loading of specimens at tensile mean stress, R=0.3, causes a decreasing of the fatigue strength at 10^9 cycles. The fatigue strength in stress amplitude in this condition is only 270 MPa. It is observed in the Haigh diagram (Figure 2.69) that the fatigue strength of R5 steel without any corrosion does not follows the Goodman threshold but the Gerber's parabola.

It is important to remark that these fatigue results, without any corrosion and with pre-corrosion, have been taken into account for the modification of the DNV-OS-302 standard in 2008 [7]. The fatigue curve presenting the actual and the previous one is shown in Figure 2.70. DET NORSKE VERITAS (DNV) is an autonomous and independent foundation with the objectives of safeguarding life, property and the environment, at sea and onshore. DNV undertakes classification, certification, and other verification and consultancy services relating to quality of ships, offshore units and installations, and onshore industries worldwide, and carries out research in relation to these functions.

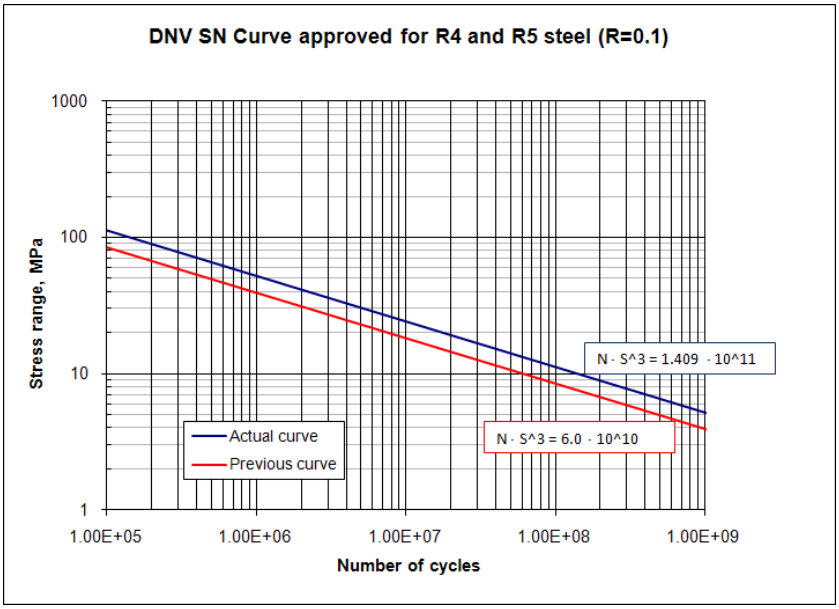

Figure 2.70. S-N curve for R5 steel at R=0.1 according to DNV standard [7].

3.4.4. Crack growth tests results

Following the methodology described in Section 1.2 crack growth tests were carried out at room temperature, R=–1, and 20 kHz, in air and under sea water flow in situ.

Figure 2.71 shows the d*a*/d*N* curve obtained for both conditions, air and sea water corrosion. Due to the difficulty to carry out tests under sea water flow the number of points is less than in air. Nevertheless, it is noted that the crack growth rate is faster in sea water than in air as reported under conventional test frequency (Figure 1.26 of Chapter I)

In air, it is observed that ΔK_{th}≈3.27 MPa√m. On the contrary, under sea water corrosion is difficult to determine a tendency of the results. Two ideas have been traced on the Figure 2.71. The stress intensity threshold is also difficult to determine, but it is probably similar o smaller than in air.

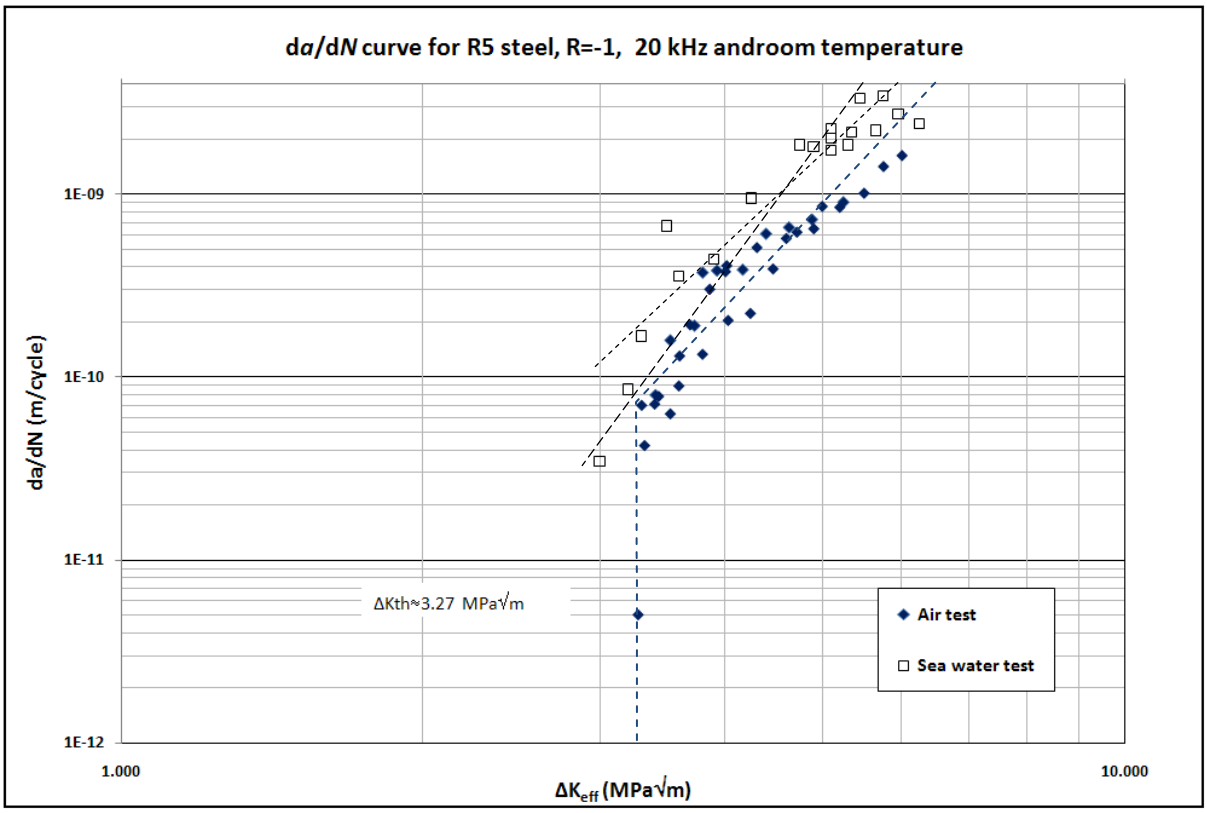

Figure 2.71. d*a*/d*N* curve for R5 steel at R=-1, in air and under sea water flow at room temperature.

These crack growth results are discussed in Chapter IV in order to compare the crack growth rate behavior with the Paris-Hertzberg law and to try to determine the crack growth period duration in the gigacycle regime.

References of chapter II

1. ASTM E45, 2002, *Standard Test Methods for Determining the Inclusion Content on Steel*, American Society for Testing and Materials, Pennsylvania, USA.
2. ASTM G85, 2009, *Standard Practice for Modified Salt Spray (Fog) testing*, American Society for Testing and Materials, Pennsylvania, USA.
3. ASTM E466, 2007, *Standard Practice for Conducting Force controlled Constant Amplitude Axial Fatigue Tests of Metallic Materials*, American Society for Testing and Materials, Pennsylvania, USA.
4. ASTM E606, 2004, *Standard Practice for Strain Controlled Fatigue Testing*, American Society for Testing and Materials, Pennsylvania, USA.
5. ASTM E647, 2008, *Standard Test Method for Measurement of Fatigue Crack Growth Rates*, American Society for Testing and Materials, Pennsylvania, USA.
6. AMS 2301, 2001, *Aircraft Quality Steel Cleanliness: Magnetic Particle Inspection Procedure*, Aerospace Materials Specifications of SAE International, London UK.
7. DNV-OS-302 Standard, 2008, *Offshore Mooring Chains*, Det Norske Veritas, Hovik, Norway.
8. Zun, Z.D., 2000, *Etude du seuil de fissuration à haute fréquence en fatigue et en fretting fatigue*, PhD Thesis, ITMA-CNAM, Paris, France.
9. Wu, T.Y., 1992, *Modélisation de la fissuration en fatigue vibratoire à haute température, applications aux alliages à base de nickel*, PhD Thesis, ECP, France.
10. Wu, T.Y., and Bathias, C., 1994, *Application of fracture mechanics concepts in ultrasonic fatigue*, Engineering Fracture Mechanics, Volume 47(5), pp. 683-690.
11. Bathias, C., Paris, P.C., 2005, *Gigacycle Fatigue in Mechanical Practice*, Marcel Dekker Publisher Co., New York USA.
12. Bathias, C., 2010, *Influence of the metallurgical instability on the gigacycle fatigue regime*, International Journal of Fatigue 32, pp. 535-540.
13. Ranc, N., Wagner, D., Paris, P.C., 2008, *Study of thermal effects associated with crack propagation during very high cycle fatigue tests*, Acta Materialia 56, p.p. 4012-4021.
14. Palin-Luc, T., 1996, *Fatigue multiaxiale d'une fonte GS sous sollicitations combinées d'amplitude variable*, PhD Thesis, ENSAM Bordeaux, France.
15. Koutiri, I, and Morel, F., and Bellett, D., and Augustins, L., 2009, *Effect of high hydrostatic stress on the fatigue behavior of metallic materials*, Proceedings of 12th International Conference on Fracture ICF2009, Otawa, Canada.
16. Lieurade, H.P., 1982, *La pratique des essais de fatigue*, Societé française de métallurgie, PYC Édition, Paris, France, pp. 27-35, 62-99.
17. TECHLAB, 1995, *ESOPE Logiciel pour Windows*, User manual, Metz, France.
18. Bastenaire, F., 1960, *Etude statistique et physique de la dispersion des résistances et des endurances à la fatigue*, PhD Thesis, Paris University.
19. Itoga, H., and Tokaji, K., and Nakajima, and M., Ko, H., 2003, *Effect of surface roughness on step-wise S-N characteristics in high strength steel*, International Journal of Fatigue 25, pp. 379-385

Chapter III. Fractography Analysis and discussion

Table of contents

1. Analysis of AS7G06 cast aluminium alloy results 120
   1.1. Fractography of specimens tested at room temperature 120
      1.1.1. Tension-Compression (R=-1) at room temperature 120
      1.1.2. Tension-Tension (R=0.01) at room temperature 121
      1.1.3. Tension-Tension (R=0.5) at room temperature 124
   1.2. Fractography of specimens tested at 150 °C 126
      1.2.1. Tension-Compression: R=-1 at 150 °C 126
      1.2.2. Tension-Tension (R=0.01) at 150 °C 129
   1.3. Discussion 131
2. Analysis of R5 steel results 134
   2.1. Fractography of specimens tested without any corrosion 134
      2.1.1. Tension-Compression (R=–1) 134
      2.1.2. Tension-Tension (R=0.3) 136
   2.2. Fractography of specimens with corrosion 138
      2.2.1. Tension-Compression (R=-1) with pre-corrosion 139
      2.2.2. Tension-Compression (R=-1) under sea water flow 142
   2.3. Discussion 147

References of Chapter III 151

1. Analysis of AS7G06 cast aluminium alloy results

This section contains the analysis of the fracture surface of the specimens made of AS7G06-T6 cast aluminium alloy tested in gigacycle fatigue. All the fracture surfaces presented hereafter were observed using a scanning electron microscope (SEM) JEOL 840-A at 15 kV. The specimens which did not break totally during the fatigue tests were put several minutes in liquid nitrogen, and then separated in two parts by monotonic quasi-static tension.

1.1. Fractography of specimens tested at room temperature

This section shows fractographies of AS7G06-T6 specimens tested at room temperature and different stress ratios, R. At this moment, it is important to remark that it has been observed that temperature in the specimen during testing is around 20 °C without any air cooling. Even if a small temperature increase of the specimen during the fatigue test was possible (some degrees Celsius) it was not more than 25 °C, we consider that this does not change significantly the mechanical behavior, crystallographic properties and the crack initiation and fracture mechanisms.

1.1.1. Tension-Compression (R=-1) at room temperature

Figure 3.1 and Figure 3.2 show the fracture surface of an ASG06-T6 specimen tested at R=–1 in air and room temperature. It has to be noticed that crack initiates at shrinkages near the specimen surface. This is characteristic in all the fractured specimens observed during this work. Furthermore, it is observed that rupture by quasi-cleavage occurs in some zones around porosities. This was observed before by C. Bathias et al [1] for the same alloy.

In these zones quasi-cleavage slip bands can be distinguished (arrows in Figure 3.2). The same kind of fracture characteristics have been observed by Ammar et al [2] in the megacycle regime for a A356-T6 cast aluminium alloy, which is an alloy very similar to AS7G06-T6. In fact, these authors have pointed out that the presence of porosities is the main cause of fatigue fracture in this kind of alloy, whereas the slip bands are the cause of only a few of crack initiation and then fractures.

Yi et al [3] have studied the same type of alloy A356-T6 at R=–1 and 70 Hz. They found that an important number of microstructural features and defects can be responsible of crack initiation in this alloy, including porosities, oxide films around defects, and a feature that consists of Al-matrix and associated Si-particles, that they called “micro-cell”. These characteristics are not observed in our fractographies, but porosities and slip bands are present. We assume that they play a competition in the fracture of the specimen.

In this case it is possible to indentify a crack initiation site, but sometimes the fracture surface showed a complex feature, and probable sites were identified.

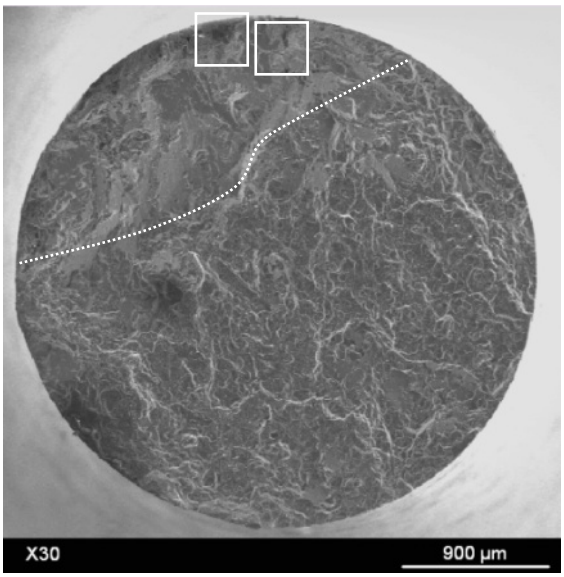

Figure 3.1. Fracture surface of a specimen tested at R= –1 in air and room temperature, σ_a=85 MPa, N_f =6.9×10^7 cycles

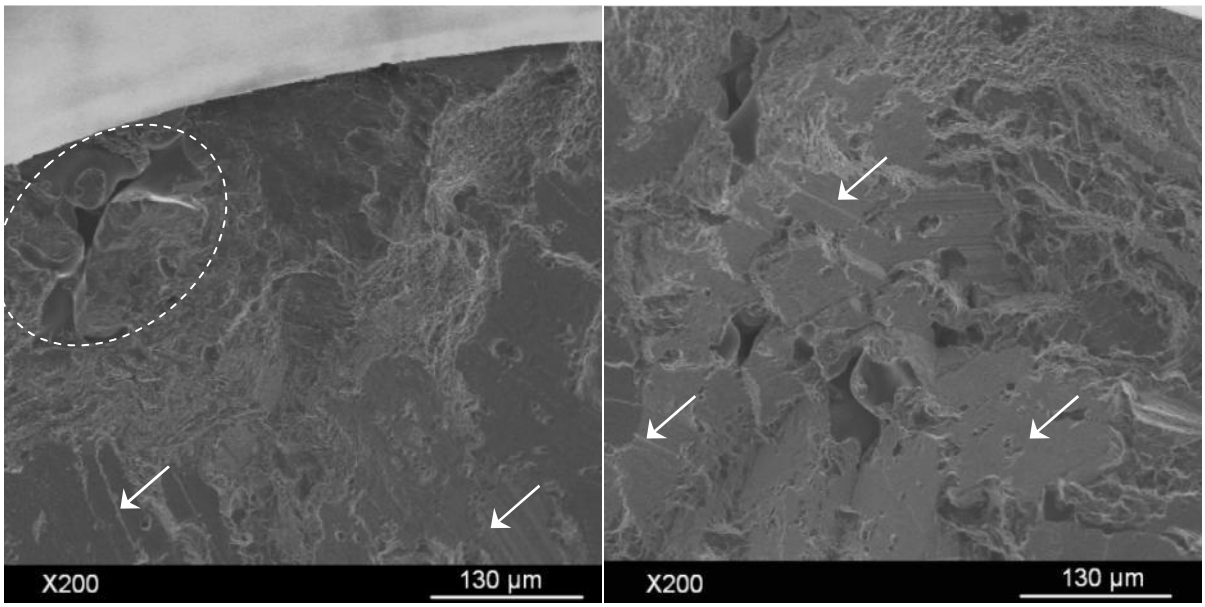

Figure 3.2. Details of the Figure 3.1.

1.1.2. Tension-Tension (R=0.01) at room temperature

Figure 3.3 and Figure 3.4 show the characteristic fracture surface in tests at R=0.01 and room temperature. In this case the shrinkages are located at the specimen surfaces internally and they cause the crack initiation. Slip bands are more visible (Figure 3.4 right) compared to the fracture surface of specimens tested under fully reversed loading (R= –1) and room temperature. Indeed, under R=0.01 and any other positive value of the R ratio, the fracture surface is not "damaged" by the compression part of each loading cycle (no friction of the crack lips), observations are then easier.

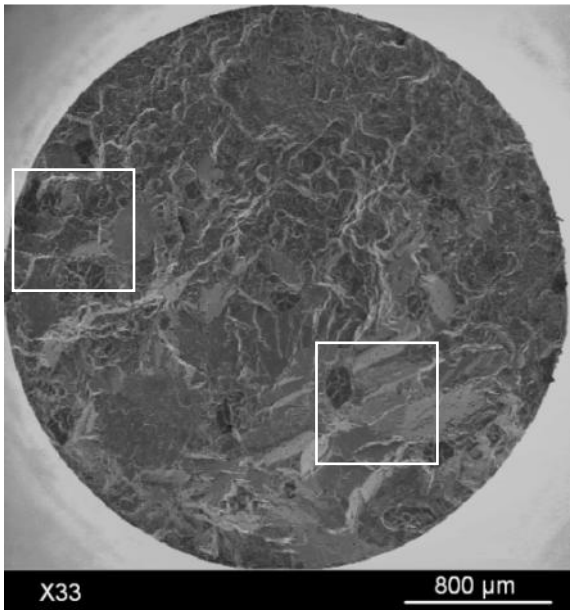

Figure 3.3. Fracture surface of the specimen tested at R=0.01, in air and room temperature, σ_a=50 MPa, N_f =6.38×10^8 cycles.

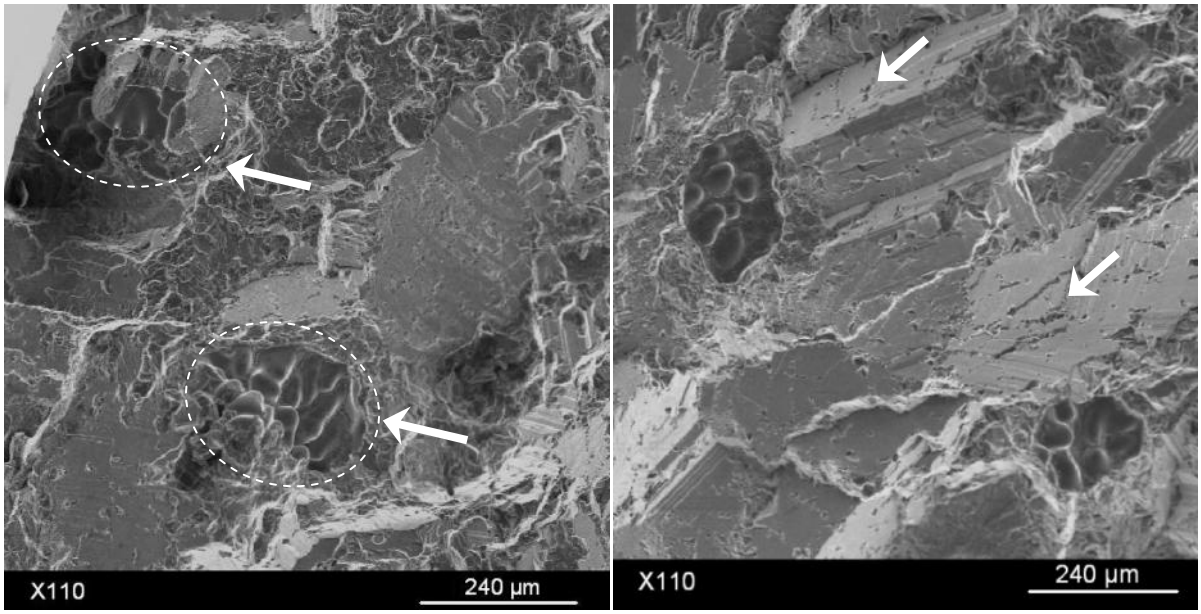

Figure 3.4. Details of the fracture face remarked in Figure 3.3, slip bands in arrows.

Figure 3.5 and Figure 3.6 show the fracture faces for lower stress amplitude compared with the specimen in Figure 3.3. This time, the number of cycles was smaller. That can be related to the size of the pores contained in the specimen. Ammar et al [2] carried out fatigue tests in the megacycle regime at the same stress amplitude (R= –1) and they compared the fatigue life as function of the pore size. Fatigue life was lower as the pore size was bigger.

In this case, it is noticeable that quasi-cleavage around the shrinkage zones does not appear like for a specimen with a longer lifespan. It is possible to assume that two fracture mechanisms co-exist and compete.

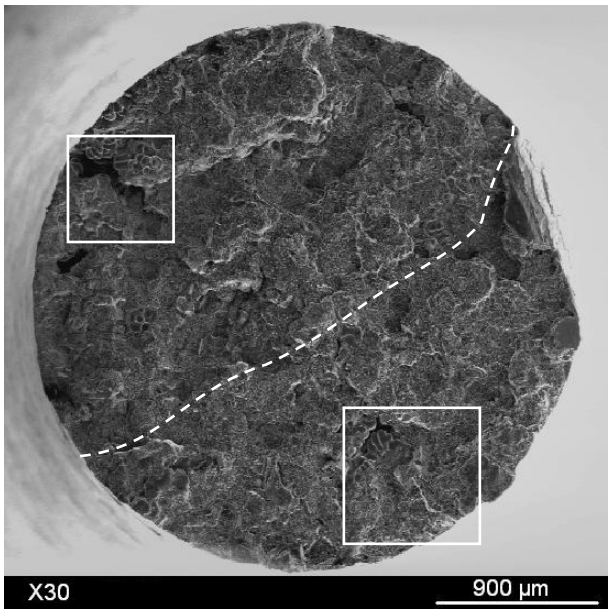

Figure 3.5. Fracture face of a specimen tested at R=0.01, in air and room temperature, σ_a=40 MPa, N_f =4.8×10^7 cycles.

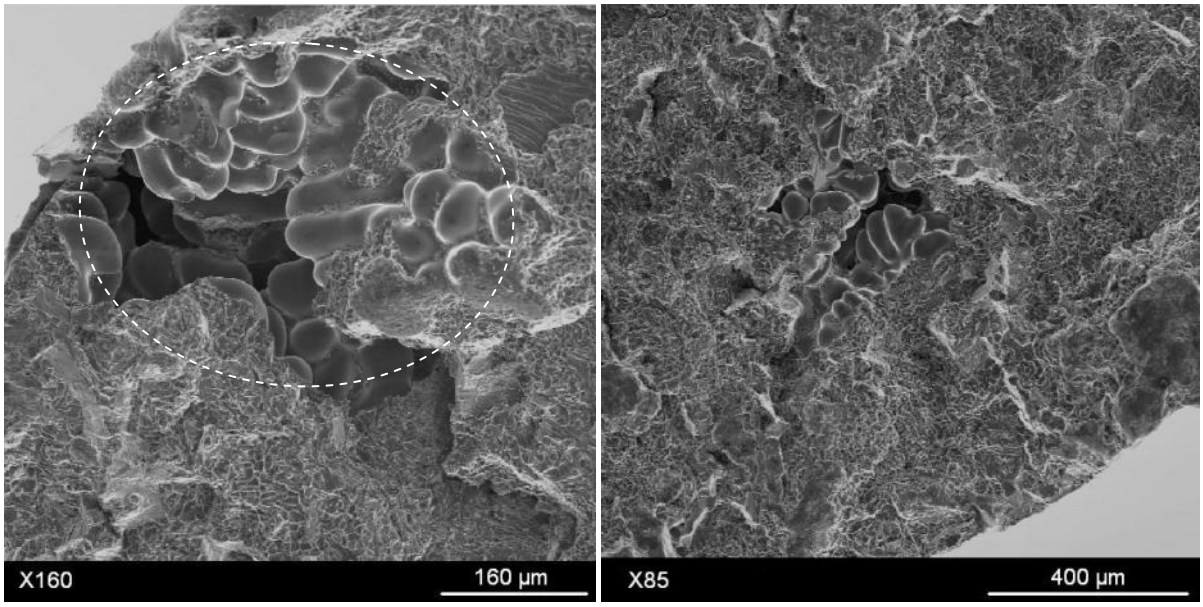

Figure 3.6. Detail for the specimen in Figure 3.5.

The area of pores indicated by arrows in Figure 3.4 (left) and the pore in Figure 3.6 (left) can be measured doing an approximation of their shape to an ellipse. The big pore in Figure 3.6 (left) has an area of 712,230 µm^2 (√area=421.96 µm) while the addition of the two pores in Figure 3.4 (left) gives an area of 255,870 µm^2 (√area=252.8 µm).

1.1.3. Tension-Tension (R=0.5) at room temperature

In Figure 3.7 to Figure 3.10 it is observed that fracture faces at R=0.5 in air and room temperature are different in some aspects in relation to the specimens tested at R= –1 or R=0.01. Quasi-cleavage around the crack initiation sites is less important even at high number of cycles. The crack initiation sites under this loading condition present also porosities as previously but the appearance of a high relief ("strong roughness") makes difficult to observe them.

It is important to note that for R=0.5 the maximum stress in the specimen is close to the tensile strength of the material and surpasses its yield stress. As mentioned by Koutiri et al [4] this fact leads to a change in the fatigue crack mechanisms in cast Al-Si-Mg alloys. According to them, under cyclic loading at common frequency (80 Hz), under high mean stress testing conditions (tension, R=0.95) a large degree of material damage occurs in the first quarter of the cycle (or initial monotonic increase in load). This damage can be described as a local rupture or "material decohesion" in the eutectic zone which contains a large number of silicon particles (harder and more brittlee than the α phase of aluminium dendrites) [4]. On the other hand, at high stress levels it is easier to have localized plasticity causing permanent deformation in slip bands, resulting in localized surface relief (Figure 3.10 left). Such a scenario in our gigacycle fatigue tests is possible. Indeed, for our cast aluminium alloy loaded at its fatigue strength at 10^9 cycles, the maximum stress in each cycle (216 MPa) is close (75%) to the UTS of the alloy (288 MPa), see Figure 2.44 in Chapter II; this is similar to the test conditions in the Koutiri et al. experiments.

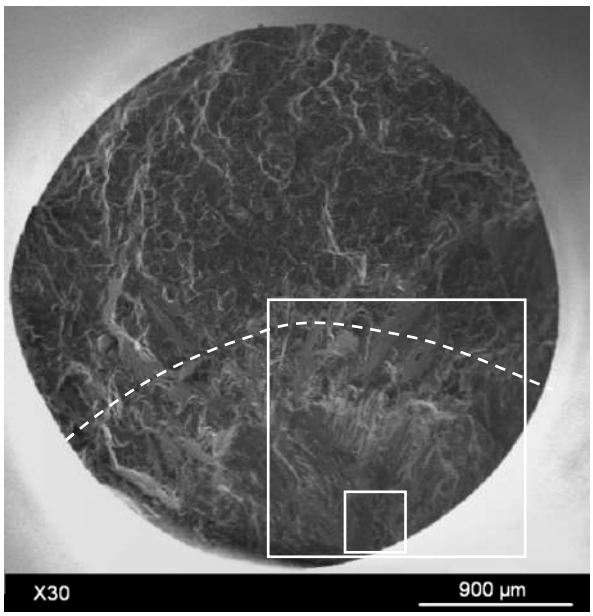

Figure 3.7. Fracture surface of a specimen tested at R=0.5 in air and room temperature, σ_a=60 MPa, N_f =2.32×10^8 cycles.

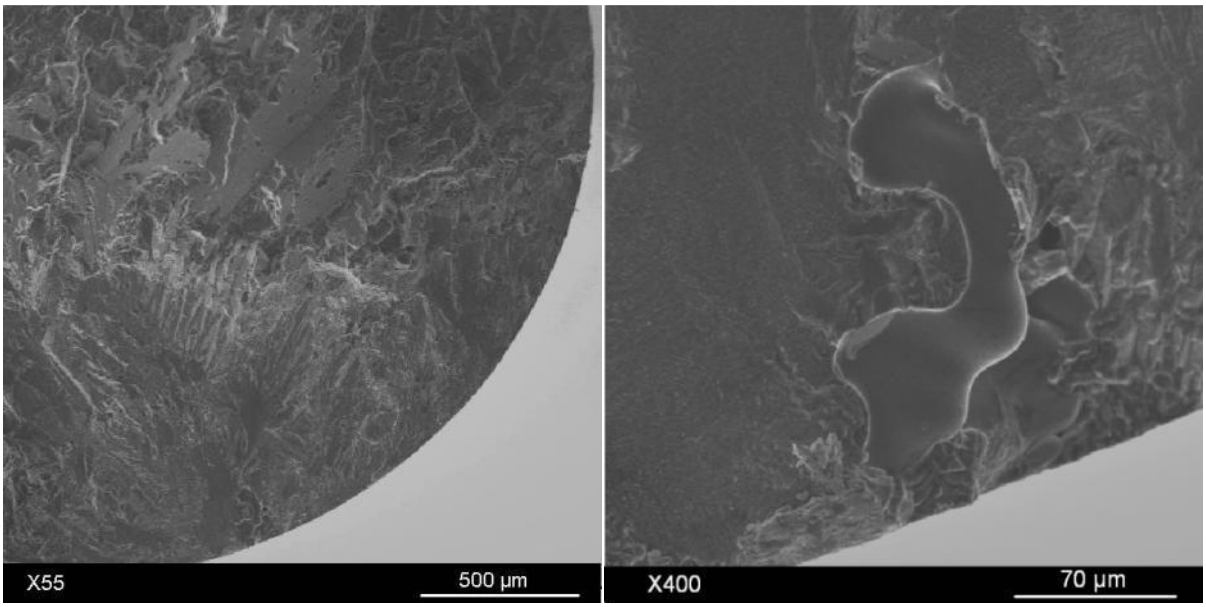

Figure 3.8. Detail of the marked zone in Figure 3.7 crack initiation site.

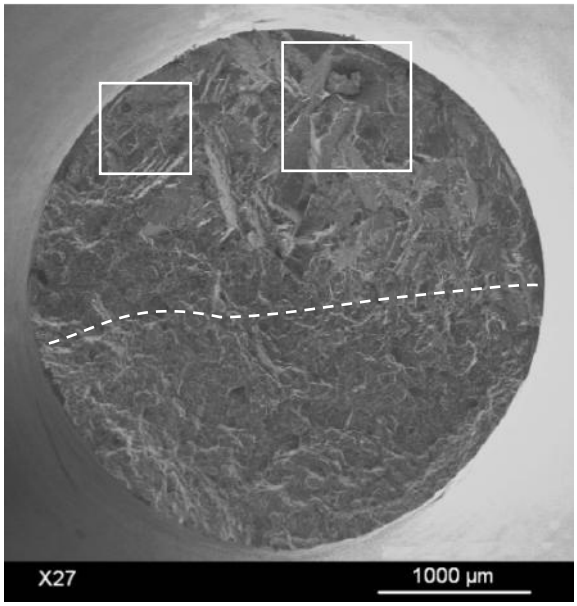

Figure 3.9. Fracture surface of a specimen tested at R=0.5 in air and room temperature, σ_a=55 MPa, N_f =3.95×10^8 cycles.

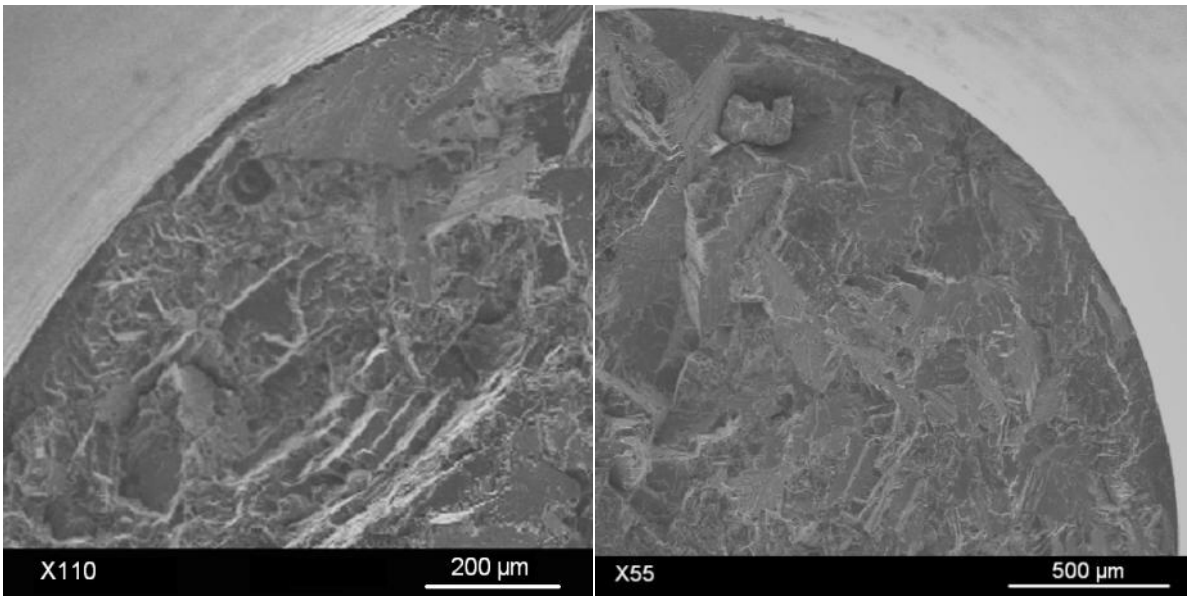

Figure 3.10. Details marked in Figure 3.9 showing the two possible crack initiation sites.

1.2. Fractography of specimens tested at 150 °C

In this section fractographies of AS7G06 broken specimens at 150 °C are shown. The temperature was practically constant during the tests, with a variation inside the climatic chamber of around ±1 °C. At this temperature no metallurgical transformations occur even in the Al alloy.

1.2.1. Tension-Compression: R=-1 at 150 °C

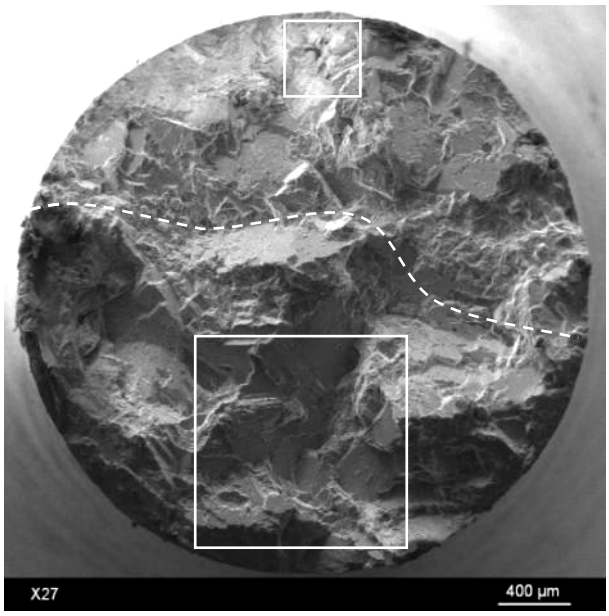

Figure 3.11. Fracture surface of a specimen tested at R=-1 in air and 150 °C, σ_a=60 MPa, N_f=7.26×10^8 cycles.

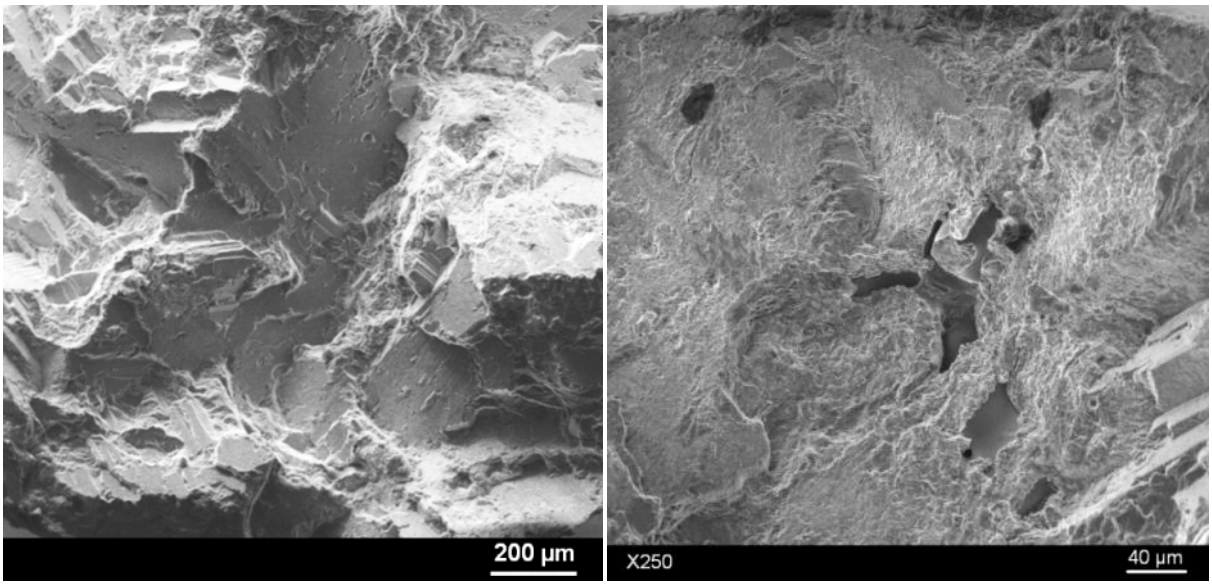

Figure 3.12. Detail of sites marked in Figure 3.11.

Figure 3.11 and Figure 3.13 show the fracture surfaces of specimens tested at R=–1, in air and 150 °C. These fracture surfaces are different compared with the specimens tested at room temperature. The fracture surfaces show a characteristic more intercrystalline than at room temperature. It is observed in Figure 3.12 (left) a rupture by quasi-cleavage as the end of the fracture. In this same Figure 3.12 (right) it is observed the shrinkage that starts the crack. The end of the crack (front) is marked by a dashed line.

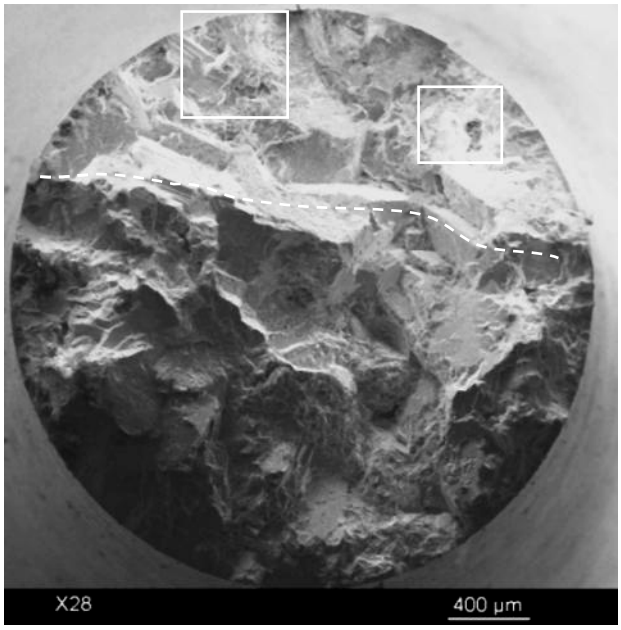

Figure 3.13. Fracture surface of a specimen tested at R=–1 in air and 150 °C. σ_a=70 MPa, N_f=9.72×10^7 cycles

A similar characteristic occurs in Figure 3.13 and is detailed in Figure 3.14. In this case the stress amplitude was higher. In this image a final rupture by quasi-cleavage is also observed but with a bigger surface than Figure 3.11. It seems that there is a competition between crack initiation at slipping bands against porosities, and the influence of the first one is higher as stress is high. Figure 3.15 shows the fracture surface of a specimen tested at 80 MPa of stress amplitude. The surface looks as a completely rupture caused by slip bands and porosities were difficult to reveal.

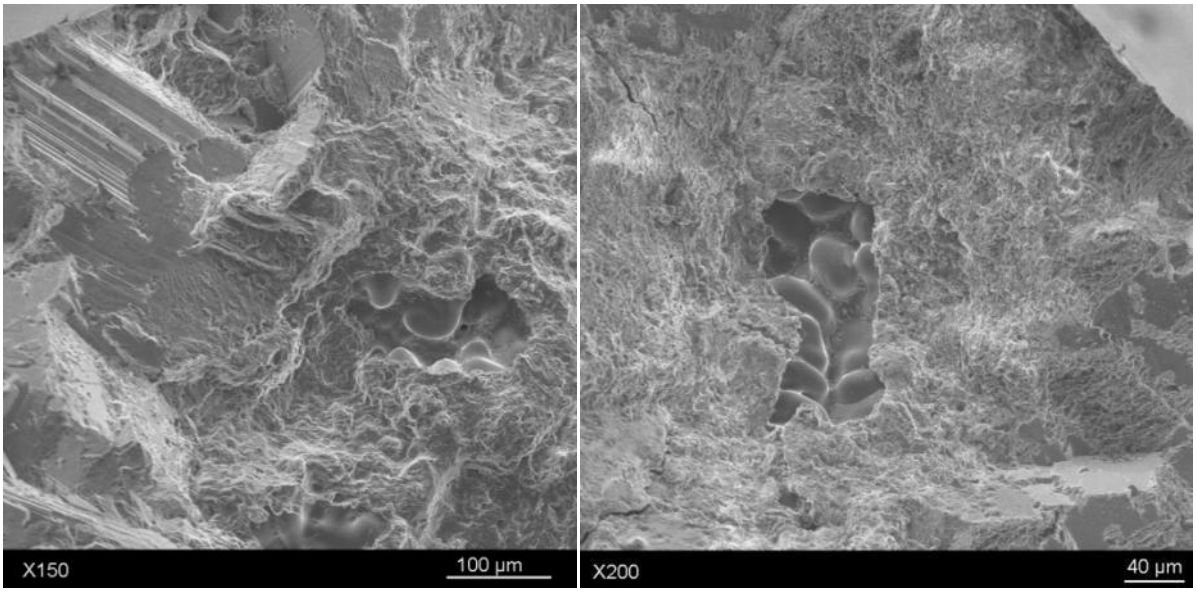

Figure 3.14. Detail of the specimen shown in Figure 3.13.

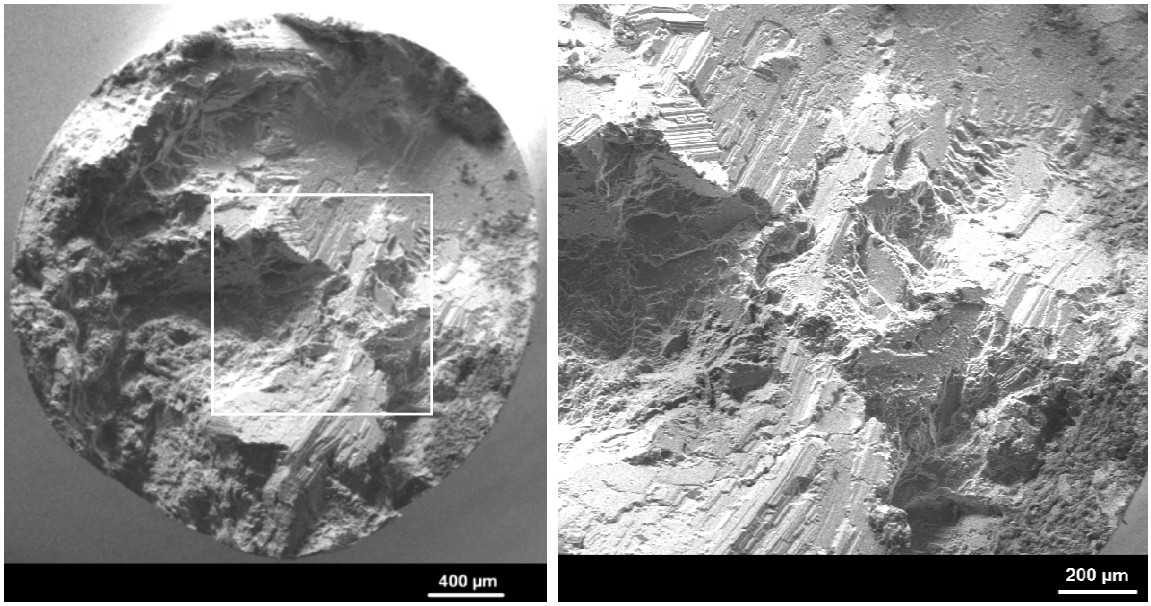

Figure 3.15. Fracture surface of a specimen tested at R=–1 in air and 150 °C. σ_a=80 MPa, N_f=2.25×10^7 cycles

1.2.2. Tension-Tension (R=0.01) at 150 °C

At R=0.01 and 150 °C, porosities are the main causes of crack initiation too; the final fracture zone presents quasi-cleavage characteristics. This is observed in Figure 3.16 and Figure 3.18.

Figure 3.18 shows the fracture surface of a specimen tested at R=0.01 at higher stress level than in Figure 3.16. It is observed that there is more quasi-cleavage as the stress amplitude applied in the test is high.

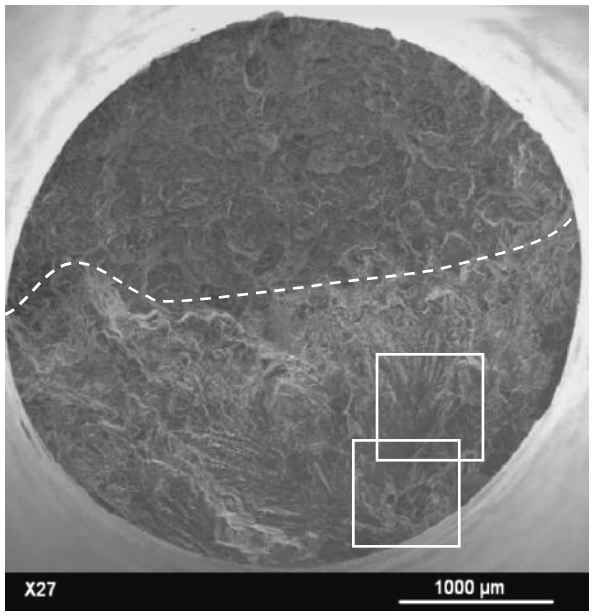

Figure 3.16. Fracture surface of a specimen tested at R=0.01, in air and 150 °C, σ_a=50 MPa, N_f=5.91×10^8 cycles.

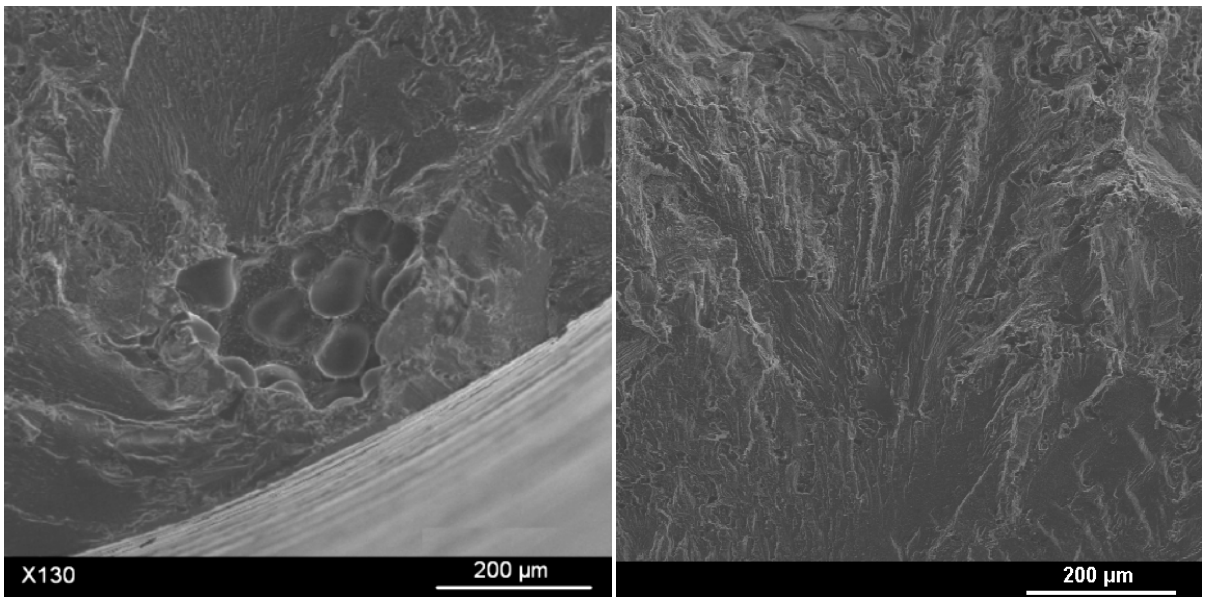

Figure 3.17. Detail of the crack initiation site marked in Figure 3.16.

Sirvatsan et al. [5] carried out fatigue tests in tension-tension (R=0.1) on a 7075-T7751 aluminium alloy at low frequency at 190 °C. This is an alloy with aluminium and magnesium and high zinc and copper content, and artificial ageing can be obtained at 190 °C. The microstructure is almost similar than AS7G06-T6, with aluminium dendrites with smaller precipitates around the grain boundaries. The fatigue results in the low cycle fatigue regime showed that fatigue strength decreased with temperature at 190 °C. Fatigue strengths (2×10^5 cycles) were 300 MPa and 200 MPa in stress amplitude at 27°C and 190 °C respectively. Specially, in the tests at higher stress levels and 190 °C they identified a region of slow and stable crack growth characterized for the appearance of very small voids created by high cyclic deformation at elevated temperature.

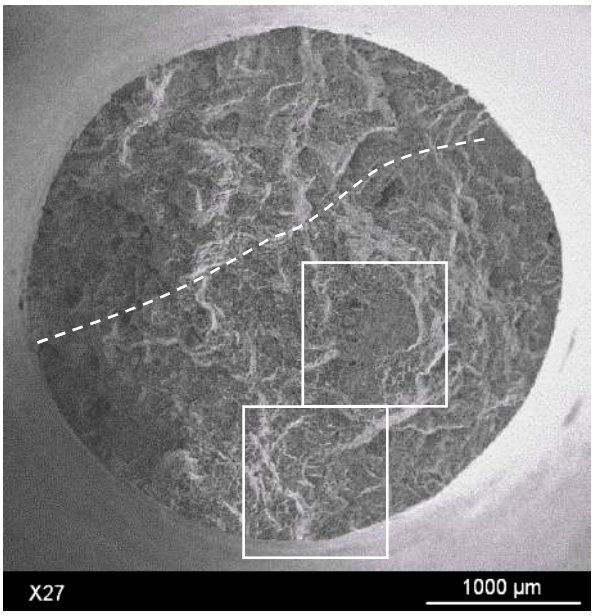

Figure 3.18. Fracture surface of a specimen tested at R=0.01 in air and 150 °C, σ_a=60 MPa, N_f=1.68×10^8 cycles.

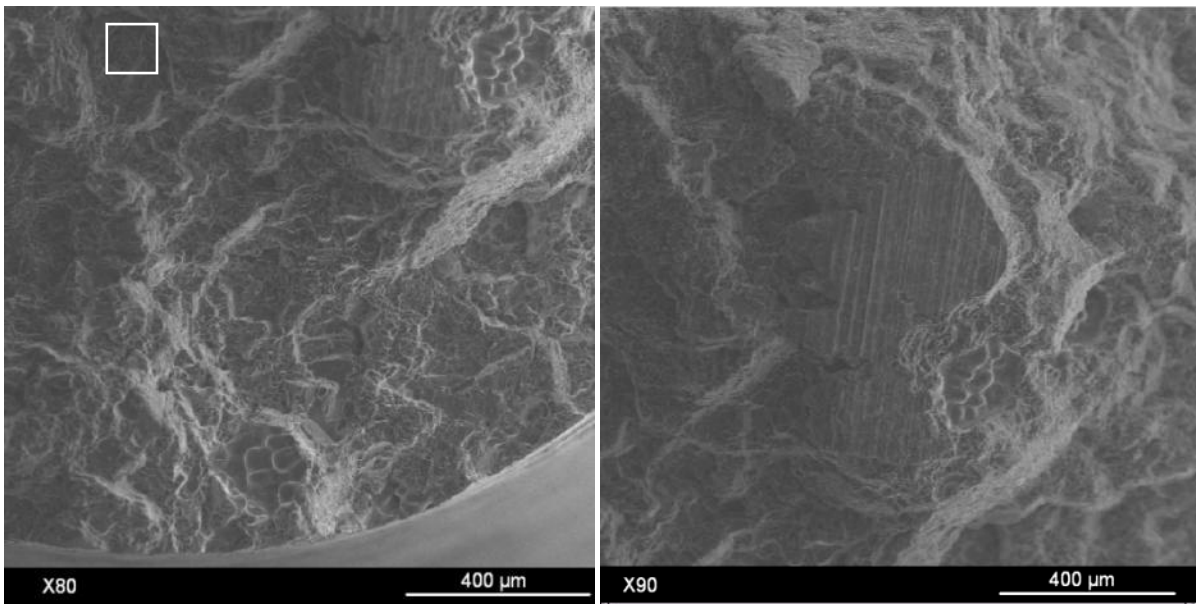

Figure 3.19. Marked zones of Figure 3.18 showing the crack initiation site.

According to [5] the presence of this population of voids, transforms the polycrystalline 7055-T7751 alloy into a “composite” comprising both grains and voids. The voids can essentially be considered as being equivalent to second-phase particles having “zero” stiffness. Since the voids are essentially “soft particles” compared with the plastically deformed grains of the polycrystalline aluminum alloy, the local strain rate is greater for the voids than for the grains. This kind of voids can be observed in the crack propagation area of specimens tested at R=0.01 and 150 °C (Figure 3.20) but they are not observed at R=–1 at the same temperature.

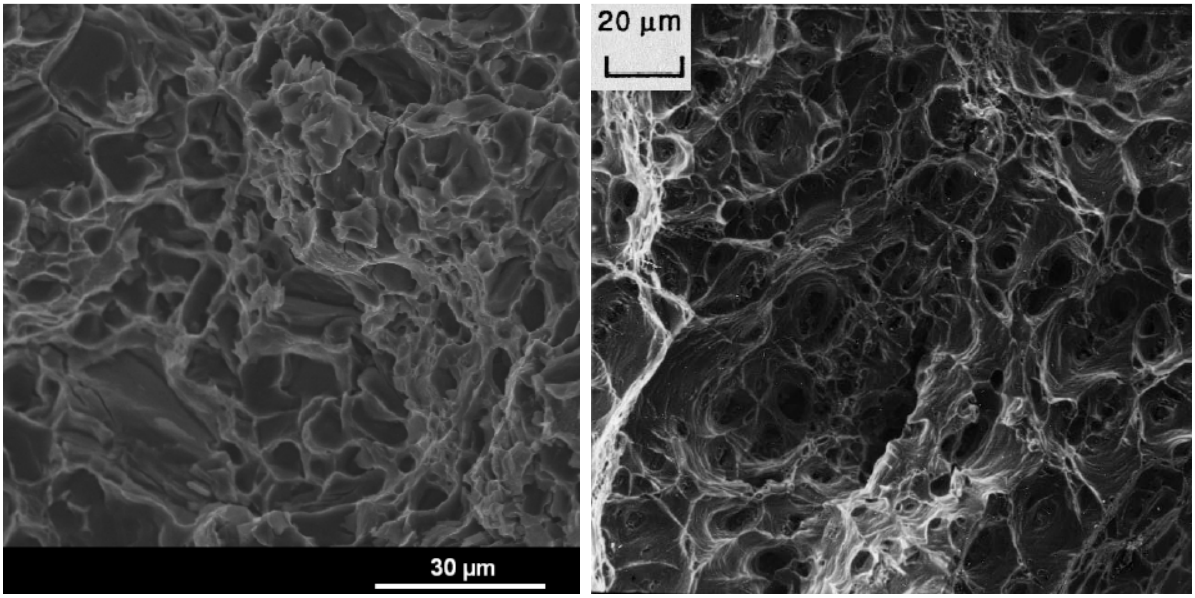

Figure 3.20. (Left) Small voids in AS7G06-T6 specimen tested at R=0.01, 150 °C (square of Figure 3.19 left) and (right) in a 7055-T7751 specimen tested at R=0.1, 190 °C from [5].

1.3. Discussion

The previous fractographies carried out on AS7G06-T6 cast aluminium alloy specimens tested under different testing conditions have shown different characteristics, but shrinkages are always present and participates to the fatigue crack initiation mechanism.

At room temperature under tension-compression R= –1, defects as shrinkages or porosities near or at the specimen surface are the main cause of crack initiation, although at high stress levels rupture by quasi-cleavage starts to appear. At R=0.01 and room temperature, porosities at the specimen surface or little inside of the specimen are even the crack initiation sites, however slip bands are more present in the fracture surface. At the same way, porosities are the crack initiation sites at R=0.5, though quasi-cleavage around the crack initiation sites is less than for R=0.01 or R=–1.

An issue has arisen in the fatigue results at room temperature in the previous Chapter II (Section 2.4.3), specially about the results at room temperature. A lower fatigue strength was expected at R=0.5 than at R=0.01 according to the information in literature. On the contrary, fatigue strength was higher at R=0.5 than R=0.01.

After fractography analysis, it was observed that characteristics crack initiation sites were porosities near to the specimen surface.

Figure 3.21 shows the fatigue strength at 10^9 cycles as function of the average size of porosities found at each stress ratio tested at room temperature and 150 °C. The segments beside represent more or minus the standard deviation. The measure of areas was done by approximating a porosity by an ellipse, as explained by Murakami (Figure 1.35-b of Chapter I). In this case the parameter compared is $\sqrt{area}$. The tests at R= –1 and R=0.01 at room temperature were carried out on a first set of specimens in Prof. Bathias' laboratory and it was observed that porosities were bigger in this set of specimens compared with the set of specimens tested in LAMEFIP laboratory. Then, it is observed that big defects such as porosities influence negatively the fatigue strength and the fatigue life of AS7G06 aluminium alloy.

Figure 3.22 shows the fatigue life of individual specimen tested and failed near to the gigacycle life as function of the testing stress amplitude and as function of their characteristic pore size at initiation. A graphic of fatigue life as function of $\sqrt{area}$ is extracted from the first graphic. It is clearly observed that pore size influences the fatigue life. The fatigue life is decreasing when the size of the porosity is increasing.

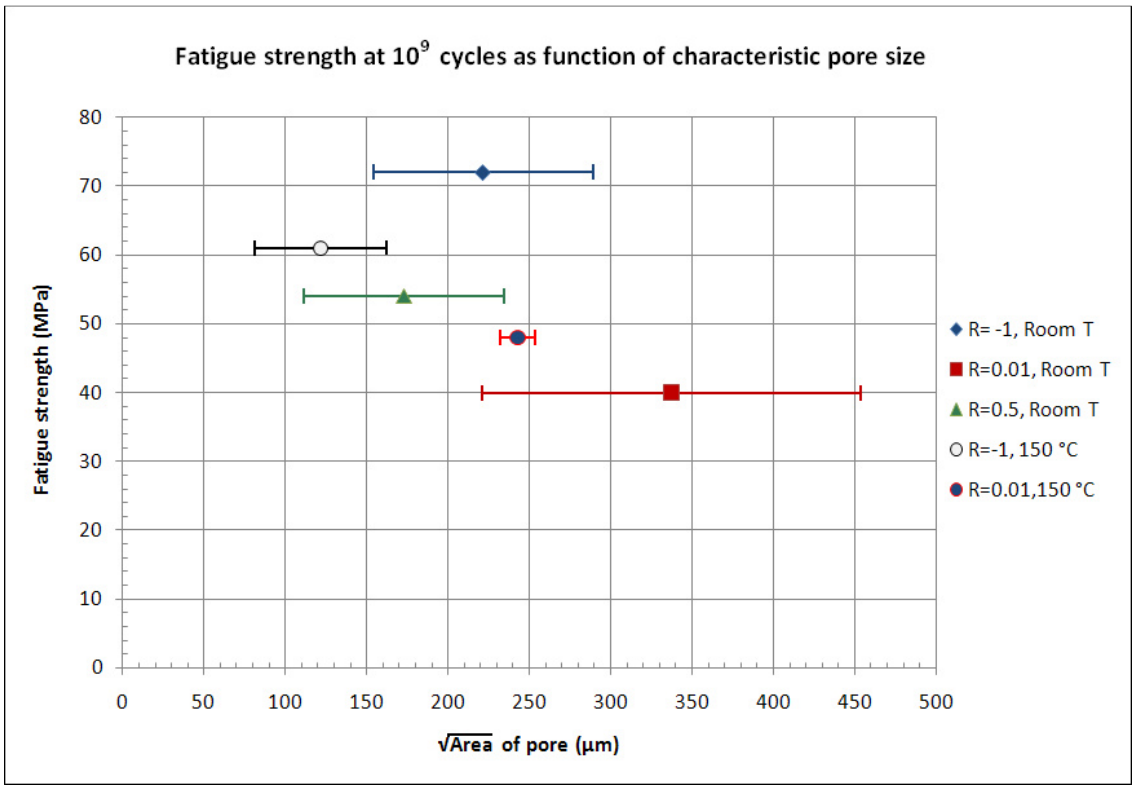

Figure 3.21. Fatigue strength of AS7G06 as function of the characteristic area of pore at room temperature.

At 150 °C and R=–1 the fracture surface showed a characteristic more intercrystalline than at room temperature, but shrinkage are even present causing crack initiation. Competition between rupture caused by quasi-cleavage and shrinkage seems appeared observing almost complete quasi-cleavage rupture at high stress levels. At R=0.01 and 150 °C fracture surface present also quasi-cleavage characteristics with the presence of porosities. At R=–1, quasi-cleavage rupture is more present as stress applied is higher.

Another important aspect of fractografies is the appearance of micro-voids in tension-tension fatigue tests at 150 °C which it is presumed are created by high deformation at elevated temperature. This voids act as local strain concentrators and it is possible that they contribute in the decreasing of the fatigue strength at imposed temperature.

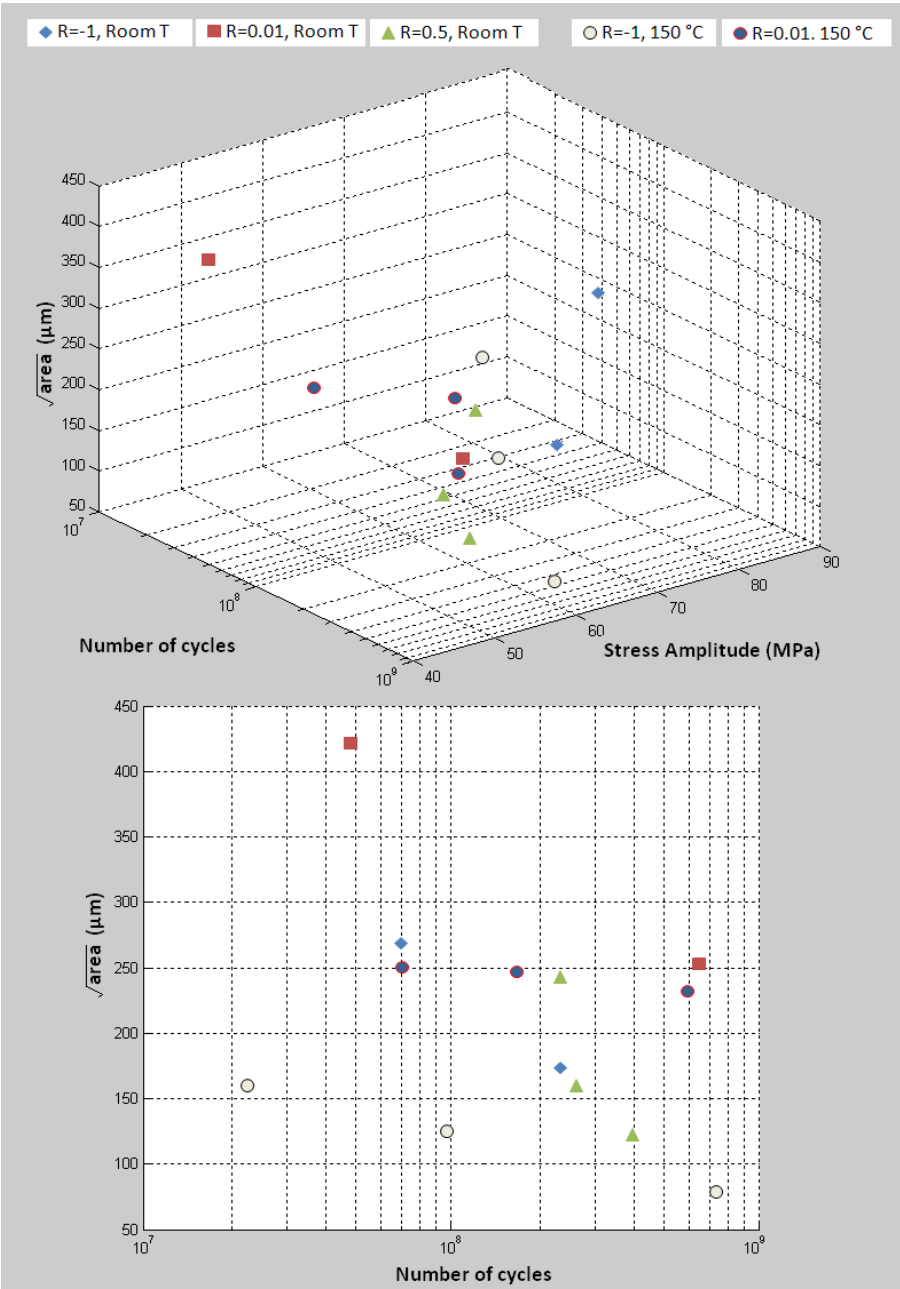

Figure 3.22. Fatigue life and fatigue strength as function of porosities size in AS7G06.

2. Analysis of R5 steel results

This section is devoted to fractographic analysis of specimens in R5 steel tested in gigacycle fatigue. Images taken by scanning electron microscopy were used in order to analyze the fracture surface of R5 steel specimens.

2.1. Fractography of specimens tested without any corrosion

R5 steel specimens without any corrosion were tested in an ultrasonic fatigue machine. The curves of the results in air and room temperature were presented in Chapter II Section 3.4. In the next section fractographies of R5 steel broken specimens without any corrosion at room temperature and two different stress ratio R are shown looking at the crack initiation sites and the main characteristics of fracture.

2.1.1. Tension-Compression (R=–1)

The fracture surfaces of R5 steel without any corrosion at R=–1, in air and room show two different fracture mechanisms. In the first case, crack initiation sites are inside the specimen, in some inclusions. In the second case, the crack initiation is observed near or at the specimen surface.

Figure 3.23 shows the fracture surface of a R5 specimen without any corrosion, tested at R=–1, in air and room temperature. The crack initiation is observed at the specimen surface.

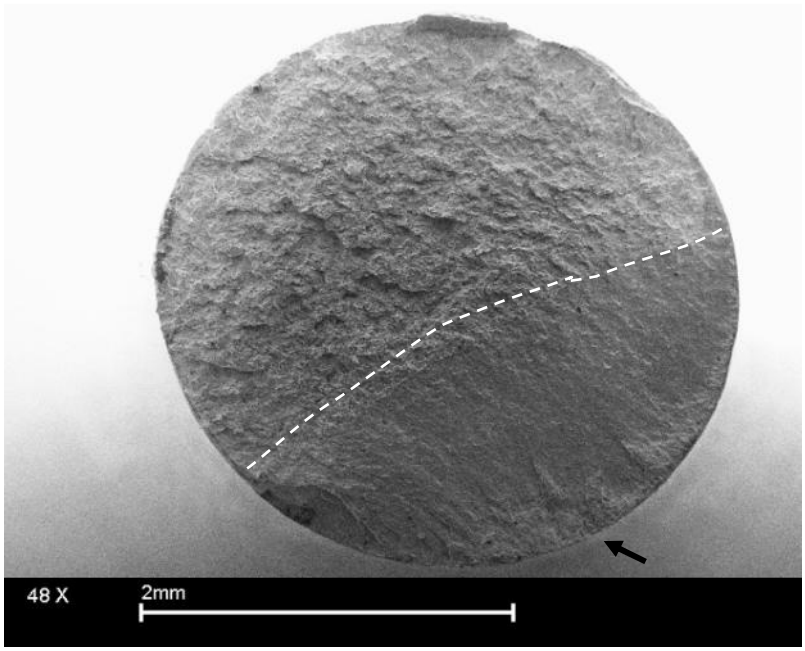

Figure 3.23. Fracture surface of a R5 steel specimen without corrosion, tested at R=–1, in air and room temperature, σ_a=390 MPa, failed at N_f= 5.61×10^8 cycles.

Figure 3.24 shows the fracture face of a R5 steel specimen without any corrosion tested at R= –1, in air and room temperature. It is observed that crack initiated on internal defect.

An approach to the defect is shown in Figure 3.25. The defect that causes the fracture is a kind of particle such as a non metallic inclusion in the core of the specimen. The size of this defect is around 19 µm in diameter.

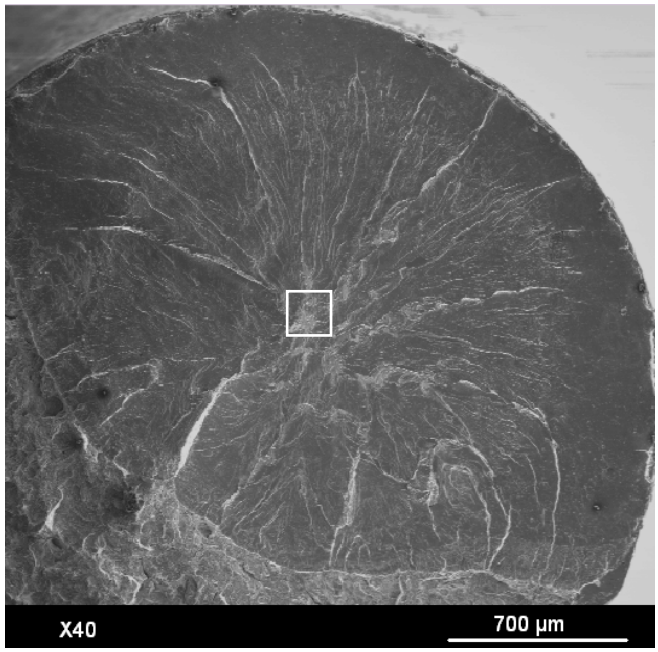

Figure 3.24. Fracture surface of a R5 steel specimen without corrosion tested at R=–1, in air and room temperature, σ_a=380 MPa, failed at N_f= 2.78×10^6 cycles.

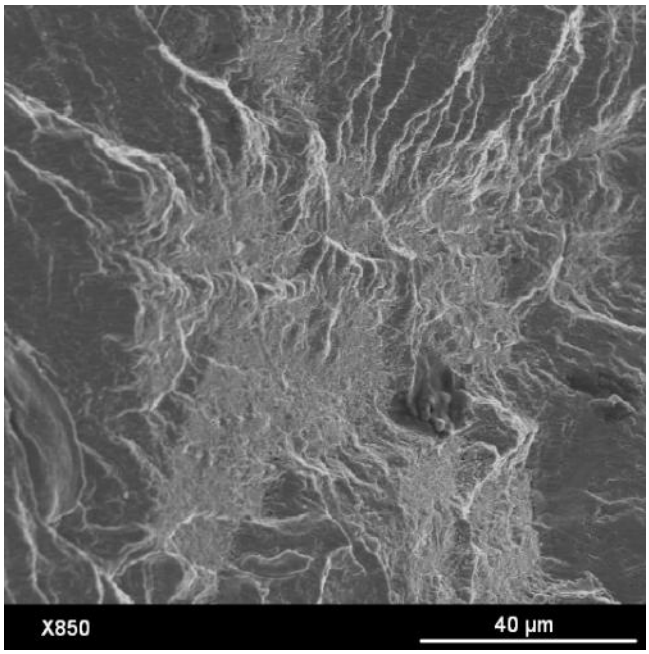

Figure 3.25. Detail of the marked zone in Figure 3.24 showing defect.

2.1.2. Tension-Tension (R=0.3)

Figure 3.26 and Figure 3.30 show the characteristic fracture surfaces of R5 steel specimens without corrosion tested at R=0.3, in air and room temperature.

Fracture initiation sites were found in the subsurface in both cases. The appearance of these particles seems that they are some kind of inclusions but they could be caused by charge at SEM for instance they were detached metallic particles. A microanalysis was done to check this observation.

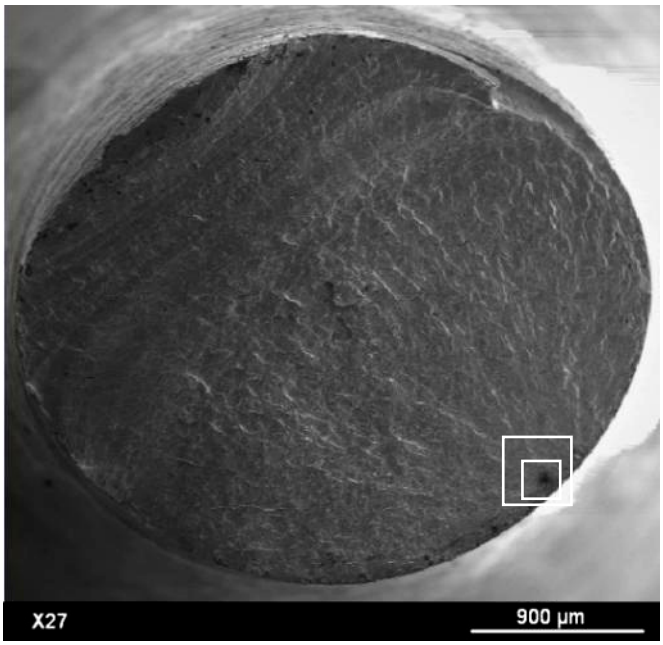

Figure 3.26. Fracture surface of a R5 steel specimen tested at R=−1, in air and room temperature, σ_a=280 MPa, failed at N_f=4.06×10^8 cycles.

Figure 3.28 show the result of a microanalysis carried out in the zone of the particle showed in Figure 3.27. In this spectrum, besides the iron, it is possible to observe the presence of zinc, aluminium, silicon and sulfur in important concentration. It was not possible to determine exactly which kind of matter are present in this crack initiation sites but they are inclusions.

Figure 3.29 shows an example taken from literature, a 4240 steel tested at R=−1 presenting both internal and surface initiation. The general opinion is that for a longer fatigue life (low stress amplitude), the defects causing the fatigue crack initiation are localized in the interior of the specimen, while for surface defects is not expected a long fatigue life [1]. But, for R5 steel that is not the case.

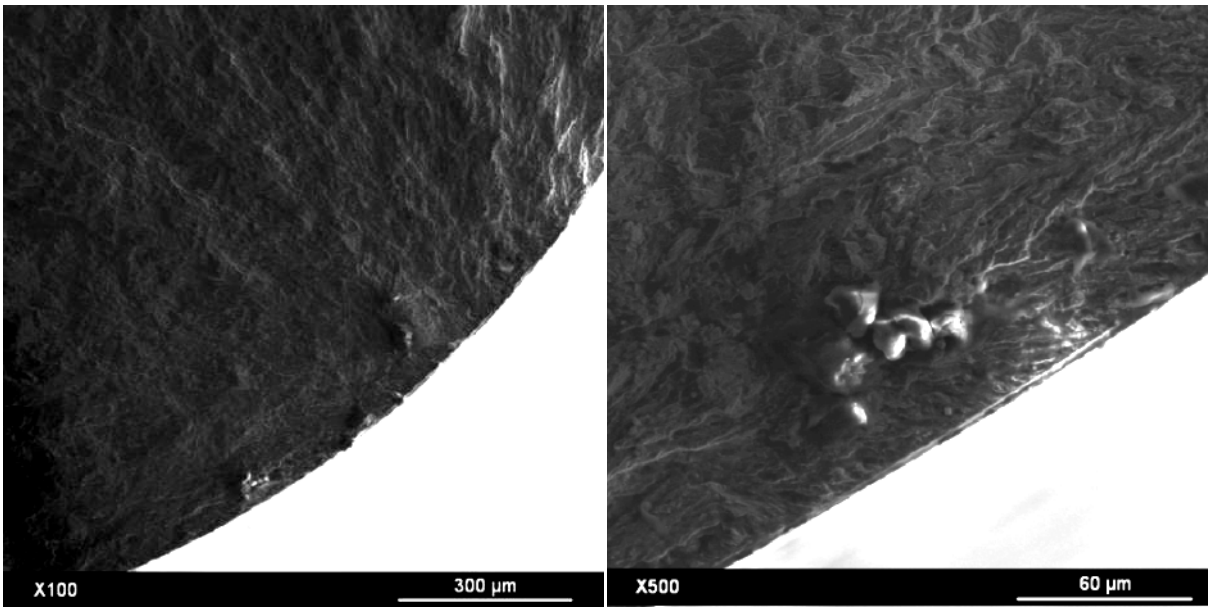

Figure 3.27. Details of the marked zones in Figure 3.26.

The left figure is very dark, please try to increase the brightness

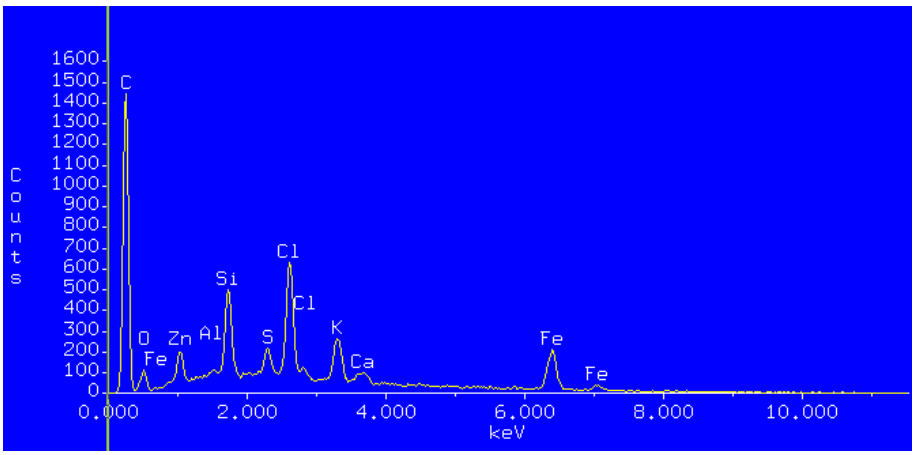

Figure 3.28. Microanalysis of the particle shown in Figure 3.27 (right).

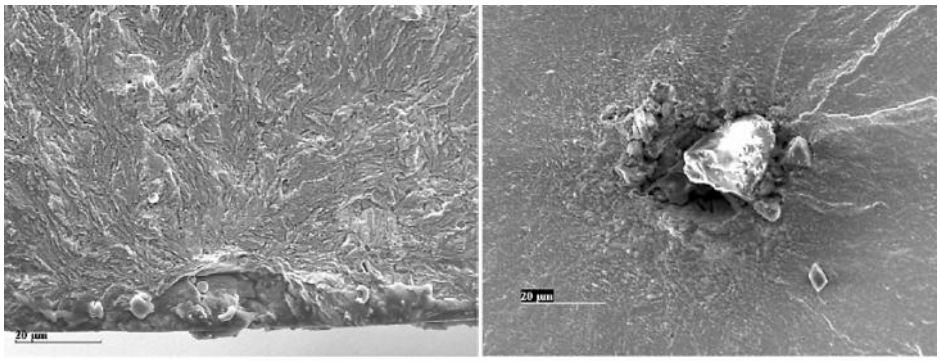

Figure 3.29. Crack initiation at surface inclusion (3×10^5 cycles) and at internal inclusion (5×10^8 cycles) in a 4240 steel tested in air at R=–1, σ_{max}=760 MPa [1]

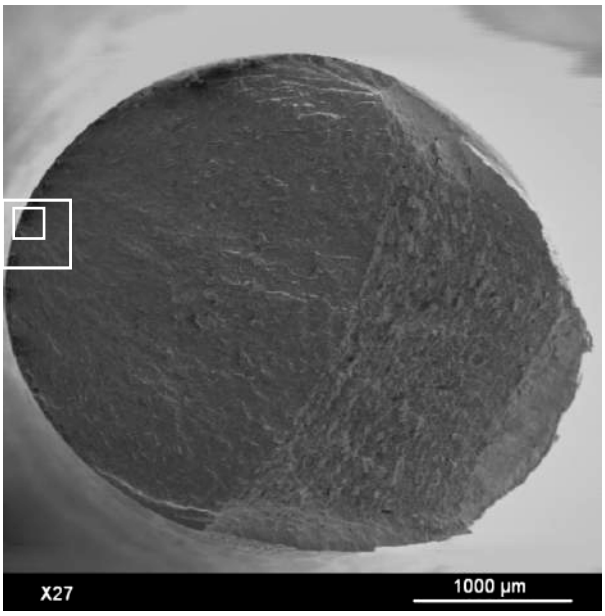

Figure 3.30. Fracture surface of a R5 steel specimen without corrosion at R=−1, in air and room temperature. σ_a=270 MPa, failed at N_f=9.12×10^8 cycles.

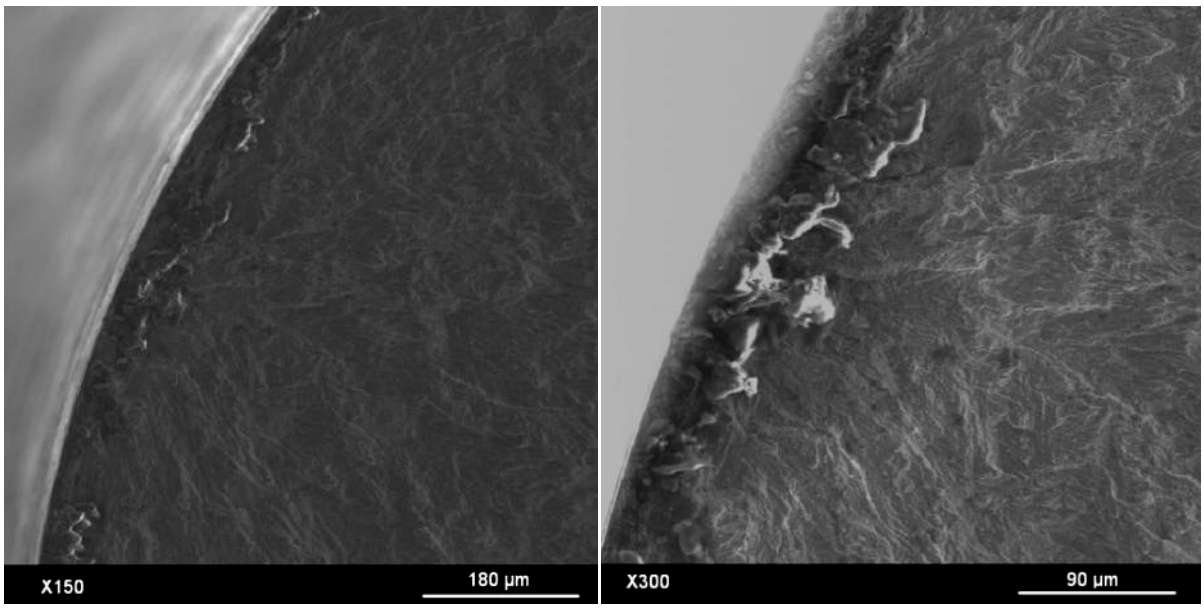

Figure 3.31. Details of the marked zones in Figure 3.30.

2.2. Fractography of specimens with corrosion

In Chapter II it was shown that specimens of R5 steel with pre-corrosion had fatigue strength lower than specimens without any corrosion as it was expected. But a large scatter of the results was also noticed. For the case of the fatigue tests under sea water flow the decreasing on the fatigue strength was even more drastic.

A fractography analysis have been carried out on the two specimen batches tested with corrosion: (i) pre-corroded specimens and (ii) tested under sea water flow,. for observing the characteristics of the crack initiation under the different conditions.

2.2.1. Tension-Compression (R=-1) with pre-corrosion

Figure 3.32 to Figure 3.37 show the fracture surfaces and details of R5 steel specimens with pre-corrosion tested at R=–1, in air and room temperature. In all the cases, pits that have been created by the pre-corrosion process are the cause of crack initiation and fracture. These pits have a diameter from 25 to 150 µm.

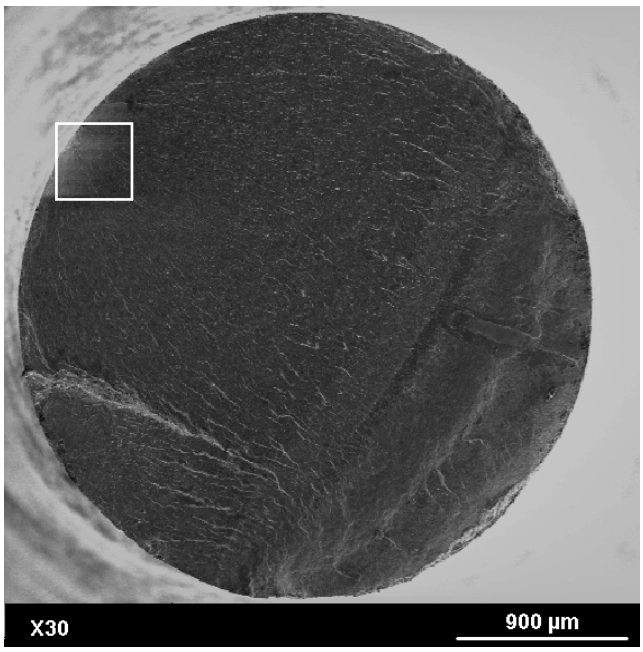

Figure 3.32. Fracture surface of a R5 steel specimen with pre-corrosion tested at R=–1, in air and room temperature, σ_a=370 MPa, N_f=4.37×10^8 cycles

Figure 3.33, Figure 3.35 and Figure 3.37 show the details of the pits that cause the fatigue fracture and their size. The shape of the pits are approached to a regular shape such a circumference or an ellipse. In some cases two pits are close one each other, then the distance between the center of the circles or ellipses have been measured.

It is observed in this Figure 3.33 that two close corrosion pits are in the crack initiation site. The distance between them is around 260 µm. It is known that defects such as pits which are voids act as stress concentration sites.

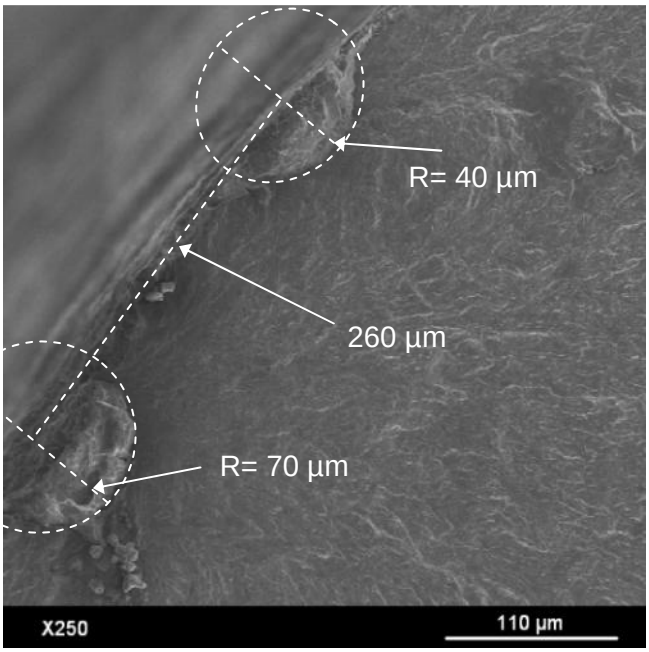

Figure 3.33. Detail of the marked zone in Figure 3.32.

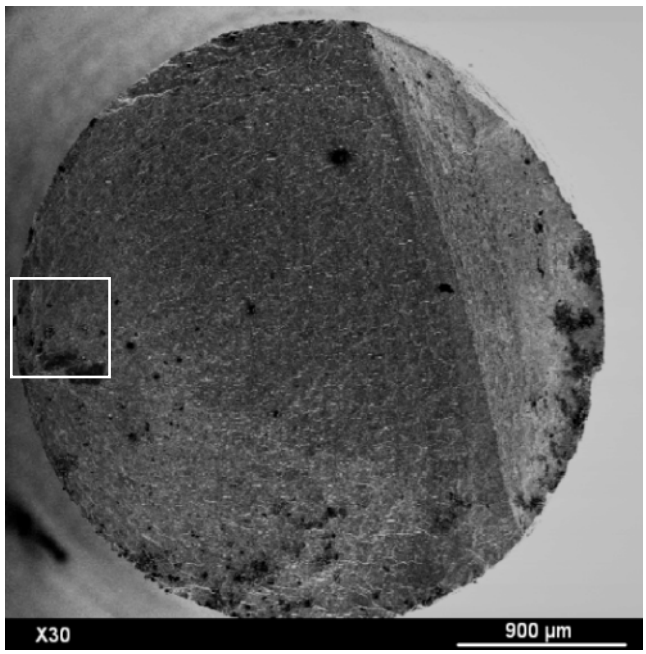

Figure 3.34. Fracture surface of a R5 steel specimen with pre-corrosion tested at R=–1, in air and room temperature, σ_a=360 MPa, Failed at N_f= 5.48×10^8 cycles

One pit alone is observed in Figure 3.35. Its size is in the same order compared with the specimen shown in Figure 3.33. In fact, the stress amplitude that these two specimens were submitted to are 370 MPa and 360 MPa and the fatigue life have been in the order of 5×10^8 cycles.

On the other hand, smaller but closer pits present in the specimen of Figure 3.37 tested at higher stress level (σ_a=425 MPa) caused crack initiation after a life of only 1.57×10^7 cycles. It

raises the hypothesis that closer pits can act as a high stress concentrator, causing a quicker crack initiation and then a faster failure. This have been presented by Dominguez et al [6].

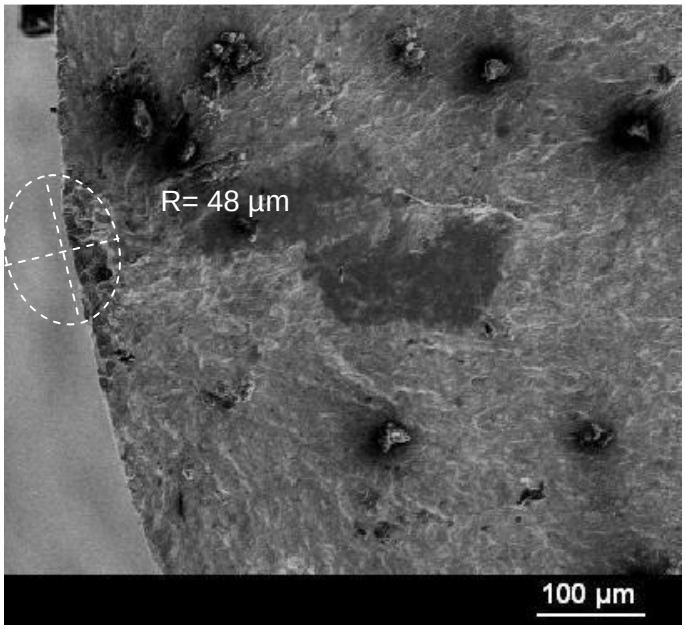

Figure 3.35. Detail of the marked zone in Figure 3.34.

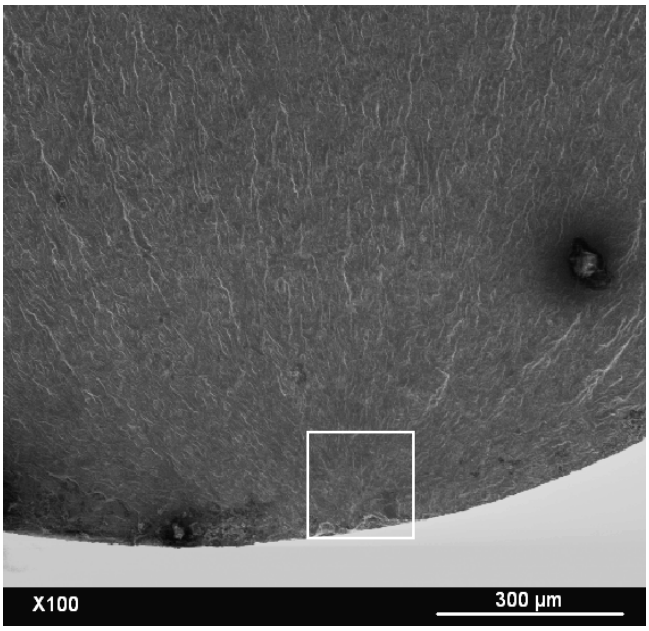

Figure 3.36. Fracture surface of a R5 steel with pre-corrosion tested at R=–1, in air and room temperature, σ_a=425 MPa, failed at N_f= 1.56×10^7 cycles.

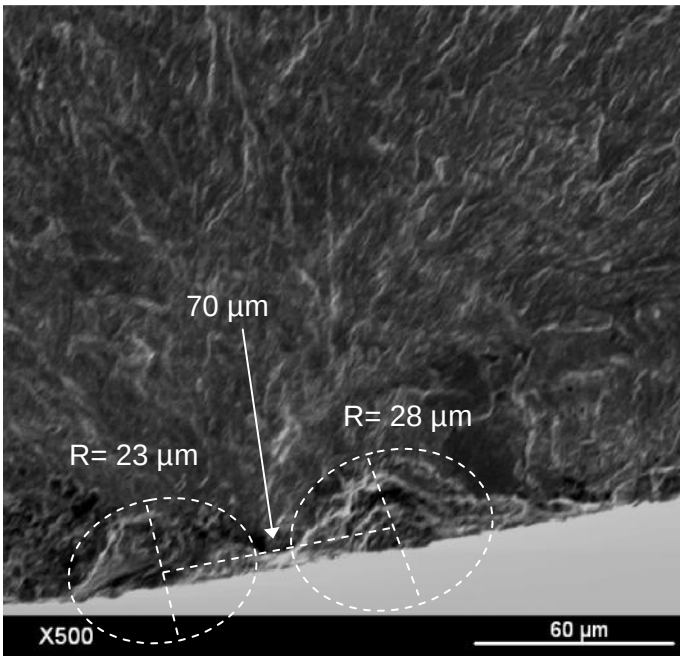

Figure 3.37. Detail of the marked zone in the Figure 3.36.

2.2.2. Tension-Compression (R=-1) under sea water flow

Figure 3.38 to Figure 3.46 show aspects of the fracture surfaces of R5 steel specimens tested under sea water flow in situ at R= –1 and room temperature. Figure 3.38 and Figure 3.41 correspond to tests in sea water flow on specimens with an average roughness surface Ra=0.6 µm.

It is observed that corrosion due to sea water is very aggressive with the R5 steel while cyclic loading is applied. The interaction between corrosion process and cyclic loading has been exposed in Section 3.4.2 of Chapter II.

The pits observed after fatigue tests are bigger than those observed at the surface of the pre-corroded specimens. It is understandable that these specimens failed at lower number of cycles than pre-corroded. The size of the pits depends on the time (that is to say the number of cycles). At the moment it is difficult to show precisely experimental evidence of the coupling between corrosion and the high strain rate due to the 20 kHz frequency. In fact, it is not possible to determine the size of the pits at the crack initiation exactly. One can imagine that pits observed post mortem were smaller at the moment of crack initiation (as marked in Figure 3.39-left). However the pits size is larger (around 3 times greater) under sea water flow (50–300 µm) than for the pre-corroded specimens (30–100 µm).

Figure 3.40, Figure 3.43 and Figure 3.46 show some multiple micro-cracks perpendicular to the loading direction, that is to say on the plane of maximum normal stress. This is probably characteristic of a corrosion/cyclic-loading interaction. Simultaneously corrosion and cyclic loading create several flaws that are the cause of lower fatigue strength.

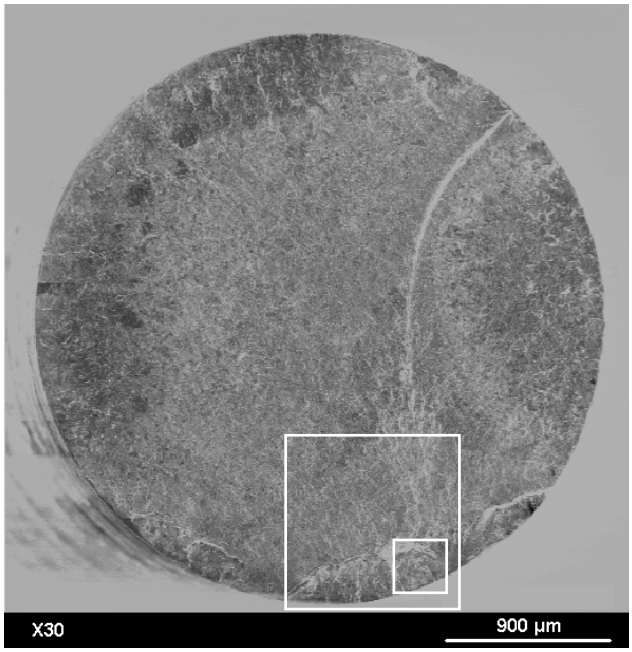

Figure 3.38. Fracture surface of a R5 specimen (Ra=0.6 µm) tested in sea water flow and room temperature at R=–1, σ_a=240 MPa, failed at N_f= 5.20×10^7 cycles.

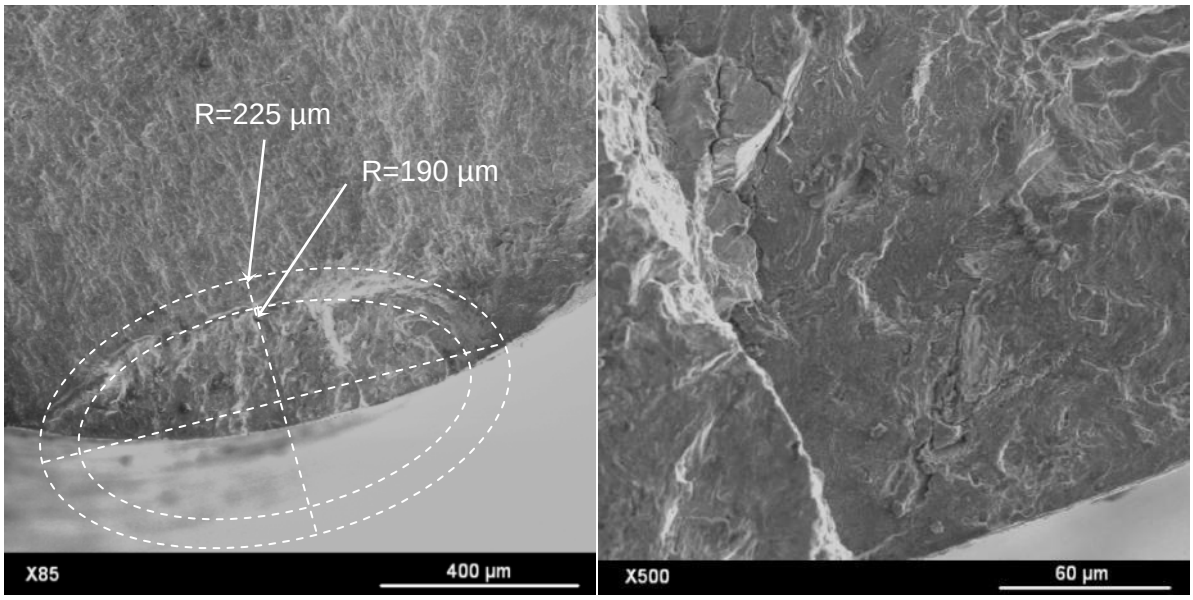

Figure 3.39. Details of the marked zones in Figure 3.38.

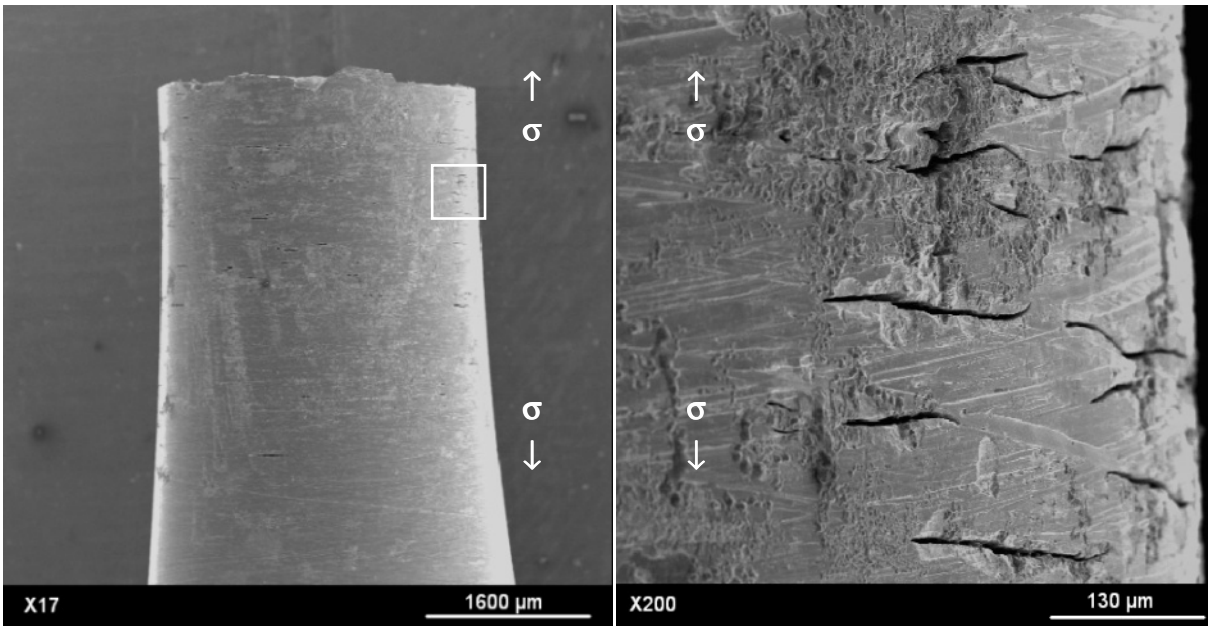

Figure 3.40. Lateral view of the fractured specimen of Figure 3.38 (Ra=0.6 µm).

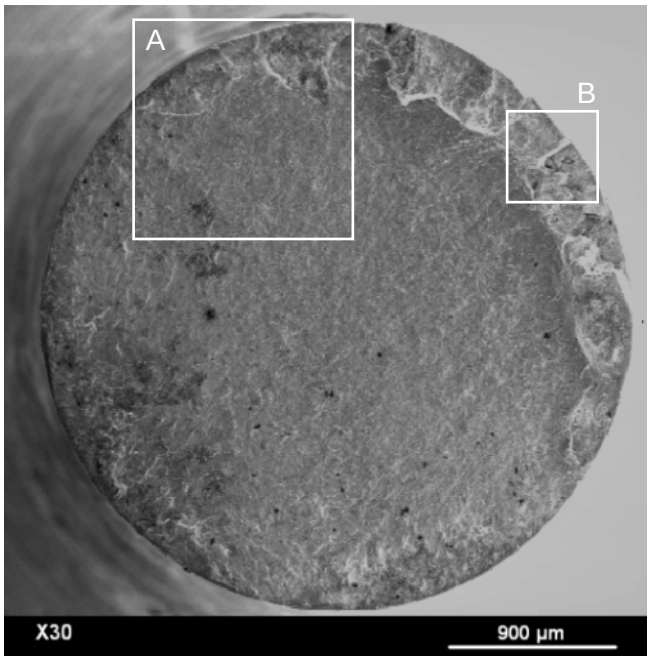

Figure 3.41. Fracture surface of a R5 steel specimen (Ra=0.6 µm) tested in sea water flow and room temperature at R=–1, σ_a=200 MPa, failed at N_f= 1.08×10^8 cycles.

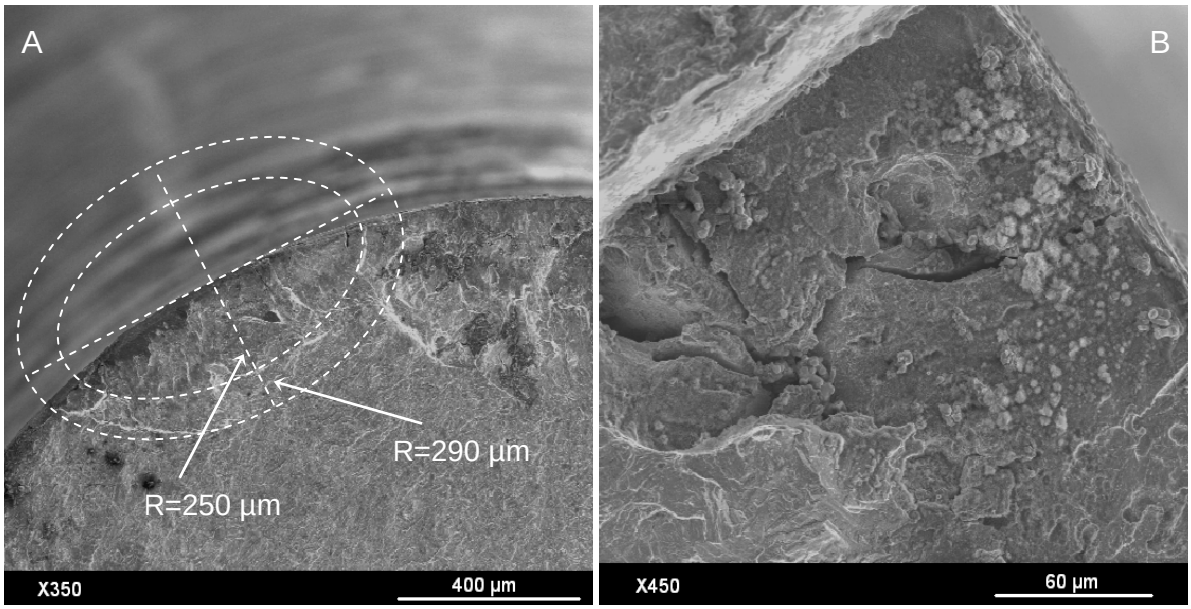

Figure 3.42. Details of the marked zones in Figure 3.41.

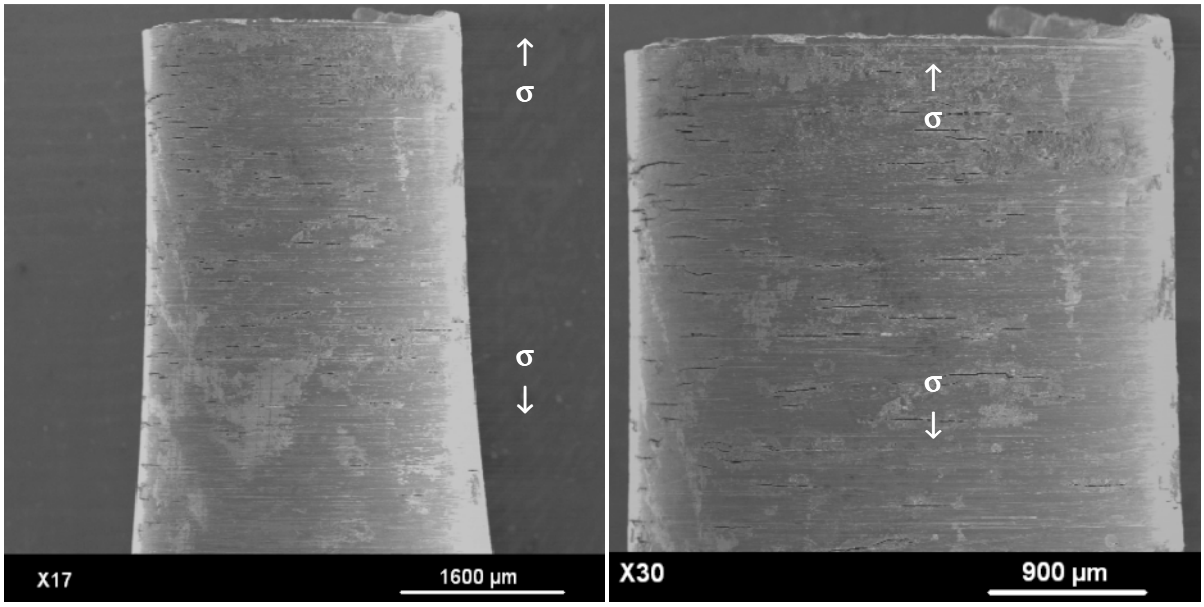

Figure 3.43. Lateral view of the fractured specimen in Figure 3.41 (Ra=0.6 µm).

Figure 3.44 show the fracture face of a better roughness R5 steel specimen (Ra=0.1 µm) tested also in sea water flow at R=–1. In Chapter II we have presented the fatigue results for both roughness surface conditions. Fatigue life corresponding to a given stress amplitude was the same for both roughness surface. In Figure 3.44 it is observed that surface condition is not an important factor in relation to the fracture mechanism. The fracture surfaces are similar for both fine and very fine roughness specimen surface.

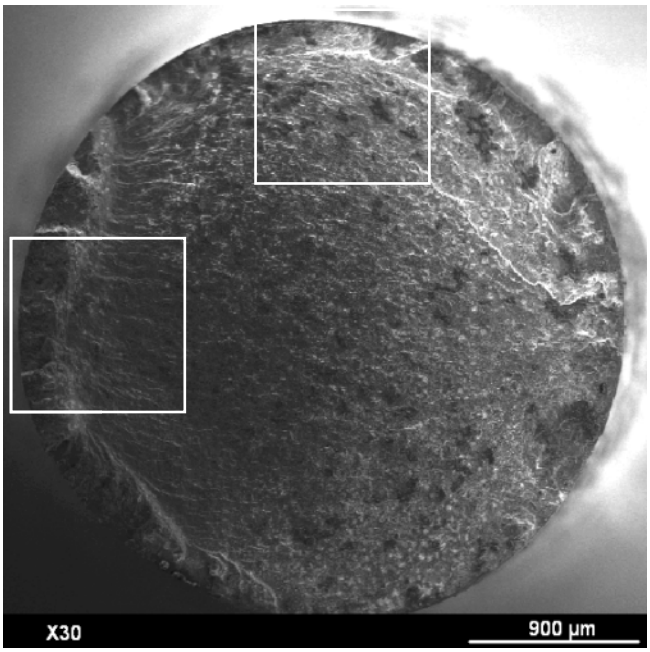

Figure 3.44. Fracture face of a R5 steel specimen (Ra=0.1 µm) tested in sea water flow and room temperature at R=–1, σ_a=250 MPa , failed at N_f= 6.14×10^7 cycles.

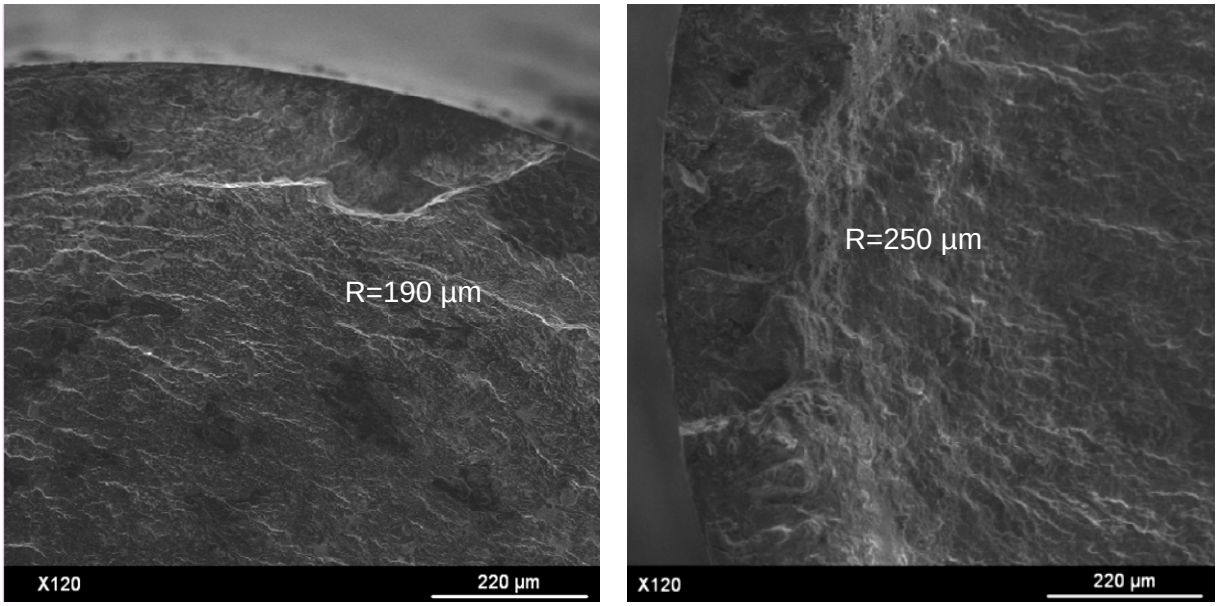

Figure 3.45. Details of the marked zones on Figure 3.44.

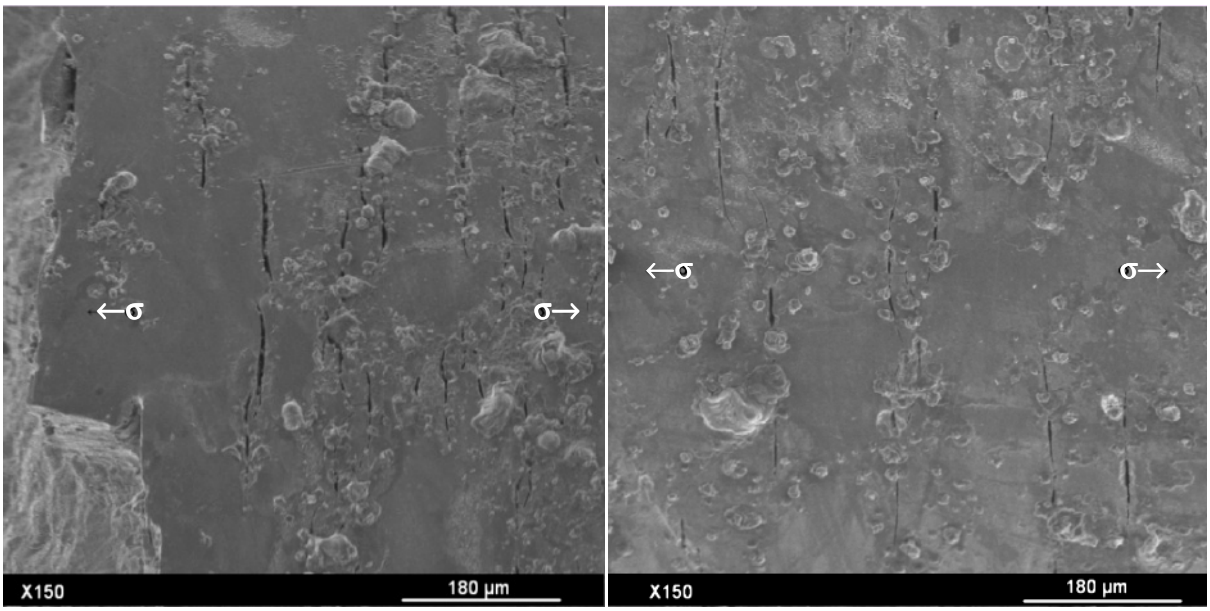

Figure 3.46. Lateral view of the fracture specimen of Figure 3.44 (Ra=0.1 µm).

2.3. Discussion

The fracture surfaces of R5 steel specimens tested in fatigue under different testing conditions and failed in the gigacycle regime were presented in this section. The characteristics of fracture are different depending of the material initial condition and the testing environment.

Without any corrosion under fully reversed tension (R= –1), crack initiation sites are located at both specimens surface and internal defects. Internal initiation sites were associated with inclusion type defects.

Initiation sites on the specimens without corrosion under R=0.3 are all located at the specimen subsurface. A microanalysis showed the presence of non-metallic inclusions common in steel, such as silicates, aluminates and sulphides.

The influence of corrosion on the fatigue results in the gigacycle regime has been noticeable. Two different corrosion conditions have been studied and each one shows different fatigue crack initiation characteristics. Specimens with pre-corrosion show crack initiation sites at corrosion pits on the specimen surface. Specimens tested under sea water flow presented crack initiation sites also at corrosion pits on the specimen surface, but in this case, corrosion pits are bigger than on the specimens with pre-corrosion. Another particular feature is the appearance of a lot of small cracks around the specimen surface all along the variable section of the specimens, being a group of these cracks which cause the drastic failure.

The important variation on fatigue life for similar specimens loaded under similar stress amplitude can be correlated to the parameters observed on the fracture surfaces. For instance, two non corroded specimens were loaded at σ_a=380 MPa and σ_a=390 MPa, the first one

attained 2.78×10^6 (Figure 3.24) cycles and the second 5.6×10^8 cycles (Figure 3.23). Internal crack initiation was observed in the first specimen associated to internal defect, probably generated during the fabrication process. In the second one crack initiation was caused by surface pits on this non-corroded specimen caused by natural environmental action. The combined effect of non controlled environmental pits and internal defect should explain the short fatigue life on the specimen tested at σ_a=380 MPa.

Two cases are considered for the pre-corroded specimens: σ_a=370 MPa and $N_f=4.38\times10^6$ cycles the first one; and σ_a=425 MPa with $N_f=1.56\times10^7$ cycles for the second. The fracture surface for the short fatigue life specimen is shown in Figure 3.37; two pits are observed at the specimen surface with radius: 23 µm and 28 µm, separated a distance of 70 µm. For the specimen that attained longer life, the presence of two pits also is observed in Figure 3.33. these pits have a radius of 40 µm and 70 µm, but this time separated by a distance of 260 µm. It is known that the presence of pitting on specimens induces stress concentration. Here, it is presumed that the presence of two close pits induces even more concentration as closer they are. Finite element analysis should be carried out to study this in details.

For tests under sea water flow the same kind of fracture surfaces was observed for specimens with two different surface roughness Ra=0.6 and Ra=0.1, demonstrating that in this case, for R5 steel under sea water corrosion in real time, the roughness surface does not have any influence in the crack initiation mechanisms (for the tested conditions).

The size of the pits created during testing under sea water flow was bigger than pits in specimens with pre-corrosion. It is important to remark that pits were observed post mortem and it is possible that their size at initiation were smaller, possibly in the order of the microstructure size. The possible coupling of both corrosion and cyclic loading processes is presumed but at the present it is no possible to determine quantitatively the effect of this interaction. Some evidence appeared in the fractographies, such as the creation of multiple pits and the appearance of multiple small cracks along the variable cross-section of the specimen.

With intention to show the effect of the size of corrosion pits on the fatigue strength and the fatigue life, a kind of chart *S*-*N*-√Area is presented in Figure 3.47. Then, from this chart, one has obtained an evolution of the fatigue life as function of the characteristic size of the pits (Figure 3.48).

Chart in Figure 3.49 presents the stress amplitude applied to individual R5 steel specimens to failure in the regime of 10^6 and 10^9 cycles as function of the characteristic size (√Area) of the pits at the crack initiation.

It is observed that specimens tested with pre-corrosion have pits which size lies in the Kitagawa threshold. There is a critical size of the pits for which the fatigue strength decreases depending of the pit size. This is in very good agreement with the Kitagawa diagram. The threshold size of the pit is around 300µm.

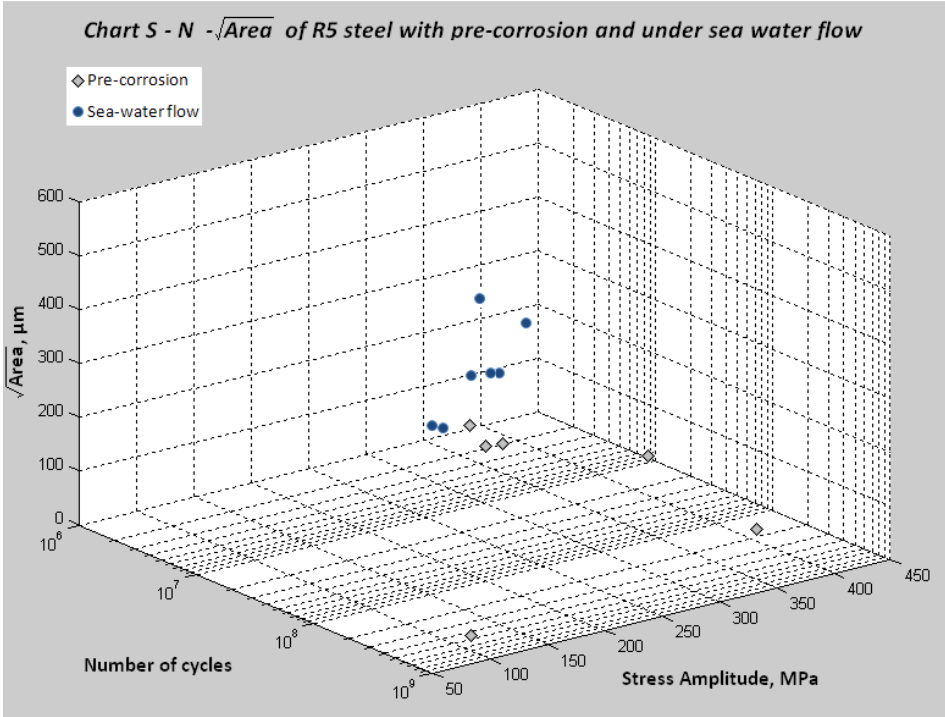

Figure 3.47. Graphic of stress amplitude versus number of cycles and √Area of pits at crack initiation.

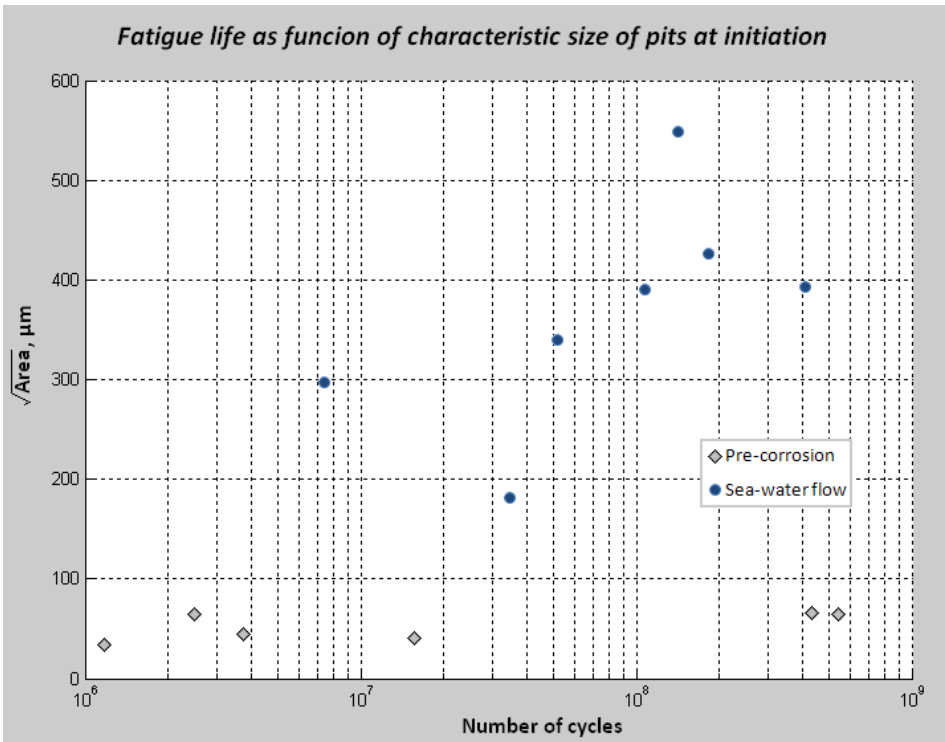

Figure 3.48. Graphic presenting the fatigue life as function of √Area of pits at crack initiation.

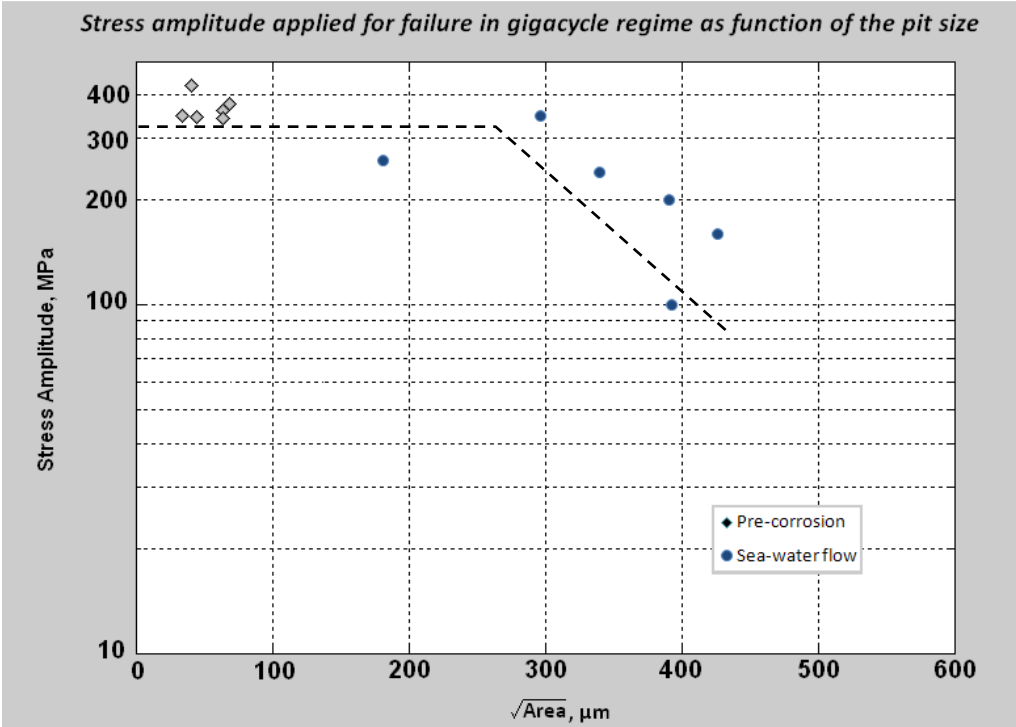

Figure 3.49. Stress amplitude for fracture between 10^7 and 10^9 cycles as a function of √Area of pits at crack initiation.

An analysis of the stages duration of the fatigue life for R5 steel specimens containing corrosion pits is presented in next chapter. An assessment of the fatigue crack propagation duration in the gigacycle regime is presented.

References of Chapter III

1. Bathias, C., Paris, P.C., 2005, *Gigacycle Fatigue in Mechanical Practice*, Marcel Dekker Publisher Co., New York USA.
2. Ammar, H.R., and Samuel, A.M., and Samuel, F.H., 2008, *Effect of casting imperfections on the fatigue life of 319-F and A356-T6 Al-Si casting alloys*, Materials Science and Engineering A, Volume 473, pp. 65-75
3. Yi, J.Z., and Lee, P.D., and Lindley, T.C., and Fukui, T., 2006, *Statistical modeling of microstructure and defect population on fatigue performance of cast A356-T6 automotive*, Materials Science and Engineering A 432, pp. 59-68.
4. Koutiri, I, and Morel, F., and Bellett, D., and Augustins, L., 2009, *Effect of high hydrostatic stress on the fatigue behavior of metallic materials*, Proceedings of 12th International Conference on Fracture ICF2009, Otawa, Canada.
5. Srivatsan, T.S., and Anand, S., and Sriram, S., and Vasudevan, V.K., 2000, *The high cycle fatigue and fracture behavior of aluminium alloy 7055*, Materials Science and Engineering A 281, pp. 292-304.
6. Perez Mora, R., and Dominguez Almaraz, G., and Palin-Luc, T., and Bathias, C., and Arana, J.L., 2010, *Very High cycle fatigue analysis of high strength steel with corrosion pitting*, Key Engineering Materials Vol. 449, pp. 104-113.

CHAPTER IV
Assessment of fatigue crack initiation and propagation duration

Table of contents

1 Paris-Hertzberg crack growth law 154
2 Application of the Paris-Hertzberg law to corrosion pits 158
2.1 Assumptions 159
2.2 Short crack initiation 160
3 Determination of the propagation stages duration 165
3.1 From a_{int} to a_0 (microstructural short crack growth regime) 166
3.2 From a_0 to a_i (physical short crack growth regime) 167
3.3 From a_i to a_{final} (long crack growth) 168
3.4 Calculation of total propagation duration 170
4 Calculation for R5 steel with pre-corrosion 172
5 Calculation for R5 steel with sea water corrosion 174
6 Discussion 176
References of chapter IV 178

Actually, there are two ways of thinking about the effect of defects on the fatigue strength (or life) of metallic materials. The first one, a defect is considered as a crack which propagates (or not) under cyclic loading. In the second one, a defect is seen as a notch (and not a crack), consequently the fatigue strength of a metal with defect is governed by a fatigue crack initiation phase.

The discussion of researchers about these two ideas is especially important in the gigacycle regime because several industrial sectors design components against fatigue with a damage tolerant approach (assuming that the first consideration of the defect effect in fatigue is correct). This is the case of aeronautic industry. Other industries, like automotive industry, use a design methodology against crack initiation (fracture mechanics approach).

Since corrosion pits are geometrical defects in a mechanical point of view, the possible chemical effect of corrosion on the grain boundaries, the mechanical behavior of the material at the tip of the defect is neglected, and because in fatigue many authors consider there is no fatigue limit [9, 10] in the gigacycle regime [11] (it is not known in the teracycle regime, 10^{12} cycles, and it is not realistic for systems during one life of a man) due to the propagation of defects very early in the life of a component, the following chapter is devoted to the assessment of the fatigue crack propagation duration in the gigacycle regime for materials containing corrosion pits.

The Paris-Hertzberg crack growth law has been applied to determine analytically the number of cycles of propagation of specimens failed in fatigue with corrosion pits causing the crack initiation. Results of fatigue crack growth tests on R5 steel have shown a behavior so that the Paris-Hertzberg crack growth law can represent them. For the application to R5 steel some assumptions and hypotheses are necessary and these ones are presented in this chapter. All the calculations of the fatigue propagation duration for different cases of both pre-corroded specimens and corroded under sea water flow in real time are presented. Finally all the results are discussed.

1 Paris-Hertzberg crack growth law

Paris et al. [1] have noted a phenomenon that occurs between 10^6 and 10^8 cycles, where failure initiation may switch its location from the specimen surface to an internal “fish-eye”. When observing this, they questioned the significance of the crack growth portion of the fatigue life. This was done by using the Paris-Hertzberg crack growth rate law, which says that at the threshold corner of the crack growth curve [1]:

$$\frac{\mathrm{d}a}{\mathrm{d}N} = b \text{ and } \frac{\Delta K_{\mathrm{eff}}}{E\sqrt{b}} = 1 \tag{4. 1}$$

And beyond of the corner:

$$\frac{\mathrm{d}a}{\mathrm{d}N} = b\left(\frac{\Delta K_{\mathrm{eff}}}{E\sqrt{b}}\right)^3 \tag{4. 2}$$

Where:

a = Crack length

N = Cycle number

b = Burger's vector

ΔK_{eff} = Effective stress intensity factor range

E = Young's modulus of the material.

To take into account crack closure effect on the crack growth rate, the effective stress intensity factor range is considered as $\Delta K_{\mathrm{eff}} = K_{\max} - K_{\mathrm{open}}$. According to Paris et al [1] no crack closure occurs at high load ratios, hence in that case the ΔK_{th} for threshold is constant. But at low load ratio, crack closure occurs at a K level which is completely independent of the minimum load, resulting in a range in which $K_{\max}$ is constant for the threshold. In case of compressive loads it is considered that fatigue cracks do not close at the tip [2] then the ΔK_{eff} can be considered the $K_{\max}$.

Paris and Hertzberg [3, 2] have shown that certain da/dN curves for some materials have a behavior as described by equations (4. 1) and (4. 2) in the threshold corner and the slope of the da/dN curve respectively (Figure 4.1 and Figure 4.2).

Figure 4.3 shows an example from Hertzberg [3] where it is observed the crack growth rate of "small cracks" is faster than "long cracks" under the same nominal crack driving force.

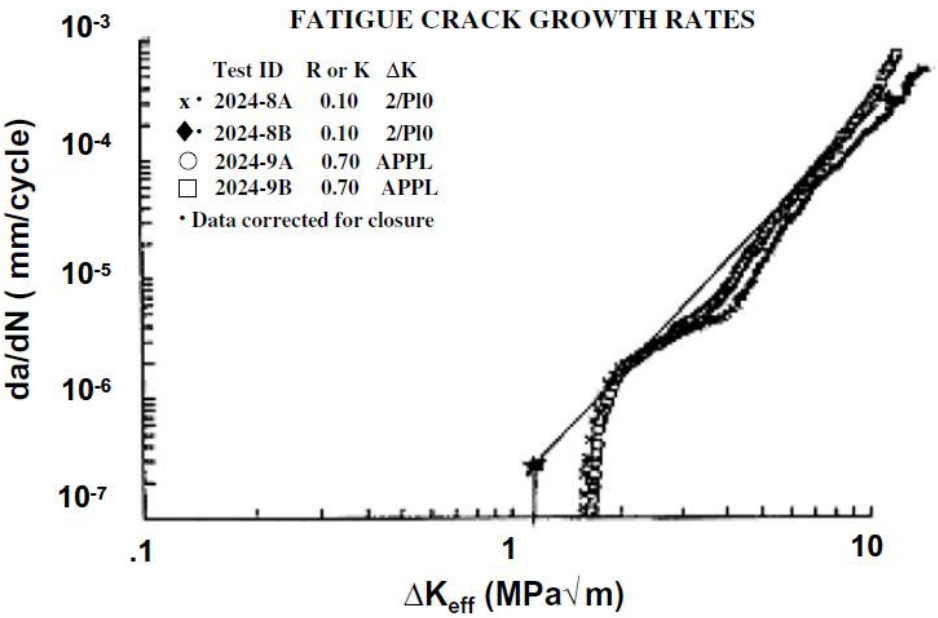

Figure 4.1. Predicted threshold corner and slope for 2024-T3 aluminium alloy [1].

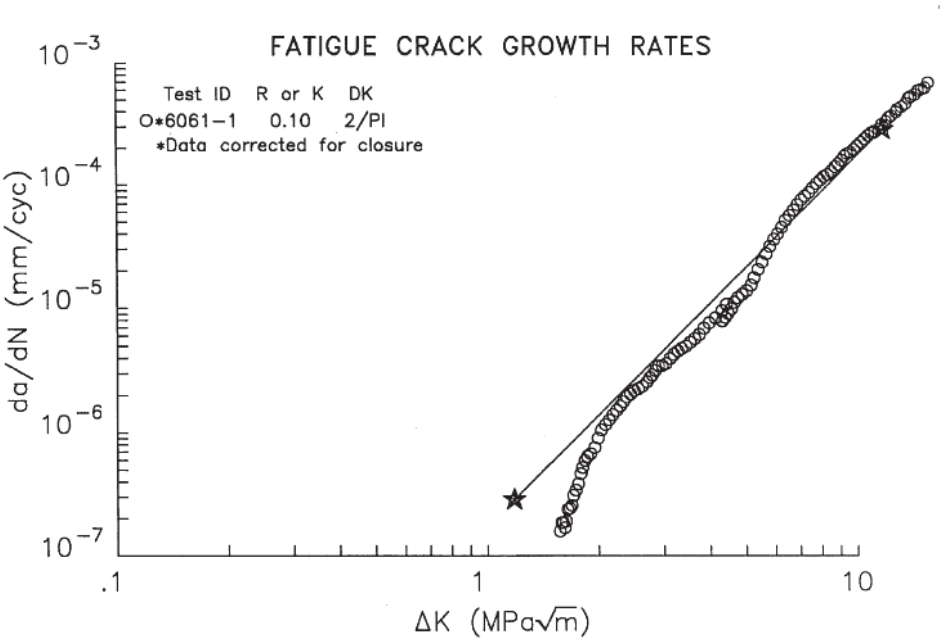

Figure 4.2. Predicted threshold corner and slope for 6061-1 aluminium alloy [1].

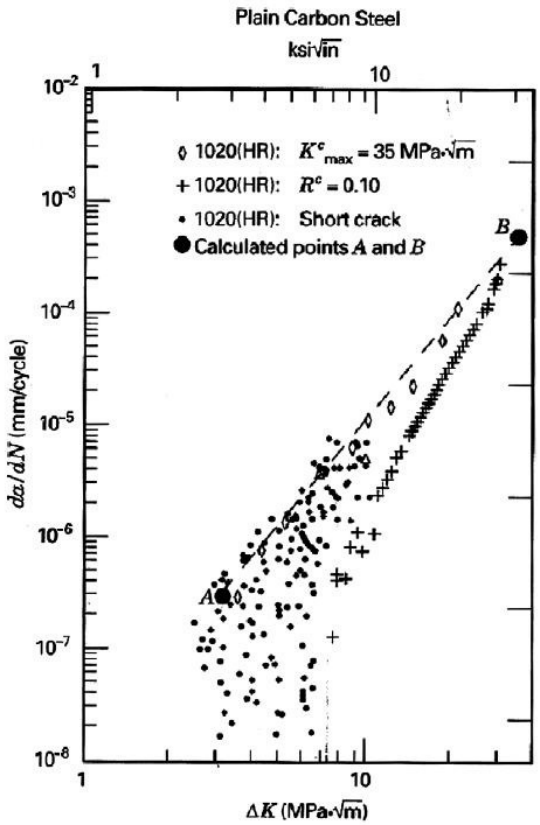

Figure 4.3. Long and short crack growth data for hot-rolled 1020 steel [2].

The Paris-Hertzberg crack growth rate law has been used to demonstrate that crack growth is not a significant portion of the total fatigue life over 10^7 cycles for a low carbon steel SAE 8620 and for a 100C6 martensitic steel, where crack initiation was located at the specimen interior, normally in defects called "fish-eye". This kind of failure only occurs at very high cycle fatigue over 10^7 cycles [1, 4 , 5].

Figure 4.4 shows schematically the hypothesis used by Paris-Marines-Hertzberg first in [1] then in [4, 5]. A small crack of size a_0 starts from a defect and propagates up to a_i. It is represented how crack growth rate is higher for small cracks than for long cracks [1, 4, 5]. The crack starts from a defect, first, with a size a_{int}. This is a short crack (short compared with the microstructural characteristics). Then this short crack propagates up to a_0 according with the following law: $\frac{\mathrm{d}a}{\mathrm{d}N} = \left(\frac{a}{a_0}\right)^{\alpha/2}$ under the threshold driving force in a dimensionless form: $\frac{\Delta K_{\text{th}}}{E\sqrt{b}} = 1$. Then the crack with length a_0 grows up to a_i (faster than long crack). This is a small crack growth (small in a mechanical point of view).

Figure 4.4 also shows a transition point from small crack to long crack which is located at a factor x in stress intensity from the threshold corner of small cracks. This factor have been observed as a maximum around 3 for low load ratios (R≈0) [1, 2, 4]. For high low ratios (R≥0.8) the factor x is around 1 [1, 2, 4].

In [1, 4, 5] the number of cycles of crack propagation of "fish-eyes" defects (Figure 4.5) was estimated by integration of Paris-Hertzberg law equations at the different stages showed in Figure 4.4. The results obtained in the gigacycle domain showed that a large portion of the fatigue life is due to initiation and the crack growth is not a significant part.

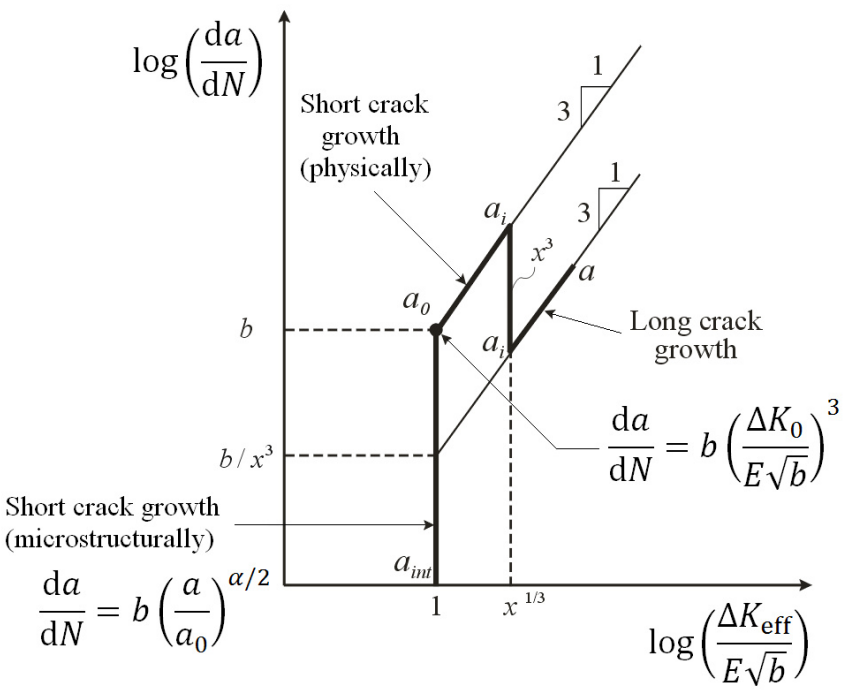

Figure 4.4. Model of fatigue crack growth behavior for short, small and long cracks according to [4].

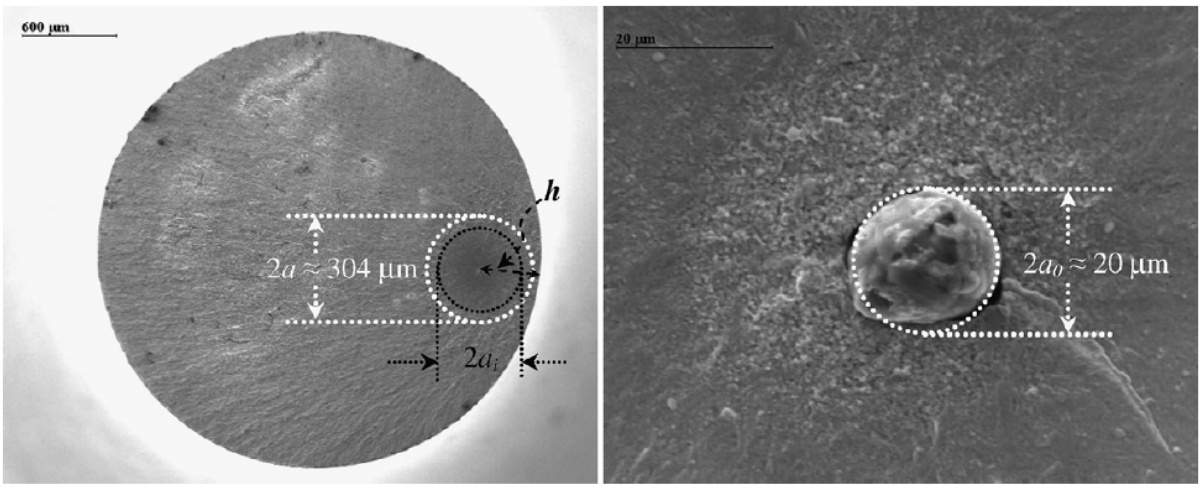

Figure 4.5. Example of internal fish-eye fatigue crack initiation of 100C6 martensitic steel (R=–1) [4].

Marines Garcia et al [4, 5] have used the Paris-Hertzberg law in order to determine the crack propagation duration period but for hemispherical corrosion pits instead of "fish eyes" (Figure 4.5). Since in this work the fatigue crack initiation sites for R5 steel are located in corrosion pits due to pre-corrosion before testing or created by corrosion under sea water flow in real time, a similar methodology to assess the crack propagation duration have been used.

2 Application of the Paris-Hertzberg law to corrosion pits

In the experimental section of this thesis the effect of corrosion on the gigacycle fatigue strength of R5 steel has been presented. Fatigue cracks initiated at corrosion pits due to pre-corrosion, if any, or at corrosion pits resulting from corrosion in real time during the cyclic loading. It has been shown that under sea water flow, the fatigue strength in the gigacycle regime is very influenced by the corrosion process.

The $da/dN = f(\Delta K)$ curve is illustrated in Figure 2.73. It shows that in air the mode I (R=–1) stress intensity threshold for R5 steel is around 3.27 MPa√m. A different way for presenting the da/dN curve is as function of the dimensionless crack driving force $\Delta K_{eff}/E\sqrt{b}$, like in the Paris-Hertzberg crack growth law. This is presented in Figure 4.6 for R5 steel in air and in sea water flow at room temperature. The Young's modulus (E) of R5 steel is 211 GPa, and the Burger's vector (b) is 0.285 nm. It is observed in Figure 4.6 that experimental $da/dN= f(\Delta K)$ results are in good agreement with equations (4. 1) and (4. 2) for the tests in air. For the tests under sea water flow we have seen in Chapter III that the crack growth is faster than in air as usually seen in literature.

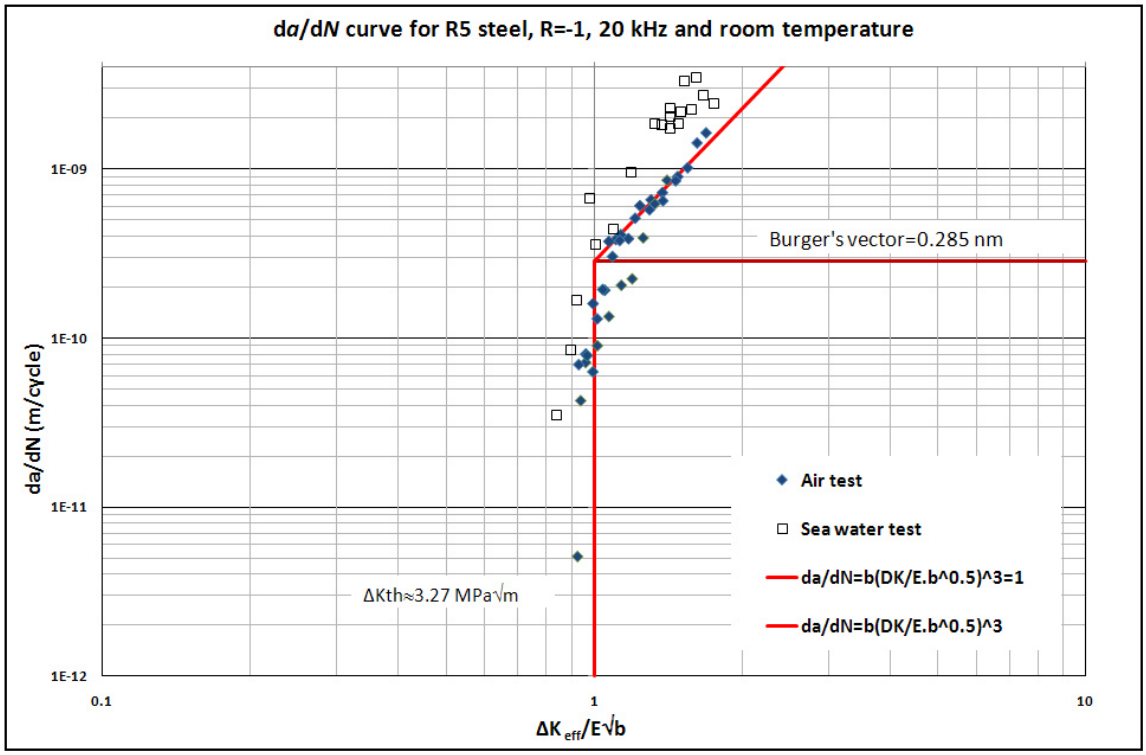

Figure 4.6. Experimental da/dN curve for R5 steel (20 kHz) as function of $\Delta K_{eff}/E\sqrt{b}$ in air and A3 sea water at R= –1 and room temperature.

2.1 Assumptions

It is necessary to list the main assumptions for using the equations of the previous section.

- Paris-Hertzberg crack growth law is applicable.
- For the experimental results, ΔK is calculated as described in section 4 of chapter II, with equation (2.3) proposed by Wu [7, 8] for the characteristic geometry of high frequency crack growth specimens (Chapter II Section 4).
- In fact, it is assumed that $\Delta K \approx K_{max}$ because K_{min} can be considered equal to zero if R<0. On the other hand, experimental determination of K_{op} is not possible at 20 kHz, then for $\Delta K_{eff} = K_{max} - K_{open}$, if K_{open} is neglected $\Delta K_{eff} \approx K_{max}$ (Figure 4.7).

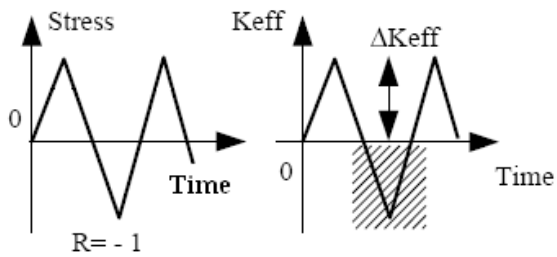

Figure 4.7. Assumption of the approximation for ΔK_{eff} assessment at 20 kHz.

- Defects are hemispherical voids (Figure 4.8) and in front of them there is an initial crack of the size a_{int} (Figure 4.8 and Figure 4.10).

2.2 Short crack initiation

To assess the duration of the crack propagation regime on R5 steel with corrosion, a corrosion pit with radius R is modeled as a hemispherical defect on the specimen surface (as shown in Figure 4.8). The occurrence of a fatigue crack of length a_{int} in the order of grain size, from the surface of the hemispherical pit and perpendicular to the loading direction (mode I) is assumed due to inter-crystalline corrosion cracking (as shown in Figure 4.10).

According to Palin-Luc et al [6] cracking from a hemispherical surface void with a spherical radius R and a crack of depth a measured from the surface of the hemispherical void (as shown in Figure 4.8) leads to a intensity factor K, which can be assessed by an asymptotic approximation:

$$K = \sigma\sqrt{\pi a}\, Y(x, \nu) \tag{4. 3}$$

Where $x = \frac{a}{R}$ for $0 \leq \frac{a}{R} \leq \infty$ and ν is the Poisson ratio and

$$Y(x, \nu) = 1.015\left[A(\nu) + B(\nu)\left(\frac{x}{1+x}\right) + C(\nu)\left(\frac{x}{1+x}\right)^2 + D(\nu)\left(\frac{x}{1+x}\right)^3\right] \tag{4. 4}$$

With the coefficients A, B, C and D:

$$A(\nu) = 1.683 + \frac{3.366}{7-5\nu}, \quad B(\nu) = -1.025 - \frac{12.3}{7-5\nu}, \quad C(\nu) = -1.089 + \frac{14.5}{7-5\nu}, \text{ and}$$
$$D(\nu) = 1.068 - \frac{5.568}{7-5\nu} \tag{4. 5}$$

For R= –1 and taking into account the assumption that $\Delta K_{eff} \approx K_{max}$ the ΔK_{eff} for a crack emanating from a hemispherical surface void with a spherical radius R and a crack of depth a can be expressed by:

$$\Delta K_{eff} = \sigma_a\sqrt{\pi a}\, Y(x, \nu) \tag{4. 6}$$

However, the factor 1.015 in Equation (4. 4) is for the deepest part of the crack in front of the surface forming the hemisphere.

For an angle θ measured from a line perpendicular to that surface (as shown in Figure 4.8), the factor 1.015 can be replaced by:

$$f(\theta) = 1.210 - 0.195\sqrt{\cos\theta} \tag{4. 7}$$

for

$$-80° \leq \theta \leq 80° \tag{4. 8}$$

in order to get the stress intensity factor along the crack front [6].

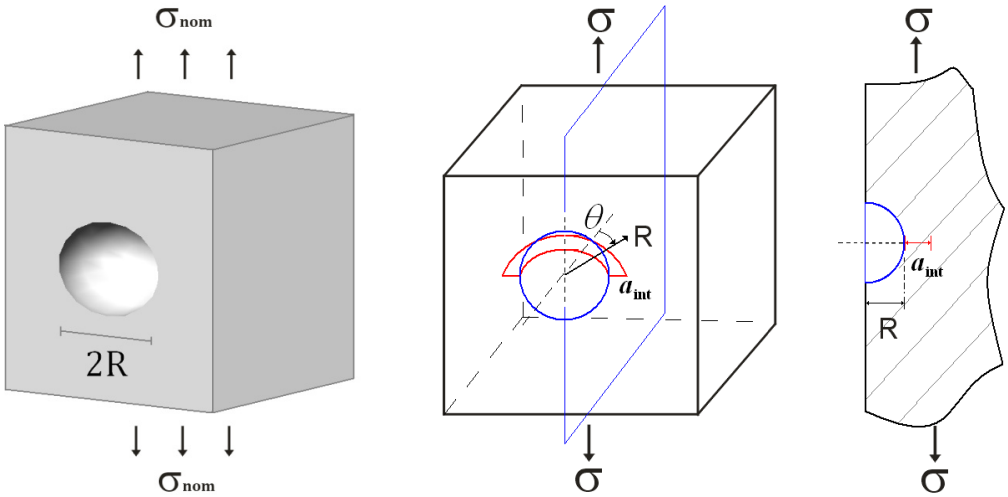

Figure 4.8. Approximation of a corrosion pit to an hemispherical void with a crack emanating from it [6].

Physical evidence

The existence of these hemispherical pits was observed by scanning electron microscopy on the surface of different specimens of R5 steel with pre-corrosion in salt fog chamber (Figure 4.9-a) and with corrosion in A3 sea water flow (Figure 4.9-b).

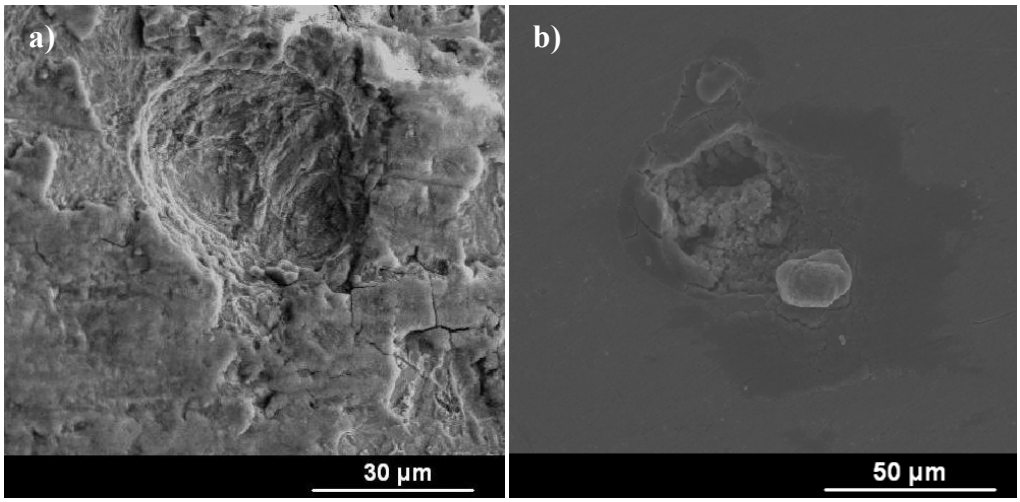

Figure 4.9. Pits created by corrosion on R5 specimens before testing. a) Pre-corroded in salt fog chamber, b) Corroded in sea water flow.

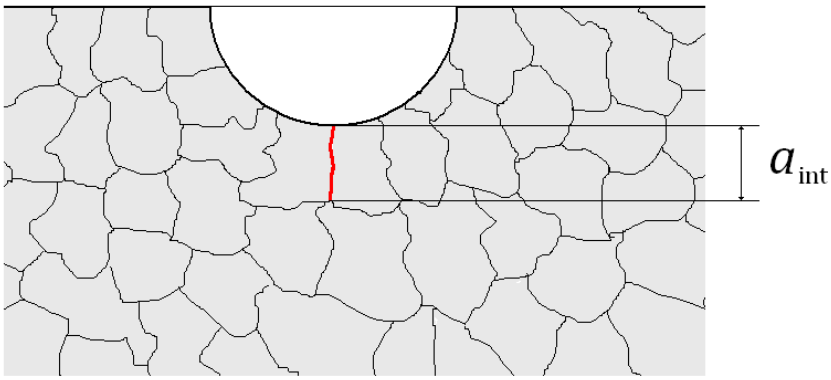

Figure 4.10. Hypothesis of crack length at initiation (scenario).

Figure 4.10 shows the scenario of an initial crack below the fracture face, in front of one pit. The crack is in the order of the grain size. To demonstrate the previous assumption, a specimen failed in fatigue containing pits was cut longitudinally (as shown in Figure 4.11) and observed by microscope.

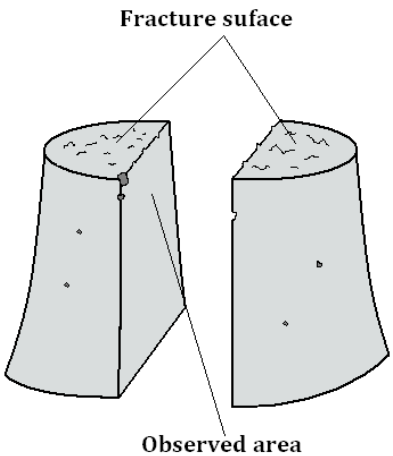

Figure 4.11. Sketch of specimen cut for observation with n optical microscope.

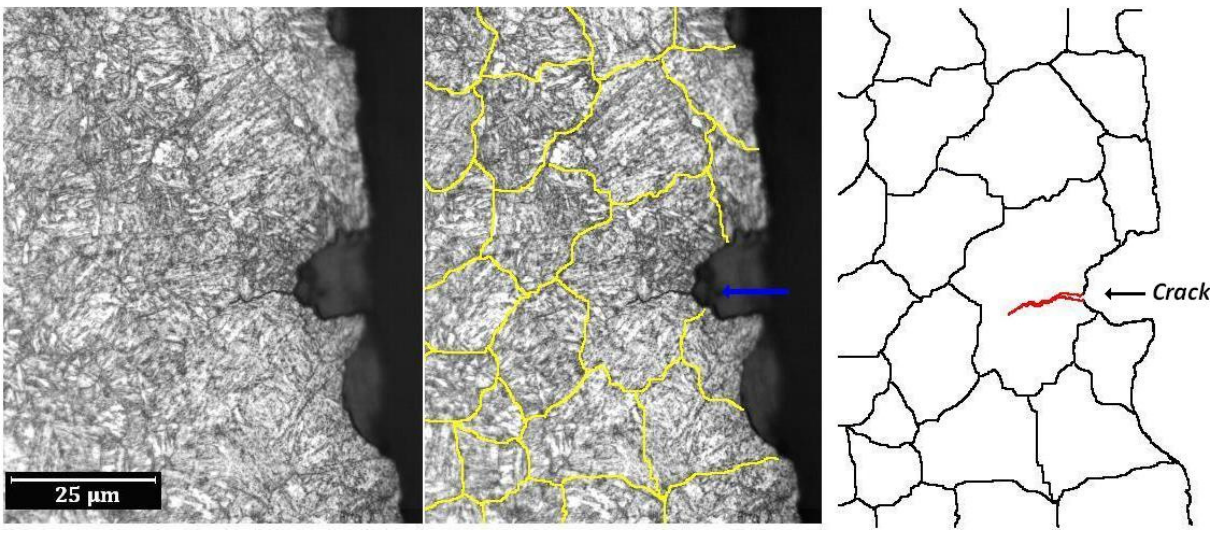

Figure 4.12. Crack in front of one corrosion pit in R5 steel (after nital etching).

In Figure 4.12 the old traces of austenite grains and a crack observed in front of a pit were highlighted in order to compare easily the initial size of this crack and the grain size. This prove the scenario proposed in Figure 4.10.

Figure 4.13 shows a comparison of R5 steel microstructure and the pits created by the two corrosion processes on the specimen surface. It is observed that corrosion is inter-crystalline. Pits are formed by grains boundary dissolution that is caused by corrosion process. In the case of corrosion in situ (by sea water flow), the pits that cause de fatigue fracture are possibly smaller in their radius when crack initiates, but the corrosion process continues during the propagation and when the fractography is carried out it is seen a bigger pit in the order of grain size (Figure 4.9 b). This is shown schematically in Figure 4.14.

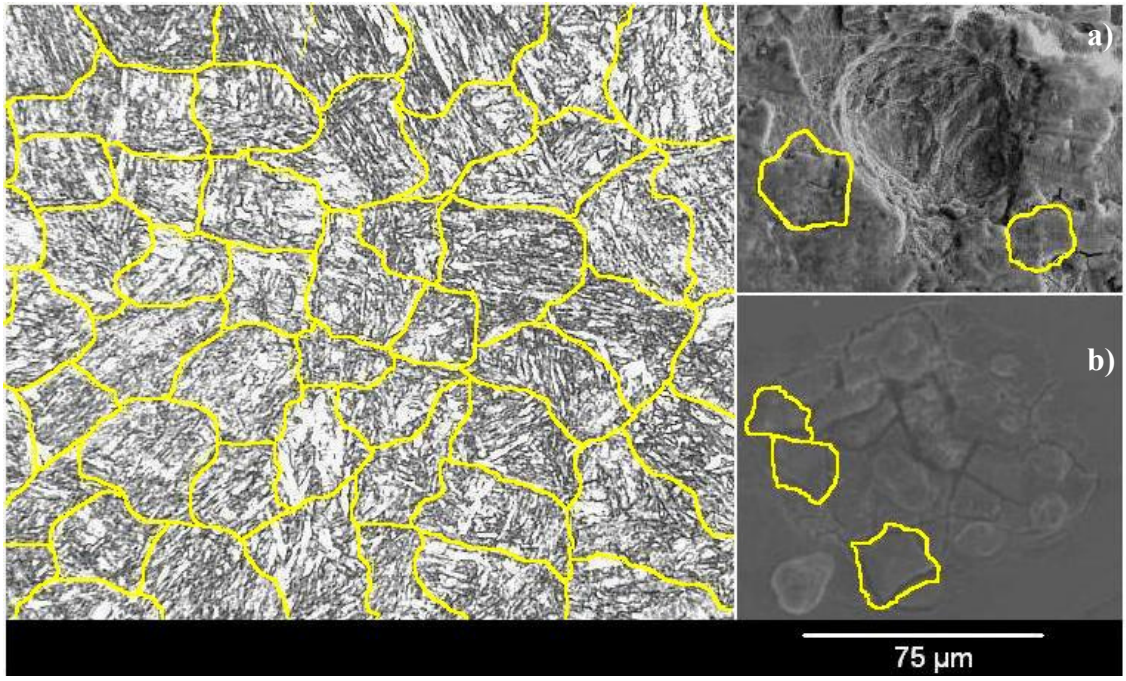

Figure 4.13. Pitting on R5 specimens surface compared with microstructure. a) pre-corroded in salt fog chamber, b) corroded in sea water flow.

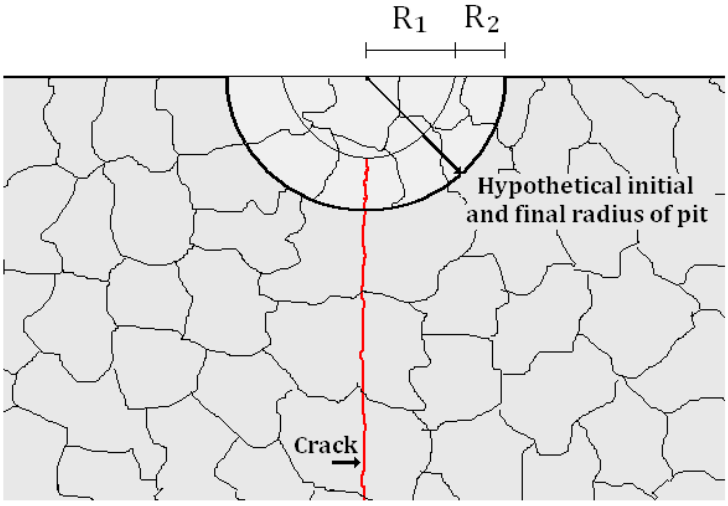

Figure 4.14. Hypothetical initial and final radius of pit due to intergranular corrosion in R5 steel.

In fact, the stress intensity factor varies as function of R and a. It can be calculated and compared for different radius with a crack at a specific stress level. The experience says us that pits created by corrosion have originally a size between 30 and 70 µm. With the assumption that initial crack is in the order of the grain size, an example can be given for an original pit with R=50 µm and a_0=10 µm (See Figure 4.12) loaded at 300 MPa and 400 MPa of stress amplitude.

ΔK calculated with Equation (4. 3) for R5 steel with Poisson's ratio ν=0.29:

At σ_a=300 MPa; for R=50 µm and a_0=10 µm; ΔK=3.059 MPa√m
for R=100 µm and a_0=10 µm; ΔK=3.426 MPa√m
for R=150 µm and a_0=10 µm; ΔK=3.572 MPa√m
for R=250 µm and a_0=10 µm; ΔK=3.609 MPa√m

At σ_a=400 MPa; for R=50 µm and a_0=10 µm; ΔK=4.077 MPa√m
for R=100 µm and a_0=10 µm; ΔK=4.568 MPa√m
for R=150 µm and a_0=10 µm; ΔK=4.726 MPa√m
for R=250 µm and a_0=10 µm; ΔK=4.903 MPa√m

It is observed that there is a variation at the initiation on the stress intensity factor depending of the pit radius, but it becomes constant as R is larger. Figure 4.15 shows a chart for the stress intensity factor as function of radius pit for an initial crack of 10 µm size and both 300 and 400 MPa of stress amplitude applied following Equation (4. 3). After a critical radius pit, no variation of ΔK is observed. This is around 250 µm for σ_a=300 MPa and 450 µm for σ_a=400 MPa. Then, if a crack initiates on a pit with radius R and we observe a bigger pit in fractographic analysis we can say that stress intensity was almost the same at initiation.

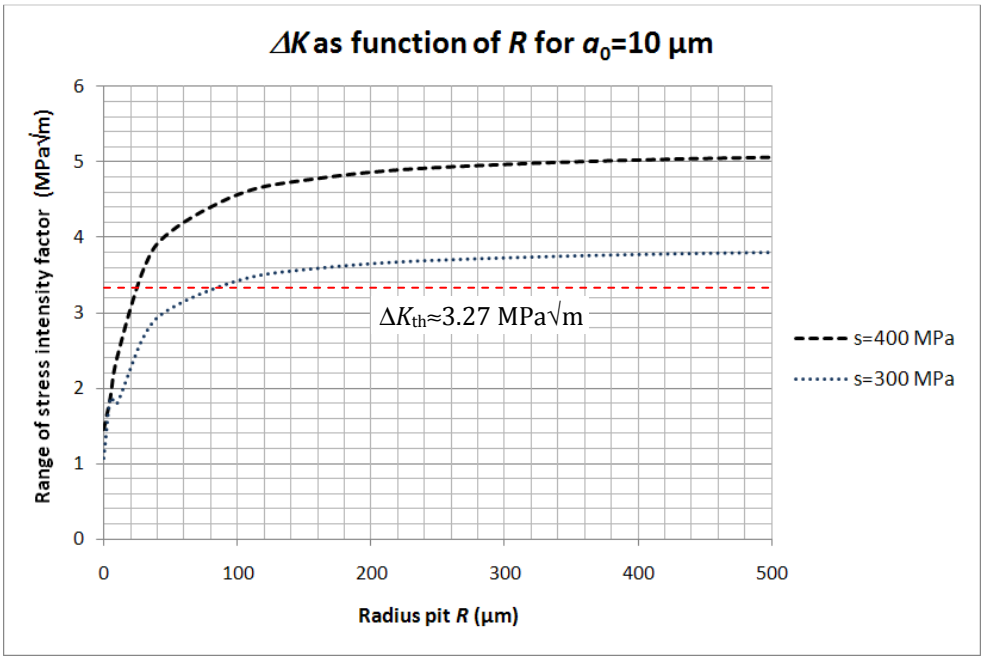

Figure 4.15. Stress intensity factor as function of radius growing with an initial crack of 10 µm of size.

Consequently all the microstructural and geometrical remarks, the following assumptions are considered:

- The crack initiation is intergranular.
- Short crack initiated in front of corrosion pits
- No interaction between crack growth and pit growth is considered because of the simultaneously corrosion process and crack propagation. Indeed crack initiation pits (areas) are observed post-mortem (there is no information of the pit size at initiation).

3 Determination of the propagation stages duration

It is assumed that the fatigue crack propagation is divided in three stages: (i) a short crack propagation during $N_{a\text{int}-a0}$ cycles, from initiation a_{int} to the crack size a_0, then (ii) a small crack propagation period of N_{a0-ai} cycles, from a_0 to the crack size a_i, and (iii) a long crack propagation N_{ai-a} cycles, from a_i to the final crack size a (See Figure 4.16). In the short crack growth regime from a_{int} to the crack size a_0, it was assumed that $\frac{\mathrm{d}a}{\mathrm{d}N} = b\left(\frac{a}{a_0}\right)^{\alpha/2}$ [1].

The integration of Equation (4. 1) and (4. 2) was done for determining the different crack growth regimes illustrated in Figure 4.4.

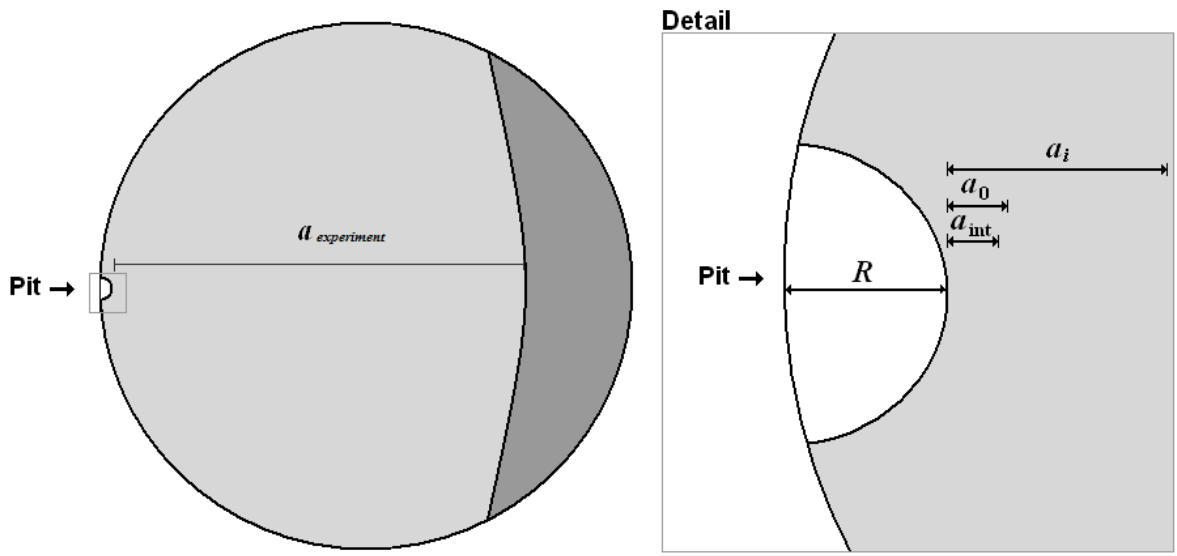

Figure 4.16. Sketch of the stages of fatigue crack propagation from pitting corrosion.

3.1 From a_{int} to a_0 (microstructural short crack growth regime)

This is the consideration of the number of cycles below the threshold corner. According to Paris et al [1] the growth curve below the corner has a very high slope, α (Figure 4.4). Then, the crack growth curve can be approximated by:

$$\frac{\mathrm{d}a}{\mathrm{d}N} = b\left(\frac{\Delta K}{E\sqrt{b}}\right)^{\alpha}\left(\frac{a}{a_0}\right)^{\alpha/2} \tag{4. 9}$$

But at the corner, by Equation (4. 1)

$$\frac{\mathrm{d}a}{\mathrm{d}N} = b\left(\frac{a}{a_0}\right)^{\alpha/2} \tag{4. 10}$$

Equation (4. 10) is integrated from an initial crack length a_{int} (Figure 4.8 and Figure 4.10) to a crack length a_0

$$N_{a_{\text{int}}-a_0} = \frac{a_0^{\alpha/2}}{b}\int_{a_{\text{int}}}^{a_0} a^{-\frac{\alpha}{2}}\mathrm{d}a \tag{4. 11}$$

Resulting

$$N_{a_{\text{int}}-a_0} = \frac{a_0^{\alpha/2}}{b\left(1-\frac{\alpha}{2}\right)}\left[a_0^{1-\alpha/2} - a_{\text{int}}^{1-\alpha/2}\right] \tag{4. 12}$$

And reordering

$$N_{a_{\text{int}}-a_0} = \frac{a_0\, a_0^{\left(\frac{\alpha}{2}-1\right)}}{b\left(\frac{\alpha}{2}-1\right)}\left[a_{\text{int}}^{-\left(\frac{\alpha}{2}-1\right)} - a_0^{-\left(\frac{\alpha}{2}-1\right)}\right] \tag{4. 13}$$

With

$$a_0 = \frac{E^2\, b}{Y\left(\frac{a_0}{R},\nu\right)^2 \sigma_a^2\, \pi} \tag{4. 14}$$

Because from Equation (4. 1) and (4. 6)

$$\frac{\sigma_a Y\left(\frac{a_0}{R},\nu\right)\sqrt{\pi a_0}}{E\sqrt{b}} = 1 \tag{4. 15}$$

Then the duration of short crack growth regime is given by:

$$N_{a_{\text{int}}-a_0} = \frac{E^2}{Y_0^2 \sigma_a^2 \pi(\alpha/2-1)}\left[\left(\frac{a_0}{a_{\text{int}}}\right)^{(\alpha/2-1)} - 1\right] \tag{4. 16}$$

With

$$Y_0 = Y\left(\frac{a_0}{R}, \nu\right) \tag{4. 17}$$

3.2 From a_0 to a_i (physical short crack growth regime)

As shown in Figure 4.4, small crack growth from a_0 to a_i will be faster than long crack growth. At the corner, the crack grows from a_0 to a_i describing a slope of 3 according to:

$$\frac{\mathrm{d}a}{\mathrm{d}N} = b\left(\frac{\Delta K}{E\sqrt{b}}\right)^3 \left(\frac{a}{a_0}\right)^{3/2} \tag{4. 18}$$

With $\frac{\mathrm{d}a}{\mathrm{d}N} = b$ and $\frac{\Delta K_0}{E\sqrt{b}} = 1$ at the corner. From Equation (4. 1) and combining with (4. 6)

$$\frac{\mathrm{d}a}{\mathrm{d}N} = \frac{b}{\left(E\sqrt{b}\right)^3}\left[Y(x,\nu)\sigma_a\sqrt{\pi a}\,\right]^3 \tag{4. 19}$$

Then, integrating Equation (4. 19) from a_0 to a_i

$$\int_{a_0}^{a_i} \mathrm{d}a \frac{\left(E\sqrt{b}\right)^3}{b\left(Y(x,\nu)\sigma_a\sqrt{\pi a}\right)^3} = \int_0^{N_{a_0-a_i}} \mathrm{d}N \tag{4. 20}$$

Assuming* that from a_0 to a_i.

$$Y\left(\frac{a}{R}, \nu\right) = \text{cte} \approx Y\left(\frac{a_0}{R}, \nu\right) \approx Y_0 \tag{4. 21}$$

* Note: Equation (4. 21) is only an assumption. However, some calculations were done in order to compare $Y(x,\nu)$ for values of a length characteristics in R5 steel experiments at this stage. The influence of the length a on ΔK is also checked, founding small differences (See Annex 8).

The integral of Equation (4. 20) can be written:

$$\frac{\left(E\sqrt{b}\right)^3}{b\left(Y\left(\frac{a_0}{R},\nu\right)\right)^3}\int_{a_0}^{a_i}\frac{\mathrm{d}a}{\left(\sigma_a\sqrt{\pi a}\right)^3}=\int_0^{N_{a_0-a_i}}\mathrm{d}N \tag{4. 22}$$

And applying the same expression of Equation (4. 15)

$$\frac{\left(\sqrt{a_0}\right)^3}{b}\int_{a_0}^{a_i}\frac{\mathrm{d}a}{\left(\sqrt{a}\right)^3}=\int_0^{N_{a_0-a_i}}\mathrm{d}N \tag{4. 23}$$

The result of integration is

$$N_{a_0-a_i}=\frac{\left(\sqrt{a_0}\right)^3}{b}\left[-2\left(\frac{1}{\sqrt{a_i}}-\frac{1}{\sqrt{a_0}}\right)\right]=\frac{2a_0}{b}\left(1-\frac{\sqrt{a_0}}{\sqrt{a_i}}\right) \tag{4. 24}$$

And considering the same expression than Equation (4. 14) and reordering

$$N_{a_0-a_i}=\frac{2E^2}{Y_0^2\sigma_a^2\pi}\left[1-\sqrt{\frac{a_0}{a_i}}\right] \tag{4. 25}$$

Equation (4. 25) describes the number of cycles for crack propagation of a crack from small length a_0 to a long length a_i.

3.3 From a_i to a_{final} (long crack growth)

The final stage of crack growth corresponds to long crack growth, which starts with a crack with a length a_i up to the final fracture of the specimen (a_{final}).

Due to the different behavior we must integrate the crack growth Equations (4. 1) and (4. 2) with a factor of reduction "$1/x^3$" (Figure 4.4).

For simplifying the notations a_{final} will be called only a in the following.

Then the equation to be integrated is:

$$\frac{\mathrm{d}a}{\mathrm{d}N}=\frac{b}{x^3}\left(\frac{\Delta K}{E\sqrt{b}}\right)^3 \tag{4. 26}$$

Or Equation (4. 26) can be written:

$$\frac{\mathrm{d}a}{\mathrm{d}N} = \frac{b}{x^3}\left(\frac{\sigma_a\,\sqrt{\pi a}\,Y\left(\frac{a}{R},\nu\right)}{E\sqrt{b}}\right)^3 \tag{4. 27}$$

Then, we integrate Equation (4. 27) from a_i to a

$$\frac{x^3\left(E\sqrt{b}\right)^3}{b}\int_{a_i}^{a}\left[\sigma_a\,\sqrt{\pi a}\,Y\left(\frac{a}{R},\nu\right)\right]^{-3}\mathrm{d}a = N_{a_i-a} \tag{4. 28}$$

Having at the corner

$$\frac{\sigma_a\,Y\left(\frac{a_0}{R}\right)\sqrt{\pi a_0}}{E\sqrt{b}} = 1 \tag{4. 29}$$

And

$$a_0 = \left(\frac{E\sqrt{b}}{\sigma_a\,Y\left(\frac{a_0}{R},\nu\right)\sqrt{\pi}}\right)^2 \tag{4. 30}$$

The integral can be written:

$$\frac{x^3\,Y\left(\frac{a_0}{R},\nu\right)\sqrt{a_0}\,E^2}{\sigma_a^2\,\pi}\int_{a_i}^{a}\left(\frac{1}{\sqrt{a}\,Y\left(\frac{a}{R},\nu\right)}\right)^3\mathrm{d}a = N_{a_i-a} \tag{4. 31}$$

Assuming * that from a_i to the final crack length a

$$Y\left(\frac{a}{R},\nu\right) \approx Y\left(\frac{a_i}{R},\nu\right) \approx \text{cte} \tag{4. 32}$$

$$N_{a_i-a} \cong \frac{-2x^3\sqrt{a_0}\,Y\left(\frac{a_0}{R},\nu\right)\,E^2}{\sigma_a^2\,\pi\,\left(Y\left(\frac{a_i}{R},\nu\right)\right)^3}\left[\frac{1}{\sqrt{a}} - \frac{1}{\sqrt{a_i}}\right] \tag{4. 33}$$

* Note: As the same way of Equation (4. 21) the assumption of Equation (4. 32) it is only simplification. Therefore, some calculations were done in order to compare $Y(x,\nu)$ for values of a, characteristics at this stage. The influence of a on ΔK was also checked, revealing small differences (See Annex 8).

Then for long crack growth next expression is given:

$$N_{a_i-a} = \frac{2E^2 Y_0}{Y(a_i/R)^3\ \sigma_a^2\ \pi}\left[x^3\sqrt{\frac{a_0}{a_i}} - x^3\sqrt{\frac{a_0}{a}}\right] \tag{4. 34}$$

3.4 Calculation of total propagation duration

The effect of the previous assumptions on the calculated number of cycles with the previous equations is not significant in comparison with numerical integration of the crack growth function. It was determined computing the different durations of Equations (4. 16), (4. 25) and (4. 34) using the assumptions for each case and comparing with the results using the mathematical integration of the crack growth curve with numerical integration depending of each stage. This numerical integration was done by using the Mathematica 5.2 software. The results of calculations using the numerical integration and using the assumptions of Equations (4. 17), (4. 21) and (4. 32) were of the same order, and the calculated propagation duration was always a small portion of the total fatigue life. A complete table of examples of such calculations is shown in Annex 8.

Finally, the total crack propagation duration is given by the addition of the results of Equations (4. 16), (4. 25) and (4. 34) (short crack + small crack + long crack):

$$N_{Prop} = N_{a_{\text{int}}-a_0} + N_{a_0-a_i} + N_{a_i-a} \tag{4. 35}$$

Furthermore, the estimation of propagation duration using Equation (4. 35) was compared with Equation (4. 36) proposed by Paris [1, 2] as a roughly approximation of the propagation period:

$$N_P = \frac{\pi E^2}{2(\sigma_a)^2} \tag{4. 36}$$

For starting a calculation, from:

$$\frac{\Delta K_{\text{eff}}}{E\sqrt{b}} = \frac{1.015\ \sigma_a \sqrt{\pi a}\ \ Y\left(\frac{a}{R}, \nu\right)}{E\sqrt{b}} \tag{4. 37}$$

With, E, b, σ_a and ν known, a_0 and a_i are obtained

$$a_0 \rightarrow \frac{\Delta K_{\text{eff}}}{E\sqrt{b}} = 1\ ; \quad a_i \rightarrow \frac{\Delta K_{\text{eff}}}{E\sqrt{b}} = 3$$

a_{int} is calculated for each value of a_{int}/a_0. a is obtained by measuring the end of the fracture observed on the fracture surface of the fractographies.

In the next sections the calculation with Equations (4. 35) and (4. 36) is presented. Both equations give results in the same order of magnitude, in a roughly approximation considering the total number of cycles experimentally.

The value of α in Equation (4. 10) and (4. 16) is implicit in the slope of the da/dN curve in the short crack regime. It means that at higher α the crack does not grow as far due to the slope of the da/dN curve in the threshold regime, then a_{int}/a_0 must be larger. On the contrary, with lower α, a_{int}/a_0 must be smaller. In the next sections some calculations are presented by using this assessment.

4 Calculation for R5 steel with pre-corrosion

Some experimental cases for R5 steel specimens tested in pre-corrosion and failed due to hemispherical pits were considered for calculating the crack propagation duration using the approximation presented in section 3. Table 4.1 shows the three stages calculation for three pre-corroded specimens tested at different stress levels and with fatigue lives between 10^7 to 10^9 cycles. $x = 3$, $\alpha = 25$, 100 and 200, and different a_{int}/a_0 ratios were considered.

For instance, the case 1 in the table 4.1 shows the example of calculation for a pre-corroded specimen with a pit of radius R=48 µm (Figure 4.17) with experimental number of cycles for failure $N_{experimental}$=5.5×10^8 cycles. In this case, 99.1% of the fatigue life is due to initiation according with the number of cycles of propagation calculated with Equation (4. 35).

α	a_{int}/a_0	$N_{a_{int}-a_0}$	$N_{a_0-a_i}$	N_{a_i-a}	N_{Prop}	N_{Prop}/N_{exp}	N_P	N_P/N_{exp}
Case 1: σ_a=360 MPa, R=48 µm, a_0=9.32 µm, a_i=88.4 µm, a=2.4 mm, $N_{experimental}$ = 5.5×10^8 cycles								
25	0.9	6,704	44,151	4,507,080	4,557,935	0.00832	539,000	0.00098
	0.94	2,947			4,554,178	0.00831		
	0.97	1192			4,552,423	0.00830		
100	0.9	115,801	44,151	4,507,080	4,667,032	0.00852		
	0.94	13,136			4,564,394	0.00833		
	0.97	2,300			4,553,531	0.00831		
200	0.9	11,184,860	44,151	4,507,080	15,736,091	0.02871		
	0.94	150,676			4,701,907	0.00858		
	0.97	6,404			4,557,635	0.00832		
Case 2: σ_a=370 MPa, R=70 µm, a_0=7.104 µm, a_i=24.9 µm, a=2.15 mm, $N_{experimental}$ = 4.4×10^8 cycles								
25	0.9	5,113	23,220	1,402,860	1,431,193	0.00327	510,836	0.00116
	0.94	2,248			1,428,328	0.00326		
	0.97	909			1,426,989	0.00326		
100	0.9	88,331	23,220	1,402,860	1,541,411	0.00346		
	0.94	10,041			1,436,121	0.00329		
	0.97	1,754			1,427,834	0.00327		
200	0.9	8,531,566	23,220	1,402,860	9,957,646	0.02278		
	0.94	114,932			1,541,012	0.00352		
	0.97	4,884			1,430,964	0.00327		
Case 3: σ_a=425 MPa, R=38 µm, a_0=6.28 µm, a_i=51.32 µm, a=1.96 mm, $N_{experimental}$ = 1.56×10^7 cycles								
25	0.9	4,519	28,651	2,717,227	2,750,397	0.17190	387,175	0.02482
	0.94	1,987			2,747,865	0.17174		
	0.97	804			2,746,682	0.17167		
100	0.9	78,065	28,651	2,717,227	2,823,943	0.17650		
	0.94	8,874			2,754,752	0.17217		
	0.97	1,550			2,747,428	0.17171		
200	0.9	7,540,073	28,651	2,717,227	10,285,951	0.64287		
	0.94	101,575			2,847,453	0.17797		
	0.97	4,317			2,750,195	0.17189		

Table 4.1. Calculation of hemispherical surface crack growth compared with experimental fatigue life on some pre-corroded specimens with x=3, α=25, 100 and 200, and different a_{int}/a_0 ratios.

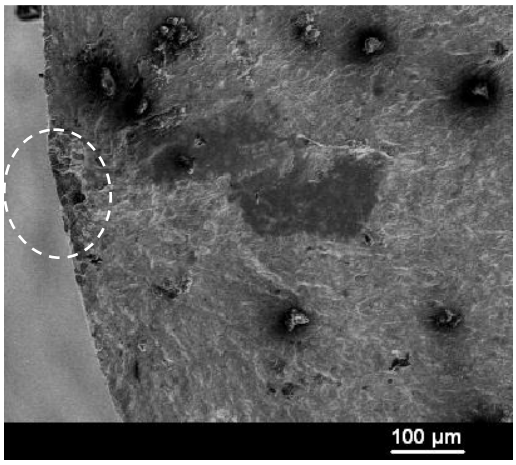

Figure 4.17. Radius of the crack initiation pit on a R5 steel pre-corroded specimen, tested at σ_a=360 MPa, failed at N_f= 5.5×10^8 cycles (R= –1).

In the 7th and 9th columns of Table 4.1 are presented the ratios between the calculated crack propagation duration and the total fatigue life of each case (experimental number of cycles to failure). In all cases the fatigue crack growth period is a small portion of the total life, except for α=200 and a_{int}/a_0=0.9 in the case 3.

For α=200 and a_{int}/a_0=0.9 the calculation gives larger estimation. That is because the relation a_{int}/a_0=0.9 implies a larger difference between a_0 and a_{int} than with a_{int}/a_0 higher, additionally, the high α=200 is related to slower crack growth rate.

Assuming a crack propagation life for each case (an average for instance, discarding the result for α=200 and a_{int}/a_0=0.9), the results can be plotted in a chart of proportionality as shown in Figure 4.18. It is observed that the proportion of crack growth period is small compared with the total life. The proportion of crack growth period is higher as the total fatigue life is smaller. This prove the high importance of crack initiation in the gigacycle regime even with pits present, all the fatigue life is not governed by propagation.

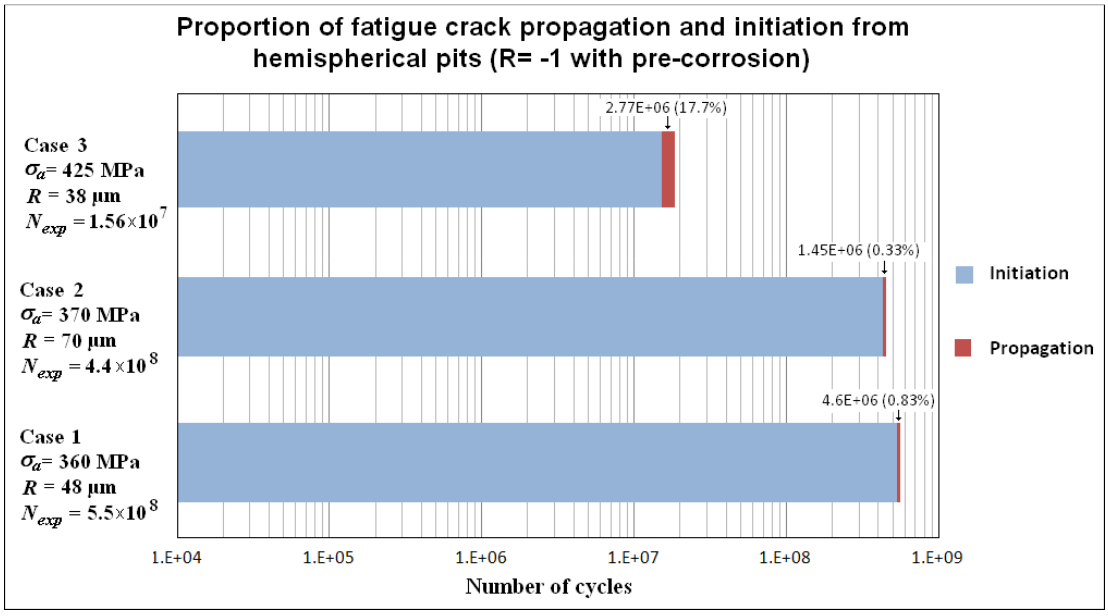

Figure 4.18. Crack propagation and crack initiation durations for R5 steel with hemispherical pits from pre-corrosion.

5 Calculation for R5 steel with sea water corrosion

Other experimental cases for R5 steel specimens tested during simultaneous corrosion in artificial sea water flow and failed due to pitting corrosion were considered for application of the approximations presented in Section 4.2. Table 4.2 shows the calculation for the three stages of propagation of five specimens tested at different stress levels and with fatigue lives between 7×10^6 and 2×10^8 cycles. x = 3, α = 25, 100 and 200, and different a_{int}/a_0 ratios were considered.

For instance, the Case 4 in the table 4.2 shows the example of a R5 steel specimen tested in sea water flow. After failure the fractography showed an initiation pit of radius R=300 µm (Figure 4.19). The experimental number of cycles to failure for this example was $N_{experimental}$=1.83×10^8 cycles, that compared with the calculated portion of crack propagation, this last portion represents 5.7% of the total life only.

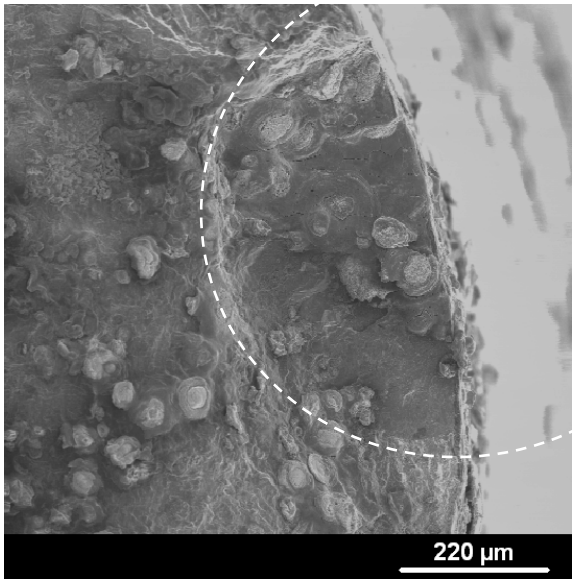

Figure 4.19. Radius of crack initiation pit on a R5 steel specimen, tested in sea water flow at σ_a=160 MPa, failed at N_f= 1.83×10^8 cycles (R= –1)

Like in Table 4.1, the 7th and 9th columns of Table 4.2 are present the proportions of the calculated crack propagation duration in relation with the total experimental number of cycles to failure for each case. It is observed that fatigue crack propagation is a small portion of the total life in all the cases and like with pre-corrosion, for α=200 and a_{int}/a_0=0.9 the calculation gives larger estimation. The reason is the same, a_{int}/a_0=0.9 implies a "large" difference between a_0 and a_{int} and the high value of α (α=200) is related to slower crack growth rate, probably unrealistic.

As with pre-corrosion, we can assume a crack propagation life for each case and plot the results in a chart of proportionality (Figure 4.20) observing that the proportion of crack growth period is very low compared with the total life. Also for pitting from corrosion in sea water flow in real time the proportion of crack growth period is higher as the total fatigue life is smaller.

α	a_{int}/a_0	$N_{a_{int}-a0}$	N_{a0-ai}	N_{ai-a}	N_{Prop}	N_{Prop}/N_{exp}	N_P	N_P/N_{exp}
Case 4: σ_a=160 MPa, R=300 µm, a_0=41.5 µm, a_i=232 µm, a=2.6 mm, $N_{experimental}$ = 1.83×10^8 cycles								
25	0.9	29,840	168,014	10,258,700	10,456,554	0.05652	2,731,700	0.01493
	0.94	13,120			10,439,834	0.05643		
	0.97	5,306			10,432,020	0.05639		
100	0.9	515,466	168,014	10,258,700	10,942,180	0.05915		
	0.94	58,593			10,485,307	0.05668		
	0.97	10,237			10,436,951	0.05642		
200	0.9	49,787,104	168,014	10,258,700	60,213,818	0.32548		
	0.94	670,703			11,097,417	0.05999		
	0.97	28,504			10,455,218	0.05651		
Case 5: σ_a=350 MPa, R=200 µm, a_0=6.66 µm, a_i=15.57 µm, a=2.3 mm, $N_{experimental}$ = 7.4×10^6 cycles								
25	0.9	4,796	16,174	902,654	923,624	0.12481	570,885	0.07714
	0.94	2,109			920,937	0.12445		
	0.97	853			919,681	0.12428		
100	0.9	82,854	16,174	902,654	1,001,682	0.13536		
	0.94	9,481			928,246	0.12544		
	0.97	1,645			920,473	0.12439		
200	0.9	8,002,548	16,174	902,654	8,921,376	1.20559		
	0.94	107,806			1,026,634	0.13873		
	0.97	4,582			923,410	0.12479		
Case 6: σ_a=260 MPa, R=135 µm, a_0=14.6 µm, a_i=54.79 µm, a=2.81 mm, $N_{experimental}$ = 3.49×10^7 cycles								
25	0.9	10,530	49,619	2,977,594	3,037,743	0.08679	1,034,518	0.02964
	0.94	4,630			3,031,843	0.08662		
	0.97	1,872			3,029,085	0.08655		
100	0.9	181,902	49,619	2,977,594	3,209,115	0.09169		
	0.94	20,677			3,047,890	0.08708		
	0.97	3,613			3,030,826	0.08660		
200	0.9	17,569,325	49,619	2,977,594	20,596,538	0.58847		
	0.94	236,684			3,263,897	0.09325		
	0.97	10,059			3,037,272	0.08678		
Case 7: σ_a=240 MPa, R=220 µm, a_0=15.65 µm, a_i=43.92 µm, a=2.88 mm, $N_{experimental}$ = 5.2 ×10^7 cycles								
25	0.9	11,267	44,271	2,431,480	2,487,018	0.04764	1,214,122	0.02335
	0.94	4,954			2,480,705	0.04752		
	0.97	2,003			2,477,754	0.04747		
100	0.9	194,621	44,271	2,431,480	2,670,372	0.05116		
	0.94	22,123			2,497,874	0.04785		
	0.97	3,865			2,479,616	0.04750		
200	0.9	18,797,746	44,271	2,431,480	21,273,497	0.40754		
	0.94	253,232			2,728,983	0.05228		
	0.97	10,762			2,486,513	0.04763		
Case 8: σ_a=200 MPa, R=290 µm, a_0=23.01 µm, a_i=67.96, a=2.81 mm, $N_{experimental}$ = 1.08 ×10^8 cycles								
25	0.9	16,566	67,524	3,624,895	3,708,984	0.03372	1,748,336	0.01619
	0.94	7,283			3,699,701	0.03363		
	0.97	2,946			3,695,364	0.03359		
100	0.9	286,158	67,524	3,624,895	3,978,576	0.03617		
	0.94	32,528			3,724,946	0.03386		
	0.97	5,683			3,698,101	0.03362		
200	0.9	27,639,000	67,524	3,624,895	31,331,418	0.28483		
	0.94	372,337			4,064,755	0.03695		
	0.97	15,824			3,708,242	0.03371		

Table 4.2. Calculation of hemispherical surface crack growth compared with experimental fatigue life on some specimens tested under sea water flow with x=3, α=25, 100 and 200, and different a_{int}/a_0 ratios.

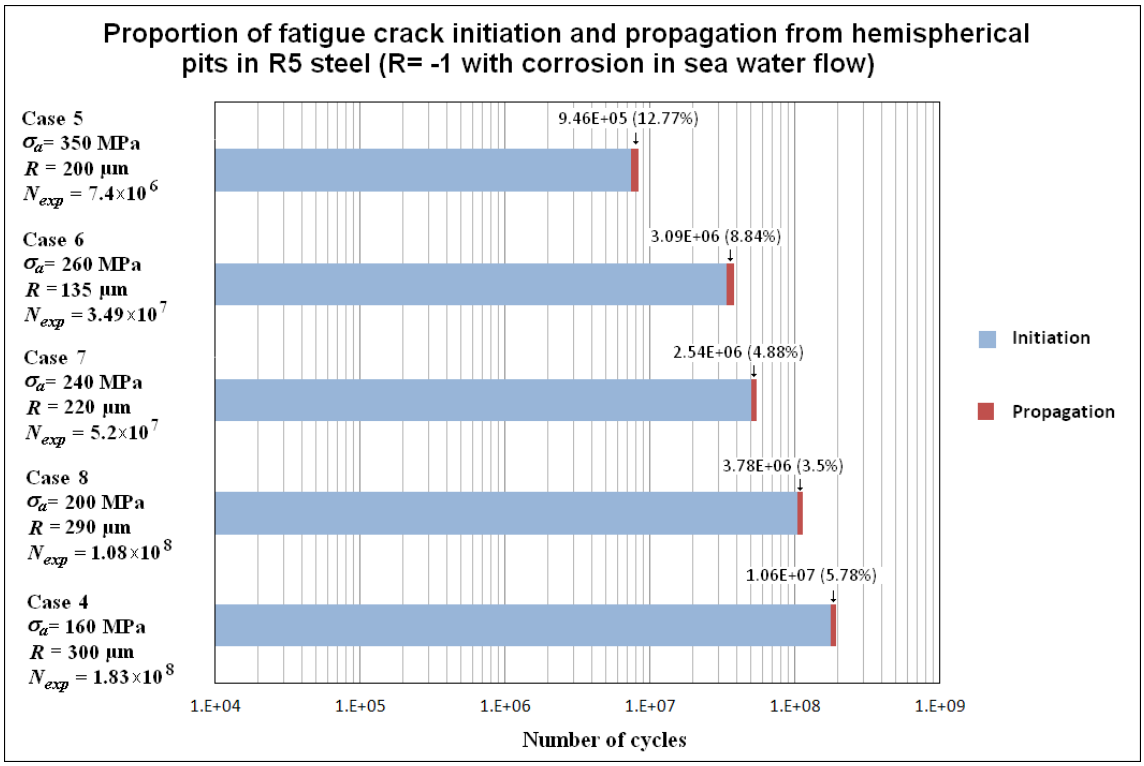

Figure 4.20. Crack propagation and crack initiation durations for R5 steel with hemispherical pits from sea water corrosion in real time.

6 Discussion

The calculation of the mode I stress intensity factor at hemispherical surface defects (pits) combined with the Paris–Hertzberg crack growth rate law showed that fatigue crack initiation regime represents most of the fatigue life even if surface defects like pits are presenta.

For both, pre-corroded specimens and specimens corroded in sea water flow, fatigue life is dominated by the crack initiation stage as soon as the fatigue life is more than ~10^7 cycles.

Results of calculations in Tables 4.1 and 4.2 show that the duration of propagation period is small compared with the total fatigue life of the specimen, except for α=200 and a_{int}/a_0=0.9.

From the examples on Tables 4.1 and 4.2 it is noticed that with high α and large a_{int}/a_0 similar N_{Prop} results are obtained than with a low α and small a_{int}/a_0. That is because with a higher α the crack does not grow as far due to the slope of the da/dN curve in the threshold region, then a_{int}/a_0 must be larger, and with a lower α, a_{int}/a_0 must be smaller.

In fact, all the cases with α=200 and a_{int}/a_0=0.9 the calculation gives larger estimation. That is because the relation a_{int}/a_0=0.9 implies a larger difference between a_0 and a_{int} than with a_{int}/a_0=0.94 or a_{int}/a_0=0.97, and the high α=200, implies a slower crack growth rate due to the slope of the da/dN curve in the threshold regime.

The calculations presented in Tables 4.1 and 4.2 were done assuming that the crack growth rate is similar in air and under sea water flow. But according with the crack growth rate results in sea water flow one can observe that crack growth is little faster than in air, then the number of cycles of propagation can be lower. This does not change the conclusion that crack initiation dominates the fatigue life.

In fact, it is necessary to keep in mind that for the specimens tested under sea water flow, crack initiation may be simultaneous with the corrosion pit growth, as mentioned before with the idea of Figure 4.14. This is not the case of the pre-corroded specimens. In this work, the part of the fatigue crack trajectory respective to the corrosion pit growth has not been distinguished. The calculations were done using the final pit size observed in fractographies. This may lead to an error in the assessment of the crack propagation duration under sea water flow, but we do not know how to do without this assumption. Future work has to be carried out to try to investigate the kinetics of corrosion pits and crack simultaneously.

References of chapter IV

1. Paris, P.C., and Marines Garcia, I., and Hertzberg, R.W., and Donald, K., 2004, *The relationship of effective stress intensity, elastic modulus and Burgers-vector on fatigue crack growth as associated with ‘‘fish eye’’ gigacycle fatigue phenomena*. In: Proceedings of VHCF-3, Kyoto, Japan, pp. 1–13.
2. Paris, P.C., and Tada, H., and Donald, J.K., 1999, *Service load fatigue damage – a historical perspective*, International Journal of Fatigue 21, pp. 35-46.
3. Hertzberg, R.W., 1995, *On the calculation of closure-free fatigue crack propagation data in monolithic metallic alloys*, Materials Science en Engineering A 190, pp. 25-32.
4. Marines García, I., and Paris, P.C., and Tada, H., and Bathias, C., and Lados, D., 2008, *Fatigue crack growth from small to large cracks on very high cycle fatigue with fish-eye failures*, Engineering Fracture Mechanics, Volume 75, pp. 1657-1665.
5. Marines García, I., and Paris, P.C., and Tada, H., and Bathias, C., 2007, *Fatigue crack growth from small to long cracks in very-high-cycle fatigue with surface and internal “fish-eye” failures for ferrite-perlitic low carbon steel SAE 8620*, Materials Science and Engineering A 468-470, pp. 120-128.
6. Paris, P.C., and Palin-Luc, T., and Tada, H., and Saintier, N., 2009, *Stresses and crack tip stress intensity factors around spherical and cylindrical voids and inclusions of differing elastic properties and with misfit sizes*, In: Proceedings of International Conference on Crack Paths (FCP2009), Vicenza, Italy, pp. 495-502.
7. Wu, T.Y., 1992, *Modélisation de la fissuration en fatigue vibratoire à haute température, applications aux alliages à base de nickel*. PhD Thesis, ECP, France.
8. Wu, T.Y., and Bathias, C., 1994, *Application of fracture mechanics concepts in ultrasonic fatigue*, Engineering Fracture Mechanics, Volume 47(5), pp. 683-690.
9. Bathias, C., 1999, *There is not infinite fatigue life in metallic materials*, Fatigue & Fracture of Engineering Materials and Structures, Volume 22, pp.559-565.
10. Terentev, V.F., 2004, *On the problem of the fatigue limit on metallic materials*, Metal Science and Heat Treatment 46, pp. 244-249.
11. Mughrabi, H., 2006, *Specific features and mechanisms of fatigue in the ultrahigh cycle regime*, International Journal of Fatigue, Volume 28, pp. 1501-1508.

Conclusion and prospects

The study of the fatigue strength in the gigacycle regime of both AS7G06-T6 cast aluminium alloy and R5 steel has been carried out in this work. The literature review has shown that there is no a fatigue limit in some metallic alloys and the *S-N* curves of some materials do not exhibit any asymptotic behavior in the very high cycle regime. For each alloy studied in this work, special testing conditions were applied for fatigue testing. The conclusions and perspectives of each material are presented in the following.

AS7G06-T6 cast aluminium alloy

The gigacycle fatigue tests carried out on smooth specimens made of AS7G06-T6 cast aluminium alloy have shown a significant decrease in the fatigue strength in the gigacycle regime compared with the fatigue strength in the megacycle regime. The reduction factor in the fatigue strength between the gigacycle regime and the megacycle regime at room temperature is about 1.6 for R= –1 and 2.0 for R=0.01. This demonstrates that there is no asymptotic fatigue behavior in the range 10^6 to 10^9 cycles. The fatigue strength at 150 °C decreases of around 10 MPa in the gigacycle regime compared with the fatigue strength at room temperature. At 150 °C there is also a decreasing in the fatigue strength in the gigacycle regime compared with the megacycle regime. Such data are significant for designing components against fatigue for very long life such as aeronautic turbines.

The cause of fatigue crack initiation in AS7G06-T6 cast aluminium alloy in the gigacycle regime are mainly fabrication defects such as porosities or shrinkages at both room temperature and 150 °C although there is a competition between these defects and slip bands generating quasi-cleavage fracture.

The tests results on AS7G06-T6 allowed us to observe the effect of two important factors in the fatigue strength: the temperature and the mean stress.

The temperature effect between 20°C and 150 °C is small for tests at R= –1. The fatigue strength at 150 °C is 11 MPa lower than the fatigue strength at 20 °C. On the contrary, for the tests at R=0.01the fatigue strength at 150 °C is 9 MPa higher than the fatigue strength at 20 °C. It is possible that the fatigue behavior is practically similar at 20 °C than 150 °C.

The experimental fatigue strengths for AS7G06-T6 alloy have been presented in the Haigh diagram. This shows that the results at room temperature do not follow the Goodman threshold. It was observed in the Haigh diagram that fatigue strengths at low R ratio lie on the Goodman threshold, but at higher R ratio, such as 0.5, the fatigue strength lies on the Gerber's parabola.

Microscopic observations (optic and SEM) of the fracture surface carried out on AS7G06-T6 have shown different characteristics depending of the testing conditions, but porosities are always the fatigue crack initiation causes. At room temperature under fully reversed tension-compression (R= –1), defects like shrinkages or porosities near or at the specimen surface are the main cause of crack initiation, although at high stress levels rupture by quasi-cleavage appears. At R=0.01 and room temperature, porosities at the specimen surface or little inside of

the specimen cause the crack initiation, however slip bands are more present than at R=–1 on the fracture surface. Porosities are the crack initiation sites at R=0.5 also, though quasi-cleavage around the crack initiation sites is present.

The results showed that fatigue strength was higher at R=0.5 than R=0.01 which is not common according to the literature. In the fractography analysis it was observed that characteristics crack initiation sites were porosities near to the specimen surface. The measure of areas of porosities was done. It was observed that porosities were bigger in the specimens tested at R=0.01 compared with the specimens tested at R=0.5. Big defects such as porosities influence negatively the fatigue strength and the fatigue life of AS7G06-T6 aluminium alloy. The pore size has an important influence on the fatigue life, fatigue life is decreasing with the size of shrinkage.

At 150 °C and R= –1 porosities are also causing crack initiation. Competition between rupture caused by quasi-cleavage and porosities appeared observing almost complete quasi-cleavage rupture at high stress levels. At R=0.01 and 150 °C fracture surface present also quasi-cleavage characteristics with the presence of porosities.

The fractography analysis revealed the appearance of micro-voids in tension-tension fatigue tests at 150 °C which could be created by high deformation at elevated temperature. These voids act as local strain concentrators and contribute in the decreasing of the fatigue strength at imposed temperature. Some additional investigation should be carried out to go deeper in this way.

R5 steel

Very high cycle fatigue tests were carried out up to the gigacycle regime on smooth specimens of R5 steel under three different conditions: virgin specimens, pre-corroded specimens and under artificial sea water flow in situ.

The fatigue strength at 10^9 cycles decreases significantly compared with the fatigue strength at 10^6 cycles for both pre-corroded specimens and specimens without any corrosion. The effect of corrosion is drastic when artificial sea water is put on the specimen surface. The fatigue strength at 10^9 cycles is around 40 MPa under corrosion with sea water flow.

At R=0.3 it exists also a decreasing of the fatigue strength at 10^9 cycles compared to the fatigue strength at 10^6 cycles. The Haigh diagram showed that the fatigue strength of R5 steel without any corrosion does not follows the Goodman threshold but the Gerber's parabola.

Without any corrosion at R= –1, the fractography analysis showed that crack initiation sites are located at both the specimens' surface and internal defects. Internal initiation sites are localized at inclusions. At R=0.3, the initiation sites were all located at the specimen subsurface. An X-ray microanalysis showed the presence of non-metallic inclusion common in steel, such as silicates, aluminates and sulphides.

The influence of corrosion on fatigue strength is very important for the two different corrosion conditions. Specimens with pre-corrosion presented crack initiation sites at corrosion pits on the specimen surface. Specimens tested under sea water flow presented

crack initiation sites at corrosion pits on the specimen surface too. The corrosion pits were bigger than specimens with pre-corrosion. Under sea water flow small cracks appeared around the specimen surface along the variable section of the specimens. This denotes the existence of a coupling of both corrosion and cyclic loading damage.

The important scatter of the fatigue life for similar specimens loaded under similar stress amplitude has been correlated to the parameters observed on the fracture surfaces. For tests without any corrosion the fatigue life was shorter when internal defects were presented compared to the specimens with surface defects. For tests with pre-corrosion the fractography analysis revealed that fatigue life is shorter when two or more corrosion pits are close together. This arises to the concentration of stresses around these defects.

For the tests under sea water flow in real time the same kind of fracture surfaces was observed for specimens with fine and very fine surface roughness, demonstrating that for R5 steel under sea water corrosion in real time, the roughness surface does not have an important influence in the fracture mechanisms (for our test conditions).

The size of the pits created during testing under sea water flow was significantly bigger than pits in specimens with pre-corrosion. It is possible that their size at initiation were smaller, possibly in the order of the microstructure size. The coupling of both corrosion and cyclic loading processes has been shown but at the moment it is not possible to determine quantitatively the effect of this interaction for modeling purpose. Some evidence appeared in the fractographies, such as the creation of multiple pits and the appearance of multiple small cracks along the variable cross-section of the specimen. Further studies have to be carried out in order to look for an understanding of this phenomena.

The crack growth tests carried out on R5 steel notched specimens at room temperature, R=–1, and 20 kHz, in air and under sea water flow in situ showed that crack growth rate is faster under sea water flow than in air. As usually written in literature at usual loading frequency.

In air, the threshold of the stress intensity range was observed at $\Delta K_{th} \approx 3.27$ MPa√m. Under sea water corrosion it was difficult to determine a tendency of the results. The stress intensity threshold was also difficult to determine, but it is probably similar or smaller than in air.

The calculation of the mode I stress intensity factor at hemispherical surface pits combined with the Paris–Hertzberg crack growth rate law showed that fatigue crack initiation regime represents most of the fatigue life for both, pre-corroded specimens and specimens corroded in sea water flow. Fatigue life is dominated by the crack initiation stage as soon as the fatigue life is more than around 10^7 cycles.

The calculations were done assuming that the crack growth rate is similar in air and under sea water flow. But the crack growth rate results in sea water flow showed that crack propagation is faster in sea water than in air, then the number of cycles of propagation is probably lower than our assessment. This does not change the conclusion: crack initiation dominates the fatigue life in the gigacycle regime. This is an important result for design departments because this shows that “damage tolerant philosophy” is not representative of reality. After this work the important question is why cracks initiates around defects and how to predict this quantitatively in the gigacycle regime?

It is necessary to keep in mind that for the specimens tested under sea water flow, crack initiation may be simultaneous with the corrosion pit growth. This is not the case of the pre-corroded specimens. In this work, the part of the fatigue crack trajectory respective to the corrosion pit growth has not been distinguished. The calculations were done considering the final pit size observed in fractographies as initial defect. This may lead to an error in the assessment of the crack propagation duration under sea water flow, but we do not know how to do without this assumption. Future work has to be carried out to try to investigate the kinetics of corrosion pits and crack simultaneously and to separate their respective speed.

The effect of sea water on the crack growth and the stress intensity factor needs to be studied. A possible coupling between environment and high frequency cyclic loading should be studied too. However, ultrasonic fatigue test immersed in flowing sea water is the only experimental way to investigate very long life of steel under corrosion conditions.

Résumé

Ce travail concerne l'étude de la résistance à la fatigue dans le domaine gigacyclique de deux matériaux. Le premier, l'AS7G06-T6 est utilisé pour la fabrication des carters de turbines pour hélicoptères, le second, l'acier R5, est utilisé pour la fabrication des chaînes pour plates-formes pétrolières.

L'alliage d'aluminium moulé AS7G06-T6 est soumis à un très grand nombre de cycles en raison de la durée d'utilisation et de la vitesse de rotation de la turbine, environ 30 000 tr/min. Les échantillons provenant de vraies pièces ont été testés à température ambiante et à 150 °C, et sous trois rapports de charge. La résistance à la fatigue à très grand nombre de cycles au delà du milliard de cycles a été étudiée, l'amorçage des fissures est systématiquement du aux retassures.

L'acier R5, selon la dénomination internationale des Sociétés de la Classification Internationale des Systèmes Offshore est un acier faiblement allié, utilisé pour la fabrication de chaînes d'amarrage pour les plates-formes pétrolières offshore. Cet acier possède une haute résistance mécanique et une bonne résistance à la corrosion. Les chaînes sont conçues pour 30 ans, et sont chargées à basse fréquence (~ 0,5 Hz) en raison des vagues en mer ; ceci représente plus de 10^8 cycles. Les échantillons provenant de chaînes en acier R5 ont été testés en fatigue à des rapports R différents, sous trois conditions différentes : éprouvettes vierges dans l'air, ou bien éprouvettes vierges cyclées in situ dans l'eau de mer synthétique, et éprouvettes pré-corrodées en brouillard salin puis cyclées à l'air. La résistance à la fatigue dans le régime gigacyclique et les causes de l'amorçage des fissures ont été étudiées.

L'analyse de la littérature a montré qu'il n'existe pas de limite de fatigue pour de nombreux alliages métalliques : les courbes *S-N* ne présentent pas de comportement asymptotique à très grand nombre de cycles. Les résultats des essais de fatigue à haute fréquence sur l'alliage AS7G06-T6 et l'acier R5 ont confirmé ce phénomène dans le domaine gigacyclique avec une diminution importante de la résistance à la fatigue entre 10^6 et 10^9 cycles.

Nous avons cherché à comprendre l'effet des défauts sur la résistance à la fatigue gigacyclique. Les fissures de fatigue dans l'alliage AS7G06 sont souvent dues aux porosités. Pour l'acier R5 pré-corrodé ou testé dans l'eau de mer, des piqûres de corrosion sont généralement la cause des ruptures par fatigue. Une modélisation de la durée de la phase de propagation des fissures de fatigue est proposée. Elle montre qu'au delà de 10^7 cycles, la durée de vie est majoritairement due à la phase d'amorçage des fissures et non a la phase de propagation même si des défauts sont responsables des amorçages.

Alliage moulé AS7G06-T6

Les essais de fatigue gigacyclique réalisés sur des éprouvettes lisses en alliage moulé AS7G06-T6 ont montré une baisse significative de la résistance à la fatigue dans le régime gigacyclique par rapport à la résistance à la fatigue dans le régime mégacyclique. Le facteur de réduction entre ces deux domaines de durée de vie est d'environ 1,6 pour R= –1 et 2,0 pour R=0,01. Ceci démontre qu'il n'existe pas de comportement asymptotique dans le domaine de 10^6 à 10^9 cycles pour l'alliage d'aluminium AS7G06-T6. La résistance à la fatigue à 150°C diminue d'environ 10 MPa dans le régime gigacyclique par rapport à la résistance à la fatigue à température ambiante. Il existe à 150 °C aussi une diminution de la résistance à la fatigue dans le régime gigacyclique comparé avec le régime megacyclique. Ces données sont importantes pour la conception contre la fatigue à très grande durée de vie des composants comme les turbines aéronautiques.

Le Tableau 1 montre un résumé des résultats des essais de fatigue à 10^6 et 10^9 cycles sur éprouvettes lisses pour différentes rapports de charge R et deux températures.

Température °C	R	Résistance à la fatigue 10^6 cycles, MPa			Résistance à la fatigue 10^9 cycles, MPa			Ecart-type méthode de l'escalier, MPa	Ecart-type selon ESOPE, MPa
		amp	moy	max	amp	moy	max		
20	-1	110	0	110	72	0	72	3,5	5,55
20	0,01	72	73,5	145	~39	~39	~78	Non estimable	8,98
20	0,5	Non testé			54	162	216	Non estimable	Non estimable
150	-1	72	0	72	61	0	61	4,5	4,48
150	0,01	95	95	192	48	48	96	4,1	6,4

Tableau 1. Résistances à la fatigue de l'alliage d'aluminium AS7G06-T6 dans l'air à 20 kHz.

Les causes des amorçages des fissures de fatigue dans l'alliage d'aluminium AS7G06-T6 dans le régime gigacyclique sont principalement des défauts de fabrication tels que des porosités ou retassures pour les deux températures testées, ambiante et 150°C, mais il existe une compétition entre ces défauts et des bandes de glissement que génèrent de rupture par quasi-clivage (voir Figure 1 et Figure 2).

Les résultats des essais de fatigue sur l'alliage AS7G06-T6 nous ont permis d'observer l'effet de deux facteurs importants pour la résistance à la fatigue dans le domaine gigacyclique : la température et la contrainte moyenne.

L'effet de la température entre 20 °C et 150 °C est faible pour les essais à R= –1. La résistance à la fatigue à 150 °C est de 11 MPa inférieure à la résistance à la fatigue à 20 °C. Au contraire, pour les essais à R=0,01, la résistance à la fatigue à 150 °C est 9 MPa supérieure à la résistance à la fatigue à température ambiante. Il n'y a donc pas de différence de résistance en fatigue à 20 °C et à 150 °C compte tenu des dispersions.

Les résistances expérimentales à la fatigue pour l'alliage d'aluminium AS7G06-T6 ont été représentées dans le diagramme de Haigh. Ceci a montré que les résultats à température

ambiante ne suivent pas le seuil de Goodman. Il a été observé dans le diagramme de Haigh que les résistances à la fatigue dans le régime gigacyclique à faible rapport de charge se trouvent sur le seuil de Goodman, mais aux rapports supérieurs, tel que R=0,5, la résistance à la fatigue se trouve sur la parabole de Gerber.

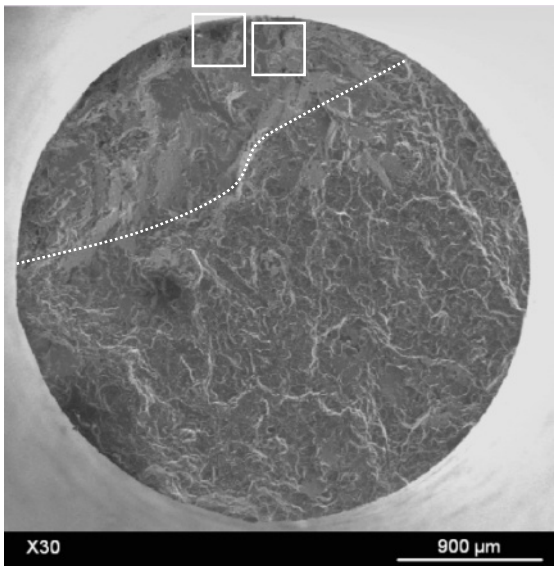

Figure 1. Surface de rupture d'un échantillon testé à R= –1 dans l'air et température ambiante, σ_a=85 MPa, N_f =6.9×10^7 cycles

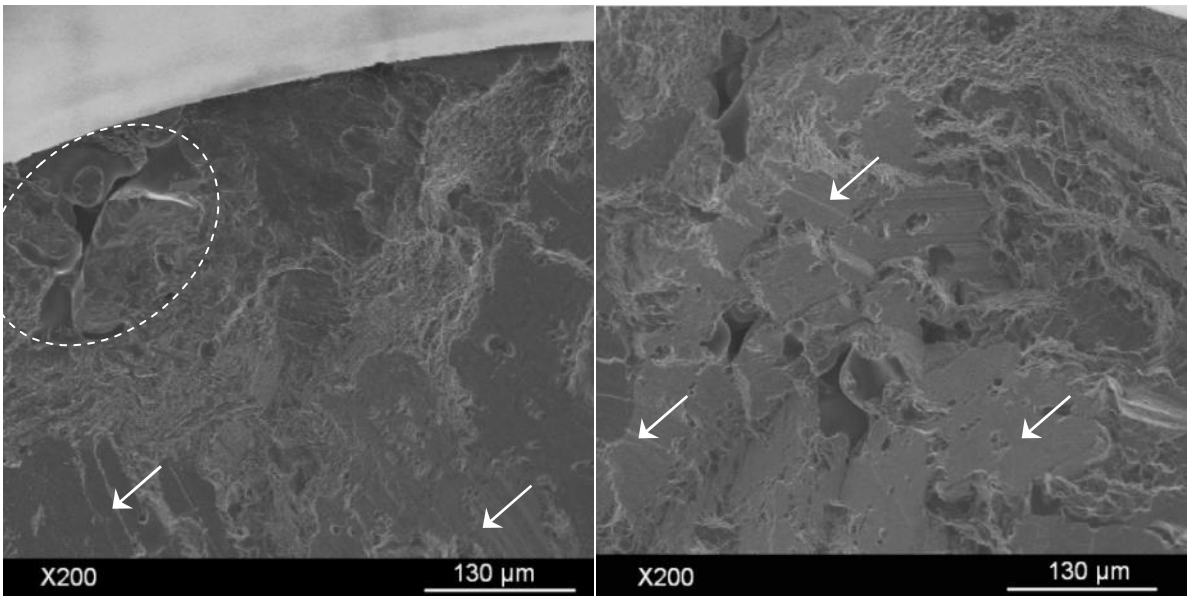

Figure 2. Détails de la Figure 1.

Les observations microscopiques (optiques et MEB) des facies de rupture réalisées sur les éprouvettes cassées de l'alliage d'aluminium AS7G06-T6 ont montré des caractéristiques

différentes en fonction des conditions des essais, mais des porosités sont toujours l'origine de l'amorçage des fissures de fatigue. À température ambiante sous traction-compression alternée symétrique (R=-1), les défauts tels que porosités ou retassures près ou à la surface de l'échantillon sont les principales causes de l'amorçage des fissures de fatigue, mais à hauts niveaux des contraintes la rupture semble être aussi due à du quasi-clivage. À R=0,01 et température ambiante, des porosités sur la surface de l'échantillon ou un peu à l'intérieur causent l'amorçage des fissures. Toutefois des bandes de glissement sont plus présentes sur la surface de rupture qu'à R = –1. À R = 0,5, des porosités sont les sites d'amorçage de fissure aussi, mais du quasi-clivage autour des sites d'amorçage de fissure est présent. (Voir Figure 3 et Figure 4).

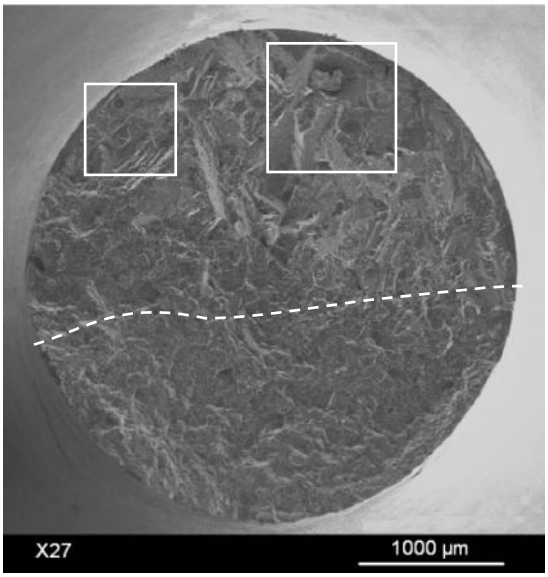

Figure 3. surface de rupture d'un échantillon testé à R=0.5 dans l'air et température ambiante, σ_a=55 MPa, N_f =3.95×10^8 cycles.

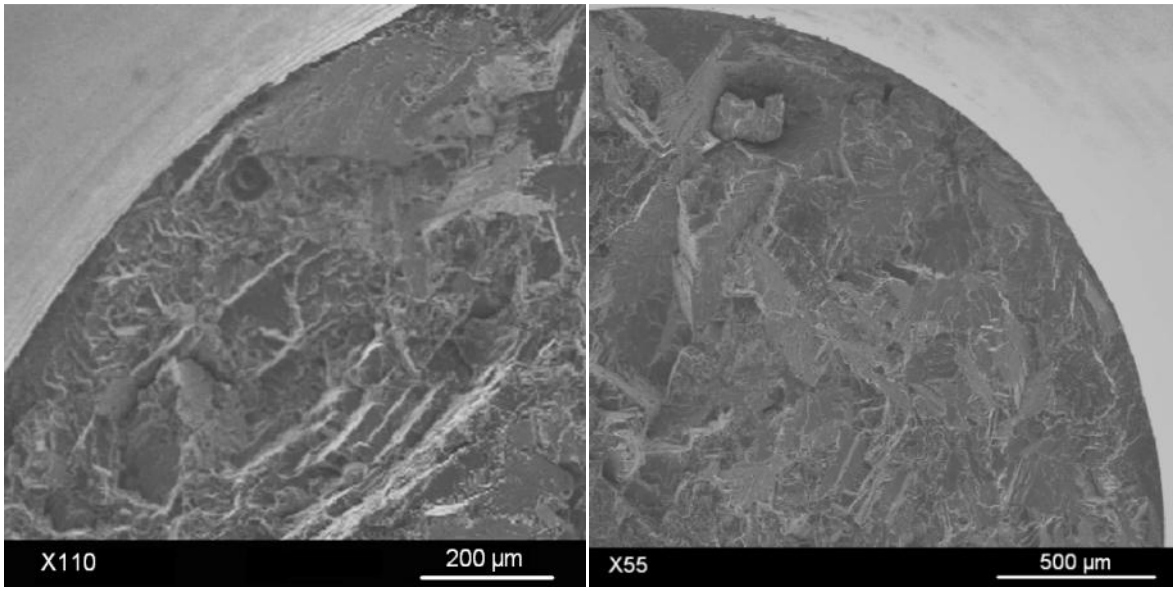

Figure 4. Détails de la Figure 3.

Les résultats des essais montrent que la résistance à la fatigue est plus élevée – en amplitude – à R=0,5 par rapport à R=0,01, ce qui n'est pas commun selon la littérature. Ceci devra être approfondi. L'analyse fractographique a montré que les sites d'amorçage caractéristiques pour l'alliage d'aluminium AS7G06-T6 sont des porosités près ou sur la surface de l'échantillon. Nous avons mesuré l'aire des porosités dans le plan (2D) des images de microscopie électronique à balayage. On a observé que les porosités qui causent la rupture sont plus nombreuses dans les échantillons testés à R = 0,01 par rapport à des échantillons testés à R = 0,5. Des gros défauts comme les porosités influencent négativement la résistance à la fatigue et la durée de vie de l'alliage d'aluminium AS7G06-T6. La taille des pores a une influence importante sur la vie en fatigue, la résistance en fatigue diminue nettement avec la taille des retassures.

À 150 °C et R= –1 les sites d'amorçage sont aussi des porosités. Il existe une compétition entre la rupture par quasi-clivage et porosités, on observe des ruptures presque complètes par quasi-clivage à hauts niveaux de contrainte. À R=0,01 et 150 °C on observe aussi la caractéristique de rupture par quasi-clivage avec la présence de porosités.

Acier R5

Les essais de fatigue à très grand nombre de cycles ont été réalisés sur des éprouvettes lisses en acier R5 sous trois conditions différentes : éprouvettes vierges dans l'air et dans l'eau de mer synthétique in situ, et éprouvettes pré-corrodées.

La résistance à la fatigue à 10^9 cycles diminue significativement par rapport à la résistance à la fatigue à 10^6 cycles pour les essais sur éprouvettes pré-corrodés et pour les essais sur éprouvettes vierges (sans corrosion). L'effet de la corrosion est drastique quand l'eau de mer synthétique est mise sur la surface de l'échantillon durant le cyclage en fatigue.

À R=0,3 il existe aussi une diminution de la résistance à la fatigue à 10^9 cycles par rapport à la résistance a la fatigue à 10^6 cycles. Dans le diagramme de Haigh il a été observé que la résistance à la fatigue de l'acier R5 sans corrosion ne suit pas le seuil de Goodman mais la parabole de Gerber.

Un résumé des résultats des essais de fatigue est présenté dans le tableau 2. Les résultats de fatigue pour l'acier R5 ont été tous obtenus à température ambiante et à 20 kHz. Dans le tableau 2, les résistances à la fatigue dans le domaine megacyclique et gigacyclique sont illustrées, dans l'air et dans l'eau de mer à température ambiante.

Condition	R	Résistance à la fatigue à 10^6 cycles, MPa			Résistance à la fatigue à 10^9 cycles, MPa			Ecart-type de l'escalier, MPa	Ecart-type selon ESOPE, MPa
		amp	moy	max	amp	moy	max		
Sans corrosion	–1	430	0	430	381	0	381	7,4	18,2
	0,3	~310	~575	~885	270	501	771	4,5	Non estimable
Pré-corrosion	–1	400	0	400	360	0	360	Non estimable	Non estimable
Eau de mer	–1	~400	0	~400	40	0	40	Non calculée	52,1

Tableau 2. Résultats de fatigue pour l'acier R5 à température ambiante à 20 kHz.

L'analyse fractographique sur des échantillons sans corrosion à R= –1 a montré que les sites d'amorçage peuvent être localisés sur la surface des échantillons ou bien sur des défauts internes. Les sites d'amorçage internes sont principalement des défauts de type inclusions. À R=0,3 les sites d'amorçage sont localisés sur la surface des échantillons. Les microanalyses aux rayons X ont montré la présence d'inclusions non-métalliques très communes dans les aciers, tels que silicates, aluminates et sulfures.

L'influence de la corrosion sur la résistance à la fatigue de l'acier R5 est très importante pour les deux différentes conditions de corrosion. Les échantillons pré-corrodées ont présenté des sites d'amorçage sur les piqures de corrosion à la surface des échantillons. Les éprouvettes testées dans l'eau de mer in situ ont présenté aussi l'amorçage sur des piqûres de corrosion à la surface des échantillons. Les piqûres de corrosion créées dans l'eau de mer sont bien plus grandes que les piqûres de corrosion créées par pré-corrosion sous brouillard salin (Figure 5). Sous l'eau de mer synthétique des petites fissures sont apparu autour de la surface des échantillons le long de la section variable. Cela montre l'existence d'un couplage de la corrosion et l'endommagement due au chargement cyclique à 20kHz.

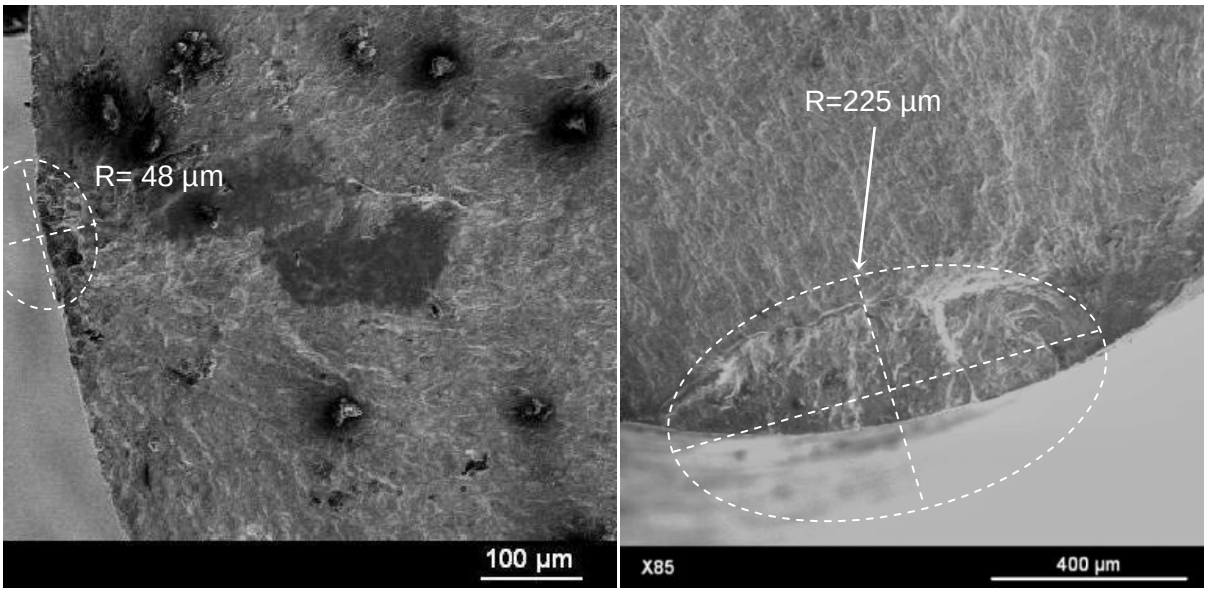

Figure 5. Piqûre créée avec pré-corrosion (brouillard salin) (gauche) et piqure crée avec eau de mer in situ (droite).

La dispersion importante de la durée de vie en fatigue pour des éprouvettes testées sous conditions similaires d'amplitude de contrainte a été corrélée aux paramètres observés sur les surfaces de rupture. Pour les essais sur éprouvettes sans corrosion la durée de vie en fatigue a été plus courte quand des défauts internes ont été activés par rapport aux éprouvettes avec des défauts de surface. Pour les essais sur éprouvettes avec pré-corrosion, l'analyse fractographique a révélé que la durée de vie est plus courte lorsque deux ou plusieurs piqures de corrosion sont rapprochées. Cela tient à la concentration des contraintes autour de ces défauts (voir Figure 6 et Figure 7).

Pour les essais sous l'eau de mer in situ le même genre des surfaces de rupture ont été observés pour les échantillons avec une rugosité fine (Ra=0.6 µm) et avec une rugosité très fine (Ra=0.1 µm). Cela démontre que pour l'acier R5 dans l'eau de mer synthétique in situ, la rugosité de la surface de l'échantillon n'a pas une influence importante sur les mécanismes de rupture (pour nos conditions d'essai) en fatigue gigacylique.

La taille des piqures créées pendant les essais sous l'eau de mer synthétique est significativement plus grande que celle des piqures créées avec pré-corrosion sous brouillard salin. Il est possible que leur taille lors de l'initiation de la fissure soit plus petite, peut être de l'ordre de la taille de la microstructure. Le couplage des processus de corrosion et chargement cyclique a été mis en évidence mais pour le moment il n'est pas possible de déterminer quantitativement les effets de cette interaction, ni de la modélisée. Certains éléments mis en évidence sur les fractographies, tels que la création de multiples piqûres et l'apparition de multiples petites fissures le long de la section variable de l'échantillon ont permis de mettre en évidence le couplage corrosion - fatigue même à 20kHz, alors que des auteurs pensent que la corrosion ne peut se révéler dangereuse que si la fréquence de cyclage est assez basse pour laisser le temps à la corrosion de se développer ; il n'en est rien dans notre cas. D'autres études doivent être réalisées afin de chercher à comprendre ce phénomène.

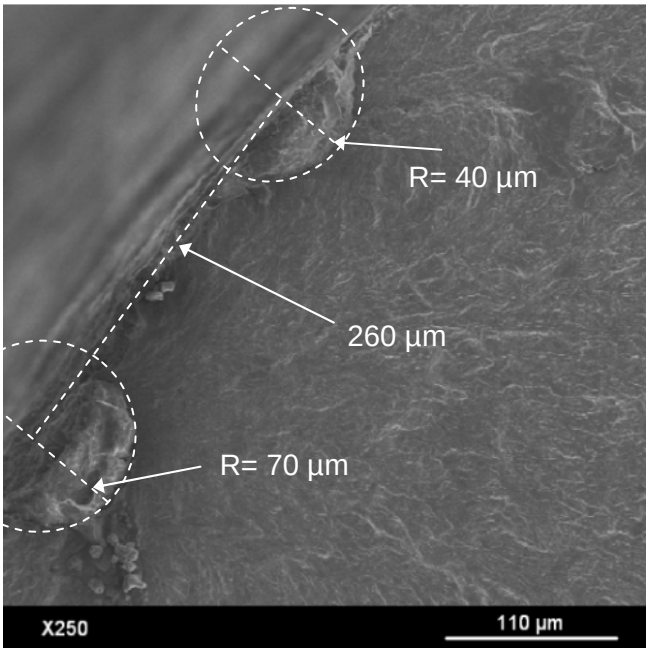

Figure 6. Site d'amorçage d'une échantillon d'acier R5 pré-corrodée, testée à R=–1, dans l'air et température ambiante, σ_a=370 MPa, N_f=4.37×10^8 cycles

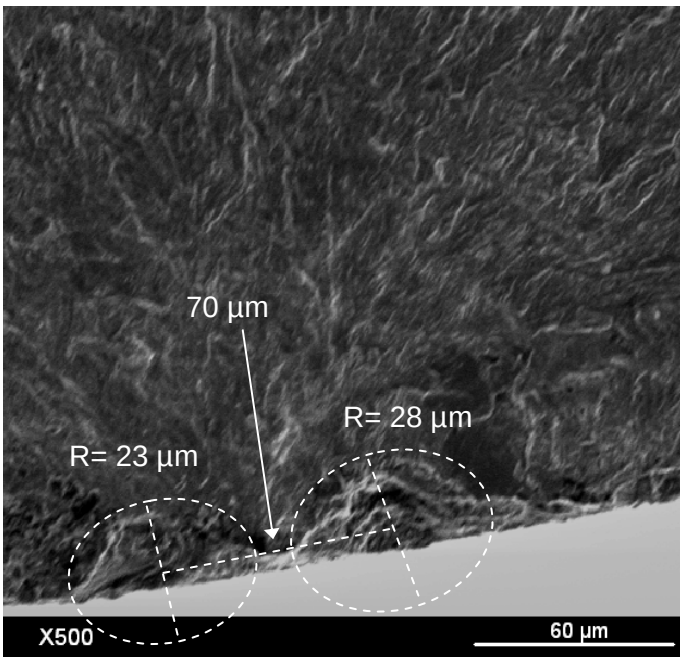

Figure 7. Site d'amorçage d'une échantillon d'acier R5 pré-corrodée, testée à R=–1, dans l'air et température ambiante, σ_a=425 MPa, N_f= 1.56×10^7 cycles.

Les essais de propagation de fissure réalisés sur des échantillon en acier R5 a température ambiante, R= –1 et 20 kHz, dans l'air et sous l'eau de mer synthétique in situ, ont montré que la vitesse de propagation des fissures est plus grande sous l'eau de mer que dans l'air (Figure 8), comme usuellement décrit dans la littérature à fréquence de chargement conventionnelle (quelques Hz ou dizaines de Hz).

Dans l'air, le seuil de l'étendue du factor d'intensité de contraintes a été observé déterminé égal à ΔK_{th}≈3.27 MPa√m. Sous corrosion avec l'eau de mer il a été difficile de déterminer une valeur précise de cette quantité, mais d'après nos essais il semble similaire ou un peu inférieur à la valeur dans l'air.

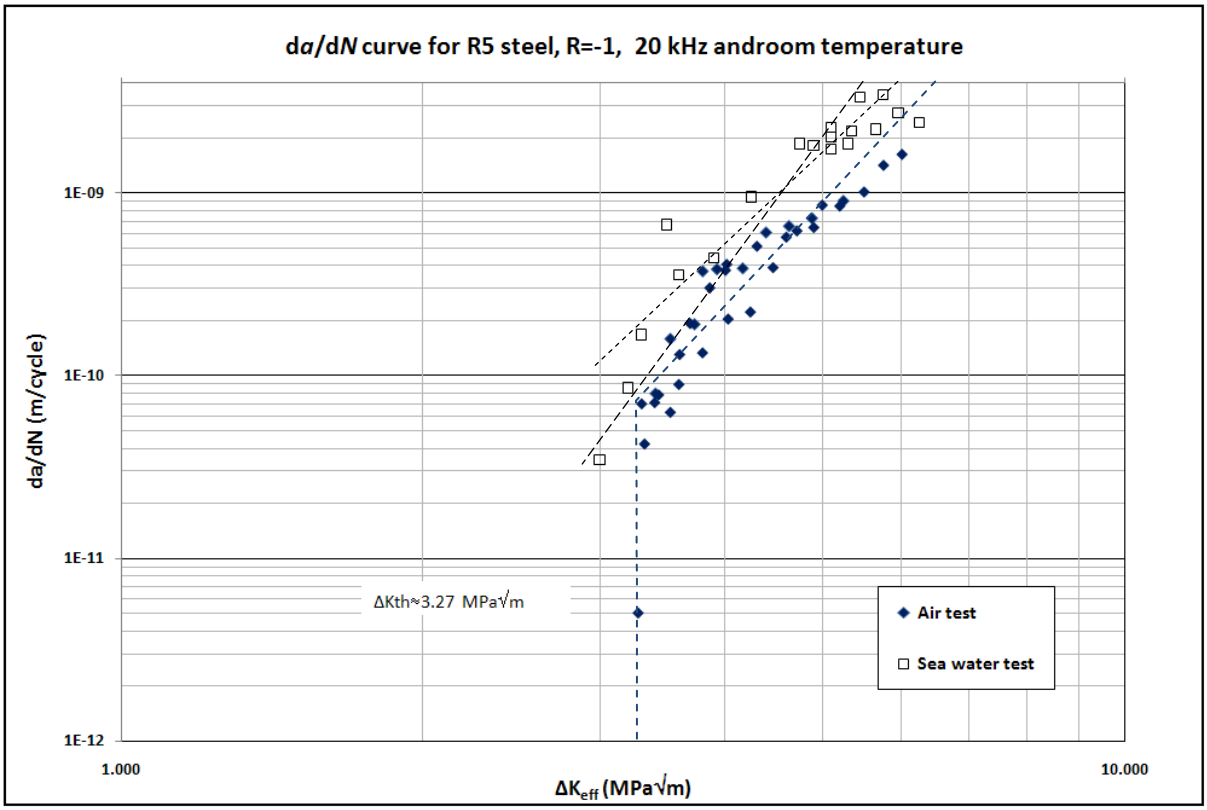

Figure 8. Courbe da/dN de l'acier R5 à R= –1 dans l'air et dans l'eau de mer à température ambiante.

Le calcul du facteur d'intensité de contraintes en mode I autour des piqûres hémisphériques sur la surface des échantillons d'acier R5 combiné avec la loi de propagation de fissure de Paris-Hertzberg nous a permis de montrer que la phase d'amorçage des fissures de fatigue représente la plus grande partie de la durée de vie en fatigue pour des échantillons pré-corrodées et pour des échantillons avec corrosion sous l'eau de mer in situ. La durée de vie en fatigue est nettement dominée pour la phase d'amorçage dès que la durée de vie est plus grande que 10^7 cycles.

Les calculs ont été faits en supposant que la vitesse de propagation des fissures est similaire dans l'air et dans l'eau de mer. Mais les résultats de l'essai de propagation de fissure dans l'eau de mer ont montré que la propagation de fissure est plus rapide dans l'eau de mer que dans l'air, donc le nombre de cycles de la phase de propagation est probablement moindre que dans nos calculs. Cela ne change pas la conclusion : la phase d'amorçage de fissure domine la durée de vie en fatigue dans le régime gigacyclique. C'est un résultat important pour les départements de conception, car cela montre que la philosophie de dimensionnement "tolérance aux dommages" n'est pas représentative de la réalité. Après ce travail la question importante est donc pourquoi les fissures s'initient autour des défauts et surtout comment prédire cela quantitativement dans le régime gigacyclique?

Il est nécessaire de rappeler que pour les échantillons testés sous l'eau de mer synthétique, l'amorçage des fissures peut être simultané avec la croissance des piqûres de corrosion. Cela n'est pas le cas pour les échantillons pré-corrodés. Dans ce travail, la part de la trajectoire des fissures de fatigue due respectivement à la croissance des piqûres de corrosion et à la

propagation sous le chargement cyclique seul n'a pas été distinguée. Les calculs ont été faits en considérant la taille finale des piqûres observés dans les fractographies comme égale au défaut initial. Cela peut conduire à une erreur dans l'approximation de la durée de propagation des fissures sous l'eau de mer, mais nous ne savons pas comment faire sans cette hypothèse. De futurs travaux doivent être réalisés pour essayer d'étudier la cinétique des piqûres de corrosion et de fissuration simultanément et pour séparer leur vitesse respective.

L'effet de l'eau de mer sur la croissance des fissures et sur le facteur d'intensité de contrainte doit être étudié. Un couplage possible entre l'environnement et le chargement cyclique à haute fréquence doit aussi être étudié. Toutefois, des essais de fatigue ultrasonique immergés dans l'eau mer restent la seule façon expérimentale pour étudier la durée de vie en fatigue à très grand nombre de cycles avec des conditions de corrosion.

Annex 1. High speed rotating bending fatigue machine.

Table of contents

Introduction 2
1. Design features 2
2. Specimen dimensions 2
3. Main systems 3
3.1. Power transmission system. 3
3.2. Support of the rotating system 4
3.3. Main control system 4
3.4. Load application system 4
3.5. Specimen rupture stop system 6
3.6. Cycle counter system 6
4. Stress calculation 7
5. Summary 8
References 9

Introduction

A rotating bending fatigue testing machine is a device used to produce bending stresses on a specimen and to determine the number of cycles of failure of such specimen, due to oscillating bending stress, which are maximum around the narrowest specimen cross-section.

This annex shows a rotating bending fatigue machine designed in CIATEQ (Advanced Technology Center) able to turn up to 199 Hz. It was conceived for testing metallic materials of turbomachinery industry and others. It contains the description of the basic components and requirements of the testing system.

1. Design features

The high speed rotating bending fatigue machine of CIATEQ has the following requirements:

- The machine allows testing in rotating bending fatigue round specimens coupled to a rotating shaft at high speed.
- The speed at the high speed shaft for testing specimens can be around 11,935 rpm (199 Hz). The possibility of changing the speed exists (from 30 to 199 Hz).
- The testing machine has a light loading system. This allows loads from 5 to 220 N and has a visualization system to see the applied load in a display.
- The testing machine has a cycle counter and devices that stop the turning when the specimen fails.

2. Specimen dimensions

Figure 1 shows the dimensions of the specimen used in the rotating bending fatigue machine. Presently, there are no standard dimensions for high frequency fatigue specimens. This geometry is used with the intention of concentrating the maximum stress at the center of the specimen, assuring the failure in the narrowest specimen section [2, 3].

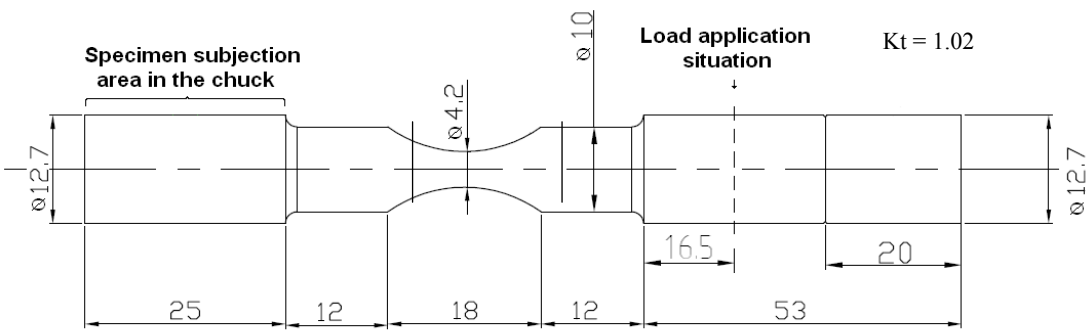

Figure 1. Dimensions in millimeters of rotating bending fatigue specimen.

3. Main systems

In this section the main system of the rotating bending fatigue machine at high frequency will be presented.

3.1. Power transmission system.

The system of rotatory motion transmission is composed by a 1.118 kW motor which is connected to a parallel shaft using two pulleys and a belt. The parallel shaft turns at 3.10 times the motor speed and is constituted by two sections connected by a flexible coupling. Figure 2 shows a picture of the rotating system.

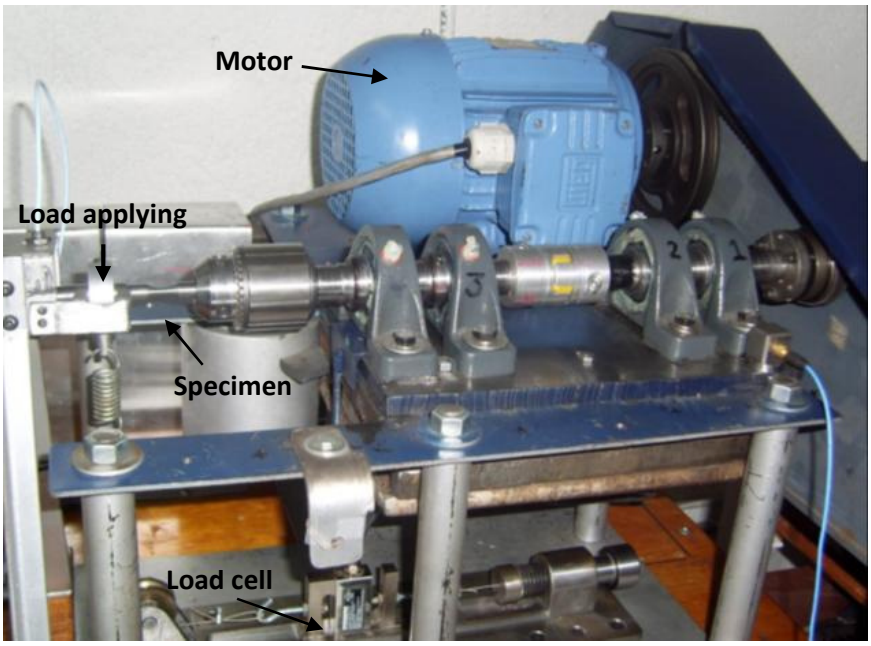

Figure 2. Rotating system of the rotating bending fatigue machine.

The last shaft has a diameter of 25.4 mm, is made of AISI-SAE-4140 steel, and it has a length around 40 cm. At the end of the shaft there is a chuck as specimen clamping. The thicker diameter of the specimen is 12.7 mm, then a bearing with 12.7 mm diameter is used in order to apply load at the end of the specimen.

The mechanical power supply is an AC synchronous motor of 1.118 kW (220 V AC/60 Hz) capable to turn up to 3850 rpm.

3.2. Support of the rotating system

The two sections of the shaft are supported on four ball bearings, two bearings per section (as shown in Figure 2). The bearings support is a metallic structure made of steel. The metallic structure contains two plates (top and bottom) assembled parallels by eight steel tubes fixed with same number of long bolts. All this structure is fixed to a wood table with metallic base. The estimated weight of this structure is 10.5 kg.

3.3. Main control system

A main control panel works as the rotating bending fatigue control system in basic operations such as start, stop and speed variation. It works also as a programming system of the machine. Figure 3 shows a picture of the main control panel.

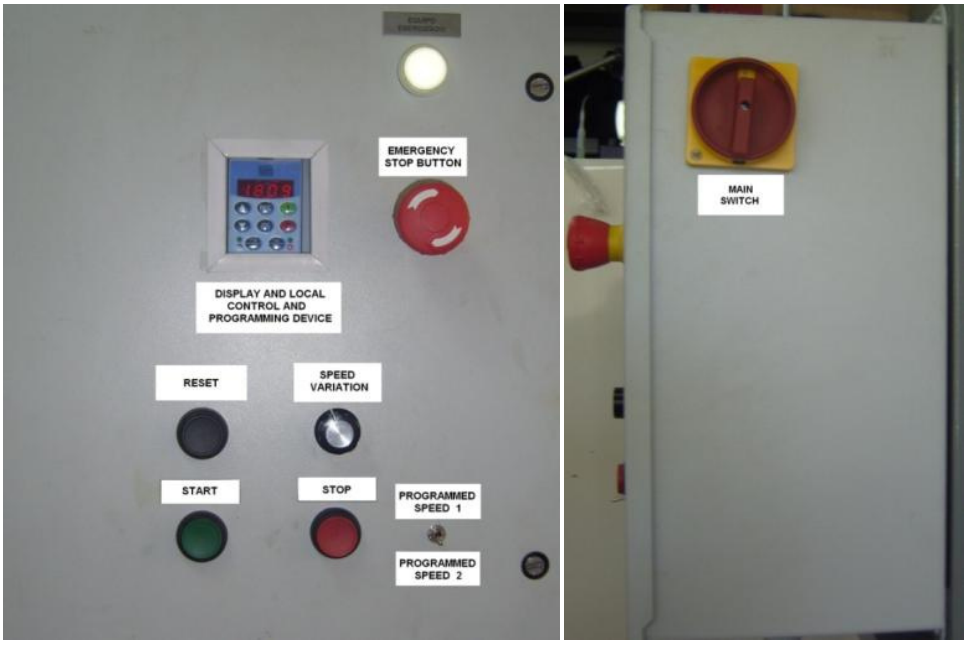

Figure 3. Main control panel basic elements.

This main control panel can work in different modes. Local or remote mode means that the system can be controlled using the external buttons (remote) or using the buttons of the local control and programming device (local).

Programmed speed or manual control speed is another mode and, it means that rotating speed can be controlled using a knob (manual) or using two programmed speed buttons (programmed).

3.4. Load application system

The system to measure the applied load is constituted by:

- A type S load cell
- A digital indicator
- A mechanical loading assembly.

The objective of this system is to apply load to the specimen and display the value of such load. The system can measure between 0 and 220 N. The display shows the load in Newton with a resolution of 0.01 N.

Figure 4 shows a schematic drawing of the loading system. This system has the aim of providing a constant lateral load to the turning specimen.

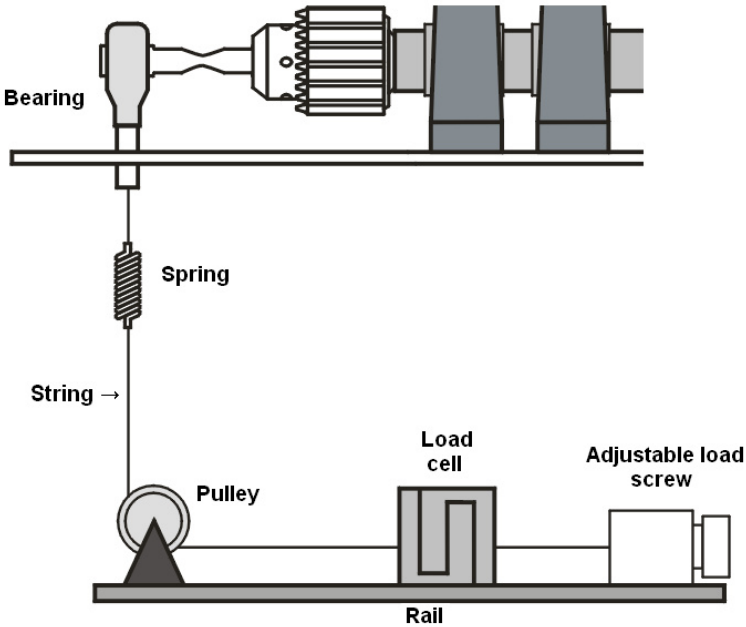

Figure 4. Scheme of the load system for the rotating bending fatigue machine.

Figure 5 shows the main components of the application load system.

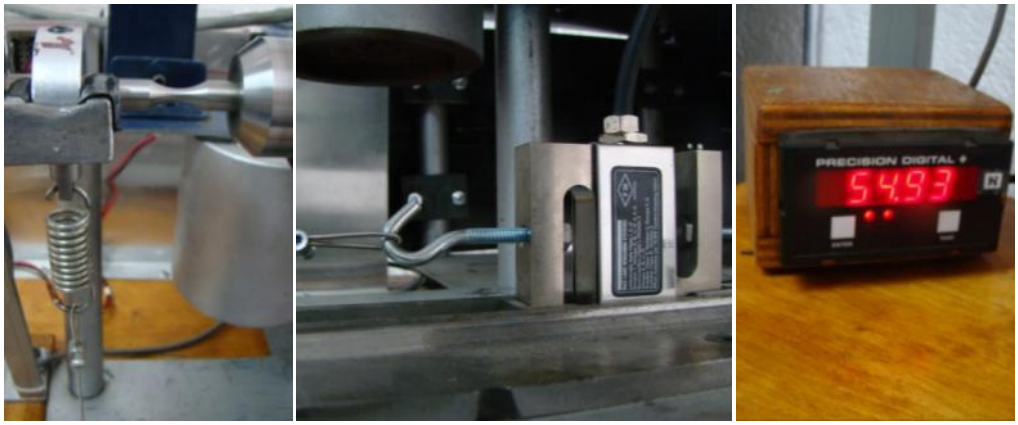

Figure 5. Application load system components.

The calibration of the load system has been carried out. The procedure consisted in checking that the value at the digital indicator is correct. Applying known masses from 0.5 to 8 kg, a register of voltage in the load cell was followed. Table 1 show the registered voltage corresponding to each applied mass.

3.5. Specimen rupture stop system

The rotating bending fatigue machine is controlled by the main control panel, with commands: start, stop and speed variation. There are three ways to stop the motor turning in the fatigue machine: the stop button in the main control panel, the emergency button and when the specimen fails due to a specimen rupture stop system.

The stop device consists in a limit-switch which is in contact with the load application bearing, on the casing. If the specimen fails this switch is activated stopping the motor. Figure 6 shows the location of the limit-switch in the rotating system.

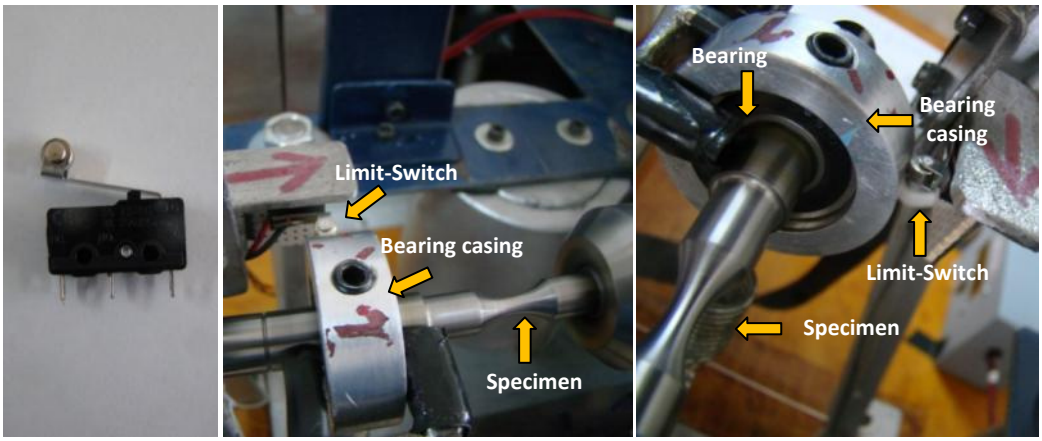

Figure 6. Limit-switch for stopping the motor when the specimen fails.

3.6. Cycle counter system

A system in order to count the number of cycles in the fatigue machine is contained. The aim of this cycle counter is to know in real time the number of cycles that the specimen has turned and to view the total number of cycles in case of the specimen failure.

Figure 7 shows the display of the counter system of the rotating bending fatigue machine. The LCD display and the voltage source are shown. This source is supplied by 120 V AC at 60 Hz and provides 5V DC.

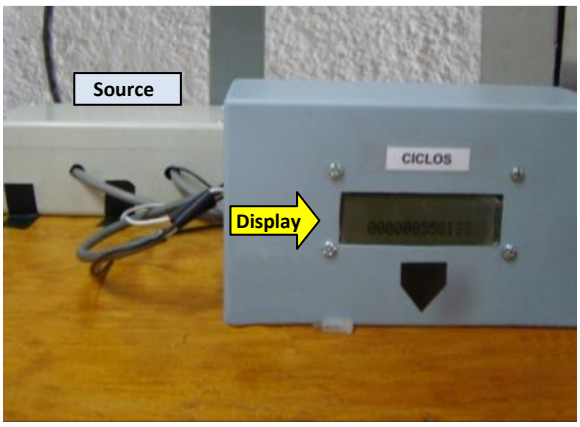

Figure 7. Cycles counter system of the rotating bending fatigue machine.

4. Stress calculation

Maximum bending stress in specimens for the rotating bending fatigue machine was calculated by using finite element calculations.

Figure 1 shows the dimensions of the specimen used in the rotating bending fatigue testing machine.

The software used for computing the bending stress, strains and displacement is ANSYS 11.0. Particularly for strain computing, AISI-SAE-1018 steel properties were considered.

The material parameters used in ANSYS were:

Young's modulus, E=200×10^9 N/m^2

Poisson ratio, ν=0.29

Density, ρ=7850 kg/m^3

Assumptions:

- Material is isotropic
- Temperature is constant

Loadings and constraints:

Load is applied at the end of the specimen. In this case the part of specimen after the length of load application was not drawn. The distance for the load application is 0.0585 m.

Restriction of zero displacement is applied in the zone of subjection of the specimen (section of 25 mm in Figure 1), at three zones through the circumference of diameter 12.7 mm, separated 120° as is shown in Figure 8.

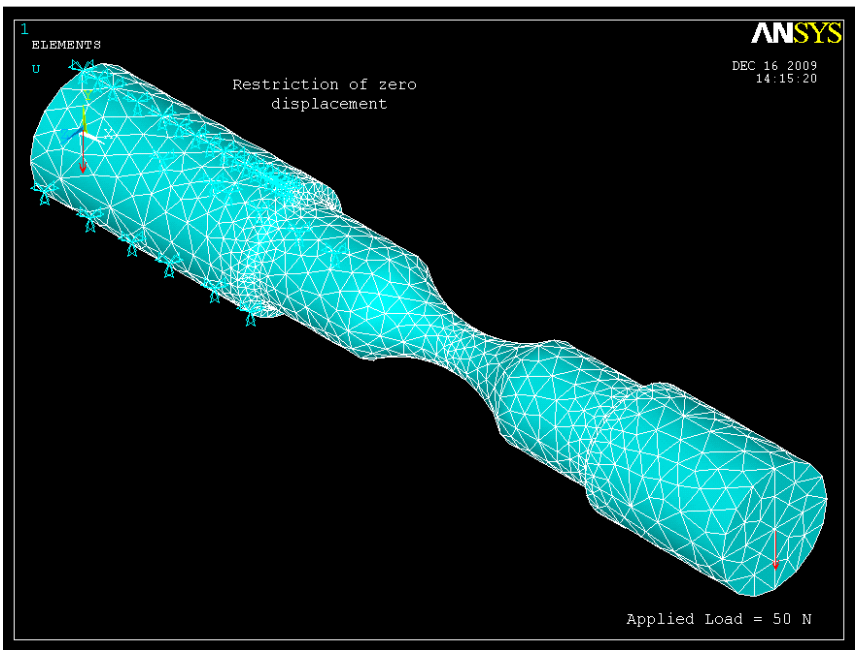

Figure 8. Load application and restrictions on the specimen in ANSYS.

Results:

Table 1 shows the maximum bending stress obtained by ANSYS for 4 different loadings.

Load, N	Maximum stress, MPa
50	272
75	412
100	553
200	1110

Table 1. Maximum bending stress as function of load.

Taking into account the numerical results, is established a linear equation that defines the maximum bending stress for the specimen with the geometry shown in Figure 1.

$$\sigma_{\max} = 5.529 \cdot P \tag{3}$$

Where P is the applied load.

5. Summary

A rotating bending fatigue testing machine was constructed at CIATEQ (Advanced Technology Center) for testing specimens of metallic materials and others. The testing machine allows testing in rotating bending fatigue specimens made on materials of interest for the turbomachinery industry but it is open to test materials for other applications. The variable frequency characteristic allows to modify the testing frequency from 30 to 199 Hz. This last frequency makes possible to achieve high number of cycles (>10^7 cycles) in some tens of hours.

References

1. Thomson W.T., 1982, Teoría de vibraciones Aplicaciones, Prentince Hall Hispanoamericana, México, pp. 444-445.

2. Bathias C., Paris, P.C., 2005, Gigacycle Fatigue in Mechanical Practice, Marcel Dekker Publisher Co., New York USA.

3. Lieurade, H.P., 1982, La pratique des essais de fatigue, Societé française de métallurgie, PYC Édition, Paris, France, pp. 27-35, 62-99.

Annex 2
Geometry of Horns and extensions and finite element analysis

The horns are the components that work as amplifiers in the ultrasonic fatigue machine. In LAMEFIP Arts et Métiers three kinds of horns are available.

Cylindrical Horn. For very low amplification, practically produces the same vibration displacement of the piezoelectric which has a maximum around 5 µm.

Conical Horn TC. For medium amplification, it produces around 5 times the displacement amplitude than the piezoelectric converter. That is around 4 µm minimum to 26 µm maximum.

Conical Horn TGD. For high amplification, iy produces much larger displacement amplitude than the converter, around 20 times at the maximum displacement amplitude of the converter. That is around 100 µm of maximum displacement.

Extensions or attachment are necessary in some fatigue tests in order to put the specimens at certain heights or inside a chamber, such a climatic chamber. Two extension of one kind of design are available in LAMEFIP to carry out fatigue tests inside a temperature chamber.

The geometries of these amplifiers horns and the extensions are presented in this Annex. Finite element calculations are presented too.

Note: For confidentiality reasons some dimensions have been suppressed from the geometry plans. The basic purpose is to show the shape of the components of the ultrasonic systems.

Geometries

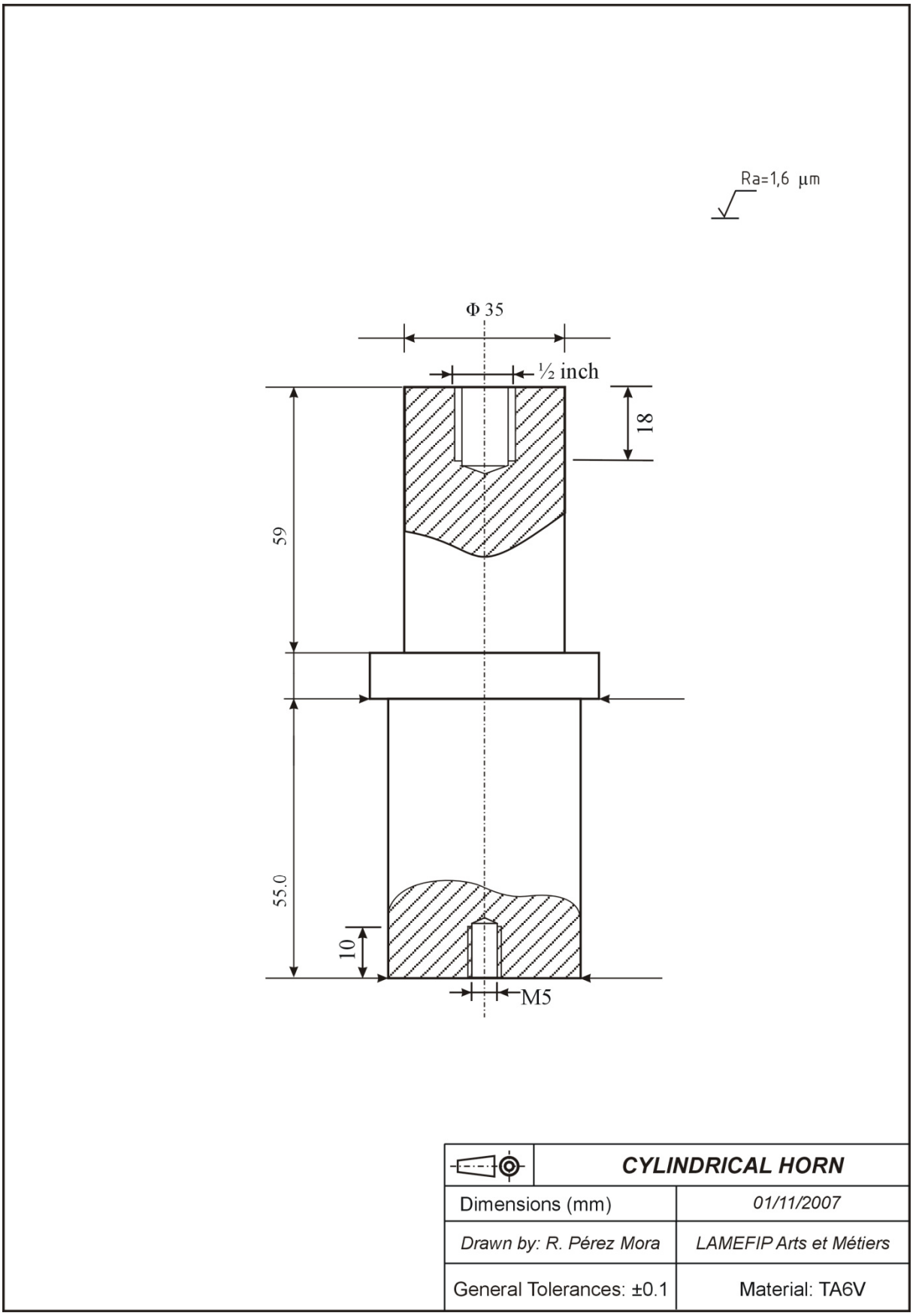
Ra=1,6 µm
Φ 35
½ inch
18
59
55.0
10
M5
CYLINDRICAL HORN
Dimensions (mm)
01/11/2007
Drawn by: R. Pérez Mora
LAMEFIP Arts et Métiers
General Tolerances: ±0.1
Material: TA6V

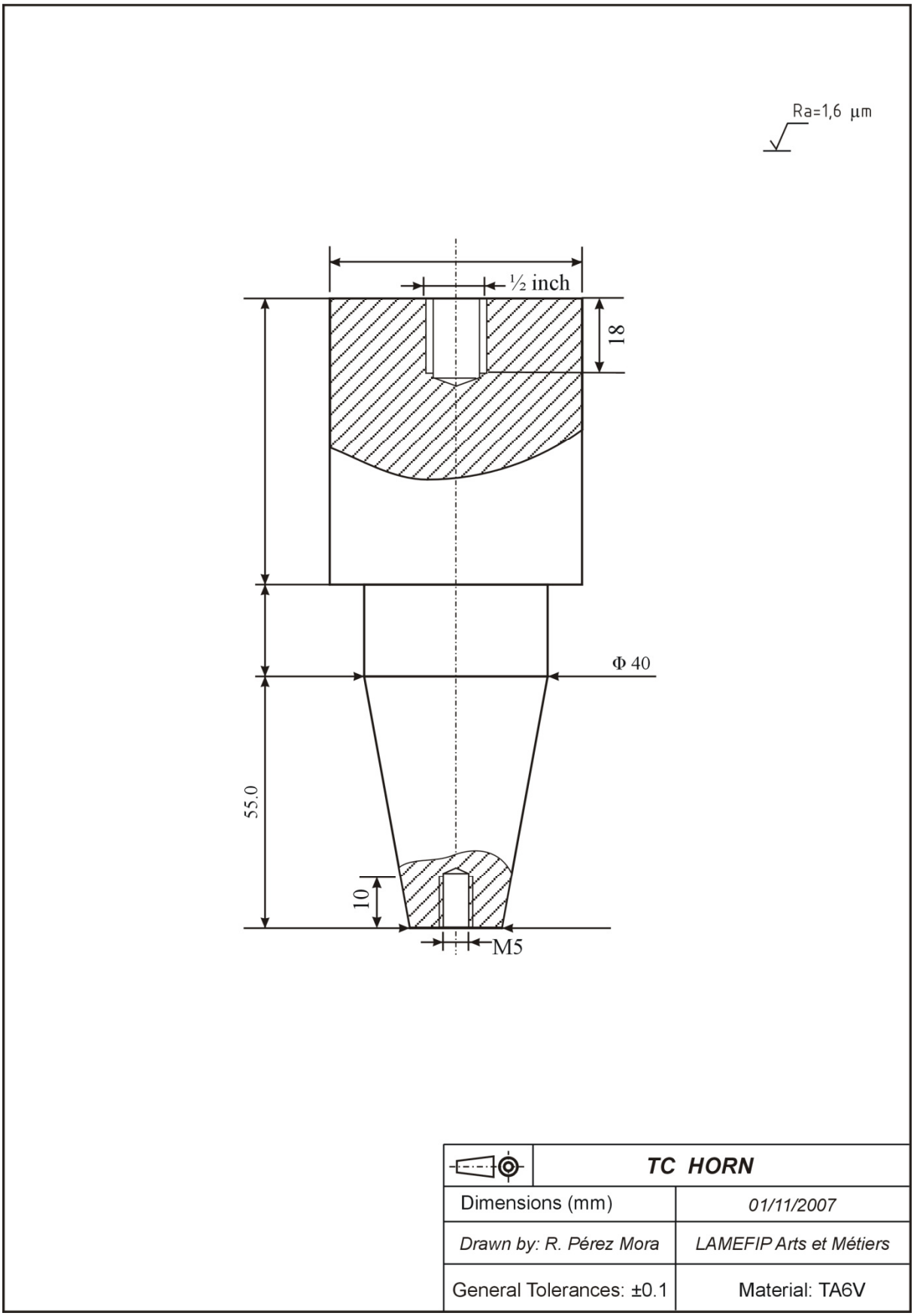
Ra=1,6 µm
½ inch
18
Φ 40
55.0
10
M5
TC HORN
Dimensions (mm)
01/11/2007
Drawn by: R. Pérez Mora
LAMEFIP Arts et Métiers
General Tolerances: ±0.1
Material: TA6V

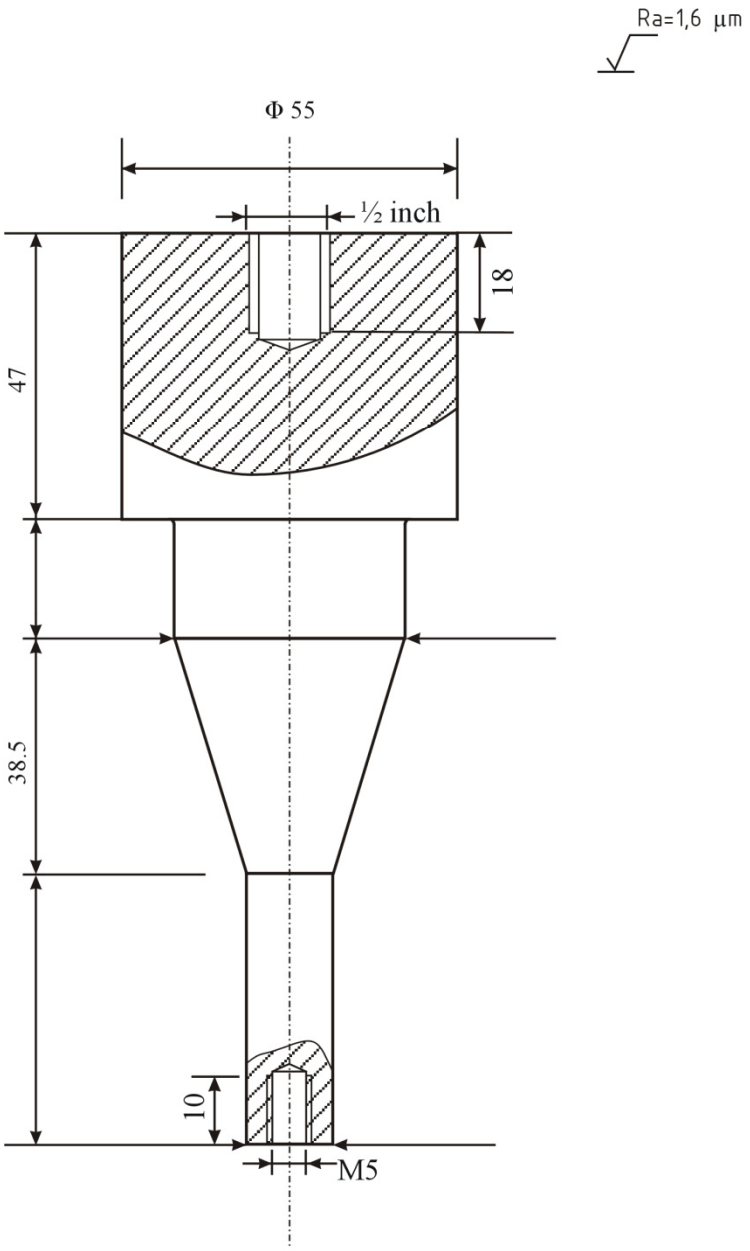

TGD HORN	
Dimensions (mm)	*01/11/2007*
Drawn by: R. Pérez Mora	*LAMEFIP Arts et Métiers*
General Tolerances: ±0.1	Material: TA6V

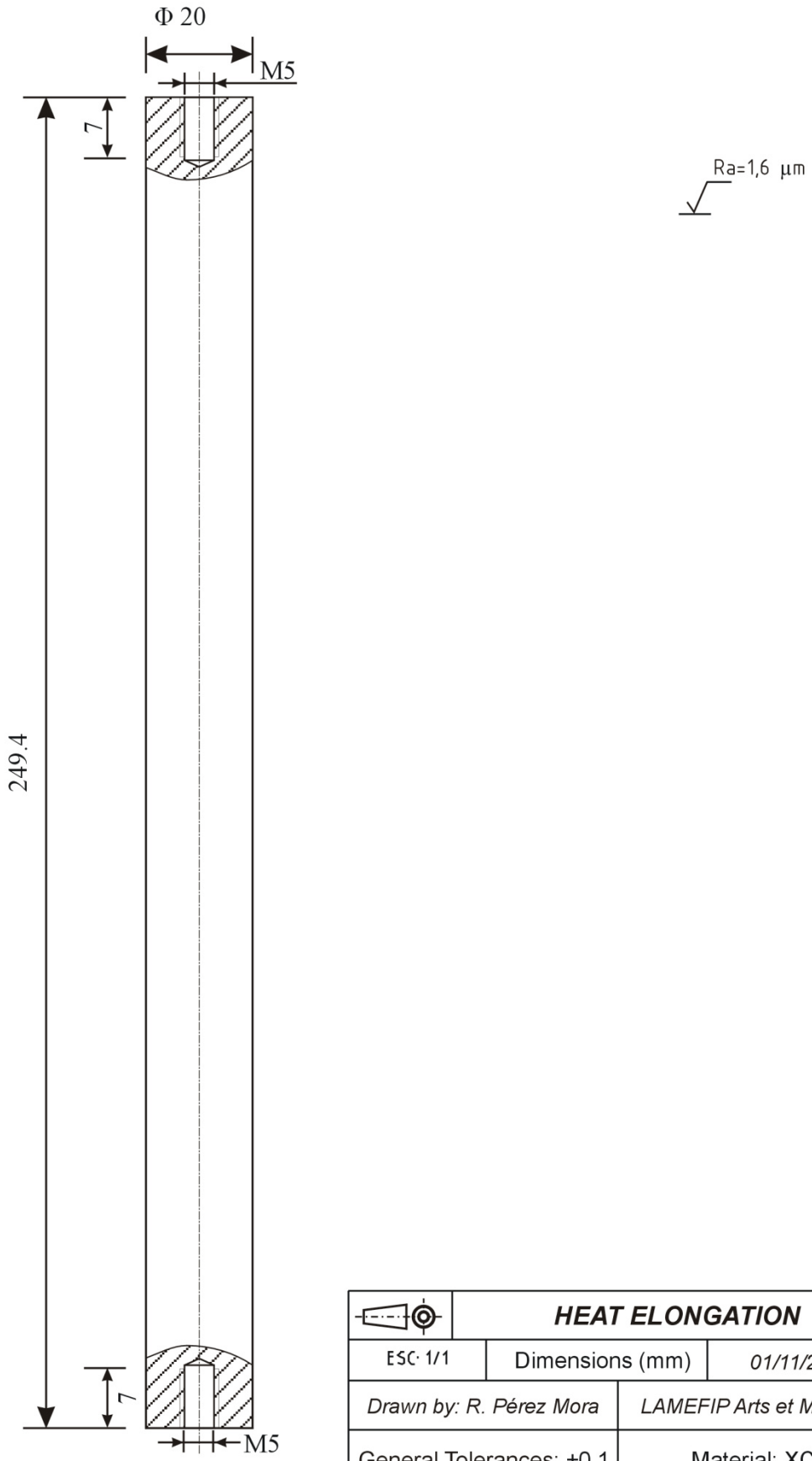

	HEAT ELONGATION	
ESC: 1/1	Dimensions (mm)	*01/11/2007*
Drawn by: R. Pérez Mora	*LAMEFIP Arts et Métiers*	
General Tolerances: ±0.1	Material: XC38	

Finite element analysis

Cylindrical horn (Figure 1)

A modal analysis have been carried out by using finite element ANSYS software in order to find the modes of vibration of this cylindrical horn. Table 1 shows the modal frequencies of this cylindrical horn obtained by finite element calculation. One of the modal frequencies is 19967 Hz, which is approximately the same than the piezoelectric convertor vibration.

Figure 2 shows the harmonic analysis solution done ANSYS for the cylindrical horn with an applied harmonic displacement at the top of 5 µm at 19967 Hz. It is observed that the same displacement at the top is reflected at the bottom of the horn.

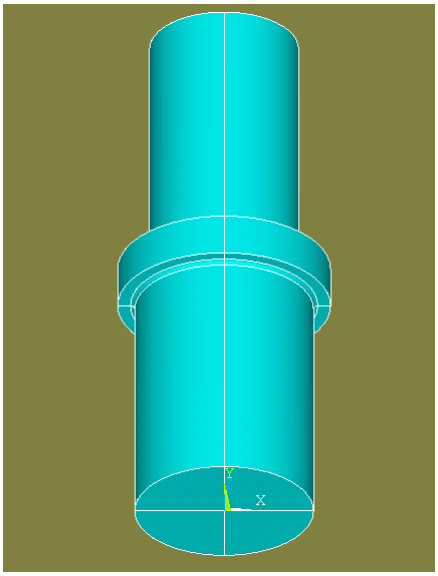

Figure 1. Cylindrical horn shape (very low amplification).

***** INDEX OF DATA SETS ON RESULTS FILE *****

SET	TIME/FREQ	LOAD STEP	SUBSTEP
1	0.0000	1	1
2	0.0000	1	2
3	0.66645E-03	1	3
4	0.18244E-02	1	4
5	0.24573E-02	1	5
6	0.28846E-02	1	6
7	8727.3	1	7
8	8727.6	1	8
9	12650.	1	9
10	19967.	1	10
11	21117.	1	11
12	21818.	1	12
13	22364.	1	13
14	30697.	1	14
15	30698.	1	15
16	37664.	1	16
17	37875.	1	17
18	39846.	1	18
19	39849.	1	19
20	45793.	1	20
21	48088.	1	21
22	48095.	1	22

Table 1. Modal frequencies of cylindrical horn (TA6V material).

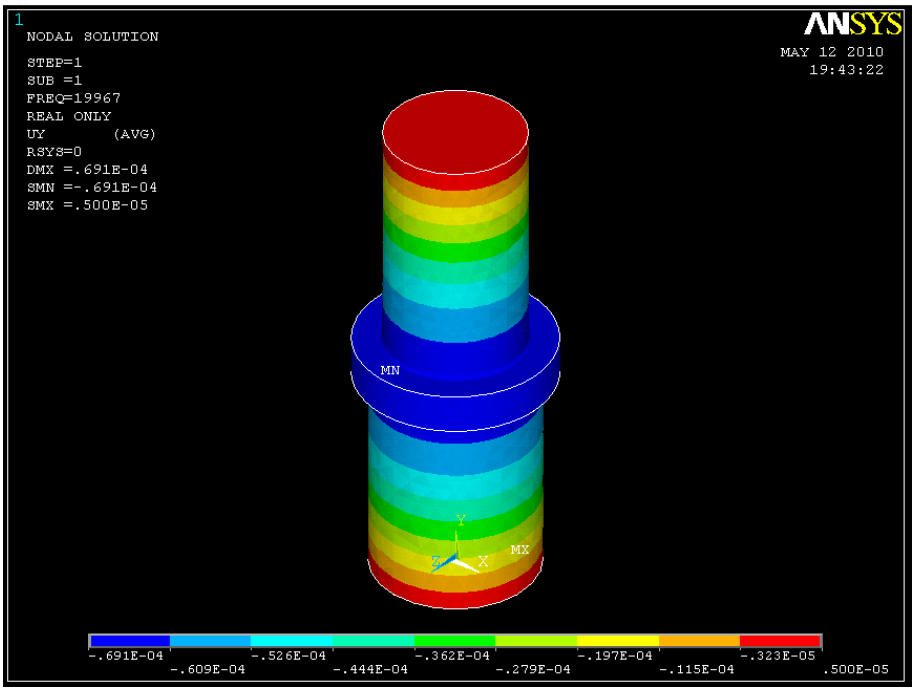

Figure 2. Harmonic analysis of cylindrical horn (TA6V material) with 5 µm top vibration.

Conical horn TC (Figure 3)

A modal analysis have been carried out by using finite element analysis ANSYS software in order to find the modes of vibration of this conical horn. Table 2 shows the modal frequencies of this cylindrical horn obtained by finite element calculation. It is observed that one of these frequencies is 20137 Hz which is practically the same of the piezoelectric converter.

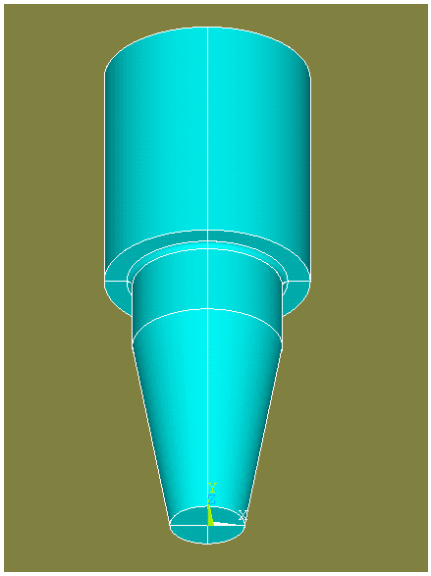

Figure 3. TC horn (conical shape medium amplification) in TA6V material.

***** INDEX OF DATA SETS ON RESULTS FILE *****

SET	TIME/FREQ	LOAD STEP	SUBSTEP
1	0.0000	1	1
2	0.0000	1	2
3	0.0000	1	3
4	0.15517E-02	1	4
5	0.21749E-02	1	5
6	0.26804E-02	1	6
7	8772.8	1	7
8	8773.0	1	8
9	15178.	1	9
10	19066.	1	10
11	19066.	1	11
12	20137.	1	12
13	25037.	1	13
14	29573.	1	14
15	29574.	1	15
16	33316.	1	16
17	36624.	1	17
18	36873.	1	18
19	36875.	1	19
20	38219.	1	20
21	38220.	1	21
22	40616.	1	22
23	40619.	1	23
24	42633.	1	24
25	42638.	1	25
26	47861.	1	26
27	47864.	1	27
28	47953.	1	28
29	48798.	1	29
30	48802.	1	30

Table 2. Modal frequencies of TC conical horn (TA6V material) from ANSYS calculation.

A harmonic analysis at 20137 Hz have been carried out in order to verify the amplification factor of the TC conical horn. A harmonic displacement of 5 µm was applied on the top of the horn, which is around the maximum amplitude displacement of the converter. In Figure 4 it is observed that for a displacement applied of 5 µm at the top of the horn, the maximum displacement at the bottom of the TC horn is around 26 µm.

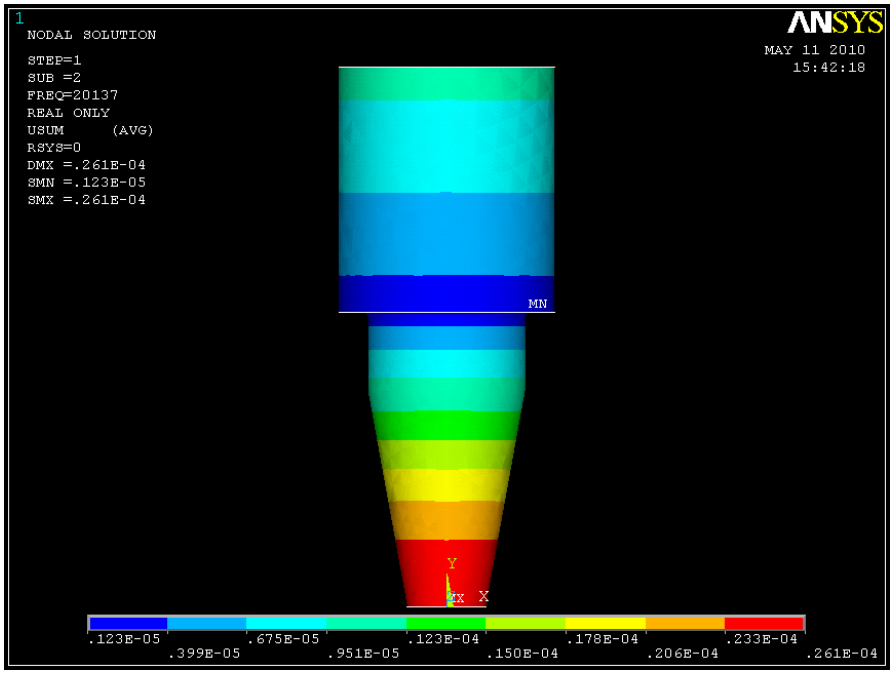

Figure 4. Harmonic analysis of TC conical horn (TA6V material) with 5 µm top vibration.

Conical high amplification horn TGD (Figure 5)

A modal analysis have been carried out by using finite element ANSYS software in order to find the modes of vibration of this high amplification conical horn. Table 3 shows the modal frequencies of this conical horn obtained by finite element calculation. Is its observed that one the modal frequencies is 19742 Hz, which is practically the same frequency of the piezoelectric converter, then it can works in resonance.

A harmonic analysis at this frequency, 19742 Hz, shows that applying 5 µm of harmonic displacement at the top of the horn, the maximum amplitude displacement obtained at the bottom of the horn is around 88 µm (Figure 6).

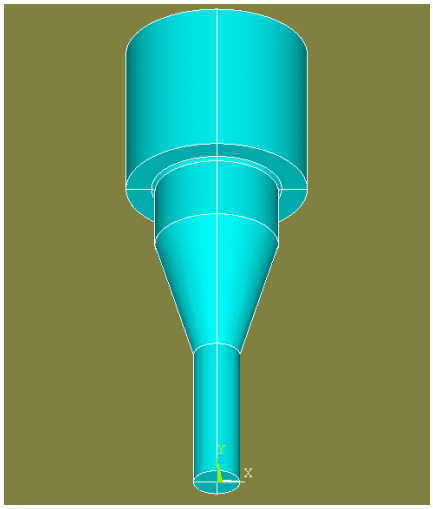

Figure 5. TGD horn (conical shape high amplification).

***** INDEX OF DATA SETS ON RESULTS FILE *****

SET	TIME/FREQ	LOAD STEP	SUBSTEP
1	0.0000	1	1
2	0.0000	1	2
3	0.0000	1	3
4	0.0000	1	4
5	0.17257E-02	1	5
6	0.21068E-02	1	6
7	3854.0	1	7
8	3854.2	1	8
9	12096.	1	9
10	12097.	1	10
11	14535.	1	11
12	19208.	1	12
13	19740.	1	13
14	19742.	1	14
15	21124.	1	15
16	29969.	1	16
17	29971.	1	17
18	30944.	1	18
19	34017.	1	19
20	37143.	1	20
21	37144.	1	21
22	38522.	1	22
23	38524.	1	23
24	41820.	1	24
25	43296.	1	25
26	43297.	1	26
27	43474.	1	27
28	43476.	1	28
29	48048.	1	29
30	48052.	1	30

Table 3. Modal frequencies of TGD conical horn (TA6V material).

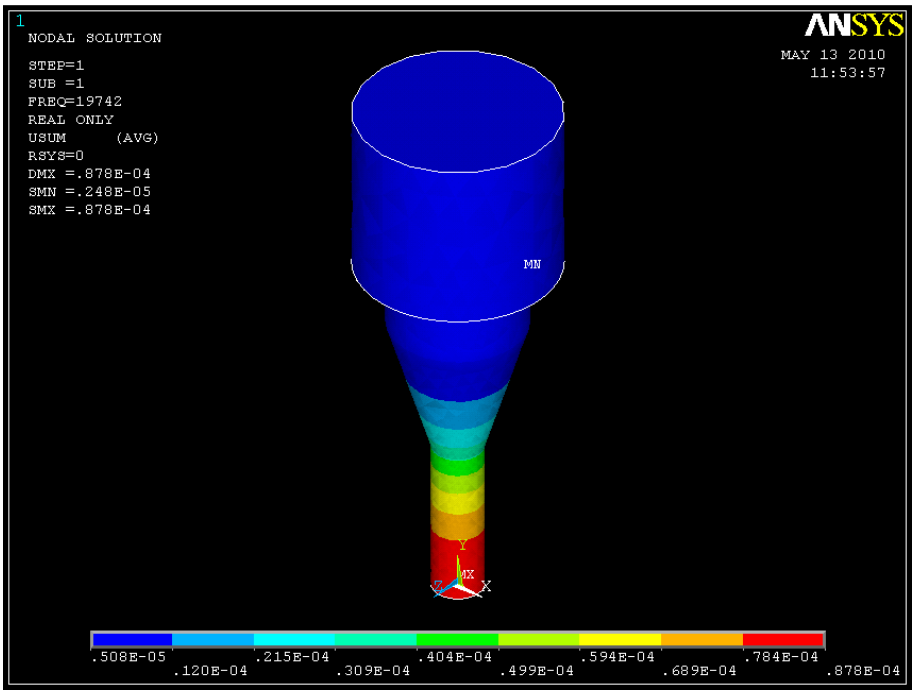

Figure 6. Harmonic analysis of TGD conical horn (TA6V material) with 5 µm top vibration.

Elongations (Figure 7)

A modal analysis have been carried out by using finite element ANSYS software in order to find the modes of vibration of these extension. Table 4 shows the modal frequencies of this extension obtained by finite element calculation. One of the modal frequencies is 20020 Hz. Then it can works in resonance with the piezoelectric converter.

Figure 8 shows the solution of a harmonic analysis carried out on the extension at 20020 Hz with ANSYS, applying 5 µm of harmonic displacement at the top. It is observed that the same displacement is reflected in the bottom of the extension. There is also a node of maximum displacement at the middle of the extension, because it has two times the resonance length.

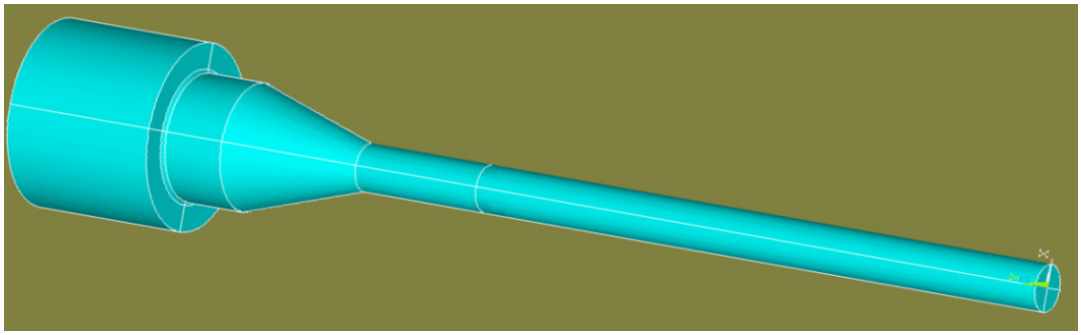

Figure 7. Extension for climatic chambers adaptation (XC36 material).

***** INDEX OF DATA SETS ON RESULTS FILE *****

SET	TIME/FREQ	LOAD STEP	SUBSTEP
1	0.0000	1	1
2	0.0000	1	2
3	0.0000	1	3
4	0.0000	1	4
5	0.25060E-02	1	5
6	0.34123E-02	1	6
7	1362.3	1	7
8	1362.3	1	8
9	3656.8	1	9
10	3656.8	1	10
11	6218.0	1	11
12	6916.8	1	12
13	6916.8	1	13
14	10020.	1	14
15	10954.	1	15
16	10954.	1	16
17	12438.	1	17
18	15601.	1	18
19	15602.	1	19
20	18664.	1	20
21	20020.	1	21
22	20717.	1	22
23	20717.	1	23
24	24899.	1	24
25	26187.	1	25
26	26188.	1	26
27	29979.	1	27
28	31140.	1	28
29	31936.	1	29
30	31936.	1	30

Table 4. Modal frequencies of extension attachment (XC36 material).

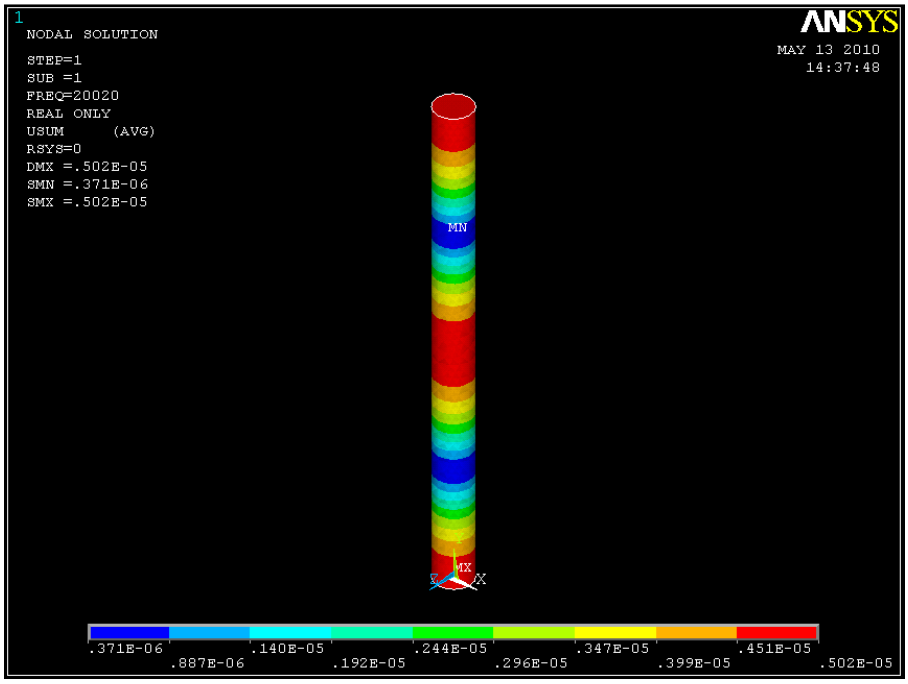

Figure 8. Harmonic analysis of the extensions (XC36 material) with 5 µm top vibration.

Annex 3
Geometry plans of endurance specimens

The specimens for ultrasonic fatigue testing are designed to work in resonance at 20 kHz, which is the excitation frequency of the piezoelectric converter of ultrasonic the fatigue testing machine.

Specimen lengths are very important to achieve a good testing frequency. Because of that, machining tolerances are important.

In this annex are presented the plans of geometry of both studied materials in this work: AS7G06 cast aluminium alloy and R5 steel.

Note: In the plans is noted a hole threaded, that is for testing at R= –1. Two threaded holes are necessary for testing at R ratio different to –1.

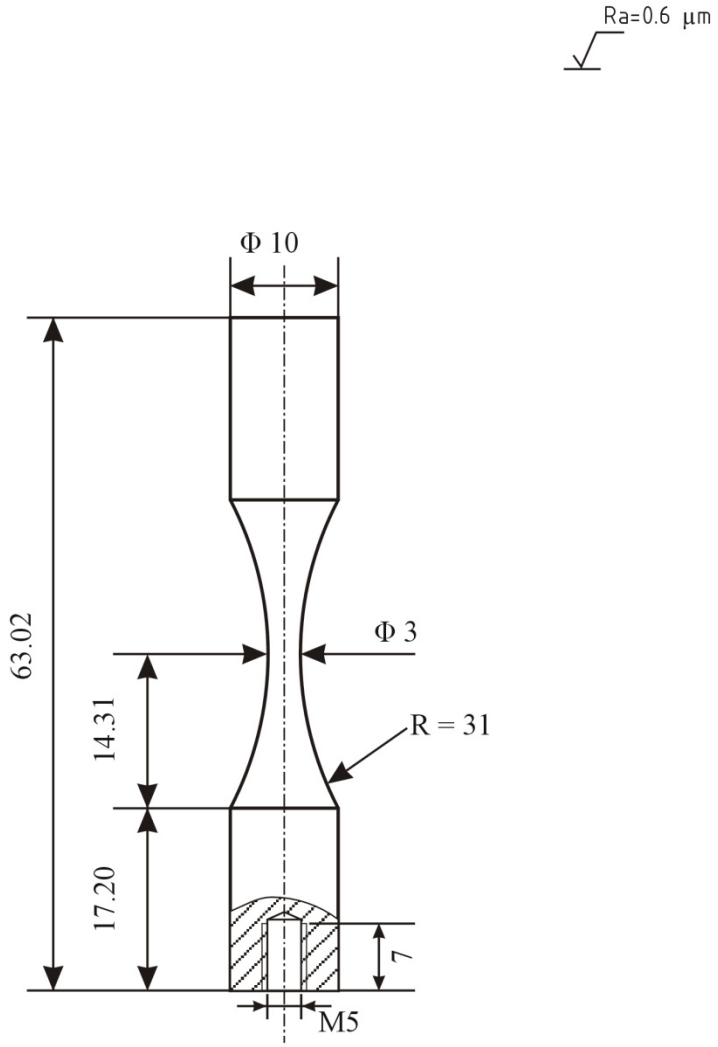

ULTRASONIC FATIGUE AS7G06 SPECIMEN		
ESC: 1/1	Dimensions (mm)	01/11/2006
Drawn by: R. Pérez Mora	LAMEFIP Arts et Métiers	
General Tolerances: ±0.02	Material: AS7G06	
E= 68 GPa	ρ = 2680 kg/m^3	

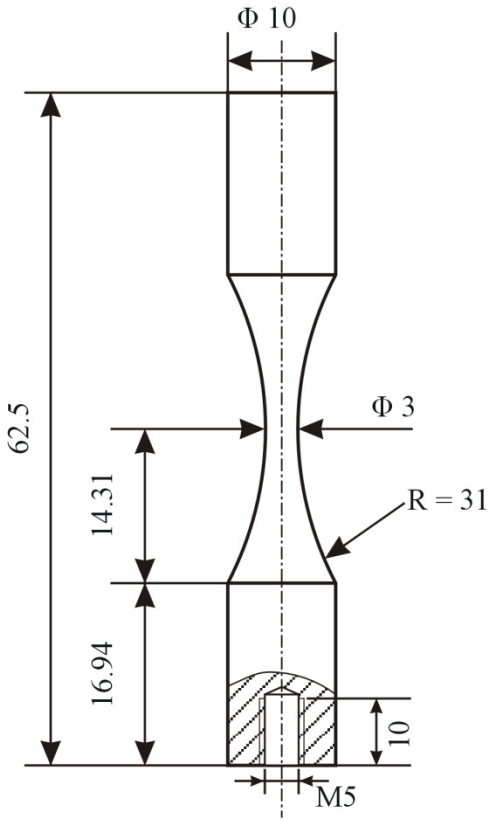

ULTRASONIC FATIGUE R5 SPECIMEN		
ESC: 1/1	Dimensions (mm)	01/11/2006
Drawn by: R. Pérez Mora	LAMEFIP Arts et Métiers	
General Tolerances: ±0.02	Material: R5 steel	
E= 211 GPa	ρ = 7900 kg/m^3	

Annex 4: Geometry plan of crack growth specimens

Next plan shows the dimensions of a fatigue crack growth specimen in ultrasonic machine.

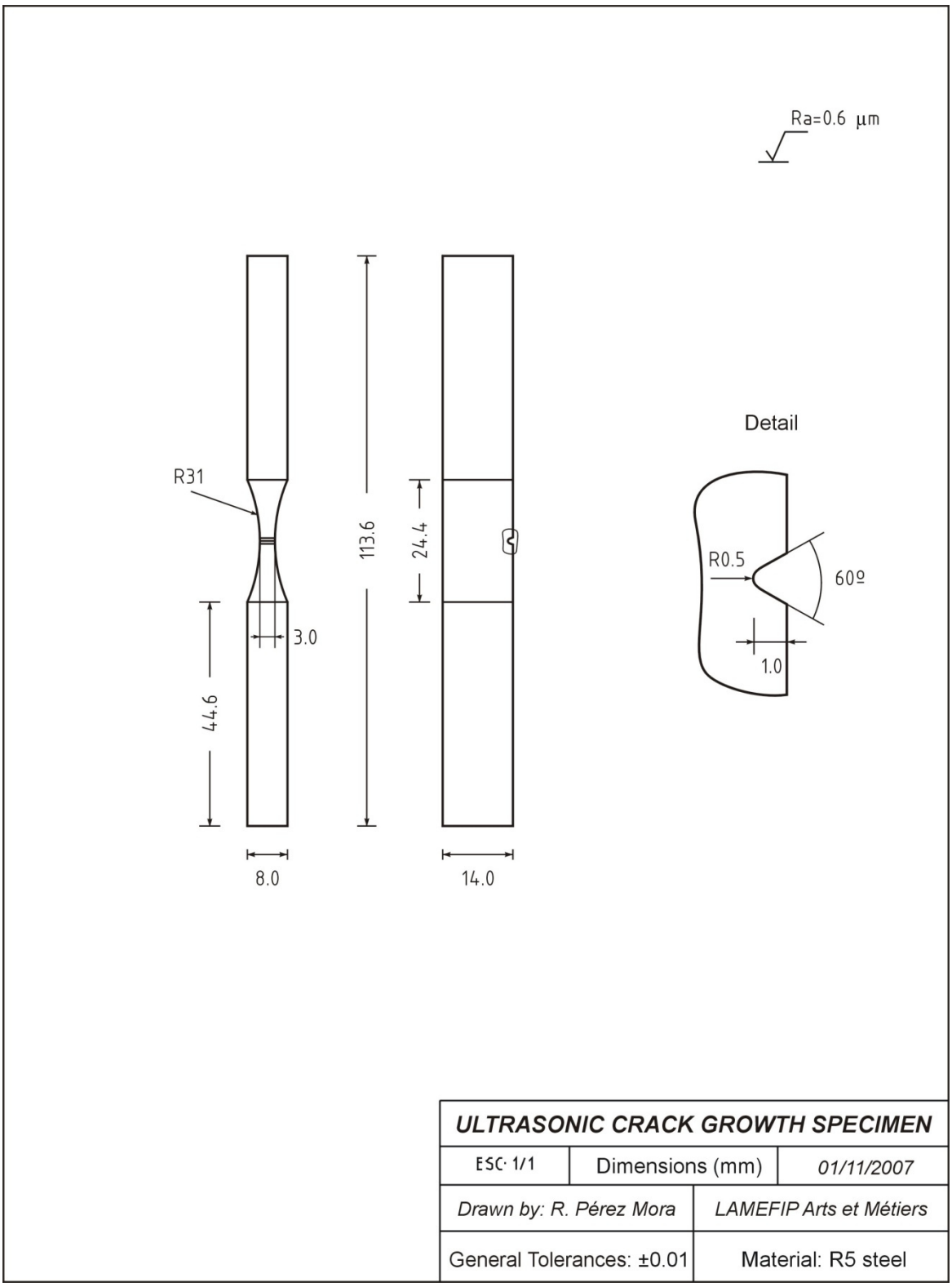

Annex 5: Methods of ultrasonic displacement Calibration

The ultrasonic fatigue machine is a displacement controlled testing equipment, it is important to calibrate the displacement amplitude in the vibration components. Different methods can be used to measure the amplitude of the displacement of vibration in the amplifiers attached to the ultrasonic fatigue testing machine. The aim of this annex is to present the procedure to calibrate the displacement amplitude related with the electrical tension imposed by the ultrasonic generator.

Laser interferometer

A calibration of one of the TC horns of the ultrasonic fatigue machine has been done by using a laser interferometer sensor that measures high frequency displacements. That has been done at the Mechanical Physical Laboratory (LMP) of Bordeaux 1 University, we thanks them for their assistance.

The laser interferometer equipment gives a tension signal and it is calibrated at different velocities of answer (125, 1000 m/s/V).

If

$$x = A_0 \sin \omega t \tag{1}$$

$$\frac{\mathrm{d}x}{\mathrm{d}t} = A_0\, \omega \cos \omega t \tag{2}$$

Its maximum

$$\frac{\mathrm{d}x}{\mathrm{d}t} = A_0\, 2\pi f \tag{3}$$

For the laser interferometer

$$A_0\, 2\pi f = V \cdot C \tag{4}$$

where

A_0 = Measured amplitude (m)

f = Frequency of vibration = 20000 Hz

V = Tension of Laser Sensor (V)

C = Constant of calibration of Laser Sensor (m/s/V)

The measured value A_0 is the displacement amplitude at the extremity of the horn attached to the specimen.

Table 1 shows the obtained data for a TC horn (Dimensions in Annex 2-A).

Step	Tension machine, V	Tension laser, V	Calibration constant m/s/V	Amplitude by Laser, micron
1	-7.5	2	125	1.00
2	-5.6	1.76	1000	7.00
3	-4	2.25	1000	8.9
4	-2	2.82	1000	11.22
5	0	3.5	1000	13.93
6	2	3.93	1000	15.63

Table 1. Measured displacement amplitude in TC horn with laser sensor.

In Table 1:

- Tension machine is the tension voltage of the ultrasonic generator corresponding to a given displacement amplitude.
- Tension laser is the given value from the laser sensor corresponding to demanded displacement amplitude.
- Calibration constant is the constant value calibrated for each velocity of displacement.
- Amplitude by laser is the calculated amplitude according to the tension as output of the laser sensor, using equation 1.

We can plot a curve of calibration of the calculated displacement amplitude as function of the tension voltage in the fatigue testing machine.

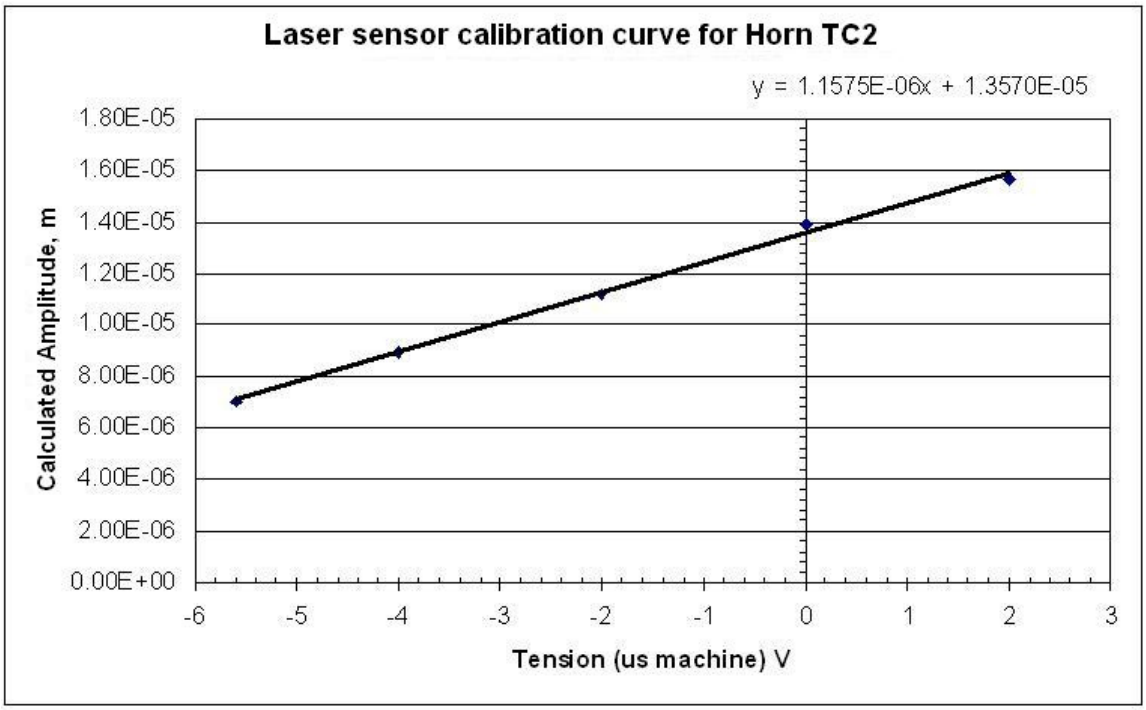

Figure 1. Calibration curve and linear function of amplitude from laser sensor according to the voltage delivered by the fatigue machine to the piezoelectric converter exciting the horn.

Using the previous curve and the linear function it is possible to calculate the amplitude for all the range of tension in ultrasonic fatigue machine.

On the other hand, it is possible calculate the stress and strain for a material using the next equations:

$$\sigma = A_0 (S/D)_{\text{ratio}} \tag{5}$$

$$\varepsilon = \sigma / E_d \tag{6}$$

where:

A_0 = Displacement amplitude

$(S/D)_{\text{ratio}}$ = Stress-Displacement ratio of the material for a specimen geometry (at 20 kHz)

E_d = Dynamic Young's modulus of the material

Strain gauges

Using strain gauges glued on specimens (as shown in Figure 2) it was possible to measure the strain in the narrowest cross-section and then the amplitude displacement applied by the horn to achieve such strain.

Parameters

Stress ratio: –1

Strain gage configuration: ¼ bridge

Equipment: 2210 Vishay Micro-measurement Conditioning

HAMEG HM303-6 Analogical Oscilloscope

PHILIPS PM2525 Voltmeter

B&K 2427 Autoranging Digital Voltmeter

Equipment settings

Applied torque between converter and horn: 55 Nm

Applied torque between screw and horn: 55 Nm

Applied torque between specimen and horn: 5 Nm recommended

2210 Conditioning Gain: ×300

Width Band (100 kHz) large band

Philips Voltmeter: peak-peak measuring

B&K voltmeter: RMS measuring

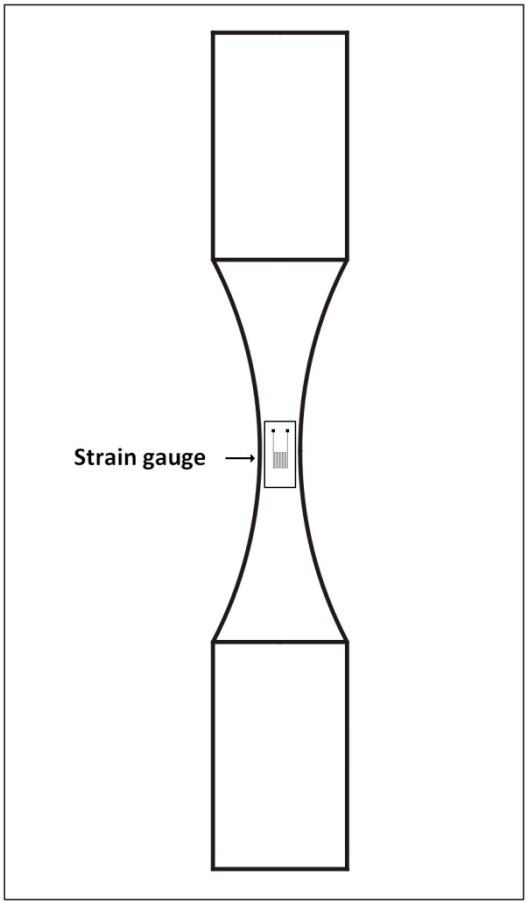

Figure 2. Scheme of gluing strain gauges on specimen.

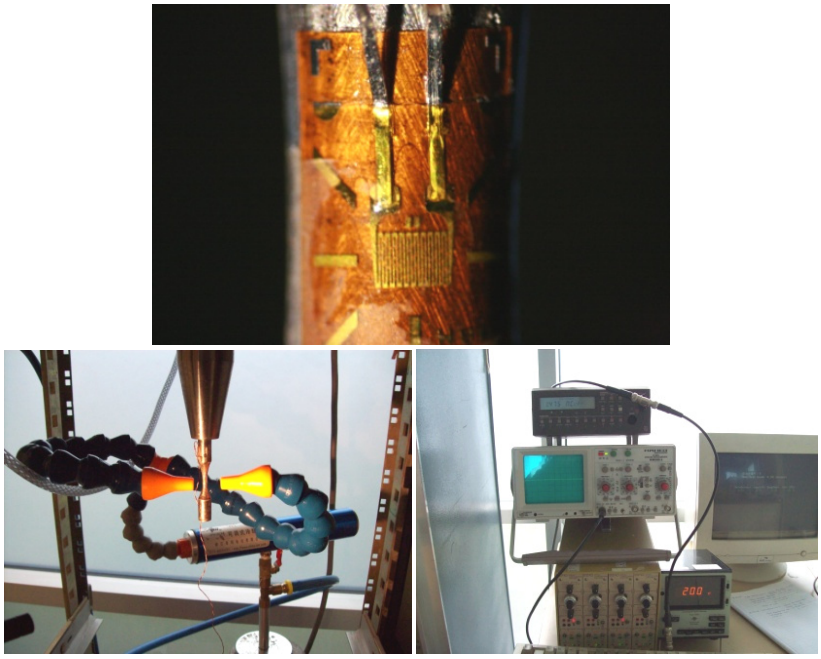

Figure 3. Setting of strain gage on specimen and acquisition data devices for calibration.

Calibration and measure procedure:

- To screw carefully the specimen with strain gauge to the horn and to connect it to the correct entrance in the Vishay Conditioner.
- To equilibrate the Conditioner (putting to zero) at "A" position.
- To note the tension of calibration A (C_A) and to start to run the test at low stress levels.
- Tension peak to peak and root mean square tension were measured with Philips PM2525 multimeter and B&K 2427 voltmeter respectively. With these values strain is calculated computed using next equations.

  V_{pp} = Tension peak to peak

  V_{RMS} = Root mean square tension

  C_A = Calibration Constant = 1176.5 μm/m

  V_C = Calibration tension value

  Strain amplitude from tension peak to peak:

$$\varepsilon_{pp} = \frac{V_{pp}}{V_C} C_A \quad \rightarrow \quad \varepsilon_{amp} = \frac{\varepsilon_{pp}}{2} \tag{7}$$

  Strain amplitude from tension RMS)

$$\varepsilon_{amp}(RMS) = \frac{V_{RMS}\sqrt{2}}{V_C} C_A \tag{8}$$

Figure 4 shows the curve for strain amplitude versus tension in the fatigue machine for a R5 steel specimen. Figure 5 shows the curve of strain amplitude versus tension for a AS7G06-T6 specimen.

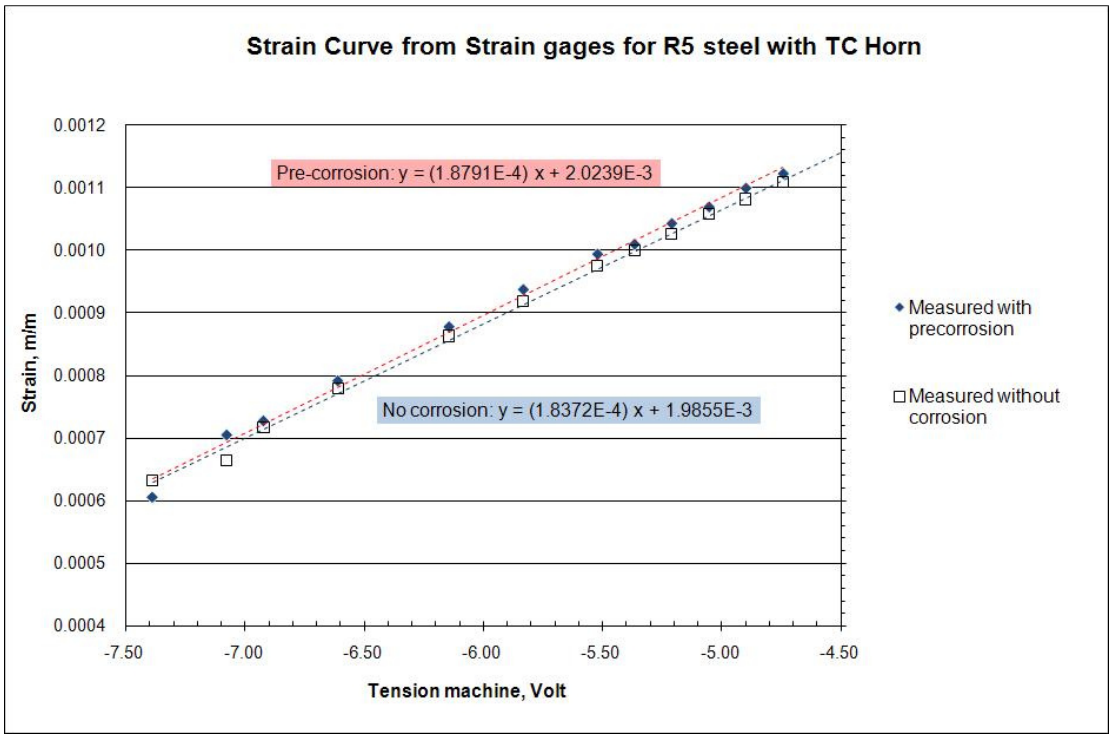

Figure 4. Strain chart from strain gauges measures for R5 steel versus voltage in ultrasonic fatigue machine.

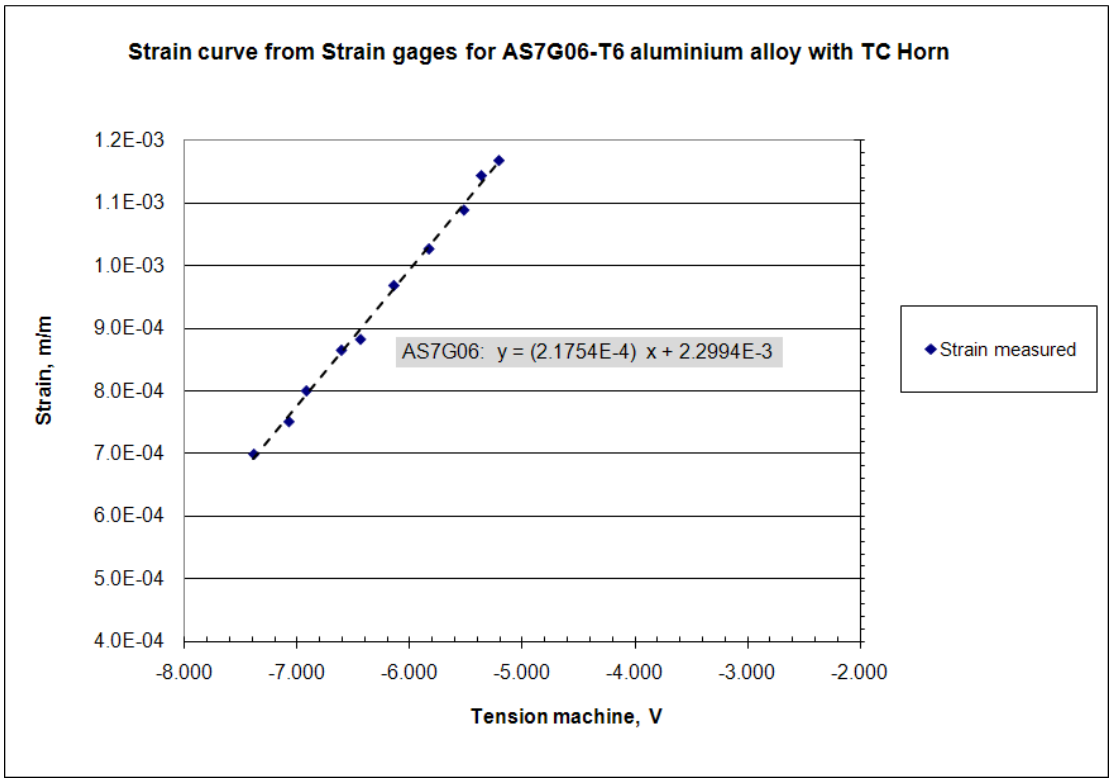

Figure 5. Strain chart from strain gauges measures for AS7G06-T6 aluminium alloy versus voltage in ultrasonic fatigue machine.

Knowing the correct strain it is possible to calculate the stress for any material using Equation (6). And with Equation (5) the amplitude displacement (A_0) can be estimated.

Table 2 shows an example for a R5 steel specimen with E_d=211 GPa, $(S/D)_{ratio}$=27.164 MPa/µm, using a conic the TC horn.

Tension, V	Strain, By linear fitting	Stress, MPa	Estimated Amplitude, µm
-7.388	0.00063562	134.1160	4.937
-7.076	0.00069425	146.4865	5.393
-6.610	0.00078181	164.9629	6.073
-6.144	0.00086938	183.4394	6.753
-5.832	0.00092801	195.8099	7.208
-5.521	0.00098645	208.1407	7.662
-5.210	0.00104489	220.4716	8.116
-5.054	0.00107420	226.6568	8.344
-4.743	0.00113264	238.9876	8.798
-5.366	0.00101557	214.2863	7.889
-4.899	0.00110333	232.8024	8.570
-6.922	0.00072319	152.5925	5.617

Table 2. Computed real amplitude, stress and strain according to linear fit.

Annex 6: Data sheet of results of AS7G06-T6 tests

Next pages contain the table of data and if it is the case the staircase method results of fatigue tests on AS7G06-T6 cast aluminium alloy.

The tests were carried out by using an ultrasonic fatigue testing machine at 20 kHz at different R ratio and temperatures

Index of Data

Data sheet of AS7G06-T6 crack initiation tests in air, R=-1 , room temperature 2

Staircase data of AS7G06-T6 tests in air, R=-1 , room temperature 3

Data sheet of AS7G06-T6 crack initiation tests in air, R=0.01 , room temperature 4

Data sheet of AS7G06-T6 crack initiation tests in air, R=0.5 , room temperature 5

Staircase data of AS7G06-T6 tests in air, R=0.5 , room temperature 6

Data sheet of AS7G06-T6 crack initiation tests in air, R=-1 , 150 °C 7

Staircase data of AS7G06-T6 tests in air, R=-1 , 150 °C 8

Data sheet of AS7G06-T6 crack initiation tests in air, R=0.01 , 150 °C 9

Staircase data of AS7G06-T6 tests in air, R=0.01 , 150 °C 10

Data sheet of AS7G06-T6 crack initiation tests in air, R=-1 , room temperature

Material:	**AS7G06-T6**	Date:	2006
	cast aluminium alloy		
Lot:	**1**	Provenance:	Turbomeca
Name of the test:	**AS7G06-T6 crack initiation in air, R=-1, room temperature**		

Solicitation type:	**Tension-Compression**	**R=**	**-1**
Lifespan aim:	**10^9 cycles**	Frequency:	20 kHz
Cycle Form:	Sinusoidal	Machine:	Ultrasonic
Test temperature:	Room	Operator:	CB
Environment:	Air	**Kt=**	1.02
Specimen Geometry:	**Smooth**	Treatment:	None
Useful diameter. (mm):	3	Fabrication:	Casting
Method of examination:	Staircase		
Number of tested specimens:	**24**	Unit of S:	MPa
Number of failed specimens:	17	Unit of Nf:	cycles

		S nominal					
Test	Spec.	Smean	Smin	Smax	Samp	N	Result
1	1	0	-100	100	100	5.90E+06	x
2	2	0	-90	90	90	2.82E+07	x
3	3	0	-80	80	80	9.39E+07	x
4	4	0	-75	75	75	8.14E+08	x
5	5	0	-70	70	70	1.00E+09	o
6	6	0	-75	75	75	1.11E+08	x
7	7	0	-70	70	70	1.00E+09	o
8	8	0	-75	75	75	1.07E+08	x
9	9	0	-70	70	70	2.24E+08	x
10	10	0	-65	65	65	1.00E+09	o
11	11	0	-70	70	70	1.00E+09	o
12	12	0	-75	75	75	1.22E+08	x
13	13	0	-70	70	70	1.44E+09	x
14	14	0	-75	75	75	1.00E+09	o
15	15	0	-80	80	80	1.51E+08	x
16	16	0	-75	75	75	1.92E+08	x
17	17	0	-70	70	70	2.34E+08	x
18	18	0	-65	65	65	1.00E+10	o
19	19	0	-70	70	70	1.00E+10	o
20	20	0	-110	110	110	1.51E+06	x
21	21	0	-105	105	105	1.02E+06	x
14*	14*	0	-95	95	95	3.62E+06	x
7*	A01	0	-85	85	85	6.87E+07	x
11*	11*	0	-90	90	90	2.17E+07	x

x = Failed, o = survivor

* Tested at LAMEFIP. The rest tested in Prof. Bathias' laboratory.

Staircase data of AS7G06-T6 tests in air, R=-1 , room temperature

Test:	**R-1, AS7G06-T6, Room temperature**	Date:	2006	Specimen Geometry:	**Smooth**
Material:	**AS7G06-T6**	Provenance:	Turbomeca		
Solicitation type:	**Tension-Compression**	**R=**	**-1**	Useful diameter. (mm):	3
Lifespan aim:	**10^9 cycles**	Frequency:	20 kHz	Treatment:	T6
Cycle form:	sinusouidal	Machine:	Ultrasonic		
Test temperature (°C):	Room	Operator:	CB	Fabrication:	Casting
Environment:	Air	Nominal or local stresses:		Nominal	

Order	1	2	3	4	5	6	7	8	9	10	11	12	13	14	15	16	17	18	19										
N° Sp.																													
Sa (MPa)																													
110																													
100	x																												
90		x																											
80			x												x														
75				x		x		x				x		o		x													
70					o		o		x		o		o				x		x										
65										o								o											
60																													

Examination: Number of failed (x): 12 Number of non failed (o): 7 Least frequent possibility (x or o): o

S (MPa)	i	Ni	i.Ni	i^2.Ni
75	2	1	2	4
70	1	4	4	4
65	0	2	0	0
	Σ=	7	6	8
		N	A	B

If least frequent possibility = o: Sd=So+d(A/N+0.5)

If least frequent possibility = x: Sd=So+d(A/N-0.5)

Here: d= 5 MPa

So= 65 MPa

Result: 71.79 MPa

Standard deviation estimation:

Test: $(NB-A^2)/N^2 =$ 0.4

If test < 0.3 estimation is impossible

If test > 0.3 $S=1.62\ d\ [(NB-A^2)/N^2+0.029]$

Result: S = 3.5 MPa

Data sheet of AS7G06-T6 crack initiation tests in air, R=0.01 , room temperature

Material:	**AS7G06-T6**	Date:	2006
	cast aluminium alloy		
Lot:	**1**	Provenance:	Turbomeca
Name of the test:	**AS7G06-T6 crack initiation in air, 20 °C, R=0.01**		

Solicitation type:	**Tension-Tension**	**R=**	**0.01**
Lifespan aim:	**10^9 cycles**	Frequency:	20 kHz
Cycle Form:	Sinusoidal	Machine:	Ultrasonic
Test temperature:	Room T	Operator:	CB
Environment:	Air	**Kt=**	1.02
Specimen Geometry:	**Smooth**	Treatment:	None
Useful diameter. (mm):	3	Fabrication:	Casting
Method of examination:	Staircase		
Number of tested specimens:	**12**	Unit of S:	MPa
Number of failed specimens:	10	Unit of Nf:	cycles

		S nominal					
Test	Spec.	Smean	Smin	Smax	Samp	N	Result
1	1	40.8	0.81	80.8	40	4.774E+07	x (failed)
2	2	40.8	0.81	80.8	40	1.000E+09	o (survivor)
3	3	40.8	0.81	80.8	40	1.990E+09	o (survivor)
4	4	40.8	0.81	80.8	40	1.542E+08	x (failed)
5	5	51	1.01	101	50	9.583E+06	x (failed)
6	6	51	1.01	101	50	6.384E+08	x (failed)
7	7	56.1	1.11	111	55	1.852E+07	x (failed)
8	8	56.1	1.11	111	55	2.300E+07	x (failed)
9	9	61.2	1.21	121	60	9.770E+05	x (failed)
10	10	61.2	1.21	121	60	9.070E+06	x (failed)
11	11	81.6	1.61	162	80	4.420E+05	x (failed)
12	12	91.8	1.82	182	90	6.360E+04	x (failed)
13	13	53.6	1.06	106	52.5	5.950E+06	x (failed)

Note: This series of tests were carried out in Prof. Bathias' laboratory. Staircase is not available.

Data sheet of AS7G06-T6 crack initiation tests in air, R=0.5 , room temperature

Material:	**AS7G06-T6**	Date:	Feb - Mar 2009
	cast aluminium alloy		
Lot:	**1**	Provenance:	Turbomeca
Name of the test:	**AS7G06-T6 crack initiation in air, room temperature R=0.5**		

Solicitation type:	**Tension-Tension**	**R=**	**0.5**
Lifespan aim:	**10^9 cycles**	Frequency:	20 kHz
Cycle Form:	Sinusoidal	Machine:	Ultrasonic
Test temperature:	Room	Operator:	RPM
Environment:	Air	**Kt=**	1.02
Specimen Geometry:	**Smooth**	Treatment:	None
Useful diameter. (mm):	3	Fabrication:	Casting
Method of examination:	Staircase		
Number of tested specimens:	**10**	Unit of S:	MPa
Number of failed specimens:	4	Unit of Nf:	cycles

			S nominal				S local				
Test	Spec.	Pocket	Smean	Smin	Smax	Samp	Smean	Smin	Smax	N	Result
1a	48	9	135	90	180	45				1.200E+09	o (survivor)
1b	48	9	165	110	220	55				3.948E+08	x (failed)
2	39	8	150	100	200	50				1.180E+09	o (survivor)
3	38	8	165	110	220	55				2.610E+08	x (failed)
4	40	8	150	100	200	50				1.500E+09	o (survivor)
5	29	6	165	110	220	55				1.160E+09	o (survivor)
6	27	6	180	120	240	60				2.320E+08	x (failed)
7	25	6	165	110	220	55				3.786E+07	x (failed)
8	26	6	150	100	200	50				1.220E+09	o (survivor)
9	23	6	165	110	220	55				1.510E+09	o (survivor)
10	22	6	180	120	240	60				1.369E+09	o (survivor)

Staircase data of AS7G06-T6 tests in air, R=0.5 , room temperature

Test:	**Crack initiation R=0.5 AS7G06-T6**	Date:	Feb-Mar 2009	Specimen Geometry:	**Smooth**
Material:	**AS7G06-T6**	Provenance:	Turbomeca		
Solicitation type:	**Tension-Tension**	**R=**	**0.5**	Useful diameter. (mm):	3
Lifespan aim:	**10^9 cycles**	Frequency:	20 kHz	Treatment:	None
Cycle form:	sinusouidal	Machine:	Ultrasonic		
Test temperature (°C):	Room	Manipulateur:	TPL JM	Fabrication:	Casting
Environment:	Air	Nominal or local stresses:		Nominal	

Order	1	2	3	4	5	6	7	8	9	10
N° Sp.	48	39	38	40	29	27	24	26	23	22
Sa (MPa)										
60						x				o
55	x		x		o		x		o	
50		o		o				o		

Examination: Number of failed (x): 4 Number of non failed (o): 6 Least frequent possibility (x or o): x

S (MPa)	i	Ni	i.Ni	i^2.Ni
60	1	1	1	1
55	0	3	0	0
	Σ=	4	1	1
		N	A	B

If least frequent possibility = o: Sd=So+d(A/N+0.5)

If least frequent possibility = x: Sd=So+d(A/N-0.5)

Here: d= 5 MPa

So= 55 MPa

Result: 53.75 MPa

Standard deviation estimation:

Test: $(NB-A^2)/N^2 =$ 0.2

If test < 0.3 estimation is impossible

If test > 0.3 $S=1.62\ d\ [(NB-A^2)/N^2+0.029]$

Result: S = 1.8 MPa

Data sheet of AS7G06-T6 crack initiation tests in air, R=-1 , 150 °C

Material:	**AS7G06-T6**	Date:	01/05/09
	cast aluminium alloy		
Lot:	**1**	Provenance:	Turbomeca
Name of the test:	**AS7G06-T6 crack initiation in air, 150 °C, R=-1**		

Solicitation type:	**Tension-Compression**	**R=**	**-1**
Lifespan aim:	**10^9 cycles**	Frequency:	20 kHz
Cycle Form:	Sinusoidal	Machine:	Ultrasonic
Test temperature:	150 °C	Operator:	RPM
Environment:	Air	**Kt=**	1.02
Specimen Geometry:	**Smooth**	Treatment:	None
Useful diameter. (mm):	3	Fabrication:	Casting
Method of examination:	Staircase		
Number of tested specimens:	**17**	Unit of S:	MPa
Number of failed specimens:	10	Unit of Nf:	cycles

			S nominal					
Test	Spec.	Pocket	Smean	Smin	Smax	Samp	N	Result
1	37	7	0	-40	40	40	1.080E+09	o (survivor)
2	36	7	0	-50	50	50	1.220E+09	o (survivor)
3	34	7	0	-70	70	70	5.000E+07	x (failed)
4	35	7	0	-60	60	60	7.260E+08	x (failed)
5	30	7	0	-50	50	50	1.670E+09	o (survivor)
6	31	7	0	-60	60	60	1.070E+09	o (survivor)
7	32	7	0	-70	70	70	9.720E+07	x (failed)
8	33	7	0	-60	60	60	1.120E+09	x (failed)
9	2	3	0	-50	50	50	1.140E+09	o (survivor)
10	5	3	0	-60	60	60	1.980E+08	x (failed)
11	4	3	0	-50	50	50	1.090E+09	o (survivor)
12	10	4	0	-70	70	70	4.303E+07	x (failed)
13	11	4	0	-80	80	80	2.256E+07	x (failed)
14	13	4	0	-80	80	80	1.782E+07	x (failed)
15	12	4	0	-90	90	90	3.560E+06	x (failed)
16	6	4	0	-90	90	90	4.360E+06	x (failed)
17	7	4	0	-60	60	60	1.020E+09	o (survivor)

Staircase data of AS7G06-T6 tests in air, R=-1 , 150 °C

Test:	**Crack initiation R= -1, AS7G06-T6, 150°C**	Date:	01/05/2009	Specimen Geometry:	**Smooth**
Material:	**AS7G06-T6**	Provenance:	Turbomeca		
Solicitation type:	**Tension-Compression**	**R=**	**-1**	Useful diameter. (mm):	3
Lifespan aim:	**10^9 cycles**	Frequency:	20 kHz	Treatment:	None
Cycle form:	sinusouidal	Machine:	Ultrasonic		
Test temperature (°C):	150	Operator:	RPM	Fabrication:	Turbomeca
Environment:	Air	Nominal or local stresses:		Nominal	

Order	1	2	17	3	4	5	6	7	8	12	10	9
N° Sp.	37	36	7	34	35	30	31	32	33	10	5	2
Sa (MPa)												
70				x				x		x		
60			o		x		o		o		x	
50		o				o						o
40	o											

Examination: Number of failed (x): 5 Number of non failed (o): 7 Least frequent possibility (x or o): x

S (MPa)	i	Ni	i.Ni	i^2.Ni
70	1	3	3	3
60	0	2	0	0
	Σ=	5	3	3
		N	A	B

If least frequent possibility = o: Sd=So+d(A/N+0.5)

If least frequent possibility = x: Sd=So+d(A/N-0.5)

Here: d= 10 MPa Result: 61 MPa

So= 60 MPa

Standard deviation estimation: Test: $(NB-A^2)/N^2 =$ 0.2

If test < 0.3 estimation is impossible

If test > 0.3 $S=1.62\ d\ [(NB-A^2)/N^2+0.029]$

Result: S = 4.4 MPa

Data sheet of AS7G06-T6 crack initiation tests in air, R=0.01 , 150 °C

Material:	**AS7G06-T6**	Date:	June 2009
	cast aluminium alloy		
Lot:	**1**	Provenance:	Turbomeca
Name of the test:	**AS7G06-T6 crack initiation in air, 150 °C, R=0.01**		

Solicitation type:	**Tension-Tension**	**R=**	**0.01**
Lifespan aim:	**10^9 cycles**	Frequency:	20 kHz
Cycle Form:	Sinusoidal	Machine:	Ultrasonic
Test temperature:	150 °C	Operator:	RPM
Environment:	Air	**Kt=**	1.02
Specimen Geometry:	**Smooth**	Treatment:	None
Useful diameter. (mm):	3	Fabrication:	Casting
Method of examination:	Staircase		
Number of tested specimens:	**12**	Unit of S:	MPa
Number of failed specimens:	9	Unit of Nf:	cycles

			S nominal					
Test	Spec.	Pocket	Smean	Smin	Smax	Samp	N	Result
1	18	5	51	1.01	101	50	1.290E+08	x (failed)
2	19	5	40.8	0.81	80.8	40	1.100E+09	o (survivor)
3	20	5	51	1.01	101	50	1.010E+09	o (survivor)
4	21	5	61.2	1.21	121.2	60	1.682E+08	x (failed)
5	14	5	51	1.01	101	50	6.930E+07	x (failed)
6	15	5	40.8	0.81	80.8	40	1.020E+09	o (survivor)
7	16	5	51	1.01	101	50	5.910E+08	x (failed)
8	17	5	40.8	0.81	80.8	40	6.400E+08	x (failed)
9	92	2	71.4	1.41	141.4	70	3.620E+07	x (failed)
10	50	10	71.4	1.41	141.4	70	9.610E+06	x (failed)
11	8	4	81.6	1.62	162	80	4.100E+06	x (failed)
12	9	4	81.6	1.62	162	80	4.960E+06	x (failed)

Staircase data of AS7G06-T6 tests in air, R=0.01 , 150 °C

Test:	**Crack initiation R=0.01 AS7G06 150°C**	Date:	April 2009	Specimen Geometry:	**Smooth**
Material:	**AS7G06**	Provenance:	Turbomeca		
Solicitation type:	**Tension-Tension**	**R=**	**0.01**	Useful diameter. (mm):	3
Lifespan aim:	**10^9 cycles**	Frequency:	20 kHz	Treatment:	None
Cycle form:	sinusouidal	Machine:	Ultrasonic		
Test temperature (°C):	150	Operator:	RPM	Fabrication:	Casting
Environment:	Air	Nominal or local stresses:		Nominal	

Order	1	2	3	4	5	6	7	8	9	10	11	12	13	14															
N° Sp.	18	19	20	21	14	15	16	17																					
Sa (MPa)																													
70																													
60				x																									
50	x		o		x		x																						
40		o				o		x																					

Examination: Number of failed (x): 5 Number of non failed (o): 3 Least frequent possibility (x or o): x

S (MPa)	i	Ni	i.Ni	i^2.Ni
50	1	1	1	1
40	0	2	0	0
	Σ=	3	1	1
		N	A	B

If least frequent possibility = o: Sd=So+d(A/N+0.5)

If least frequent possibility = x: Sd=So+d(A/N-0.5)

Here: d= 10 MPa
So= 40 MPa

Result: **48.33** MPa

Standard deviation estimation:

Test: $(NB-A^2)/N^2 =$ 0.2

If test < 0.3 estimation is impossible

If test > 0.3 $S=1.62\ d\ [(NB-A^2)/N^2+0.029]$

Result: S = 4.1 MPa

Annex 7: Data Sheet results of R5 steel tests

In this annex are presented the fatigue results of R5 steel crack initiation tests are presented and the staircase data of such results.

All the tests were carried out at room temperature by using an ultrasonic fatigue testing machine at 20 kHz at different R ratio with and without corrosion.

Index of data

Data sheet of R5 steel crack initiation tests in air, without corrosion, R=-1 2

Staircase of R5 tests in air, without any corrosion, R=-1 3

Data sheet of R5 steel crack initiation tests in air, without corrosion, R=0.5 4

Staircase of R5 tests in air, without any corrosion, R=0.3 5

Data sheet of R5 steel crack initiation tests, in air, with pre-corrosion, R=-1 6

Staircase of R5 tests in air, with pre-corrosion, R=-1 7

Data sheet of R5 steel crack initiation tests, in sea water flow, R=-1 8

Data sheet of R5 steel crack initiation tests in air, without corrosion, R=-1

Material:	**R5 steel**	Date: Dec 2006 - May 2007
	specimens without any corrosion	
Lot:	**1**	Provenance: Vicinay Cadenas
Name of the test:	**R5 steel crack initiation of non corroded specimens**	

Solicitation type:	**Tension-Compresion**	**R=**	**-1**
Lifespan aim:	**10^9 cycles**	Frequency:	20 kHz
Cycle Form:	sinusoidal	Machine:	Ultrasonic
Test temperature:	Room	Operator:	RPM
Environment:	Air		
Specimen Geometry:	**Smooth**	Treatment:	Quenching
Kt (tension):	1		
Useful diameter. (mm):	3	Fabrication:	Foundry
Method of examination:	Staircase	Unit of S:	MPa
Number of tested specimens:	**18**	Unit of Nf:	cycles
Number of failed specimens:	14	Unit of Uo:	µm

Test	Spec.	Uo	Stress amp., MPa	Nf	Result
18	18	15.71	425	3.20E+05	x (failed)
19	19	15.61	422.5	6.20E+05	x (failed)
20	20	15.52	420	7.80E+05	x (failed)
21	21	14.78	400	2.10E+07	x (failed)
22	22	14.59	395	5.61E+08	x (failed)
23	23	14.41	390	1.25E+06	x (failed)
24	24	14.22	385	3.62E+07	x (failed)
25	25	14.04	380	2.78E+06	x (failed)
26	26	13.85	375	1.10E+09	o (Not failed)
27	27	14.04	380	7.27E+07	x (failed)
28	28	13.95	375	1.50E+09	o (Not failed)
29	29	14.04	380	1.70E+09	x (failed)
31	31	14.13	385	1.50E+09	o (Not failed)
34	34	14.59	395	2.13E+08	x (failed)
35	35	14.51	392.5	5.11E+08	x (failed)
36	36	14.41	390	1.85E+07	x (failed)
37	37	14.22	385	1.20E+09	o (Not failed)
38	38	14.32	387.5	7.21E+08	x (failed)

Staircase of R5 tests in air, without any corrosion, R=-1

Test:	**Crack initiation R=-1 R5 steel**	Date:	July 2009	Specimen Geometry:	**Smooth**
Material:	**R5 steel**	Provenance:	Vicinay Cadenas		
Solicitation type:	**Tension-Compression**	**R=**	**-1.0**	Useful diameter. (mm):	3
Lifespan aim:	**10^9 cycles**	Frequency:	20 kHz	Treatment:	None
Cycle form:	sinusouidal	Machine:	Ultrasonic		
Test temperature (°C):	Room	Operator:	RPM	Manufacturing	Vicinay Cadenas
Environment:	Air	Nominal or local stresses:		Nominal	

Order	1	2	3	4	5	6	7	8	9	10	11
N° Sp.	21	22	23	37	36	24	25	26	27	28	29
Sa (MPa)											
400	x										
395		x									
390			x		x						
385				o		x					
380							x		x		x
375								o		o	

Examination: Number of failed (x): 8 Number of non failed (o): 3 Least frequent possibility (x or o): o

S (MPa)	i	Ni	i.Ni	i^2.Ni
385	2	1	2	4
380	1	0	0	0
375	0	2	0	0
	Σ=	3	2	4
		N	A	B

If least frequent possibility = o: Sd=So+d(A/N+0.5)

If least frequent possibility = x: Sd=So+d(A/N-0.5)

Here: d= 5 MPa
So= 375 MPa

Result: **380.83** MPa

Standard deviation estimation:

Test: $(NB-A^2)/N^2 =$ 0.9

If test < 0.3 estimation is impossible

If test > 0.3 $S=1.62\ d\ [(NB-A^2)/N^2+0.029]$

Result: S = 7.4 MPa

Data sheet of R5 steel crack initiation tests in air, without corrosion, R=0.5

Material:	**R5 steel**	Date:	July 2009
	without any corrosion		
Lot:	**1**	Provenance:	Vicinay Cadenas
Name of the test:	**R5 steel crack initiation in air, room temperature, R=0.3**		

Solicitation type:	**Tension-Tension**	**R=**	**0.3**
Lifespan aim:	**10^9 cycles**	Frequency:	20 kHz
Cycle Form:	Sinusoidal	Machine:	Ultrasonic
Test temperature:	Room	Operator:	RPM
Environment:	Air	**Kt=**	1.02
Specimen Geometry:	**Smooth**	Treatment:	None
Useful diameter. (mm):	3	Fabrication:	Foundry
Method of examination:	Staircase		
Number of tested specimens:	**8**	Unit of S:	MPa
Number of failed specimens:	4	Unit of Nf:	cycles

			S nominal					
Test	Spec.	Pocket	Smean	Smin	Smax	Samp	N	Result
1	B45	1	501.4	231.4	774.4	270	3.970E+08	x (failed)
2	B53	1	482.9	222.8	742.8	260	1.000E+09	o (survivor)
3	B52	1	501.4	231.4	774.4	270	9.120E+08	x (failed)
4	B54	1	482.9	222.8	742.8	260	1.020E+09	o (survivor)
5	B47	1	501.4	231.4	774.4	270	1.030E+09	o (survivor)
6	B41	1	520.0	240.0	800.0	280	4.055E+08	x (failed)
7	B44	1	501.4	231.4	774.4	270	1.000E+09	o (survivor)
8	B50	1	520.0	240.0	800.0	280	2.880E+07	x (failed)

Staircase of R5 tests in air, without any corrosion, R=0.3

Material:	**R5 steel**	Provenance:	Vicinay Cadenas		
Solicitation type:	**Tension-Tension**	**R=**	**0.3**	Useful diameter. (mm):	3
Lifespan aim:	**10^9 cycles**	Frequency:	20 kHz	Treatment:	None
Cycle form:	sinusouidal	Machine:	Ultrasonic		
Test temperature (°C):	Room	Operator:	RPM	Manufacturing	Vicinay Cadenas
Environment:	Air	Nominal or local stresses:		Nominal	

Order	1	2	3	4	5	6	7	8	9	10	11	12	13	14															
N° Sp.	B45	B53	B52	B54	B47	B41	B44	B50																					
Sa (MPa)																													
280						x		x																					
270	x		x		o		o																						
260		o		o																									

Examination: Number of failed (x): 4 Number of non failed (o): 4 Least frequent possibility (x or o): o

S (MPa)	i	Ni	i.Ni	i^2.Ni
270	1	2	2	2
260	0	2	0	0
	Σ=	4	2	2
		N	A	B

If least frequent possibility = o: Sd=So+d(A/N+0.5)

If least frequent possibility = x: Sd=So+d(A/N-0.5)

Here: d= 10 MPa
So= 260 MPa

Result: **270.00** MPa

Standard deviation estimation: Test: $(NB-A^2)/N^2 =$ 0.3

If test < 0.3 estimation is impossible

If test > 0.3 $S=1.62\ d\ [(NB-A^2)/N^2+0.029]$

Result: S = 4.5 MPa

Data sheet of R5 steel crack initiation tests, in air, with pre-corrosion, R=-1

Material:	**R5 steel**	Date: Dec 2006 - Mar 2008
	pre-corroded specimens	
Lot:	**1, 2**	Provenance: Vicinay Cadenas
Name of the test:	**R5 steel crack initiation of pre-corroded specimens**	

Solicitation type:	**Tension-Compresion**	**R=**	**-1**
Lifespan aim:	**10^9 cycles**	Frequency:	20 kHz
Cycle Form:	sinusoidal	Machine:	Ultrasonic
Test temperature:	Room	Operator:	RPM
Environment:	Air		
Specimen Geometry:	**Smooth**	Treatment:	None
Kt (tension):	1		
Useful diameter. (mm):	3	Fabrication:	Foundry
Method of examination:	Staircase	Unit of Stress:	MPa
Number of tested specimens:	**19**	Unit of Nf:	cycles
Number of failed specimens:	8	Unit of Uo:	µm

Test	Spec.	Uo	Stress	Nf	Result
Prof. Bathias' Lab					
4	4	14.71	400	7.75E+05	x (failed)
5	5	7.35	200	1.00E+09	o (Not failed)
6	6	11.03	300	1.00E+09	o (Not failed)
7	1	12.87	350	1.18E+06	x (failed)
8	8	11.95	325	1.00E+09	o (Not failed)
9	6	12.87	350	2.49E+06	x (failed)
10	12	12.69	345	3.76E+06	x (failed)
11	15	12.32	340	5.00E+09	o (Not failed)
12	17	12.5	340	1.50E+05	x (failed)
LAMEFIP Bordeaux					
1	C2	11.044	300	1.07E+09	o (Not failed)
2	C5	11.965	325	1.90E+09	o (Not failed)
3	C8	12.884	350	1.27E+09	o (Not failed)
4	C7	13.252	360	5.48E+08	x (failed)
5	C4	12.884	350	5.17E+09	o (Not failed)
6	C6	13.068	355	1.51E+09	o (Not failed)
7	C3	13.252	360	1.38E+09	o (Not failed)
8	C9	13.621	370	4.37E+08	x (failed)
9	C10	14.71	400	1.58E+09	o (Not failed)
10	C10	15.63	425	1.56E+07	x (failed)

Note: An initial part of the tests was carried out in Prof. Bathias' laboratory in Paris
Final part was carried out at LAMEFIP Bordeaux.

Staircase of R5 tests in air, with pre-corrosion, R=-1

Test:	**Crack initiation R=-1 R5 steel**	Date:	July 2009	Specimen Geometry:	**Smooth**
Material:	**R5 steel**	Provenance:	Vicinay Cadenas		
Solicitation type:	**Tension-compression**	**R=**	**-1.0**	Useful diameter. (mm):	3
Lifespan aim:	**10^9 cycles**	Frequency:	20 kHz	Treatment:	None
Cycle form:	sinusouidal	Machine:	Ultrasonic		
Test temperature (°C):	Room	Operator:	RPM	Manufacturing	Vicinay Cadenas
Environment:	Air	Nominal or local stresses:		Nominal	

Order	1	2	3	4	5	6	7	8																					
N° Sp.	C15	C8	C7	C4	C3	C9																							
Sa (MPa)																													
370						x																							
360			x		o																								
350		o		o																									
340	o																												
330																													
320																													

Examination: Number of failed (x): 2 Number of non failed (o): 4 Least frequent possibility (x or o): x

S (MPa)	i	Ni	i.Ni	i^2.Ni
370	1	1	1	1
360	0	1	0	0
	Σ=	2	1	1
		N	A	B

If least frequent possibility = o: Sd=So+d(A/N+0.5)

If least frequent possibility = x: Sd=So+d(A/N-0.5)

Here: d= 10 MPa
So= 360 MPa

Result: **360.00** MPa

Standard deviation estimation: Test: $(NB-A^2)/N^2 =$ 0.3

If test < 0.3 estimation is impossible

If test > 0.3 $S=1.62\ d\ [(NB-A^2)/N^2+0.029]$

Result: S = 4.5 MPa

Data sheet of R5 steel crack initiation tests, in sea water flow, R=-1

Material:	**R5 steel**	Date:	April-October 2008
Lot:	**1**	Provenance:	Vicinay Cadenas
Name of the test:	**R5 steel crack initiation in sea water flow**		

Solicitation type:	**Tension-Compresio**	**R=**	**-1**
Lifespan aim:	**10^9 cycles**	Frequency:	20 kHz
Cycle Form:	sinusoidal	Machine:	Ultrasonic
Test temperature:	Room	Operator:	RPM/TPL
Environment:	Sea water flow A3 100 ml/min		
Specimen Geometry:	**Smooth**	Treatment:	None
Kt (tension):	1		
Useful diameter. (mm):	3	Fabrication:	Foundry
Method of examination:	Staircase		
Number of tested specimens:	**19**	Unit of S:	MPa
Number of failed specimens:	19	Unit of Nf:	cycles

		S nominal				
Test	Spec.	Smean	Smin	Smax	Nf	Observations
1	3	0	-350	350	7.40E+06	x (failed)
2	6	0	-300	300	9.72E+06	x (failed)
3	7	0	-280	280	4.45E+07	x (failed)
4	8	0	-260	260	3.49E+07	x (failed)
5	9	0	-240	240	5.21E+07	x (failed)
6	10	0	-200	200	1.08E+08	x (failed)
7	12	0	-180	180	1.41E+08	x (failed)
8	13	0	-160	160	1.83E+08	x (failed)
9	16	0	-120	120	3.57E+08	x (failed)
10	21	0	-100	100	4.09E+08	x (failed)
11	20	0	-162	162	4.29E+07	x (failed)
12	25	0	-124	124	1.45E+08	x (failed)
13	19	0	-124	124	1.95E+08	x (failed)
14	17	0	-124	124	2.48E+08	x (failed)
15	24	0	-60	60	2.63E+08	x (failed)
16	22	0	-60	60	1.86E+08	x (failed)
17	40	0	-60	60	1.71E+09	x (failed)
18	48	0	-60	60	1.13E+08	x (failed)
19	36	0	-50	50	1.34E+08	x (failed)
20	39	0	-360	360	3.75E+06	x (failed)
21	37	0	-360	360	7.02E+06	x (failed)
22	38	0	-360	360	7.71E+06	x (failed)

Note: Staircase data are not available.

Annex 8:
Crack growth duration calculations for R5 steel with corrosion

1. Procedure for computing the crack growth life using analytical approximations

Considering a hemispherical defect on the surface of R5 steel specimen with radius R and in the front of this, an initial crack a_{int}, the Paris-Hertzberg crack growth law is applied to calculate the crack growth duration at three different stages of the crack growth: short crack growth; small crack growth; and long crack growth.

The Paris Hertzberg law establishes that the behavior of the da/dN curve of a material follows the next equations:

At the corner:

$$\frac{\mathrm{d}a}{\mathrm{d}N} = b \text{ and } \frac{\Delta K_{\text{eff}}}{E\sqrt{b}} = 1 \tag{8.- 1}$$

And beyond of the corner:

$$\frac{\mathrm{d}a}{\mathrm{d}N} = b\left(\frac{\Delta K_{\text{eff}}}{E\sqrt{b}}\right)^3 \tag{8.- 2}$$

Knowing the da/dN=f(ΔK) curve for R5 steel corresponds to such behavior, the next equations for the calculation of the three mentioned stages are used.

For short crack growth from a_{int} to a_0

$$N_{a_{\text{int}}-a_0} = \frac{E^2}{Y_0^2\sigma_a^2\pi(\alpha/2-1)}\left[\left(\frac{a_0}{a_{\text{int}}}\right)^{(\alpha/2-1)} - 1\right] \tag{8.- 3}$$

with the notation and assumption:

$$Y_0 = Y\left(\frac{a_0}{R}, \nu\right) = \text{cte} \tag{8.- 4}$$

For small crack growth from a_0 to a_i

$$N_{a_0-a_i} = \frac{2E^2}{Y_0^2 \sigma_a^2 \pi}\left[1 - \sqrt{\frac{a_0}{a_i}}\right] \tag{8.- 5}$$

Assuming from a_0 to a_i

$$Y(x,\nu) = Y\left(\frac{a_0}{R},\nu\right) \approx Y_0 = \text{cte} \tag{8.- 4}$$

To verify this assumption we can evaluate Equation (8.- 4) for the characteristic crack length for a_0 and ai.

For instance, for a radius pit R=40 µm in R5 steel (ν=0.29), an initial crack a_0=10 µm and a_i=30 µm, with Equation (8.- 10)

$Y(x, \nu)$= 1.728 for a_0=5 µm

$Y(x, \nu)$= 1.203 for a_i=30 µm

Figure 1 shows a graphic of $Y(x, \nu)$ as function of the crack length a up to the final length possible for a crack growing. It is observed a constant behavior of $Y(x, \nu)$ after a specific crack length. This constant $Y(x, \nu)$ begins before when radius pit R is smaller.

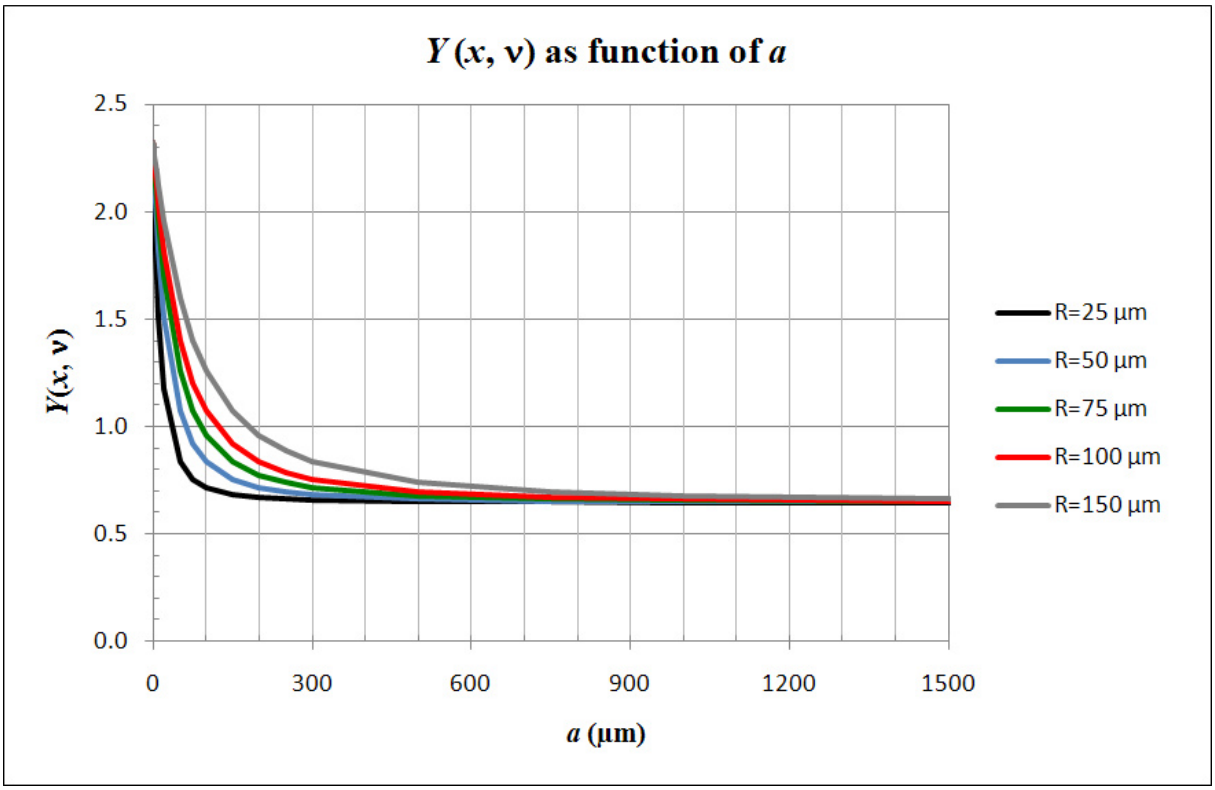

Figure 1. $Y(x,\nu)$ as function of crack length a for different radius pit R.

For long crack growth from a_i to a

$$N_{a_i-a} = \frac{2E^2 Y_0}{Y(a_i/R)^3\ \sigma_a^2\ \pi}\left[x^3\sqrt{\frac{a_0}{a_i}} - x^3\sqrt{\frac{a_0}{a}}\right] \tag{8.- 6}$$

Assuming from a_i to the final crack length a

$$Y(a/R)\ \approx Y\left(\frac{a_i}{R}, \nu\right) = \text{cte} \tag{8.- 7}$$

Like in small crack growth region, we can evaluate the Equation (8.- 7) for characteristic lengths for a_i and a.

For instance, for a radius pit R=50 µm in R5 steel (ν=0.29), a crack a_i=50 µm and a=2300 µm, with Equation (8.- 10):

$Y(x, \nu)$= 1.073 for a_i=50 µm

$Y(x, \nu)$= 0.647 for a=2300 µm

(See Figure 1)

Total number of cycles for crack propagation

The total number of cycles for crack propagation in then the addition of Equations (8.- 3), (8.- 5) and (8.- 6)

$$N_{Prop} = N_{a_{\text{int}}-a_0} + N_{a_0-a_i} + N_{a_i-a} \tag{8.- 8}$$

2. Procedure for computing the crack growth life using full numeric integration

The computing of the crack growth life using the previous procedure was done using some assumptions to simplify the calculation. Considering that in certain stages:

$$Y\left(\frac{a}{R}, \nu\right) = \text{cte}$$

But in fact

$$Y\left(\frac{a_0}{R},\nu\right) > Y\left(\frac{a_i}{R},\nu\right) > Y\left(\frac{a}{R},\nu\right) \tag{8.- 9}$$

If $a_0 < a_i < a$, as shown in Figure 2.

This function is:

$$Y(x,\nu) = 1.015\left[A(\nu) + B(\nu)\left(\frac{x}{1+x}\right) + C(\nu)\left(\frac{x}{1+x}\right)^2 + D(\nu)\left(\frac{x}{1+x}\right)^3\right] \tag{8.- 10}$$

where:

$$x = \frac{a}{R},\ A(\nu) = 1.683 + \frac{3.366}{7-5\nu},\quad B(\nu) = -1.025 - \frac{12.3}{7-5\nu},\quad C(\nu) = -1.089 + \frac{14.5}{7-5\nu},$$
$$D(\nu) = 1.068 - \frac{5.568}{7-5\nu} \tag{8.- 11}$$

Integrations are used and it is necessary to establish the numerical limits for each stage of integration.

Then, from

$$\frac{\Delta K_{\text{eff}}}{E\sqrt{b}} = \frac{1.015\,\sigma_a\sqrt{\pi a}\ Y\left(\frac{a}{R},\nu\right)}{E\sqrt{b}} \tag{8.- 12}$$

Knowing, E, b, σ_a and ν; a_0 and a_i can be obtained.

$$a_0 \rightarrow \frac{\Delta K_{\text{eff}}}{E\sqrt{b}} = 1\,;\quad a_i \rightarrow \frac{\Delta K_{\text{eff}}}{E\sqrt{b}} = 3 \tag{8.- 13}$$

a_{int} is calculated for each value of a_{int}/a_0.

a is obtained by measuring the end of the fracture observed on the fracture surface.

Due to the complexity of the function, the numerical integrations were carried out by using the software Mathematica 5.2.

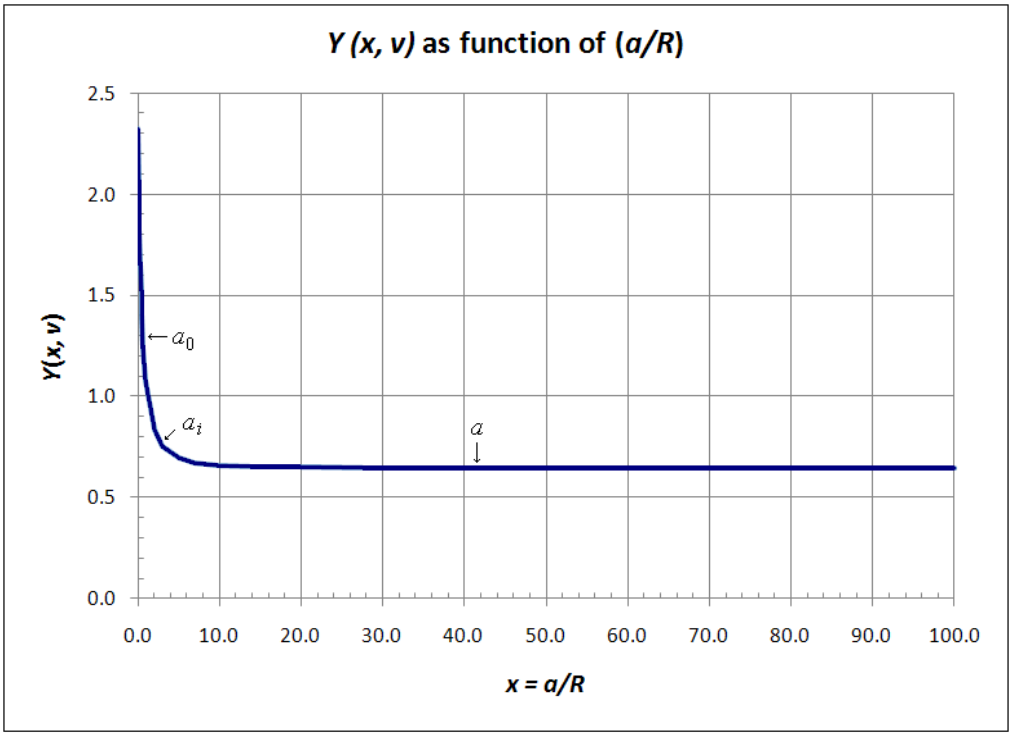

Figure 2. $Y(x,\nu)$ as function of x according to Equation (8.- 10) for R5 steel with ν=0.29

3. Example of calculation

Figure 3 shows a scheme of the characteristic fracture face in R5 steel failed in fatigue due to corrosion pitting.

A crack of length a_{int} initiates to grow in front a corrosion pit on the specimen surface. During the short crack growth it grows up to a length a_0. During the small crack growth it grows from a_0 to a_i and finally it grows up to failure to a length a (a_{final}).

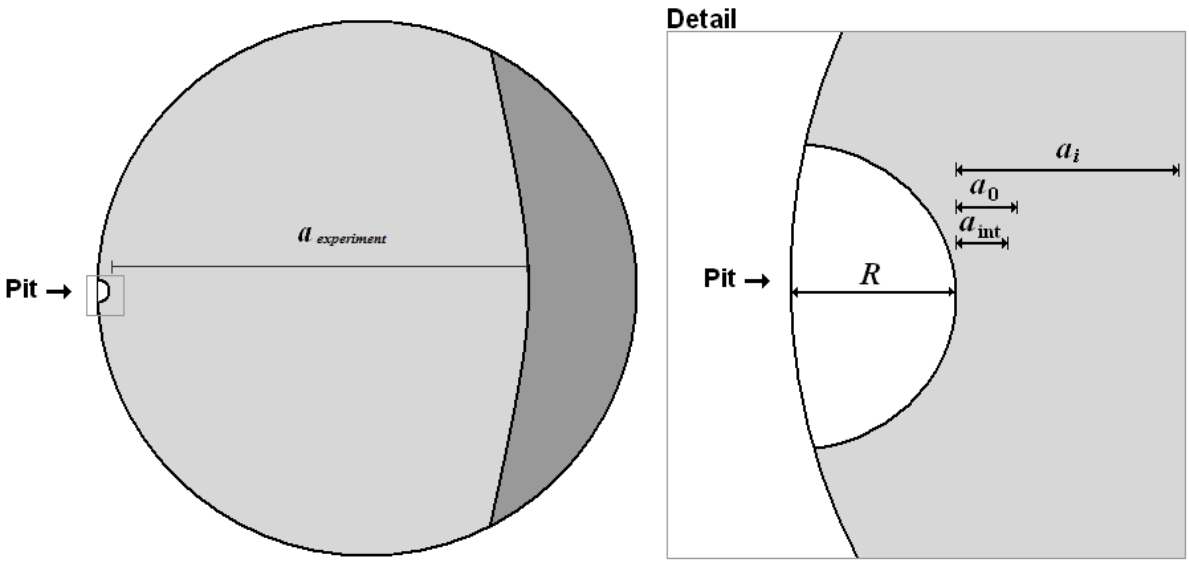

Figure 3. Sketch of a characteristic fatigue fracture face in R5 steel with pitting corrosion.

For R5 steel:

E=210 GPa, ν=0.29 and b=0.285 nm

Taking as example a test at σ_a=360 MPa that has an experimental number of cycles to failure $N_{experimental}$=5.5×10^8 where we have observed a pit as crack initiation site with a radius R=48 µm and a=2.3 mm (R and a are measured from fractography) in Figure 4.

Replacing these values in Equation (8.- 12) we must to make

$\frac{\Delta K_{\text{eff}}}{E\sqrt{b}} = 1$ for obtaining a_0 and $\frac{\Delta K_{\text{eff}}}{E\sqrt{b}} = 3$ for obtaining a_i

Then

for a_0

$$1 = \frac{(1.015)(250)\sqrt{\pi a}\ Y\left(\frac{a}{R}, \nu\right)}{210 \times 10^3\sqrt{0.285 \times 10^{-9}}}$$

for a_i

$$3 = \frac{(1.015)(250)\sqrt{\pi a}\ Y\left(\frac{a}{R}, \nu\right)}{210 \times 10^3\sqrt{0.285 \times 10^{-9}}}$$

Calculating with Mathematica 5.2 software

a_0= 9.318 µm

a_i= 88.44 µm

a_{int} is calculated for each relation a_{int}/a_0,

For a_{int}/a_0=0.9 → a_{int}= 8.386 µm

For a_{int}/a_0=0.94 → a_{int}= 8.758 µm

For a_{int}/a_0=0.97 → a_{int}= 8.038 µm

These calculated crack lengths are the parameters for solving Equations (8.- 3), (8.- 5) and (8.- 6).

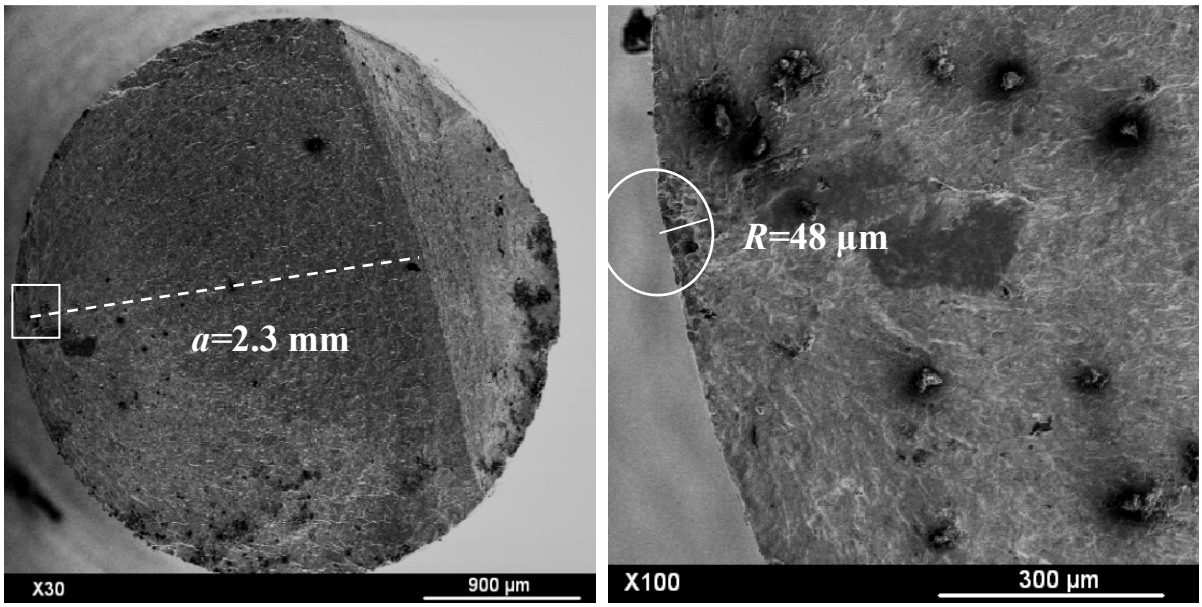

Figure 4. Fracture face of a R5 steel specimen with pre-corrosion tested at R= –1 , in air and room temperature, σ_a=360 MPa, Failed at $N_{experimental}$= 5.48×10^8 cycles

The results of calculation of the crack growth durations of this (Case 1) and other examples are presented in next sections.

4. Calculations for R5 steel with pre-corrosion and corrosion with sea water flow

Table 1 shows three calculations using the analytical approximations (*Analytical* column) of Equation (8.- 8) and the calculations using numerical integrations (*Integrated* column), for R5 specimens with pitting from pre-corrosion.

α	a_{int}/a_0	$N_{a_{int}-a_0}$	N_{a0-ai}		N_{ai-a}		N_{Prop}		%Life	
			Analytic	*Integrated*	*Analytic*	*Integrated*	*Analytic*	*Integrated*	*A*	*I*
Case 1: σ_a=360 MPa, R=48 µm, a_0=9.32 µm, a_i=88.4 µm, a=2.4 mm, $N_{experimental}$ = 5.5×10^8 cycles										
25	0.9	6,704	44,151	128,975	4,507,080	8,168,000	4,557,935	8,303,679	0.83	1.52
	0.94	2,947					4,554,178	8,299,922	0.83	1.51
	0.97	1192					4,552,423	8,298,167	0.83	1.51
100	0.9	115,801	44,151	128,975	4,507,080	8,168,000	4,667,032	8,412,776	0.85	1.54
	0.94	13,136					4,564,394	8,310,138	0.83	1.52
	0.97	2,300					4,553,531	8,299,275	0.83	1.51
200	0.9	11,184,860	44,151	128,975	4,507,080	8,168,000	15,736,091	19,481,835	2.87	3.56
	0.94	150,676					4,701,907	8,447,651	0.86	1.54
	0.97	6,404					4,557,635	8,303,379	0.83	1.52
Case 2: σ_a=370 MPa, R=70 µm, a_0=7.104 µm, a_i=24.9 µm, a=2.15 mm, $N_{experimental}$ = 4.4×10^8 cycles										
25	0.9	5,113	23,220	31,925	1,402,860	7,893,000	1,431,193	7,930,038	0.33	1.81
	0.94	2,248					1,428,328	7,927,173	0.33	1.81
	0.97	909					1,426,989	7,925,834	0.33	1.81
100	0.9	88,331	23,220	31,925	1,402,860	7,893,000	1,541,411	8,013,256	0.35	1.83
	0.94	10,041					1,436,121	7,934,966	0.33	1.82
	0.97	1,754					1,427,834	7,926,679	0.33	1.81
200	0.9	8,531,566	23,220	31,925	1,402,860	7,893,000	9,957,646	16,456,491	2.28	3.77
	0.94	114,932					1,541,012	8,039,857	0.35	1.84
	0.97	4,884					1,430,964	7,930,409	0.33	1.81
Case 3: σ_a=425 MPa, R=37.5 µm, a_0=6.28 µm, a_i=51.32 µm, a=1.96 mm, $N_{experimental}$ = 1.56×10^7 cycles										
25	0.9	4,519	28,651	68,150	2,717,227	5,928,560	2,750,397	6,001,229	17.2	37.5
	0.94	1,987					2,747,865	5,998,697	17.2	37.5
	0.97	804					2,746,682	5,997,514	17.2	37.5
100	0.9	78,065	28,651	68,150	2,717,227	5,928,560	2,823,943	6,074,775	17.6	38.0
	0.94	8,874					2,754,752	6,005,584	17.2	37.5
	0.97	1,550					2,747,428	5,998,260	17.2	37.5
200	0.9	7,540,073	28,651	68,150	2,717,227	5,928,560	10,285,951	13,536,783	64.3	84.6
	0.94	101,575					2,847,453	6,098,285	17.8	38.1
	0.97	4,317					2,750,195	6,001,027	17.2	37.5

Table 1. Analytical and numerical calculation of crack growth duration for R5 steel with hemispherical pitting made with pre-corrosion.

Table 1 shows that the difference between analytic approximation and numerical integration lead roughly to similar number of cycles of crack propagation. The differences are around a factor 2 of the integrated results in relation with the analytical approximation.

Case 3 is closer to the regime of megacycle fatigue. In this specific case the crack growth represents between 17% and 37% of the total life.

Table 2 shows some calculations using the analytical approximations (*Analytical* column) of Equation (8.- 8) and using numerical integrations (*Integrated* column), for R5 specimens with pitting from corrosion under sea water flow.

α	a_{int}/a_0	$N_{a_{int}-a_0}$	N_{a0-ai}		N_{ai-a}		N_{Prop}		%Life	
			Analytic	*Integrated*	*Analytic*	*Integrated*	*Analytic*	*Integrated*	*A*	*I*
Case 4: σ_a=160 MPa, R=300 µm, a_0=41.5 µm, a_i=232 µm, a=2.6 mm, $N_{experimental}$ = 1.83×10^8 cycles										
25	0.9	29,840	168,014	312,916	10,258,700	30,150,000	10,456,554	30,492,756	5.7	16.5
	0.94	13,120					10,439,834	30,476,036	5.6	16.5
	0.97	5,306					10,432,020	30,468,222	5.6	16.5
100	0.9	515,466	168,014	312,916	10,258,700	30,150,000	10,942,180	30,978,382	5.9	16.7
	0.94	58,593					10,485,307	30,521,509	5.7	16.5
	0.97	10,237					10,436,951	30,473,153	5.6	16.5
200	0.9	49,787,104	168,014	312,916	10,258,700	30,150,000	60,213,818	80,250,020	32.5	43.4
	0.94	670,703					11,097,417	31,133,619	6.0	16.8
	0.97	28,504					10,455,218	30,491,420	5.7	16.5
Case 5: σ_a=350 MPa, R=200 µm, a_0=6.66 µm, a_i=15.57 µm, a=2.3 mm, $N_{experimental}$ = 7.4×10^6 cycles										
25	0.9	4,796	16,174	17,360	902,654	5,003,570	923,624	5,025,726	12.5	67.9
	0.94	2,109					920,937	5,023,039	12.4	67.9
	0.97	853					919,681	5,021,783	12.4	67.9
100	0.9	82,854	16,174	17,360	902,654	5,003,570	1,001,682	5,103,784	13.5	69.0
	0.94	9,481					928,246	5,030,348	12.5	68.0
	0.97	1,645					920,473	5,022,575	12.4	67.9
200	0.9	8,002,548	16,174	17,360	902,654	5,003,570	8,921,376	13,023,478	120.6	176.0
	0.94	107,806					1,026,634	5,128,736	13.9	69.3
	0.97	4,582					923,410	5,219,512	12.5	70.5
Case 6: σ_a=260 MPa, R=135 µm, a_0=14.6 µm, a_i=54.79 µm, a=2.81 mm, $N_{experimental}$ = 3.49×10^7 cycles										
25	0.9	10,530	49,619	71,100	2,977,594	15,090,000	3,037,743	15,171,630	8.68	43.3
	0.94	4,630					3,031,843	15,165,730	8.66	43.3
	0.97	1,872					3,029,085	15,162,972	8.65	43.3
100	0.9	181,902	49,619	71,100	2,977,594	15,090,000	3,209,115	15,343,002	9.17	43.8
	0.94	20,677					3,047,890	15,181,777	8.71	43.4
	0.97	3,613					3,030,826	15,164,713	8.66	43.3
200	0.9	17,569,325	49,619	71,100	2,977,594	15,090,000	20,596,538	32,730,425	58.85	93.5
	0.94	236,684					3,263,897	15,397,784	9.33	44.0
	0.97	10,059					3,037,272	15,171,159	8.68	43.3
Case 7: σ_a=240 MPa, R=220 µm, a_0=15.65 µm, a_i=43.92 µm, a=2.88 mm, $N_{experimental}$ = 5.2 ×10^7 cycles										
25	0.9	11,267	44,271	53,136	2,431,480	14,559,000	2,487,018	14,623,403	4.76	28.0
	0.94	4,954					2,480,705	14,617,090	4.75	28.0
	0.97	2,003					2,477,754	14,614,139	4.75	28.0
100	0.9	194,621	44,271	53,136	2,431,480	14,559,000	2,670,372	14,806,757	5.12	28.4
	0.94	22,123					2,497,874	14,634,259	4.79	28.0
	0.97	3,865					2,479,616	14,616,001	4.75	28.0
200	0.9	18,797,746	44,271	53,136	2,431,480	14,559,000	21,273,497	33,409,882	40.75	64.0
	0.94	253,232					2,728,983	14,865,368	5.23	28.5
	0.97	10,762					2,486,513	14,622,898	4.76	28.0
Case 8: σ_a=200 MPa, R=290 µm, a_0=23.01 µm, a_i=67.96, a=2.81 mm, $N_{experimental}$ = 1.08 ×10^8 cycles										
25	0.9	16,566	67,524	83,604	3,624,895	19,795,000	3,708,984	19,895,166	3.37	18.1
	0.94	7,283					3,699,701	19,885,883	3.36	18.1
	0.97	2,946					3,695,364	19,881,546	3.36	18.1
100	0.9	286,158	67,524	83,604	3,624,895	19,795,000	3,978,576	20,164,758	3.62	18.3
	0.94	32,528					3,724,946	19,911,128	3.39	18.1
	0.97	5,683					3,698,101	19,884,283	3.36	18.1
200	0.9	27,639,000	67,524	83,604	3,624,895	19,795,000	31,331,418	47,517,600	28.48	43.2
	0.94	372,337					4,064,755	20,250,937	3.70	18.4
	0.97	15,824					3,708,242	19,894,424	3.37	18.1

Table 2. Analytical and numerical calculation of crack growth duration for R5 steel with hemispherical pitting made with corrosion under sea water flow.

It is observed in Table 1 that the number of cycles of crack propagation are roughly similar if the calculation is done by using analytic approximation or numerical integration . The differences in the proportion of crack growth life are around a factor between 3 and 5 for the integrated results in relation with the analytical approximation. This compared with the total fatigue life is even small.

For the cases 4, 6 and 7, the fatigue life lies near to the megacycle regime. Here, the period of crack propagation is longer, representing between 28% to 69% of the total fatigue life.

5. Conclusion

After the calculations of the propagation duration of a crack emanating from a corrosion pit, it is observed for both, pre-corroded specimens and specimens corroded in sea water flow, that fatigue crack growth is only a small portion of the total as soon as the fatigue life is more than $\sim 10^7$ cycles.

Results of calculations in Table 1 and Table 2 show that the duration of propagation period is small compared with the total fatigue life of the specimen, except for α=200 and a_{int}/a_0=0.9. It is noticeable that with high α and large a_{int}/a_0 similar N_{Prop} results are obtained than with a low α and small a_{int}/a_0. That is because with a higher α the crack does not grow as far due to the slope of the da/dN curve in the threshold region, then a_{int}/a_0 must be larger, and with a lower α, a_{int}/a_0 must be smaller.

For the cases with α=200 and a_{int}/a_0=0.9 the calculation gives always larger estimation because with the relation a_{int}/a_0=0.9 it exists a larger difference between a_0 and a_{int} than with a_{int}/a_0=0.94 or a_{int}/a_0=0.97, and at high α=200, crack growth rate is slower due to the slope of the da/dN curve in the threshold region, then a larger number of cycles is estimated.

The presented calculations were done assuming that crack growth rate is similar in air and under sea water flow. But according to the crack growth rate results in sea water flow one can observe that crack growth is little faster than in air, then the number of cycles of propagation would be less.

STUDY OF THE FATIGUE STRENGTH IN THE GIGACYCLE REGIME OF METALLIC ALLOYS USED IN AERONAUTICS AND OFF-SHORE INDUSTRIES

ABSTRACT: This work concerns the study of the gigacycle fatigue strength of two materials, the first one used in gearboxes of turbines for helicopters and the second one used in offshore chain lines (petroleum platforms).

A cast aluminium alloy AS7G06-T6 is studied. This alloy is used in the frame of the gearboxes of helicopters turbines. It is submitted to very high number of cycles due to the working duration of the engine (3,000 hours) and the rotation speed of the turbine in operating conditions: around 30,000 rpm. Specimens from real components were tested at both room temperature and 150 °C in air, and at three different stress ratios, to investigate both the temperature and the mean stress effect on the gigacycle fatigue strength. The fatigue strength at high number of cycles (10^9) and the crack initiation cause have been investigated.

A hot rolled low alloy steel, designed R5 according to the international denomination of the International Classification Societies of offshore systems is also studied. This steel is used for manufacturing mooring chains for offshore petroleum platforms in the European North Sea. It is requested to have high strength, as well as good corrosion resistance. Indeed, chains are designed for 30 years, and they are loaded at low frequency (~0.5 Hz) due to the waves in sea water environment during long time (25 to 30 years) all the day and all the year long. This represents more than 10^8 cycles. Specimens from R5 steel chains were tested in fatigue at different R ratios and at three different conditions; pre-corroded specimens in air, and virgin specimens in air and under sea water flow simultaneously. Fatigue strength in the very high cycle regime and the causes of the crack initiation were investigated.

In particular, it is looked for understand the effect of the defects on gigacycle fatigue strength. The fatigue failure in AS7G06-T6 cast aluminium alloy is due to porosities of manufacturing. For R5 steel, corrosion pits are the cause of fatigue failure. An assessment of the crack growth duration is proposed and shows that beyond to 10^7 cycles the fatigue life is dominated by the crack initiation stage and not by propagation.

Keywords : Gigacycle fatigue, fatigue corrosion, defect, crack initiation, crack growth.

ETUDE DE LA RESISTANCE A LA FATIGUE GIGACYCLIQUE D'ALLIAGES METALLIQUES UTILISES DANS L'INDUSTRIE AERONAUTIQUE ET OFF-SHORE

RESUME : Ce travail concerne l'étude de la résistance à la fatigue dans le domaine gigacyclique de deux matériaux. Le premier, AS7G06 est utilisé pour la fabrication des carters de turbines pour hélicoptères, le second, l'acier R5, est utilisé pour la fabrication des chaînes pour plates-formes pétrolières.

L'alliage d'aluminium AS7G06 moulé utilisé dans les carters de turbines est soumis à un très grand nombre de cycles en raison de la durée d'utilisation et de la vitesse de rotation de la turbine, environ 30.000 tr/min. Les échantillons provenant de vraies pièces ont été testés à température ambiante et à 150 °C, et sous trois rapports de charge. La résistance à la fatigue à très grand nombre de cycles au delà du milliard de cycles a été étudié, l'amorçage des fissures est systématiquement dues aux retassures.

L'acier R5, selon la dénomination internationale des Sociétés de la Classification Internationale des Systèmes Offshore est un acier faiblement allié. Cet acier à haute résistance est habituellement utilisé pour la fabrication de chaînes d'amarrage pour les plates-formes pétrolières offshore dans la Mer du Nord. Cet acier possède une haute résistance, et une bonne résistance à la corrosion. Les chaînes sont conçues pour 30 ans, et sont chargées à basse fréquence (~ 0,5 Hz) en raison des vagues dans en mer ; ceci représente plus de 10^8 cycles. Les échantillons provenant de chaînes en acier R5 ont été testés en fatigue à des rapports R différents, sous trois conditions différentes : éprouvettes vierges dans l'air ou pré-corrodées en brouillard salin puis cyclées à l'air ou bien éprouvettes cyclées in situ dans l'eau de mer synthétique. La résistance à la fatigue dans le régime gigacyclique et les causes de l'amorçage des fissures ont été étudiées.

En particulier, nous avons cherché à comprendre l'effet des défauts sur la résistance à la fatigue gigacyclique. La rupture en fatigue dans l'alliage AS7G06 est souvent due aux porosités. Pour l'acier R5, des piqûres de corrosion sont souvent la cause de rupture par fatigue. Une modélisation de la durée de la phase de propagation des fissures de fatigue est proposé et montre qu'au delà de 10^7 cycles, la durée de vie est essentiellement majoritairement due à la phase d'amorçage des fissures et non a la phase de propagation.

Mots clés : Fatigue gigacyclique, fatigue corrosion, défauts, amorçage de fissure, propagation de fissure.